Additively Manufactured TPMS Structures for Advanced Transpiration Cooling in Next-Generation Gas Turbines

Juchan Son

Thesis submitted to the University of Ottawa Department of Mechanical Engineering
in partial fulfillment of the requirements for the degree of

Doctor of Philosophy in Mechanical Engineering.

Faculty of Engineering - Department of Mechanical Engineering
University of Ottawa
Ottawa, Ontario, Canada

© Juchan Son, Ottawa, Canada, 2026

Abstract

In response to increasingly stringent emission regulations and demands for more efficient propulsion systems, research aimed at improving overall gas turbine efficiency through the increase of turbine inlet temperature (TIT) has become a continuously important topic. However, the elevated TIT exceeds the allowable operating temperature limits of superalloys (such as Hast-X) used in gas turbine hot gas path components. Consequently, the development of advanced cooling technologies has emerged as a critical engineering challenge.

In this context, transpiration cooling has attracted considerable attention as a potentially ideal cooling strategy. Nevertheless, conventional stochastic porous media have been limited in practical gas turbine applications due to their low mechanical strength and the difficulty of achieving uniform pore structures. With the recent advancement of additive manufacturing technologies, it has become possible to fabricate lattice-based deterministic porous media featuring complex and continuous flow passages that were previously unattainable using traditional manufacturing processes. Among such lattice-based structures, Triply Periodic Minimal Surface (TPMS) geometries are characterized by continuous curvature without sharp edges or dead-end pores, as well as a high wetted surface area. These features make TPMS structures promising candidates for transpiration cooling applications.

Accordingly, the objective of this study is to evaluate the applicability of TPMS-based deterministic porous media for transpiration cooling in next-generation gas turbine hot-section components. To this end, the effects of key TPMS morphological parameters—including type of TPMS, unit cell size, porosity, orientation angle, and morphological variation—on cooling performance were systematically investigated to identify optimal design conditions. Furthermore, the influence of internal tangential flow and porosity optimization were investigated to develop strategies for accelerating coolant-film formation. Finally, the cooling mechanisms of conventional effusion cooling and TPMS-based transpiration cooling were systematically compared through simultaneous measurements of adiabatic film effectiveness (AFE) and overall film effectiveness (OFE). This comparison provided a fundamental understanding of the relative

contributions of coolant-film protection and conjugate heat transfer, thereby clarifying the thermal protection mechanisms of TPMS-based transpiration cooling.

Experimental investigations employed binary pressure-sensitive paint (PSP) in conjunction with heat–mass transfer analogy to measure adiabatic film cooling effectiveness (AFE), while temperature-sensitive paint (TSP) measurements were used to determine overall film cooling effectiveness (OFE). The results demonstrate that TPMS-based transpiration cooling achieves superior cooling performance compared to conventional effusion cooling. In addition, by mathematically controlling spatial porosity distributions, coolant redistribution can be regulated to mitigate cooling non-uniformity caused by internal tangential flow, thereby enabling more uniform cooling performance over the entire surface. Overall, the findings of this study suggest that TPMS-based deterministic porous media represent a promising advanced cooling solution for next-generation gas turbine liners.

Acknowledgements

I would like to express my deepest gratitude to my supervisor, Professor Bertrand Jodoin, for his invaluable guidance, continuous encouragement, and unwavering support throughout my doctoral studies. His expertise, patience, and insightful mentorship have been instrumental in shaping both this dissertation and my growth as an independent researcher. It has been a privilege to learn from and work under his supervision. Professor Jodoin's passion for research and unwavering commitment to academic excellence have profoundly influenced my development as a researcher and will continue to serve as a lasting source of inspiration and a guiding principle throughout my career.

I would also like to express my sincere appreciation to my co-supervisor, Dr. Zekai Hong, Principal Research Officer at the National Research Council Canada and Adjunct Professor at the University of Ottawa, for his invaluable mentorship, technical expertise, and continuous encouragement throughout this research. His insightful guidance and constructive feedback have been instrumental in refining this dissertation and advancing my development as a researcher.

I am sincerely grateful to Dr. Patrick Richer, Assistant Professor, for providing me with the opportunity to undertake this research. His insightful advice, thoughtful guidance, and innovative ideas have been invaluable in shaping the direction of this work.

I would like to express my appreciation to all members of the Thermal Management Group of the Zero Carbon Research Team in the Gas Turbine Laboratory at the National Research Council Canada, especially Dr. Sean Yun, Dr. Mohsen Broumand, and Dr. Sina Kashanj, for their valuable suggestions and contributions to this project.

I am also grateful to the members of the Cold Spray Laboratory at the University of Ottawa, including Dr. Mohammed Yandouzi, Dr. Aleksandra Nastic, Yeongmin Pyo, Parisa Hasanpour Dastjerdi, Krutik Mistry, Hamid Rahmati, Mohammed Waleed Qanbar, Simon Beaulne, Yomna Elsahli, and Mathieu Jackson Symons, for their support, technical assistance, and collaborative spirit throughout my doctoral

studies. The insightful discussions and valuable feedback shared during our weekly group meetings have been invaluable to this research and have greatly enriched my learning experience.

Finally, I would like to express my deepest gratitude to my family, especially my wife, who has shared in the challenges of this journey, for their unconditional love, patience, and encouragement. Their unwavering belief in me has been my greatest source of strength throughout my doctoral studies. This dissertation is dedicated to them.

Table of Contents

Abstract ii
Acknowledgements iv
List of Figures viii
List of Tables xii
List of Abbreviations xiii
Chapter 1 Introduction 1
1.1 Background 1
1.2 Overview of Research Objectives 6
1.3 Thesis Outline 7
Chapter 2 Literature Review 9
2.1 Historical Development of Thermal Management Technologies for Gas Turbine Components 9
2.2 Fundamental Mechanisms of Effusion and Transpiration Cooling 12
2.3 Effusion Cooling as the Current State-of-the-Art 14
2.3.1 Effect of inclination and compound angles 14
2.3.2 Effect of hole pitch spacing 16
2.3.3 Effect of hole geometry 16
2.3.4 Effect of blowing and density ratios 18
2.4 Transpiration Cooling as a Next-Generation Cooling Technique 21
2.4.1 Effect of type of porous medium 21
2.4.2 Previous efforts to optimize transpiration cooling 24
2.4.3 Challenges of conventional transpiration cooling 28
2.4.4 Prior efforts in adopting additive manufacturing for transpiration cooling 31
2.5 TPMS Structures as Promising Architectures for Transpiration Cooling 33
Chapter 3 Research Objectives 37
3.1 The Influence of TPMS Unit Cell Size on Transpiration Cooling Performance 38
3.2 The Influence of TPMS Porosity on Transpiration Cooling Performance 38
3.3 The Influence of TPMS Orientation Angle on Transpiration Cooling Performance 38
3.4 The Influence of TPMS Morphology on Transpiration Cooling Performance 39
3.5 The Influence of Internal Tangential Flow on Transpiration Cooling 39
3.6 Porosity Grading for Uniform Coolant Distribution 40
3.7 Cooling Mechanisms of Effusion and TPMS-based Transpiration Cooling 40
Chapter 4 Methodology and Research Approach 42

4.1 TPMS Structure 42
4.2 Fabrication of TPMS Test Coupons 47
4.3 Overview of Experiment Setup 51
4.4 Fundamentals of Pressure Sensitive Paint 56
Chapter 5 Results 60
5.1 The Influence of TPMS Unit Cell Size on Transpiration Cooling Performance 62
5.2 The Influence of TPMS Porosity on Transpiration Cooling Performance 76
5.3 The Influence of TPMS Orientation Angle on Transpiration Cooling Performance 89
5.4 The Influence of TPMS Morphology on Transpiration Cooling Performance 102
5.4.1 Experimental study 103
5.4.2 Numerical study 118
5.4.2.1 Computational domain and boundary conditions 118
5.4.2.2 Turbulent model verification 120
5.4.2.3 Results: Adiabatic film cooling effectiveness distribution at different morphological variations 124
5.4.2.4 Results: Effect of injection ratio on coolant film thickness 125
5.4.2.5 Results: Effect of morphological variation on coolant film thickness 129
5.4.2.6 Conclusion 131
5.5 The Influence of Internal Tangential Flow on Transpiration Cooling 133
5.6 Porosity Optimization of TPMS Structures for Uniform Coolant Distribution 164
5.7 Comparison of Cooling Mechanisms Between Effusion and TPMS-Based Transpiration Cooling 182
Chapter 6 Conclusions 198
Chapter 7 Future Work 201
7.1 Potential Challenges for Engine Applications and Future Work 201
Bibliography 204

List of Figures

Figure 1 Main parts of a gas turbine [1]..... 1
Figure 2 (a) T-s diagram of the air-standard Brayton cycle [2] (b) Effect of turbine inlet temperature on the overall GT performance [3] 2
Figure 3 Evolution of gas turbine hot gas temperatures, materials, and cooling technology [6]..... 2
Figure 4 Overview of advances in cooling schemes..... 4
Figure 5 Different kinds of porous materials: (a) powder sintered [18], (b) fiber sintered [19], (c) melt casting [20], (d) metal deposition[23], (e) laser perforation [21], and (f) composite porous [22] 5
Figure 6 Overview of TPMS structure applications 6
Figure 7 Evolution of turbine blade cooling technology, illustrating the progression from single-pass internal cooling (left) to multi-feed internal cooling with film cooling (center) and advanced multi-pass internal cooling with extensive film cooling (right) [34]..... 10
Figure 8 Film cooling development leading to state of the art [35]..... 11
Figure 9 Conceptual schematic of effusion and transpiration cooling (a) without film cooling (b) effusion cooling (c) transpiration cooling..... 12
Figure 10 Diagram of a sample effusion cooling hole with the hole diameter (d), compound angle (β) and inclination angle (α) denoted [38]..... 15
Figure 11 Typical-shaped holes used in film cooling[48]. 17
Figure 12 Centerline adiabatic film cooling effectiveness plotted vs the effective blowing ratio (M(denoted as BR in this thesis)/AR), where AR denotes the exit-to-inlet hole area ratio, for cylindrical and shaped holes in the near field [49]. 18
Figure 13 Spatial average one-periodic 2D film cooling effectiveness [43]..... 19
Figure 14 Effect of density ratio (DR) on adiabatic film cooling effectiveness of a 35-degree injection discrete film cooling hole at different blowing ratios (M(denoted as BR in this thesis)) [50]. 19
Figure 15 PIV measurement of axial velocity contours for different blowing ratios (M (denoted as BR in this thesis)), density ratios (DR), and corresponding momentum ratios (I) [51] 20
Figure 16 (a) Schematic of the double-layer porous structure with a porous armor; (b) SEM image of the sintered bronze porous plate; and (c) SEM image of the nickel foam [54]. 22
Figure 17 Weaving pattern and sample structure of the dutch weave [19]..... 23
Figure 18 Turbine blade geometry with a perforated cooling plate and a magnified view of the hole distribution [56]. 23
Figure 19 Film effectiveness of Panels 1, 5, 6 and 7 at x/d = 75 at different average blowing ratios [56]. 24

Figure 20 (a) Schematics of mucus secreting on the earthworm skin and transpiration cooling on the bio-inspired non-smooth porous surface (b) bio-inspired non-smooth surfaces [57]..... 24
Figure 21 Porous plates with partition walls investigated for transpiration cooling with different blockage ratios (BR) of the partition walls [58]..... 25
Figure 22 (a) Transpiration cooling efficiency distributions for additive manufactured porous plates with different blockage ratios. (b) Tensile stress-strain curves [58]..... 26
Figure 23 Schematic diagram and configuration photo of the specimen [61] 27
Figure 24 (a) Ceramic matrix composite (CMC)-based porous plates used in the experiments. (b) Surface temperature distributions at different blowing ratios and the corresponding pore distributions obtained from CT scans [22]..... 28
Figure 25 (a) Relation between bending strength and porosity (b) Relation between Vickers hardness and porosity [69]..... 30
Figure 26 Overall averaged cooling effectiveness and its uncertainty as a function of the random blockage ratio (γ), where γ is the fraction of blocked cooling holes relative to the total number of holes [71]..... 31
Figure 27 (a) shows photographs and schematic illustrations of five transpiration structures, from left to right: sparse full-coverage effusion cooling with a hole pitch of 3D (RH-3D), dense full-coverage effusion cooling with a hole pitch of 2D (RH-2D), sphere packing (SP), wire mesh (WM), and a blood-vessel-shaped structure (BV). (b) Overall film cooling effectiveness distributions of six types of cooling structure [74]..... 32
Figure 28 Geometric model and boundary conditions of the Gyroid-type TPMS, (a) Sectional view of a domain heat exchanger model for hot fluids, (b) The domain of hot fluids, (c) The domain of cold fluids, (d) Heat transfer core built by TPMS, (e) Adiabatic wall [82]..... 33
Figure 29 Wedge-shaped models: (a) baseline (pin fin design); (b) uniform Diamond; (c) optimized Diamond (volume fraction of 0.4) and (d) optimized Diamond (volume fraction of 0.5) [86] 34
Figure 30 (a) Physical models of four configurations: double wall (DW), transpiration–film (TF), silica aerogel-coated double wall (SA-DW), and silica aerogel-coated transpiration–film (SA-TF); (b) comparison of experimental and numerical cooling effectiveness for DW and TF configurations with and without silica aerogel coating [87]..... 35
Figure 31 Various types of TPMS found in nature [93] 42
Figure 32 Porosity variation of TPMS lattices as a function of the level-set constant c..... 43
Figure 33 Unit iso-surfaces (left) and corresponding unit lattice structures (right) of various TPMS geometries at a porosity of 0.5..... 45
Figure 34 Wetted surface area of unit cells for various TPMS geometries at a porosity of 0.5. The wetted surface area was calculated for a unit cell volume of 2.5 × 2.5 × 2.5 mm³..... 46

Figure 35 Unit cell cube of a Gyroid type TPMS structure with 50% porosity 46
Figure 36 Pore diameter Dp as functions of porosity εd, for different TPMS geometries. 46
Figure 37 Schematic of test coupon with an active area featuring TPMS lattices. 47
Figure 38 Unit cell cube of the Diamond type TPMS structure with 50% porosity illustrating excess printed layer formation during additive manufacturing. 48
Figure 39 Profile of the solid–void boundary at the top surface of a Diamond-type TPMS structure with L_c=3.1 mm and 44% design porosity: (a) CAD-designed top surface profile (b) microscopic image of the printed top surface 49
Figure 40 Actual porosity as a function of unit cell size and design porosity presented as (a) a 3D surface plot and (b) a 2D representation of the same data. 50
Figure 41 Schematic of the experimental setup 51
Figure 42 3D CAD model of the test rig: (a) without the vent system and (b) with the vent system. 52
Figure 43 (a) Cutaway view of the CAD model of the test section, illustrating the boundary layer control vent and the hot-wire measurement arrangement. (b) Comparison of the measured velocity profiles with and without the vent, together with the corresponding CFD predictions 53
Figure 44 Schematic of binary pressure sensitive paint (top) and temperature sensitive paint (bottom). .. 54
Figure 45 PSP calibration curve for single luminophore PSP [100] 58
Figure 46 PSP calibration curve for binary PSP[103] 59
Figure 47 Geometry model used for simulation. (a) Computational domain, and (b) Parallel, (c) Perpendicular, and (d) Grid configurations of the TPMS structure. 119
Figure 48 Workflow of STL based TPMS geometry conversion to STP for CFD analysis 119
Figure 49 Computational mesh for the Gyroid-type structure, showing boundary-layer refinement near the channel–porous interface and internal surfaces. 120
Figure 50 Comparison of spanwise-averaged AFE ($\eta ad, span\, avg$) obtained from CFD and PSP measurements at injection ratios of (a) $F = 0.68\%$ and (b) $F = 1.60\%$. 121
Figure 51 Schematic of the test coupon used for PSP measurements 121
Figure 52 Comparison between experimentally measured and numerically predicted AFE distributions for injection ratios of $F = 0.68\%$, 1.14%, and 1.60%. Panels (a)–(c) show PSP measurements, while panels (d)–(f) present CFD predictions obtained using the Standard k-ε turbulence model. The gray contour line represents $\eta ad = 0.15$, defining the boundary of the effective cooling region. 122
Figure 53 Area averaged AFE for three different grid resolutions at F=1.60%. 123
Figure 54 AFE distributions at the top surface for gyroid-type TPMS structures under three different configurations: (a) Parallel, (b) Perpendicular, and (c) Grid. Results are shown for three injection ratios

(*F*=0.68%, 1.14%, and 1.60%). The effective cooling area is defined by the grey contour line corresponding to $\eta ad = 0.15$ 124
Figure 55 Temperature contours visualizing coolant film development at different injection ratios. (a) Isometric view. (b–d) Temperature contours at the mid-span plane for (b) *F*=0.68%, (c) *F*=1.14%, and (d) *F*=1.60%, with δt (black contour) and δcf (gray contour). 127
Figure 56 Streamwise distributions of the thermal boundary-layer thickness (δt) and coolant-film thickness (δcf) for the Parallel configuration at injection ratios of (a) $F = 0.68\%$, (b) $F = 1.14\%$, and (c) $F = 1.60\%$. 128
Figure 57 Isosurfaces visualizing of δt (Red) and δcf (Yellow) at an injection ratio of *F*=1.60%, for three different morphological configurations: (a) Parallel, (b) Perpendicular, and (c) Grid. 129
Figure 58 Streamwise distributions of the thermal boundary-layer thickness (δt) and coolant-film thickness (δcf) under different surface configurations at *F*=1.60%: (a) Parallel, (b) Perpendicular, and (c) Grid. 130

List of Tables

Table 1 Trigonometric level-set equations utilized for each TPMS generation..... 43
Table 2 Comparison of geometric characteristics and stress distribution between strut-based and TPMS-based lattices. 44
Table 3 Summary of test conditions. 53

List of Abbreviations

NOMENCLATURE

A_{active}	Active area [mm^2]
A_w	Internal wetted area [mm^2]
A	1st order coefficient of the polynomial fitting curve
B	2nd order coefficient of the polynomial fitting curve
Bi	Biot number
C	3rd order coefficient of the polynomial fitting curve
C_{O2}	Oxygen concentration
c	TPMS level set constant
D_p	Pore diameter [mm]
d	Effusion-hole diameter [mm]
d_h	The hydraulic diameter of TPMS [mm]
F	Injection ratio [%]
G_x	Mass-flux components in the x directions [kg/(m²·s)]
G_y	Mass-flux components in the y directions [kg/(m²·s)]
h	Convective heat-transfer coefficient [W/(m²·K)]
I	Intensity of PSP
K	Stern–Volmer quenching constant
k	Thermal conductivity of the coupon material [W/(m·K)]
L_C	Unit cell length [mm]
Le_t	Turbulent Lewis number
l	Arc length of a surface void within a unit cell [mm]
M_a	Mass of the fabricated TPMS lattice [kg]

M_s	Mass of a solid specimen with the same external dimensions [kg]
$\dot{m}_c$	Coolant mass flow rate [kg/s]
MM	Molecular weight [$kg/kmol$]
P	Pressure [Pa]
$\dot{Q}_c$	Coolant volumetric flow rate [m³/s; also reported in SLPM]
q''	Convective heat flux [W/m²]
r	Binary-PSP luminescence intensity ratio
Re	Reynolds number
Re_{eff}	Effusion jet Reynolds number
Re_{TPMS}	TPMS Reynolds number
S	Henry's law coefficient in the Stern–Volmer relation
T	Temperature [K]
TI	Turbulence intensity
u	Velocity
X_{O2}	Mole fraction

GREEKS

α	Unit cell constant for x direction
α	Cooling-hole inclination angle [°]
β	Unit cell constant for y direction
β	Cooling-hole compound angle [°]
γ	Unit cell constant for z direction
δ_t	Thermal boundary layer thickness
δ_{cf}	Coolant film thickness
ε	Porosity [%]
ε_a	Actual porosity [%]
ε_d	Design porosity [%]
$\varepsilon_{surface}$	Surface porosity [%]
η_{ad}	Film cooling effectiveness
θ	rotation of angle
$\theta(z)$	Dimensionless temperature
λ	Ratio of wetted surface area to volume [cm^2/cm^3]
μ	Dynamic viscosity [Pa·s]
ρ	Fluid density [kg/m^3]
τ	Tortuosity
$\emptyset$	Level-set equation
Φ	Overall film cooling effectiveness

SUBSCRIPTS

ad	Adiabatic
air	Air
avg	Averaged quantity
c	Coolant
$dark$	Dark condition
m, ∞	Mainstream
max	Maximum value
mix	Coolant–mainstream mixture adjacent to the surface
ref	Reference
$span\ avg$	Spanwise-averaged quantity

ACRONYMS

AFE	Adiabatic cooling film effectiveness
AM	Additive manufacturing
BR	Blowing ratio
CFD	Computational fluid dynamics
CHT	Conjugate heat transfer
EDM	Electrical discharge machining
$FWHM$	Full width at half maximum
$NURBS$	Non-uniform rational B-splines
PSP	Pressure sensitive paint
SLA	Stereolithography
$SLPM$	Standard liter per minute
$TPMS$	Triple periodic minimal surface
TSP	Temperature sensitive paint

Chapter 1

Introduction

1.1 Background

Gas turbines are widely used in propulsion and power generation applications due to their high efficiency and power density. As illustrated in Figure 1, the main parts of a gas turbine consist of four main components: an inlet, a compressor, a combustor, and a turbine.

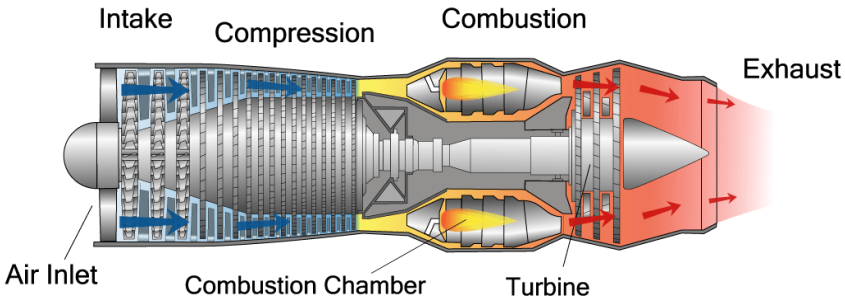

Figure 1 Main parts of a gas turbine [1]

Each component performs thermodynamic processes such as compression, combustion, expansion, and exhaust, as illustrated in the T-s diagram in Figure 2 (a). The thermal efficiency of the system tends to increase as the turbine inlet temperature (TIT) rises, as illustrated in Figure 2 (b). Figure 2(b) illustrates the relationship between thermal efficiency and compressor pressure ratio for turbine inlet temperatures (TITs) ranging from 900 to 1500 K. The thermal efficiency increases with compressor pressure ratio up to an optimum value, after which it decreases. The optimum pressure ratio increases with increasing TIT.

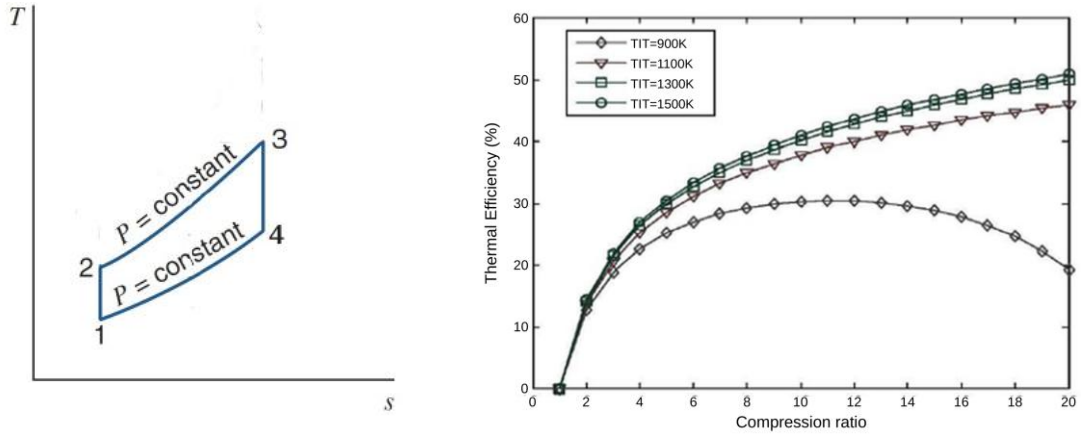

Figure 2 (a) T-s diagram of the air-standard Brayton cycle [2] (b) Effect of turbine inlet temperature on the overall GT performance [3]

To achieve higher thermal efficiency, gas turbines TIT has been continuously increased, as can be seen in Figure 3.

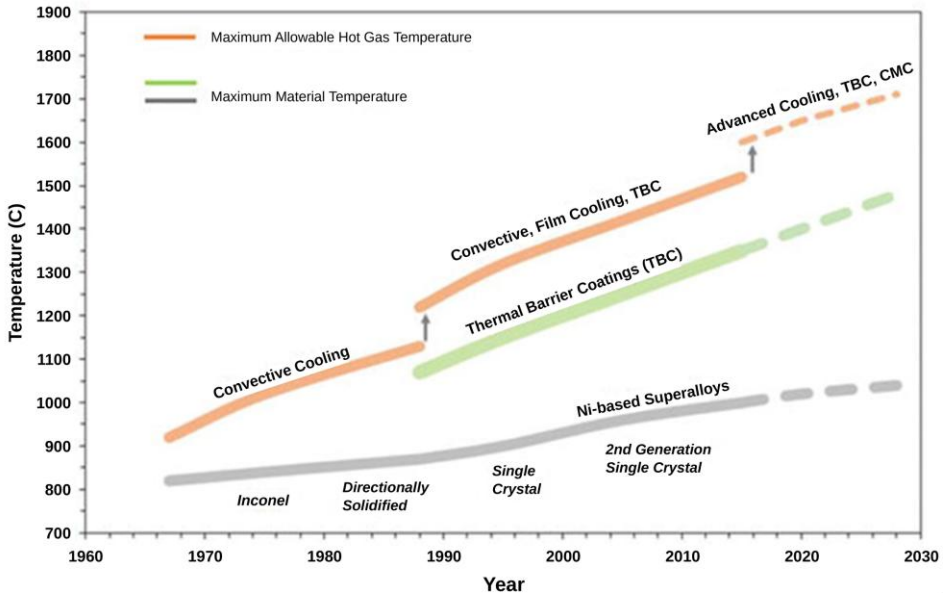

Figure 3 Evolution of gas turbine hot gas temperatures, materials, and cooling technology [6] (Reproduced under the terms of the Creative Commons Attribution 3.0 (CC BY 3.0) License from S. Naik, "Basic Aspects of Gas Turbine Heat Transfer", InTech, 2017.)

However, as shown in Figure 3, this temperature surpasses the maximum allowable temperature of nickel-based superalloys, such as Inconel (Ni-Cr-Fe based) and Hastelloy X (Ni–Cr–Fe–Mo based) [4], highlighting the critical need for the development of advanced cooling technologies capable of withstanding such extreme thermal conditions. Consequently, thermal barrier coatings (TBCs) and advanced cooling technologies have become indispensable for protecting hot-section components and maintaining their structural integrity under severe thermal loading.

Gas turbine cooling techniques are generally categorized into internal and external cooling. Figure 4 provides an overview of the evolution of thermal management methods for turbine liners, ranging from the simplest convection cooling to more advanced transpiration cooling with increasing efficiency. First, the basic convection cooling method using convection diverts a portion of the compressed air supplied from the compressor into the liner, circulating it internally to dissipate heat [5–7]. However, this approach has inherent limitations in delivering adequate cooling under the severe operating conditions of modern gas turbines. To address this, various enhancement methods have been developed to improve cooling efficiency, among which impingement cooling, utilizing impinging jets to promote higher heat transfer, has been developed [8,9]. Nevertheless, the fundamental drawback of internal cooling methods is that the surface of the turbine liner remains directly exposed to high-temperature gases [10]. For this reason, external cooling approaches have gained prominence, with film cooling emerging as the most widely adopted technology [11]. Among film cooling methods, effusion cooling is considered a state-of-the-art technology, in which air discharged through discretely arranged holes forms a thin insulating film over the surface, thereby effectively reducing heat transfer to the liner [12]. Over the past several decades, extensive efforts have been devoted to optimizing and enhancing the effectiveness of film cooling. For example, recent studies have investigated the combination of jet impingement and film cooling, which is often applied in double-wall configurations to maximize performance [13].

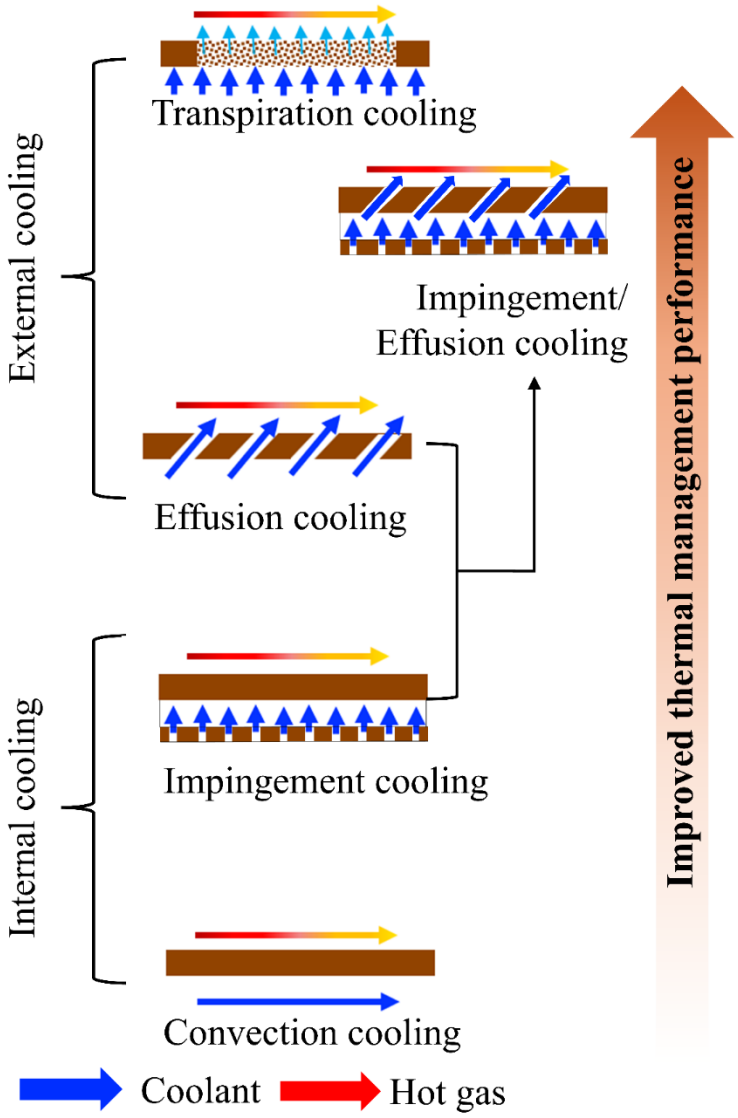

Figure 4 Overview of advances in cooling schemes

However, effusion cooling consumes a substantial amount of high-pressure compressor discharge air as coolant, thereby increasing the demand for advanced cooling methods that can achieve high efficiency while minimizing coolant consumption. However, excessive coolant extraction reduces the amount of compressed air available for combustion, resulting in penalties in engine performance and thermal efficiency. Therefore, advanced cooling technologies should not only enhance cooling effectiveness but also minimize coolant consumption to maximize overall engine performance [14]. From this perspective, transpiration cooling is considered an ideal and promising approach for protecting hot gas path components in next-generation gas turbines.

Initially proposed in the early 1950s, transpiration cooling is recognized for its superior heat sink capability and its ability to promote coolant film formation over a broad surface, known as boundary layer heat-blocking, without causing coolant film lift-off [15–17]. In generic transpiration cooling, coolant was transpired through a porous medium, such as sintered powder [18], woven mesh wires [19], melt casting [20], perforated plates [21], and composite porous materials [22], as illustrated in Figure. 5.

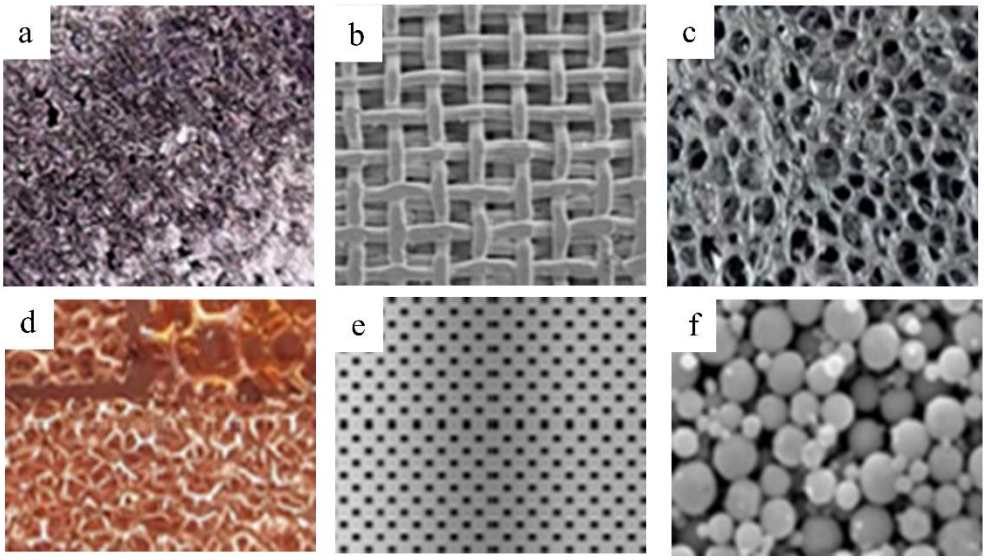

Figure 5 Different kinds of porous materials: (a) powder sintered [18], (b) fiber sintered [19], (c) melt casting [20], (d) metal deposition[23], (e) laser perforation [21], and (f) composite porous [22]

(Reprinted by permission from Elsevier: "Research Progress of Transpiration Cooling for Aircraft Thermal Protection," Applied Thermal Engineering, published January 5, 2024. Copyright © 2023 Elsevier Ltd. All rights reserved.)

The discharged coolant forms a continuous coolant film over the surface, thereby providing an effective thermal barrier that significantly reduces heat transfer by convection. Despite these substantial merits in cooling performance, transpiration cooling has not yet seen wide adoptions in engine applications, and its commercial use in turbine components has been limited due to challenges related to structural strength and manufacturability [24]. Moreover, conventional porous media are often expensive, difficult to engineer for complex geometries, and unable to achieve uniform pore distribution.

However, recent advances in additive manufacturing technologies, commonly known as 3D printing, have made it feasible to fabricate lattice structures as deterministic porous media.

Among these, the family of triply periodic minimal surfaces (TPMS) has gained significant attention as one of the most ideal lattice structures across various engineering fields [25], as shown in Figure. 6. This is due to their highly desirable characteristics, including periodic interconnected channels without abrupt edges and a high wetted surface-to-volume ratio. These unique features make TPMS structures widely applicable not only in heat sinks but also in transpiration cooling. [26–28].

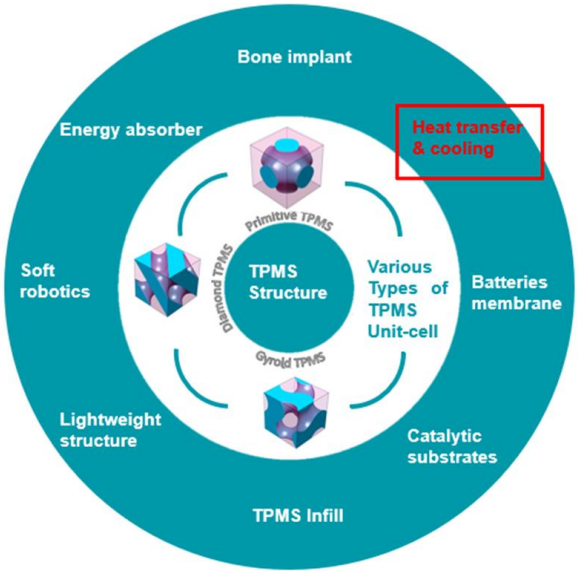

Figure 6 Overview of TPMS structure applications

Based on the previous discussions, the objective of this study is to develop a transpiration cooling technology for next-generation gas turbines using TPMS structures, and to evaluate and optimize its efficiency in comparison with conventional cooling methods.

1.2 Overview of Research Objectives

The objective of this study is to investigate the practical implementation of transpiration cooling using Triply Periodic Minimal Surface (TPMS) structures for transpiration cooling of gas turbine hot-gas path components. Earlier transpiration cooling attempts based on stochastic porous media have demonstrated excellent cooling performance; however, their non-uniform pore distribution and high manufacturing complexity limit their practical application in turbine engines. In contrast, TPMS-based deterministic porous structures can be precisely engineered and can be readily designed for complex geometries. In addition, these structures can be fabricated using additive manufacturing (AM), which significantly enhances their feasibility for engineering

applications. Furthermore, TPMS structures are anticipated to exhibit improved mechanical strength compared with conventional porous media due to their more uniform stress distribution and reduced stress concentrations, thereby enhancing structural integrity and mechanical durability.

Nevertheless, the practical application of TPMS-based transpiration cooling in turbine engines was not previously investigated, and therefore it is necessary to systematically evaluate the influence of key design parameters and optimize them to improve cooling performance. The primary parameters considered in this study include the type, unit cell size, porosity, orientation angle, and morphological variations of the TPMS structure. Since TPMS structures are generated using mathematically explicit equations, these parameters can be precisely controlled and adjusted during the design process.

In addition to geometric parameters, the internal flow behavior within the porous structure also plays a critical role in transpiration cooling performance. To suppress the internal tangential coolant flow of the coolant as a result of high porosity of the porous medium, the effectiveness of baffles installed perpendicular to the mainstream flow was investigated. Furthermore, a porosity-gradient design, in which the porosity is adjusted along the mainstream flow direction, was examined to achieve a more uniform coolant distribution.

Based on this background, the specific objectives of this study are as follows:

1. The Influence of TPMS Unit Cell Size on Transpiration Cooling Performance
2. The Influence of TPMS Porosity on Transpiration Cooling Performance
3. The Influence of TPMS Orientation Angle on Transpiration Cooling Performance
4. The Influence of TPMS Morphology on Transpiration Cooling Performance
5. The Influence of Internal Tangential Fluid Flow on Transpiration Cooling
6. Porosity Optimization of TPMS Structures for Uniform Coolant Distribution
7. Comparison of Cooling Mechanisms between Effusion and TPMS-Based Transpiration Cooling

1.3 Thesis Outline

This thesis is organized into seven chapters, each of which is briefly summarized in the following sections.

Chapter 1 provides an introductory overview of the thesis, including the research background, the objectives of the study, and a brief outline of the thesis structure.

Chapter 2 presents a comprehensive review of thermal management technologies for turbine components, covering both their historical development and current advancements. It introduces the fundamental fluid mechanics underlying cooling technologies and provides a detailed review of film cooling, with a particular focus on effusion cooling as the current state-of-the-art approach. The chapter then examines transpiration cooling as a next-generation technique by reviewing previous studies, identifying key limitations of conventional approaches, and highlighting recent research trends. Finally, TPMS structures are introduced as promising architectures for transpiration cooling, along with a review of their relevant engineering applications.

Chapter 3 defines the research objectives of this study, detailing the key investigations related to TPMS-based transpiration cooling, including the effects of unit cell size, porosity, orientation angle, morphology, internal tangential flow, porosity distribution, and the underlying cooling mechanisms.

Chapter 4 describes the experimental methodology and research approach. It includes detailed information on the design of TPMS structures, fabrication of test coupons, experimental setup, and the application of Pressure Sensitive Paint (PSP) for measuring adiabatic film cooling effectiveness.

Chapter 5 presents the experimental results corresponding to the research objectives defined in Chapter 3. The effects of key geometric and flow parameters on transpiration cooling performance are analyzed, and their practical implications are discussed.

Chapter 6 summarizes the main findings and conclusions of the study.

Chapter 7 discusses potential directions for future research. The thesis concludes with references, which provide additional information and supporting materials for readers seeking further details.

Chapter 2

Literature Review

2.1 Historical Development of Thermal Management Technologies for Gas Turbine Components

The turbine inlet temperature (TIT) has steadily increased to achieve higher turbine efficiency. Since gas-turbine performance is strongly linked to the development of advanced superalloys capable of withstanding extreme thermal environments and rising TIT, substantial research efforts have been devoted to developing high-temperature materials for turbine components[29]. Superalloys are widely used for turbine hot-section components owing to their high temperature ratings and their superior resistance to fatigue, thermal creep, and oxidation[30,31]. However, despite the continuous rise in achievable TIT, the maximum allowable temperature of turbine components remains constrained by the metallurgical limits of the materials. To address these limitations, extensive research has focused on the development of advanced cooling technologies in combination with thermal barrier coatings (TBCs). TBCs are advanced ceramic coatings applied to metallic hot-section components to increase thermal resistance and reduce the heat flux from the hot gas to the substrate [32,33]. However, despite advances in material development and TBCs, which are typically used in conjunction with internal cooling techniques such as convective cooling, the continuously increasing turbine inlet temperatures (TITs) in modern gas turbines have pushed conventional cooling technologies close to their performance limits. To overcome these limitations, the necessity and interest in advanced cooling technologies have continuously grown. Figure 7 illustrates the progressive development of turbine blade cooling techniques, from left to right. Advanced turbine cooling technologies enable higher operating temperatures, thereby enhancing both engine power output and efficiency.

In the early stages, simple single-pass internal cooling was employed. However, as the need for more complex and advanced cooling techniques emerged, combined approaches incorporating external cooling through film cooling were introduced.

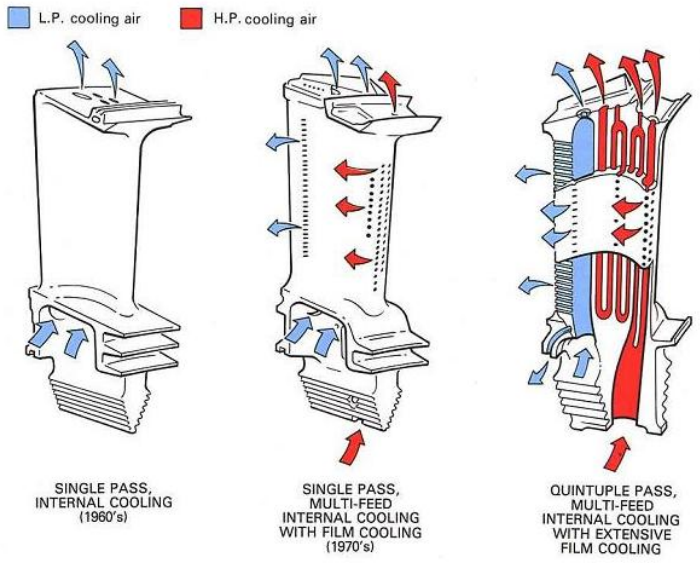

Figure 7 Evolution of turbine blade cooling technology, illustrating the progression from single-pass internal cooling (left) to multi-feed internal cooling with film cooling (center) and advanced multi-pass internal cooling with extensive film cooling (right) [34]

(Reprinted by permission from Rolls-Royce plc: ISBN 0902121235. Copyright © 1986 Rolls-Royce plc. All rights reserved.)

Film cooling enables effective protection of hot-gas path components by forming a thin layer of cooling air over the surface, thereby shielding surface from high-temperature gases. At present, film cooling and effusion cooling are regarded as state-of-the-art technologies, and extensive research has been conducted over the past several decades to optimize their performance. Figure. 8 summarizes the historical development of film cooling technology and the major research directions that have contributed to improving cooling performance over the past several decades.

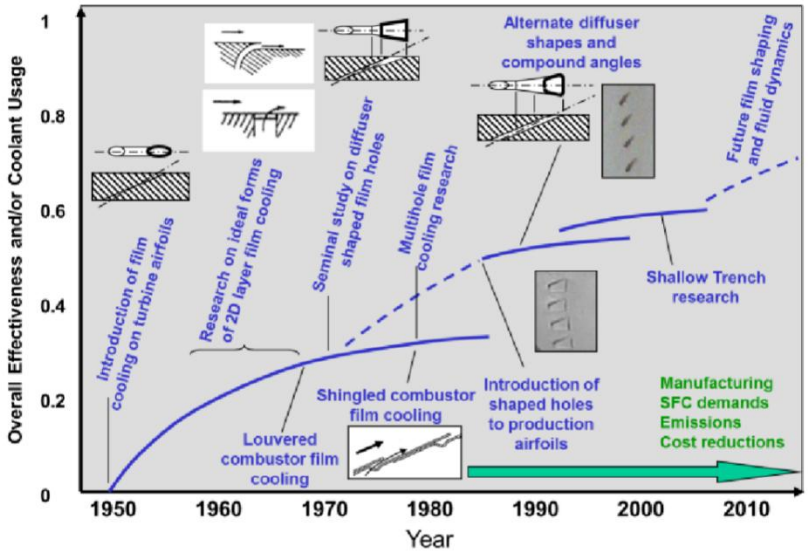

Figure 8 Film cooling development leading to state of the art [35]

(Reprinted by permission from ASME: "Evolution of Turbine Cooling," Proceedings of the ASME Turbo Expo 2017: Turbomachinery Technical Conference and Exposition, Paper No. GT2017-63205. Copyright © 2017 ASME.)

Early studies focused on slot film cooling and louvered combustor configurations, followed by extensive investigations into shaped-hole geometries to enhance coolant coverage and improve film attachment. As manufacturing technologies advanced, increasingly sophisticated effusion hole configurations, including diffuser-shaped holes and trench-assisted designs, became feasible, leading to further improvements in film cooling effectiveness while reducing coolant usage. Accordingly, the following chapter introduces the mechanisms of effusion cooling and reviews previous research in this area.

2.2 Fundamental Mechanisms of Effusion and Transpiration Cooling

Figure 9 presents conceptual schematics of three representative heat transfer scenarios: (a) a baseline case without film cooling, (b) effusion cooling, and (c) transpiration cooling. In the absence of film cooling (Figure 9(a)), the hot mainstream gas directly interacts with the combustor liner surface, resulting in a relatively high wall temperature (T_w) and heat flux to the liner, corresponding to the heat transfer model described by Equation (1). In contrast, both effusion cooling (Figure 9(b)) and transpiration cooling (Figure 9(c)) reduce the wall heat load by forming a protective coolant film over the surface. Effusion cooling generates this coolant film through discrete cooling holes, whereas transpiration cooling continuously supplies coolant through a porous medium, producing a more uniformly distributed coolant layer. Consequently, the coolant film reduces the hot-gas-side heat transfer, resulting in a lower wall temperature than that of the baseline case without film cooling.

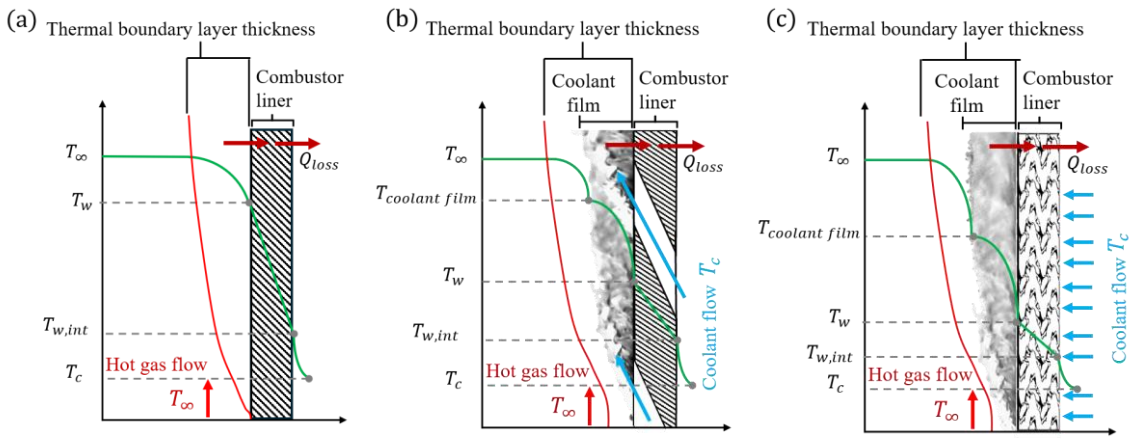

Figure 9 Conceptual schematic of effusion and transpiration cooling (a) without film cooling (b) effusion cooling (c) transpiration cooling

Based on Newton's law of cooling, the convective heat fluxes without and with film cooling are expressed by Equations (1) and (2), respectively.

$$q_o'' = h_0(T_\infty - T_\mathrm{w}) \quad (1)$$

$$q'' = h(T_\mathrm{f} - T_\mathrm{w}) \quad (2)$$

In Equation (1), T_∞ and T_w represent the freestream temperature and the surface wall temperature, respectively, while in Equation (2), T_f denotes the effective temperature of the coolant film formed over the wall as a result of various level of mixing between injected coolant and the hot mainstream

gas. Consequently, T_f is lower than T_∞ but generally higher than T_w. For a surface cooled by a coolant injected at temperature T_c, the surface cooling performance can be assessed using the overall film cooling effectiveness, ϕ, which is defined as follows:

$$\phi = \frac{T_\infty - T_w}{T_\infty - T_c} \tag{3}$$

When the overall film cooling effectiveness ϕ approaches unity, the cooling air provides complete protection of the wall, and in this case $T_{wall} = T_c$. Furthermore, when materials with very low thermal conductivity, such as thermal barrier coatings (TBC) [36], are employed, the wall can be assumed to behave under adiabatic conditions. In this case, the convective heat flux in Equation (2) becomes zero at the wall.

$$q'' = 0 = h(T_f - T_w)|_{wall}, \text{ which implies that } T_w = T_f = T_{aw} \tag{4}$$

Under this condition, the effectiveness is referred to as the adiabatic film cooling effectiveness, defined as:

$$\eta_{ad} = \frac{T_\infty - T_{aw}}{T_\infty - T_c} \tag{5}$$

Several nondimensional numbers are known to influence film cooling performance. Among these parameters, the density ratio is defined as the ratio of the coolant density to the mainstream gas density. In conventional gas turbines, both flows originate from the compressor and therefore share the same working fluid, with the density ratio arising primarily from the temperature difference between the hot mainstream gas and the coolant, as given in Equation (6).

$$DR = \frac{\rho_c}{\rho_\infty} \approx \frac{T_\infty}{T_c} \tag{6}$$

Another important parameter is the velocity ratio between the mainstream and the coolant, which is expressed by Equation (7) [37].

$$VR = \frac{u_c}{u_\infty} \tag{7}$$

where u and ρ denote the velocity and density, respectively, and the subscripts c and ∞ represent the coolant and mainstream flows. The blowing ratio (BR), defined as the ratio of coolant to mainstream mass fluxes, is expressed as follows:

$$BR = \frac{\rho_c u_c}{\rho_\infty u_\infty} \tag{8}$$

which can also be represented as the product of the density and velocity ratios, as given in Equation (8). In turn, u_c can be calculated from coolant volumetric flow rate $\dot{Q}_c$, active area A_{active} (the area with active cooling holes) and surface porosity resulting from cooling holes of the test coupon $\varepsilon_{surface}$:

$$u_c = \frac{\dot{Q}_c}{A_{active}\varepsilon_{surface}} \tag{9}$$

Similar to blowing ratio, a distinct non-dimensional parameter, the injection ratio F, is specifically defined to characterize transpiration cooling, as the surface porosity in transpiration systems is substantially greater than that in typical effusion cooling configurations.

$$F = \frac{\dot{m}_c}{A_{active}}\frac{1}{\rho_\infty u_\infty} = \frac{\rho_c u_c}{\rho_\infty u_\infty}\frac{A_{active}\varepsilon_{surface}}{A_{active}} = BR * \varepsilon_{surface} \tag{10}$$

Here, $\dot{m}_c$, denotes the mass flow rate of the coolant. The injection ratio represents the ratio of the coolant mass flow rate per unit active area to the mass flux of the mainstream flow ($\rho_\infty u_\infty$). By normalizing in this way, the parameter allows the cooling performance to be evaluated independently of the surface porosity and see the direct influence of the coolant mass flow rate.

2.3 Effusion Cooling as the Current State-of-the-Art

Effusion cooling is considered as the state-of-the-art cooling technology, extensively used in gas turbine liners, often in conjunction with thermal barrier coatings [36]. Over the past few decades, significant research efforts have focused on improving the effectiveness of effusion cooling. Various design parameters, including inclination angle [38], compound angle [12], pitch spacing [39], and shape [40,41], as well as fluid dynamic parameters such as blowing ratio (BR) [42,43] and density ratio [44], have been extensively investigated.

2.3.1 Effect of inclination and compound angles

The inclination angle (α) and compound angle (β) of the cooling holes are illustrated in Figure 10. The inclination angle, α, is defined as the angle between the coolant ejection direction

and the liner surface, which influences how effectively the coolant film adheres to the surface. Typically, the inclination angle is selected within a range that allows the coolant jet to remain attached to the surface, thereby minimizing coolant jet lift-off and reducing mixing with the mainstream flow.

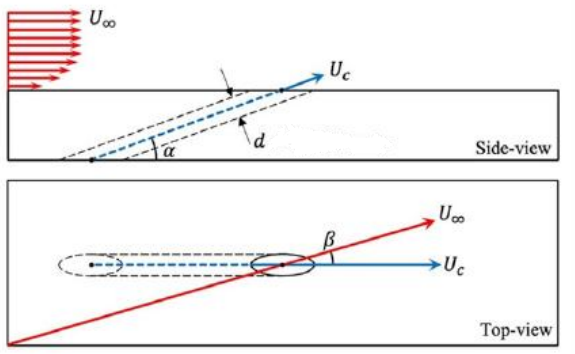

Figure 10 Diagram of a sample effusion cooling hole with the hole diameter (d), compound angle (β) and inclination angle (α) denoted [38].

Andreini et al. [45] investigated the impact of hole inclination angle (α, 20°, 30°, and 90° degrees) on the performance of effusion cooling under realistic swirling flow conditions. The results demonstrated that a smaller inclination angle (α=20 degrees) provided the best film protection, enhancing adiabatic film cooling effectiveness and optimizing the stability of the coolant layer and its interaction with the mainstream flow. Typically, the inclination angle is selected within a range that discourages the coolant jet to lift-off from the surface, thereby minimizing mixing with the mainstream flow. This approach can increase the surface area protected by the coolant downstream of the film cooling hole and improve the uniformity of cooling.

The compound angle, β, is defined as the angle between the main flow and the coolant jets on the top surface as shown in Figure 10. Accordingly, several studies have investigated the film cooling characteristics of discrete holes under compound angle injection conditions. Schmidt et al., [46] experimentally investigated film cooling effectiveness using compound angle (β = 60°) injection for both round and shaped holes. Their results demonstrated that compound angle configurations, especially those with expanded exits, yielded improved lateral coolant coverage and higher spatially averaged adiabatic effectiveness across a wider range of momentum flux ratios compared to streamwise-aligned round holes. Pyo et al., [12] investigated the impact of non-zero compound angles on adiabatic film cooling effectiveness while maintaining a constant effusion

cooling hole pitch, defined as the center-to-center spacing between adjacent holes in both the streamwise and spanwise directions. They found that a compound angle between 30° and 60° optimizes jet penetration and mixing, enhancing cooling effectiveness, with 45° recommended as an ideal starting point for future designs.

2.3.2 Effect of hole pitch spacing

Pitch, defined as the center-to-center distance between adjacent cooling holes, also has a significant impact on film cooling performance. The optimal hole pitch is determined by a complex interplay between the coolant mass flow rate, the thermal load on the combustor liner, and the geometric constraints of the liner design. A pitch that is too small may lead to excessive cooling and inefficient use of coolant air, whereas a pitch that is too large may result in insufficient cooling coverage, potentially causing local hot spots and thermal damage. Yang et al., [47] investigated the effect of hole pitch on coolant superposition defined as the interaction and accumulation of coolant films discharged from adjacent cooling holes, and it's influence on effusion cooling performance. Their study demonstrated that hole pitch significantly affects the resulting adiabatic cooling effectiveness. Specifically, their results showed that the interaction between coolant jets from neighboring holes plays a dominant role in the overall cooling performance. As the pitch spacing decreases, the overlap between adjacent coolant jets becomes stronger, enhancing the superposition effect and improving surface coverage. The study quantitatively demonstrated that local cooling effectiveness is significantly influenced by the contributions of neighboring coolant ejections.

2.3.3 Effect of hole geometry

The cooling holes geometry strongly affects the coolant trajectory and dispersion as it is discharged into the high-temperature combustor environment. Conventional round holes, despite their manufacturing simplicity, offer limited capability to control the lateral spreading of the coolant. Advances in manufacturing technologies have enabled the implementation of complex cooling hole geometries, such as diffuser-shaped and fan-shaped holes, as illustrated in Figure 11. Shaped cooling holes modify the cross-sectional area of the metering section as the flow approaches the surface. This modification is typically achieved through expansion or contraction in two principal directions: the lateral direction and the forward direction (i.e., along the mainstream flow). Holes expanded in the lateral direction are commonly referred to as fan-shaped holes, whereas those expanded in the forward direction are known as laidback or forward-diffused holes. When

the metering section is expanded in both directions, the configuration is generally referred to as a double-beveled hole.

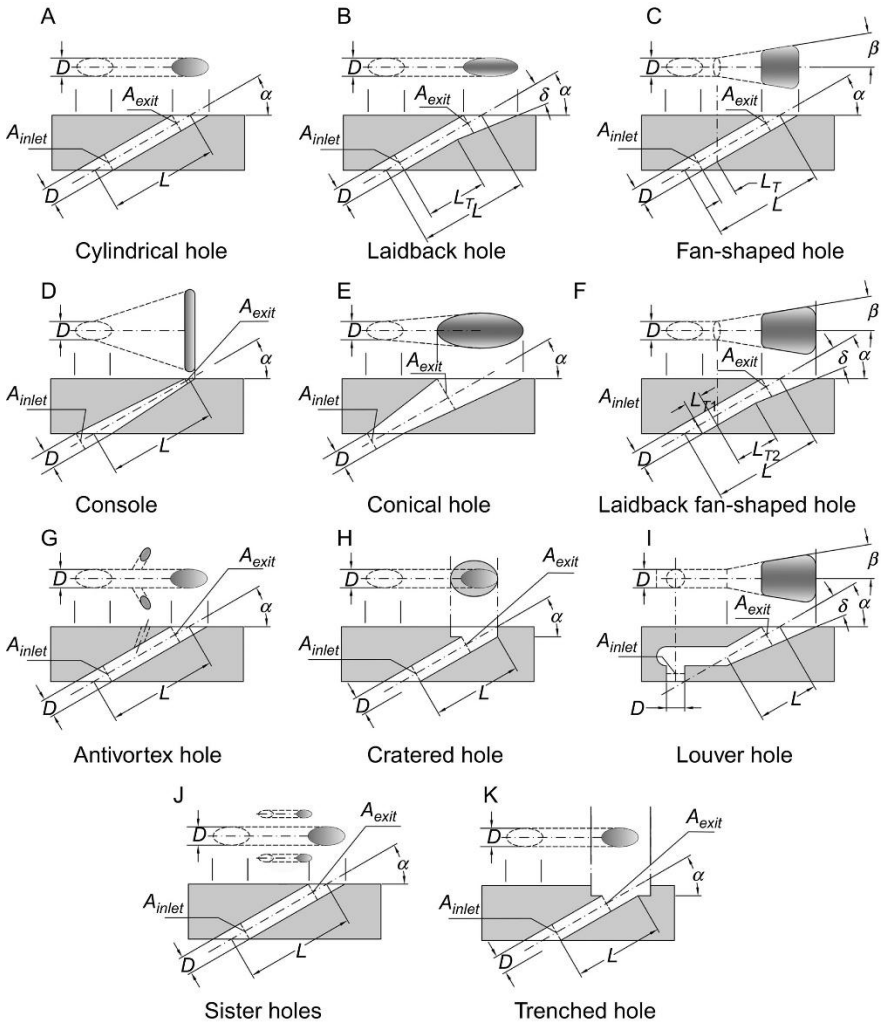

Figure 11 Typical-shaped holes used in film cooling[48].

(Reprinted by permission from Elsevier: "Advances in Film Cooling Heat Transfer," Advances in Heat Transfer, 2017. Copyright © 2017 Elsevier Inc. All rights reserved.)

Goldstein et al. [49] reported that double-beveled holes provide significantly higher film cooling effectiveness than conventional cylindrical holes at blowing ratios greater than 0.5, as illustrated in Figure 12. They further demonstrated that the centerline adiabatic film cooling effectiveness correlates with the effective blowing ratio, M (denoted as BR in this thesis)/AR, where AR is the exit-to-inlet hole area ratio. Their results suggest that both cooling effectiveness and jet penetration are governed by the mean mass–velocity ratio. Furthermore, increasing the exit area enhances film cooling effectiveness by reducing the nominal blowing ratio based on the exit velocity.

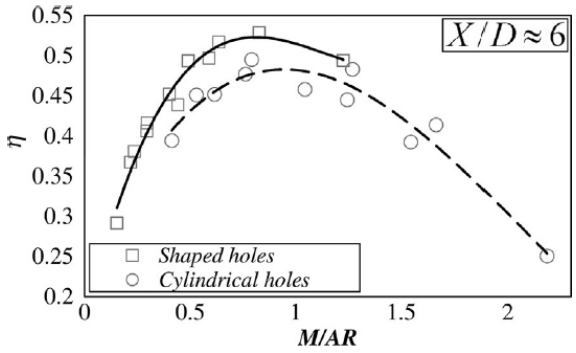

Figure 12 Centerline adiabatic film cooling effectiveness plotted vs the effective blowing ratio (M(denoted as BR in this thesis)/AR), where ***AR*** denotes the exit-to-inlet hole area ratio, for cylindrical and shaped holes in the near field [49].

(Reprinted by permission from Elsevier: "Effects of Hole Geometry and Density on Three-Dimensional Film Cooling," International Journal of Heat and Mass Transfer, 1974. Copyright © 1974 Published by Elsevier Ltd.)

2.3.4 Effect of blowing and density ratios

The blowing ratio (BR), defined in Equation (8), is widely used to represent the operating conditions of film cooling systems. As shown in Figure 13, Wang et al. [43] evaluated the cooling performance at different BR by measuring the adiabatic film cooling effectiveness. The interaction between the coolant jet and the mainstream flow is strongly governed by the BR. At low BR, the coolant jet possesses relatively low momentum and remains attached to the surface, forming a stable cooling film. However, when the BR is excessively low, the coolant may not spread sufficiently to provide full surface coverage, resulting in incomplete thermal protection. In contrast, at higher BR, the coolant jet gains greater momentum and penetrates further into the mainstream flow. If the BR becomes too high, the jet may lift off from the surface, thereby reducing its cooling effectiveness on the liner.

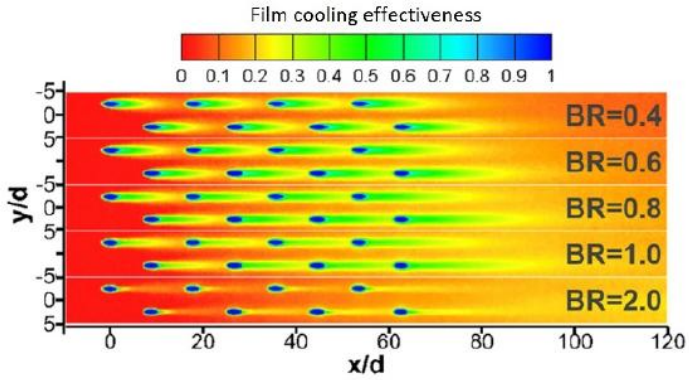

Figure 13 Spatial average one-periodic 2D film cooling effectiveness [43]

(Reprinted by permission from ASME: "Experimental Study of Effusion Cooling with Pressure-Sensitive Paint," Journal of Engineering for Gas Turbines and Power, Vol. 139, No. 5, 2017, Article 051601. Copyright © 2017 ASME.)

The density ratio, defined in Equation (6), is also an important parameter in film cooling. Since gas turbine combustors operate at very high temperatures, the typical density ratio under engine conditions is approximately 2 [50]. Higher adiabatic film cooling effectiveness (AFE) can be achieved under engine conditions with higher density ratios, as an increase in density ratio results in lower coolant velocity at a fixed blowing ratio (BR). This effect is illustrated in Figure 14, which presents the centerline film cooling effectiveness measured by Sinha et al. [50] for various blowing ratios and density ratio.

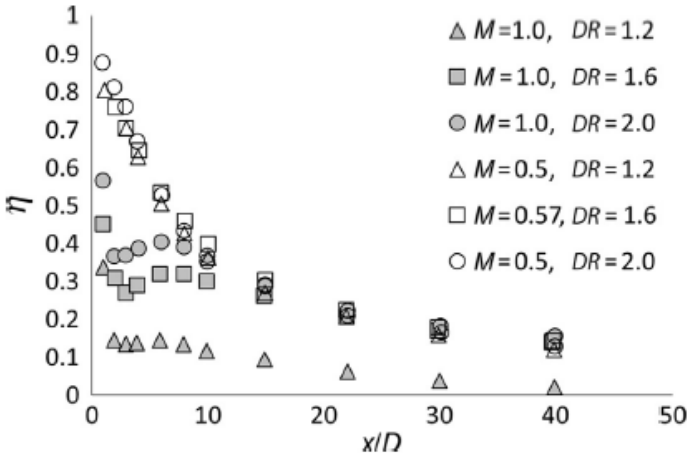

Figure 14 Effect of density ratio (DR) on adiabatic film cooling effectiveness of a 35-degree injection discrete film cooling hole at different blowing ratios (M(denoted as BR in this thesis)) [50].

(Reprinted by permission from ASME: "Film-Cooling Effectiveness Downstream of a Single Row of Holes With Variable Density Ratio," Journal of Turbomachinery, Vol. 113, No. 3, 1991, pp. 442–449. Copyright © 1991 ASME.)

Bernsdorf et al. [51] reported PIV measurements for coolant injection from an inclined cylindrical hole on a flat plate at various blowing ratios (*M* (denoted as BR in this thesis)) and density ratios (*DR*) (see Figure 15). At a constant blowing ratio, increasing the density ratio reduces the momentum ratio (I), resulting in a lower jet exit momentum. Consequently, the axial velocity along the jet centerline decreases, and the counter-rotating vortex pair (CRVP) moves closer to the wall. Furthermore, the maximum upward velocity along the jet centerline occurs closer to the wall and increases in magnitude. These results indicate that the coolant jet is more likely to lift off from the surface at lower density ratios, consistent with the higher momentum ratio under identical blowing ratio conditions.

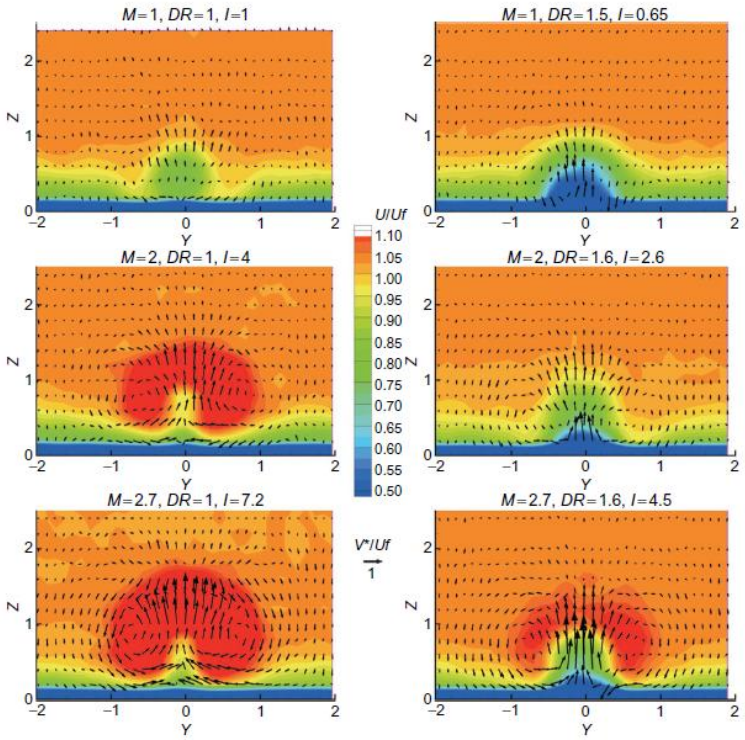

Figure 15 PIV measurement of axial velocity contours for different blowing ratios (*M* (denoted as BR in this thesis)), density ratios (*DR*), and corresponding momentum ratios (*I*) [51]

(Reprinted by permission from ASME: "Modeling of Film Cooling—Part I: Experimental Study of Flow Structure," Journal of Turbomachinery, Vol. 128, No. 1, 2006, pp. 141–149. Copyright © 2006 ASME.)

2.4 Transpiration Cooling as a Next-Generation Cooling Technique

Transpiration cooling was first proposed in the early 1950s and was recognized for its outstanding cooling performance [15,17]. Transpiration cooling is a technique in which a coolant is passed through a porous medium (PM), forming a protective film on the surface that reduces convective heat transfer from the hot mainstream gas, while simultaneously cooling the internal structure. Coolant film can thicken the boundary layer and modify the local temperature and velocity gradients near the surface, also known as boundary-layer heat blocking [23]. As a result, heat transfer from the high-temperature mainstream flow to the surface of a hot-gas path component is significantly reduced. In addition, the porous medium provides a high wetted surface area relative to its volume, which enhances convective heat transfer between the solid structure and the coolant in the interior of the porous medium [16]. The combination of effective film cooling and enhanced internal heat transfer makes transpiration cooling a strong candidate for cooling for next-generation gas turbines.

2.4.1 Effect of type of porous medium

Type of the porous medium plays a major role in transpiration cooling performance. Conventional stochastic metal porous media can be classified into powder-sintered structures [18,52], laser-perforated plates [20], woven wire meshes [19], open-cell foams [53], and melt-cast porous materials [20]. Numerous studies have been conducted to evaluate the performance of these various porous media in transpiration cooling applications. Early applications of powder-sintered porous metals were demonstrated by NASA, where copper was used as the base material to fabricate porous structures with porosities ranging from 25% to 50% for cooling injection panels and combustion chambers in rocket engines through powder sintering [52] Huang et al. [54] proposed a transpiration cooling system using a sintered bronze porous plate combined with a porous nickel foam armor layer, as shown in Figure 16.

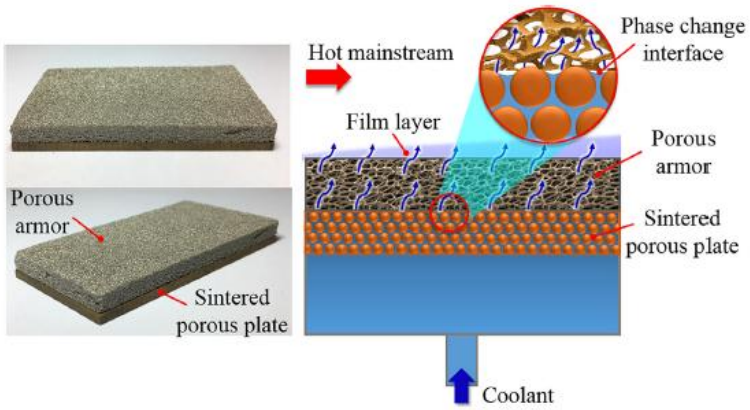

(a)

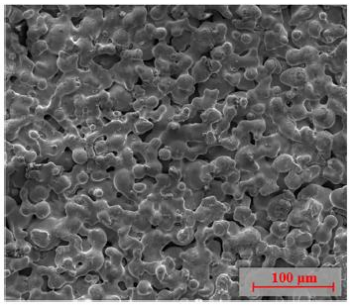

(b)

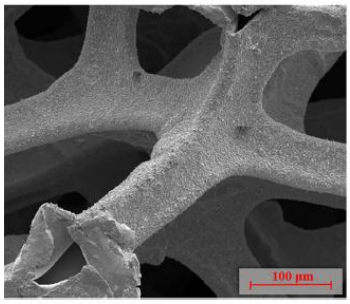

(c)

Figure 16 (a) Schematic of the double-layer porous structure with a porous armor; (b) SEM image of the sintered bronze porous plate; and (c) SEM image of the nickel foam [54].

(Reprinted by permission from Elsevier: "Self-Pumping Transpiration Cooling with a Protective Porous Armor," Applied Thermal Engineering, 2020. Copyright © 2019 Elsevier Ltd. All rights reserved.)

The micro-porous sintered plate generated capillary forces that supplied liquid water to the heated surface without external pumping. The experimental results demonstrated stable cooling performance and approximately 39% coolant savings, highlighting the potential of sintered metal porous media for transpiration cooling applications. Liu et al. [18] investigated the flow and heat transfer characteristics of transpiration cooling through sintered porous flat plates with different particle diameters (40 and 90 μm). Their results demonstrated that even a small amount of coolant injection significantly reduces heat transfer from hot gases, with cooling effectiveness increasing as the injection ratio rises and particle diameter decreases. Ma et al.[19] examined the performance of transpiration cooling using double and triple laminated sintered woven wire mesh structures (see Figure 17) with varying porosities and showed that porosity and layer arrangement significantly

affect cooling performance, while increasing the number of layers has a limited impact when the porosity composition remains the same.

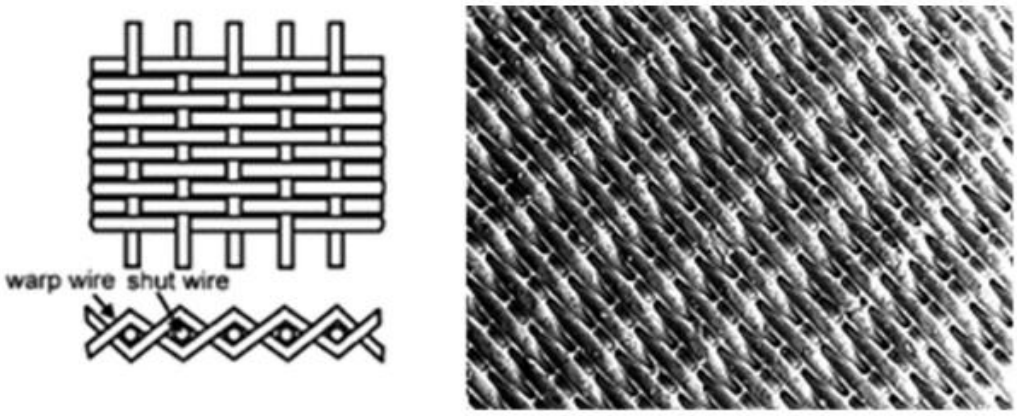

Figure 17 Weaving pattern and sample structure of the dutch weave [19].

(Reprinted by permission from the authors: "An Experimental Investigation on Transpiration Cooling Based on the Multi laminated Sintered Woven Wire Mesh Structures.")

Transpiration cooling through the perforated hole (also known as a full coverage effusion cooling) was also investigated through the past decades. Murray et al. [55] examined the influence of hole pitch on effusion-cooled plates. Their results demonstrated that, for a given coolant mass flow rate per unit area, decreasing the spacing between coolant holes significantly enhanced the average film cooling effectiveness. In particular, reducing the pitch-to-diameter ratio from 5.75 to 3 resulted in more than a twofold increase in cooling effectiveness. Wambersie et al.[56] evaluated transpiration cooling performance using perforated plate with an estimated porosity greater than 25% (see Figure 18).

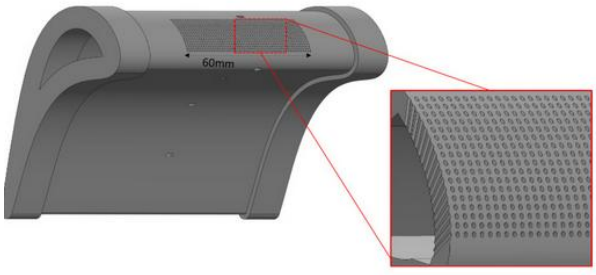

Figure 18 Turbine blade geometry with a perforated cooling plate and a magnified view of the hole distribution [56].

The results, shown in Figure 19, indicate that this approach can achieve a film cooling effectiveness of over 95% while using a relatively low coolant mass flow rate.

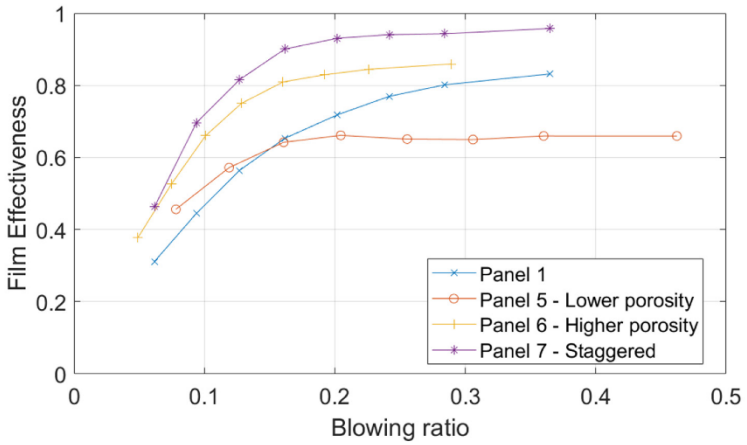

Figure 19 Film effectiveness of Panels 1, 5, 6 and 7 at x/d = 75 at different average blowing ratios [56].

2.4.2 Previous efforts to optimize transpiration cooling

To achieve high cooling performance while minimizing coolant consumption, various approaches have been investigated, including geometric modifications and variable porosity designs. Huang et al. [57] proposed a biomimetic non-smooth porous surface inspired by the rough skin of earthworms (see Figure 20).

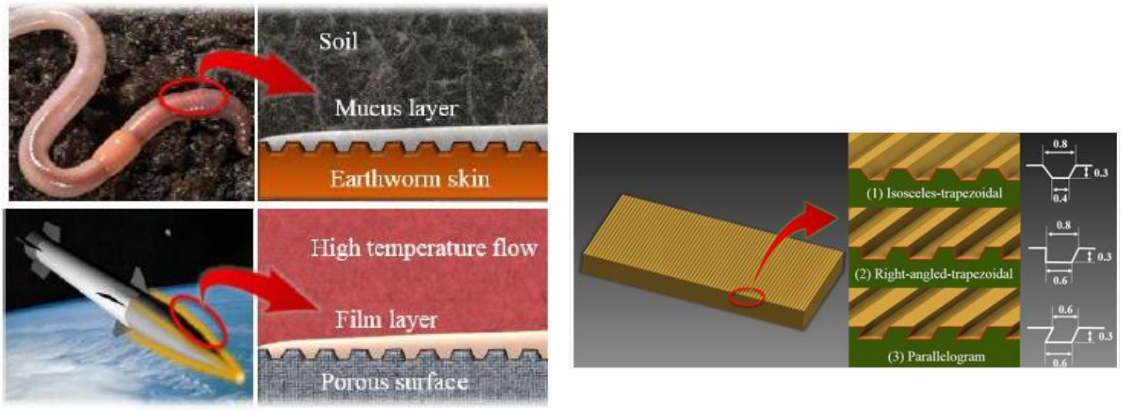

(a) (b)

Figure 20 (a) Schematics of mucus secreting on the earthworm skin and transpiration cooling on the bio-inspired non-smooth porous surface (b) bio-inspired non-smooth surfaces [57].

(Reprinted by permission from IOP Publishing: "Transpiration Cooling with Bio-Inspired Structured Surfaces," Bioinspiration & Biomimetics, Vol. 15, No. 3, 2020, Article 036016. Copyright © 2020 IOP Publishing Ltd.)

Numerical investigations of several groove geometries showed that the structured surface could thicken the protective film layer and enhance cooling performance. In particular, the parallelogram-shaped groove structure increased the film thickness by approximately 22.7% and improved the overall transpiration cooling efficiency by about 12% compared to a smooth surface. Huang et al. [58] investigated porous plates with reinforcing partition walls for transpiration cooling (see Figure 21).

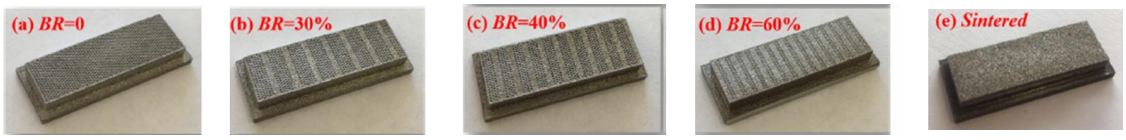

Figure 21 Porous plates with partition walls investigated for transpiration cooling with different blockage ratios (BR) of the partition walls [58].

(Reprinted by permission from Elsevier: "Transpiration Cooling for Additive Manufactured Porous Plates with Partition Walls," International Journal of Heat and Mass Transfer, 2018. Copyright © 2018 Elsevier Ltd. All rights reserved.)

The results showed that cooling effectiveness approached that of conventional sintered porous plates, reaching about 0.7 at a blowing ratio (F, (denoted as BR in this thesis)) of 2%, while the mechanical strength was significantly improved, with the ultimate tensile strength increasing by approximately 440%, as shown in Figure 22.

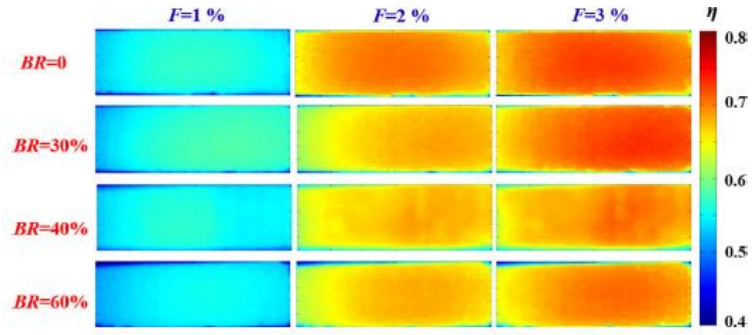

(a)

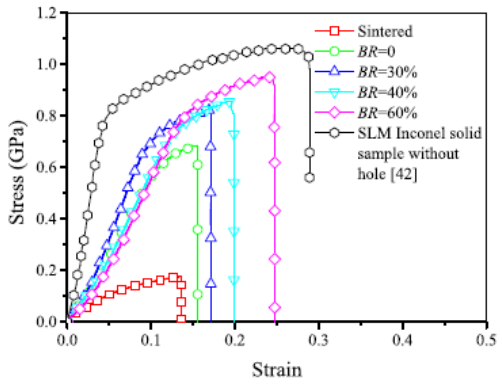

(b)

Figure 22 (a) Transpiration cooling efficiency distributions for additive manufactured porous plates with different blockage ratios. (b) Tensile stress-strain curves [58].

(Reprinted by permission from Elsevier: "Transpiration Cooling for Additive Manufactured Porous Plates with Partition Walls," International Journal of Heat and Mass Transfer, 2018. Copyright © 2018 Elsevier Ltd. All rights reserved.)

An uneven distribution of coolant mass flow was found when uniform porous media are used for transpiration cooling [59]. Hinse et al. [53] investigated transpiration cooling using metal foam porous media and found that viscous entrainment from the mainstream flow induces tangential coolant motion within the porous matrix. This internal tangential flow results in non-uniform coolant discharge and leads to uneven adiabatic film cooling effectiveness. Therefore, to achieve a more uniform cooling performance, a configuration with varying porosity along the mainstream direction has been considered. Dong et al. [60] conducted a numerical investigation showing that locally varying porosity can reduce the maximum hot-side temperature by approximately 40%. Liu et al. [61] investigated transpiration cooling with a gradient porosity layout for the thermal protection of a nose cone, as shown in Figure 23.

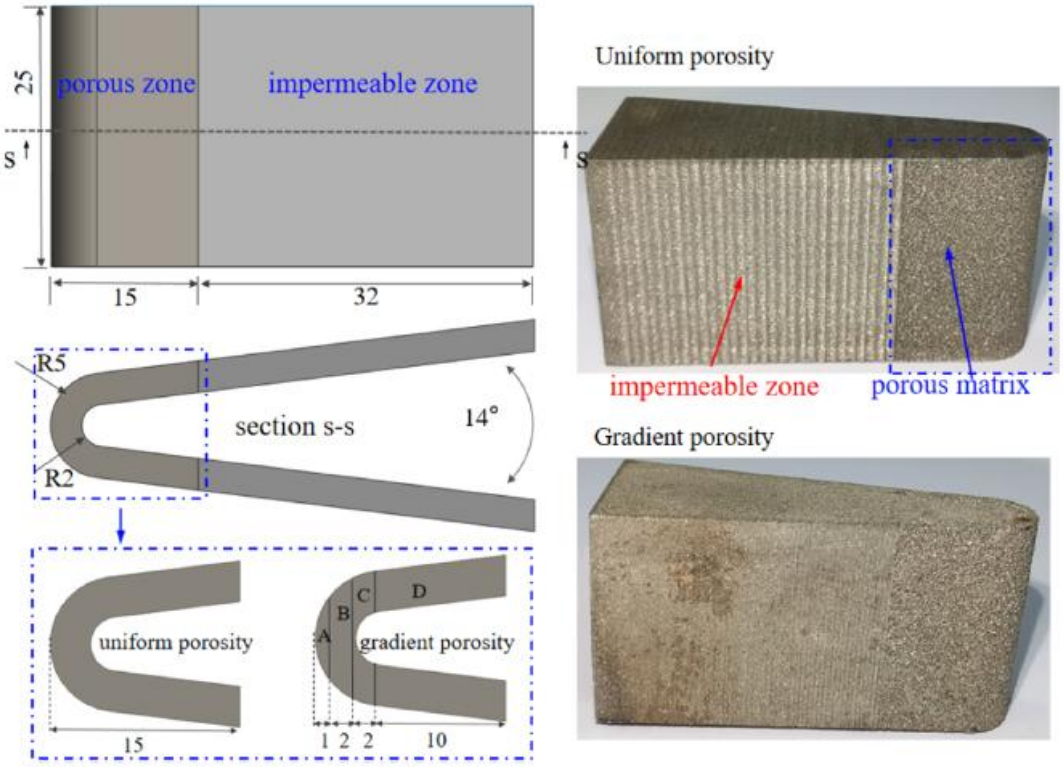

Figure 23 Schematic diagram and configuration photo of the specimen [61]

(Reprinted by permission from Elsevier: "Experimental and Numerical Investigation of Transpiration Cooling with Gradient Porosity Layout for the Thermal Protection of Nose Cone," Aerospace Science and Technology, 2024. Copyright © 2024 Elsevier Masson SAS. All rights reserved.)

Through combined experimental and numerical studies, they demonstrated that the graded porosity structure optimized coolant distribution within the porous medium and significantly enhanced the cooling performance at the hot spot. Han et al. [62] performed a numerical investigation on transpiration cooling in heterogeneous porous media and demonstrated that spatially graded porosity significantly affects coolant flow distribution and cooling performance. Their results showed that porous structures with spatially varying porosity provide improved flow uniformity and higher overall cooling effectiveness compared with homogeneous porous media.

2.4.3 Challenges of conventional transpiration cooling

Transpiration cooling has demonstrated high cooling efficiency and thus shows strong potential as a next-generation thermal management technology. However, several challenges remain unresolved for its practical application in turbine components [23].

First, porous media for transpiration cooling are typically fabricated using powder sintering or mechanical weaving techniques. However, these manufacturing processes inherently introduce structural imperfections. In powder sintering, particle agglomeration and irregular pore formation can occur within the structure, while mechanical weaving may produce non-uniform interlayer spacing. As a result, the subsequent porous media inherently contain pores of various sizes [63]. Variations in pore size can lead to either insufficient or excessive local coolant supply. In regions where the coolant supply is insufficient, rapid temperature rises may occur, causing thermal stress concentration that can ultimately lead to structural failure [64]. Li et al. [22] investigated phase-change transpiration cooling in heterogeneous ceramic matrix composites, emphasizing the critical influence of pore structure on cooling performance. Specifically, variations in pore size and permeability resulted in non-uniform coolant distribution, which led to the formation of local hot spots and a reduction in overall cooling effectiveness, as shown in Figure 24.

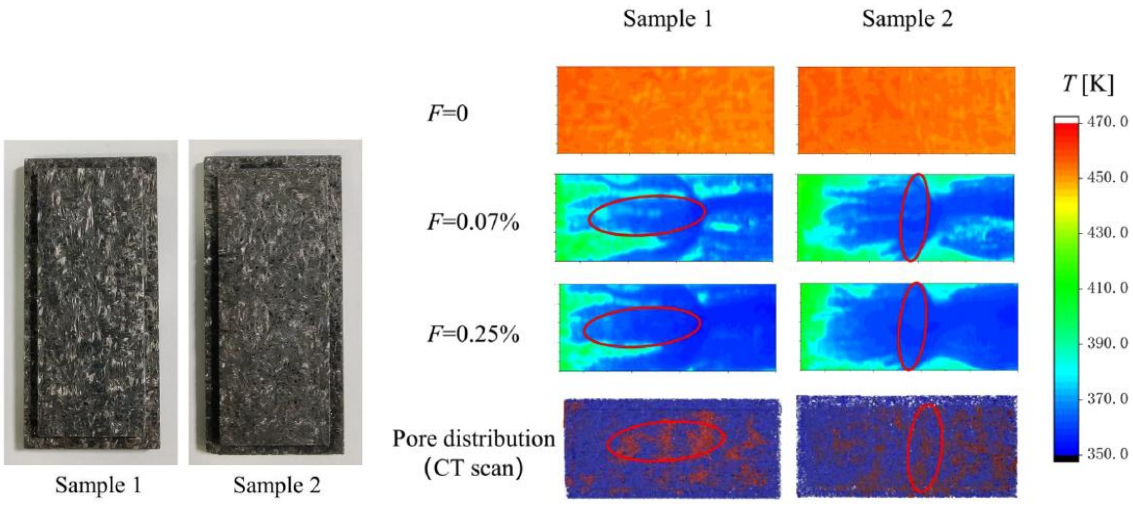

Figure 24 (a) Ceramic matrix composite (CMC)-based porous plates used in the experiments. (b) Surface temperature distributions at different blowing ratios and the corresponding pore distributions obtained from CT scans [22].

(Reprinted by permission from Elsevier: "Phase-Change Transpiration Cooling in Heterogeneous Composite Porous Plates: Heat Transfer Characteristics and Their Prediction," International Journal of Heat and Mass Transfer, 2024. Copyright © 2024 Elsevier Ltd. All rights reserved.)

König et al. [65] conducted experimental and numerical investigations on transpiration cooling using carbon/carbon (C/C) ceramic matrix composites, with particular emphasis on the effects of nonuniform coolant outflow caused by the porous structure. Their results showed that stochastic porous nature induced non-uniform coolant outflow significantly affects the cooling film distribution and overall cooling performance, demonstrating that the internal porous structure plays a critical role in transpiration cooling effectiveness.

Second challenge: conventionally manufactured porous media with stochastic pore distributions inherently exhibit low mechanical strength and structural instability due to their random pore morphology [66,67]. Under extremely harsh conditions involving coupled high temperature and pressure, such materials are prone to structural failure, which may lead to metal deformation, softening, and creep. Consequently, transpiration cooling structures can fail due to insufficient material strength. Ryshkewitch [68] conducted an investigation on the influence of porosity on mechanical strength, and the results revealed a negative correlation between porosity and strength. Miyazaki et al [69] investigated the strength characteristics of porous alumina over a wide porosity range (0.803–57.8%) and reported an overall exponential decrease in strength with increasing porosity, as shown in Figure 25. However, their results also demonstrated that strength is not governed solely by bulk porosity; variations in pore size and spatial distribution can significantly influence mechanical performance, with finer and more uniformly distributed pores leading to higher strength even at higher porosity levels.

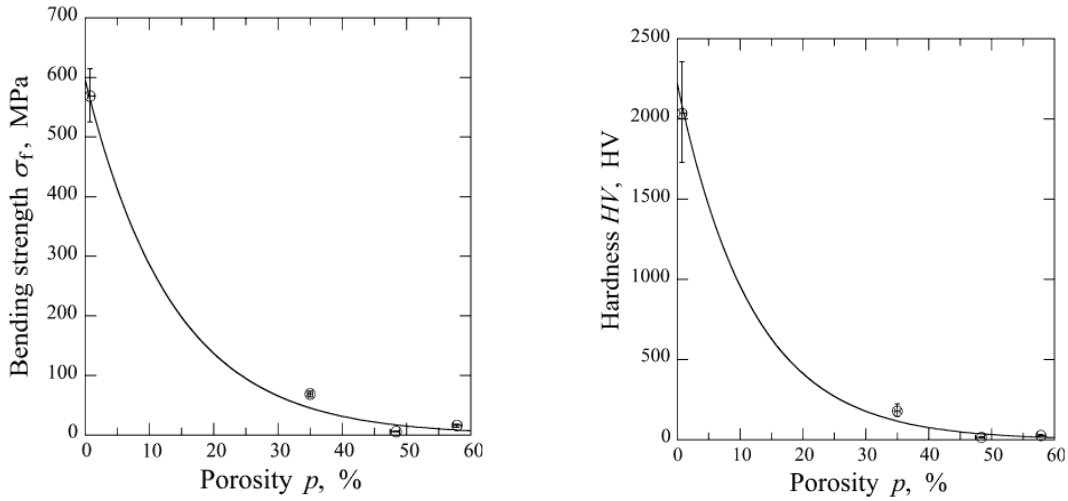

(a) (b)

Figure 25 (a) Relation between bending strength and porosity (b) Relation between Vickers hardness and porosity [69].

(Reprinted by permission from ASM International: "Influence of Porosity and Pore Distributions on Strength Properties of Porous Alumina," Journal of Materials Engineering and Performance, 2018. Copyright © 2018 ASM International.)

Lastly, stochastically distributed pores and variations in pore size may contribute to pore blockage issues. Metallic materials generally exhibit limited oxidation resistance at high temperatures, which can lead to degradation and performance issues under long-term operating conditions [70]. Yang et al. [71] conducted numerical studies on the clogging effect in transpiration cooling systems and found that holes closer to the leading edge are highly susceptible to plugging. As shown in Figure 26, where γ denotes the random blockage ratio (i.e., the fraction of blocked cooling holes relative to the total number of holes, with $\gamma = 0$ indicating no blockage and $\gamma = 1$ indicating complete blockage), the averaged cooling effectiveness decreases and becomes increasingly sensitive to stochastic pore blockage as the blockage probability increases.

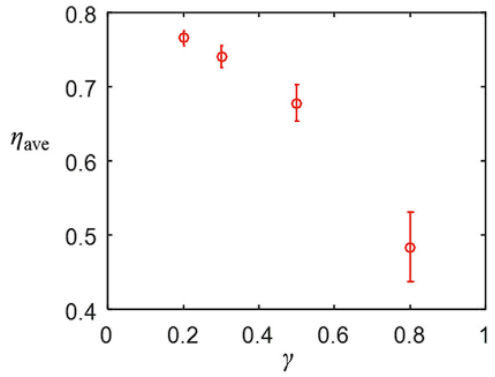

Figure 26 Overall averaged cooling effectiveness and its uncertainty as a function of the random blockage ratio ($\boldsymbol{\gamma}$), where $\boldsymbol{\gamma}$ is the fraction of blocked cooling holes relative to the total number of holes [71].

(Reprinted by permission from Elsevier: "A Convolution Modeling Method for Pore Plugging Impact on Transpiration Cooling Configurations Perforated by Straight Holes," International Journal of Heat and Mass Transfer, 2018. Copyright © 2018 Elsevier Ltd. All rights reserved.)

Although significant efforts have been made to prevent blockages and precisely control pore size in conventional porous media, it remains a persistent challenge.

Despite extensive research efforts toward the optimization of cooling structures and systems, inherent limitations of transpiration cooling still remain. Accordingly, there is a continuing need for the development of deterministic porous media with well-controlled and uniform structures.

2.4.4 Prior efforts in adopting additive manufacturing for transpiration cooling

More recently, advancements in additive manufacturing (AM), commonly known as 3D printing, have enabled the fabrication of precisely controlled, deterministic porous media, expanding its potential for application in transpiration cooling [72]. Kim et al.[73] compared the cooling effectiveness of effusion cooling with that of transpiration cooling using a metal 3D-printed porous surface. Transpiration cooling achieved a nearly uniform coolant film over a broad area and demonstrated higher effectiveness compared to effusion cooling. Min et al. [74] conducted experiments to assess and compare the cooling effectiveness of an effusion cooling design with five transpiration cooling designs fabricated using SLS additive manufacturing. As shown in Figure 27, transpiration cooling designs—particularly the BV type—exhibit superior cooling effectiveness

compared to effusion cooling (FM), primarily due to the larger internal heat transfer area within the porous structure, which enhances heat exchange between the coolant and the solid matrix.

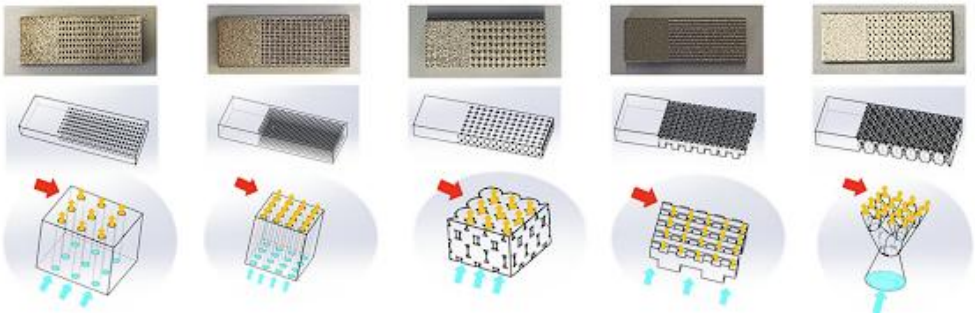

(a)

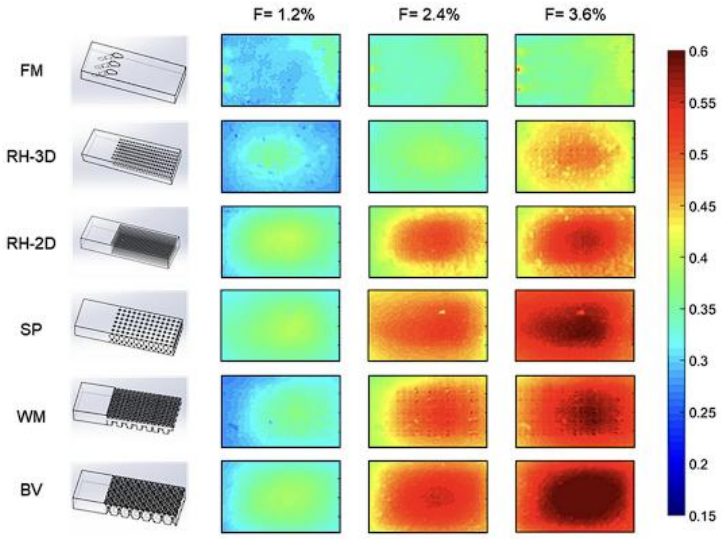

(b)

Figure 27 (a) shows photographs and schematic illustrations of five transpiration structures, from left to right: sparse full-coverage effusion cooling with a hole pitch of 3D (RH-3D), dense full-coverage effusion cooling with a hole pitch of 2D (RH-2D), sphere packing (SP), wire mesh (WM), and a blood-vessel-shaped structure (BV). (b) Overall film cooling effectiveness distributions of six types of cooling structure [74]

(Reprinted by permission from ASME: "Experimental Investigation on Additively Manufactured Transpiration and Film Cooling Structures," Journal of Turbomachinery. Copyright © American Society of Mechanical Engineers (ASME).)

2.5 TPMS Structures as Promising Architectures for Transpiration Cooling

Previous researches have highlighted the advantages of transpiration cooling using porous media fabricated via 3D printing. Building on these developments, recent studies have focused on optimizing deterministic porous structures, which offer well-defined internal channels and precise control over pore size, distribution, and overall architecture. Among these, Triply Periodic Minimal Surfaces (TPMS) have attracted particular attention as advanced porous architectures. First described in the 1860s [75], TPMS geometries are characterized by zero mean curvature, enabling smooth and continuous surfaces that can facilitate uniform fluid distribution. Furthermore, unlike conventional stochastic porous media, TPMS structures are mathematically defined, enabling precise control and tunability of their geometrical features [76,77]. As a result, TPMS lattices have found applications across a wide range of engineering fields, including soft robotics [78], structure weight reductions [79] and medical devices [80]. Among these, their use in heat sinks and heat exchangers is particularly prominent, owing to their highly convoluted internal channels and exceptionally high surface area-to-volume ratio, which contribute to significant improvements in thermal performance [27,81]. Song et al. [82] conducted a numerical analysis to evaluate the thermal and flow characteristics of a gyroid-type TPMS heat exchanger (see Figure 28).

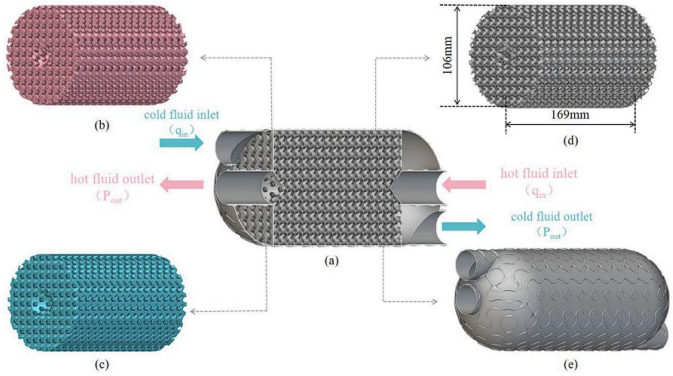

Figure 28 Geometric model and boundary conditions of the Gyroid-type TPMS, (a) Sectional view of a domain heat exchanger model for hot fluids, (b) The domain of hot fluids, (c) The domain of cold fluids, (d) Heat transfer core built by TPMS, (e) Adiabatic wall [82].

(Reprinted by permission from Elsevier: "Numerical Simulation Study on the Heat Transfer and Flow Characteristics of Fuel/Lubricating Oil Heat Exchanger Based on Triply Periodic Minimal Surface (TPMS)," Applied Thermal Engineering, 2024. Copyright © 2024 Elsevier Ltd. All rights reserved, including those for text and data mining, AI training, and similar technologies.)

The results demonstrated that reducing the lattice size significantly increases the heat transfer surface area, thereby enhancing convective heat transfer performance. Reynolds et al. [26] experimentally demonstrated that gyroid-based TPMS heat exchangers can enhance heat transfer performance compared to conventional designs, while maintaining competitive pressure drop characteristics.

Owing to their uniform and well-defined pore distribution and large heat transfer surface area, TPMS structures hold strong potential as deterministic porous media for transpiration cooling applications. Following our earlier work on TPMS-based transpiration cooling [83], Zhou et al.[84] conducted a pore-scale investigation of transpiration cooling using TPMS structures. Their study revealed that the shape and size of the pore throat significantly influence coolant flow resistance and cooling effectiveness. Brimacombe et al. [85] experimentally investigated transpiration cooling using Gyroid TPMS structures of varying porosity (ϕ =0.3–0.5) manufactured via stereolithography, demonstrating that cooling effectiveness is primarily governed by the injection ratio. Yeranee et al. [86] applied density-based topology optimization to printable diamond-type TPMS lattices for gas turbine trailing edge cooling and demonstrated that such optimized TPMS configurations (volume fraction of 0.4, as shown in Figure 29 (c).) could significantly enhance heat transfer, achieving up to 150% improvement over conventional pin fin designs.

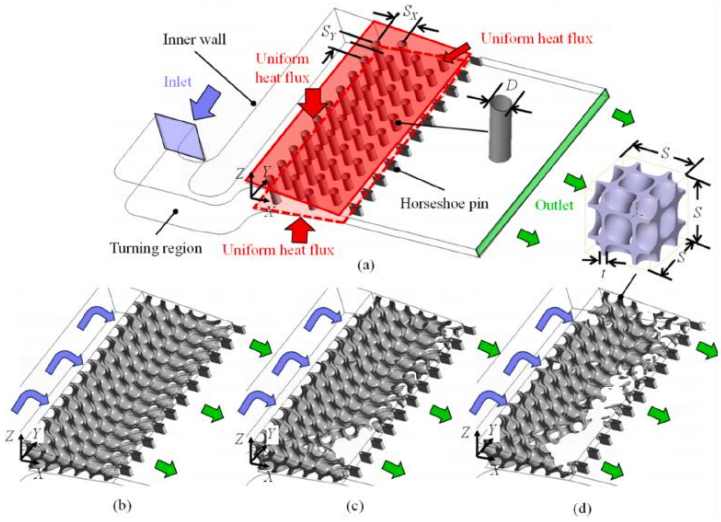

Figure 29 Wedge-shaped models: (a) baseline (pin fin design); (b) uniform Diamond; (c) optimized Diamond (volume fraction of 0.4) and (d) optimized Diamond (volume fraction of 0.5) [86]

(Reprinted by permission from Elsevier: "Thermal Performance Enhancement for Gas Turbine Blade Trailing Edge Cooling with Topology-Optimized Printable Diamond TPMS Lattice,"

International Journal of Heat and Fluid Flow, 2024. Copyright © 2024 Elsevier Inc. All rights reserved, including those for text and data mining, AI training, and similar technologies.)

He et al. [87] further proposed a TPMS-based transpiration–film cooling configuration with a porous TPMS layer beneath a conventional effusion cooling surface (Figure 30 (a)), demonstrating enhanced cooling performance through improved internal convection and uniform film formation (Figure 30 (b)).

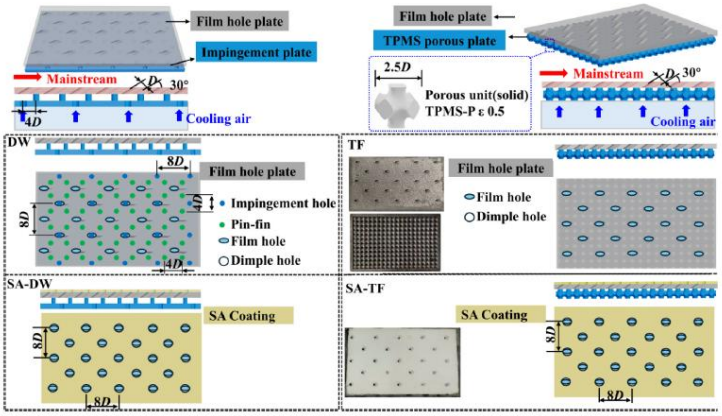

(a)

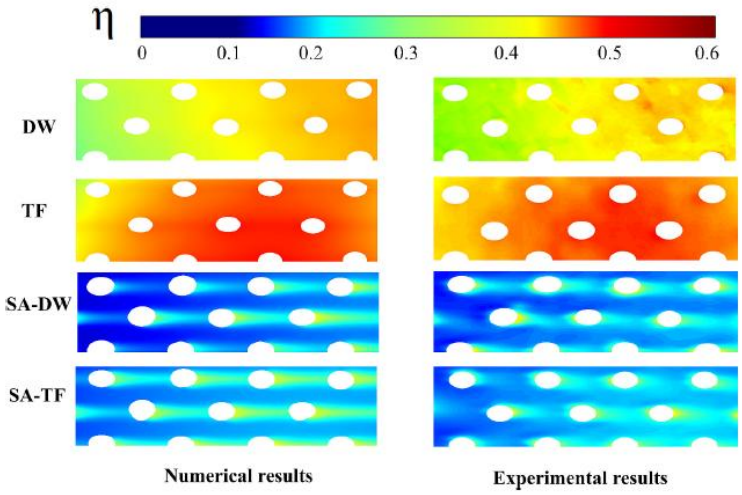

(b)

Figure 30 (a) Physical models of four configurations: double wall (DW), transpiration–film (TF), silica aerogel-coated double wall (SA-DW), and silica aerogel-coated transpiration–film (SA-TF); (b) comparison of experimental and numerical cooling effectiveness for DW and TF configurations with and without silica aerogel coating [87].

(Reprinted by permission from Elsevier: "Synergistic Thermal Protection Performance of TPMS Transpiration-Film Cooling Coupled with Silica Aerogel Thermal Barrier Coating," Applied Thermal Engineering, 2026. Copyright © 2026 Elsevier Ltd. All rights reserved, including those for text and data mining, AI training, and similar technologies.)

However, despite these studies, systematic investigations into the use of TPMS structures for transpiration cooling remain absent. Therefore, this study aims to systematically investigate the potential of TPMS structures for transpiration cooling.

Chapter 3

Research Objectives

TPMS structures are mathematically defined in three-dimensional Cartesian space using trigonometric functions such as sine and cosine, which generate inherently triply periodic geometries. This formulation enables precise control over key parameters, including unit cell size, porosity, orientation, and topology.

The objective of this study is to investigate and evaluate the influence of geometrical characteristics of additively manufactured TPMS lattice structures on cooling performance, with the aim of advancing transpiration cooling as a viable thermal management strategy for next-generation gas turbines.

By systematically examining the effects of porosity (Diamond TPMS), cell size (Diamond TPMS), orientation (Diamond, Gyroid, and Koch TPMS), and morphological variations (Diamond, Gyroid, and Koch TPMS)—both independently and in combination—this study seeks to elucidate the underlying mechanisms governing cooling performance and to establish design guidelines for enhanced transpiration cooling strategies.

Accordingly, this study defines a set of specific research objectives to comprehensively assess the thermal performance of TPMS structures:

1. The Influence of TPMS Unit Cell Size on Transpiration Cooling Performance
2. The Influence of TPMS Porosity on Transpiration Cooling Performance
3. The Influence of TPMS Orientation Angle on Transpiration Cooling Performance
4. The Influence of TPMS Morphology on Transpiration Cooling Performance
5. The Influence of Internal Tangential Flow on Transpiration Cooling
6. Porosity Optimization of TPMS Structures for Uniform Coolant Distribution
7. Comparison of Cooling Mechanisms Between Effusion and TPMS-Based Transpiration Cooling

3.1 The Influence of TPMS Unit Cell Size on Transpiration Cooling Performance

The influence of TPMS geometric parameters on transpiration cooling performance remains insufficiently understood. As part of a broader effort to systematically develop optimized TPMS-based transpiration cooling systems, this study focuses on evaluating the effect of unit cell size as a key geometric parameter.

To isolate its influence, three test coupons with different unit cell sizes were fabricated while maintaining all other parameters—TPMS type, porosity, and orientation angle—constant. This controlled approach ensures that variations in cooling performance can be attributed solely to unit cell size. The findings of this study are expected to provide a more systematic understanding of the relationship between unit cell size and the transpiration cooling behavior of TPMS structures and provide guidance for improved design.

3.2 The Influence of TPMS Porosity on Transpiration Cooling Performance

This study investigates the influence of TPMS porosity on the cooling performance of gas turbine hot gas path components. To investigate the influence of porosity, three TPMS structures with porosities of 30%, 40%, and 50% were evaluated while maintaining a constant unit cell size. The two-dimensional distribution and area-averaged adiabatic film cooling effectiveness of these TPMS-based transpiration cooling configurations are experimentally evaluated and compared with those of a conventional discrete-hole effusion cooling design.

3.3 The Influence of TPMS Orientation Angle on Transpiration Cooling Performance

While unit cell size and porosity are global geometric parameters influencing cooling performance, additional factors may also play a significant role in transpiration cooling. As coolant is discharged through a porous structure, it forms a surface film under the influence of the mainstream flow. In this context, the angle between the coolant flow paths and the mainstream flow can significantly affect film cooling performance [12,88]. This effect is well documented in effusion cooling as the compound angle effect [46,89], but remains largely unexplored for transpiration cooling.

This study investigates the influence of the orientation angle of surface voids in TPMS lattice structures relative to the mainstream flow. The objective is to identify TPMS configurations that (i) enhance film cooling effectiveness and (ii) exhibit reduced sensitivity to flow direction.

An experimental approach is adopted to examine the effect of surface void orientation on cooling performance for three TPMS solid-network geometries—Diamond, Koch, and Gyroid—which are introduced in the following section.

3.4 The Influence of TPMS Morphology on Transpiration Cooling Performance

Despite the promising potential of TPMS-based transpiration cooling, further parametric investigations are required before this technology can be considered for practical gas turbine applications. While the previous section investigates the influence of lattice orientation by rotating the TPMS unit cell, the present section examines the influence of TPMS morphology. Here, morphology refers to changes in the surface pattern and internal flow passages of the TPMS unit cell that arise from geometric transformations, such as offsets or surface curvature.

Such morphological variations are inevitable when TPMS lattices are conformed to the complex geometries of practical gas turbine components and may significantly affect coolant distribution and heat transfer. Therefore, this study aims to identify TPMS morphologies that maintain robust transpiration cooling performance despite geometry-induced morphological variations, thereby providing design guidelines for practical engine applications.

3.5 The Influence of Internal Tangential Flow on Transpiration Cooling

Despite systematic efforts in previous studies to optimize TPMS-based transpiration cooling, several unresolved issues remain. As reported by Hinse et al. [53], when a mainstream flow (33 m/s) passes over a porous medium, the injected coolant is entrained downstream due to viscous effects. This internal streamwise transport, referred to as internal tangential flow, can redistribute the coolant within the lattice, resulting in non-uniform coolant discharge and cooling effectiveness. A similar mechanism occurs in TPMS structures, where fully interconnected internal channels can promote tangential flow within the lattice. This internal flow may lead to excessive coolant discharge in downstream regions while reducing coolant supply upstream, resulting in localized hot spots.

Although various mitigation strategies have been proposed, including geometrical modifications [90–92], a systematic investigation providing both quantitative and qualitative insight into the effects of internal tangential flow on cooling performance remains lacking. In response, this study verifies the influence of internal tangential flow in TPMS-based transpiration cooling by introducing partition walls perpendicular to the mainstream flow direction that were designed to suppress such internal tangential flow.

3.6 Porosity Grading for Uniform Coolant Distribution

One of the key challenges in transpiration cooling is to promote the rapid formation of a continuous coolant film over the protected surface. As discussed in the previous subsection, internal tangential flow within the porous matrix entrains coolant toward the downstream region, delaying coolant discharge near the leading edge. Consequently, the formation of the protective coolant film is postponed, reducing cooling performance, particularly in the upstream region.

To overcome this limitation, spatially varying porosity has emerged as a promising strategy to locally regulate coolant discharge, thereby accelerating the formation of a continuous coolant film. In TPMS structures, porosity can be precisely tailored through their mathematical formulation using level-set equations. However, the application of functionally graded TPMS structures to transpiration cooling remains largely unexplored.

This study therefore aims to investigate the influence of porosity distribution on coolant flow behavior and to establish design guidelines by identifying porosity configurations that enhance cooling performance.

3.7 Cooling Mechanisms of Effusion and TPMS-based Transpiration Cooling

The previous sections investigated the influence of TPMS geometric parameters on adiabatic film cooling effectiveness (AFE), which focuses on the contribution of coolant-film formation by assuming an adiabatic wall and therefore excludes the effects of conjugate heat transfer (CHT). Although AFE is an effective metric for evaluating coolant-film performance, it does not represent the overall thermal protection achieved under practical operating conditions, where both external film cooling and internal heat transfer contribute to the cooling process.

This section therefore investigates the cooling mechanisms of effusion and TPMS-based transpiration cooling by comparing three representative cooling configurations: a baseline effusion cooling of 0° compound angle, a 45° compound-angle effusion cooling , and a Koch-type TPMS-based transpiration cooling . By combining AFE and overall film cooling effectiveness (OFE) measurements, the respective contributions of coolant-film formation and conjugate heat transfer are quantified to provide a comprehensive understanding of the cooling mechanisms governing TPMS-based transpiration cooling. Consequently, this study aims to clarify the fundamental differences in cooling mechanisms and to identify the advantages of TPMS-based transpiration cooling for gas turbine liner applications.

Chapter 4

Methodology and Research Approach

4.1 TPMS Structure

TPMS (triply periodic minimal surface) is ubiquitous in nature. For example, similar configurations can be found in butterfly wings, sea sponges, diamonds, and even soap films (see Figure 31). Such biological systems exhibit micro- and nano-scale architectures composed of interpenetrating solid and void phases, providing an advantageous combination of high strength and low weight required for mobility, support, and protection.

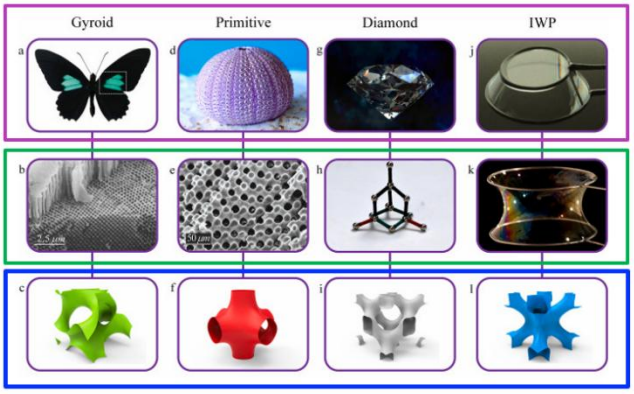

Figure 31 Various types of TPMS found in nature [93]

Schwarz [75], mathematically described nature-inspired Primitive and Diamond types of TPMS structures in the early 1860s. Although these structures have been regarded as theoretically superior, they have not been practically applied due to the limitations of conventional manufacturing methods. With the recent advancements in 3D printing technology, it has become possible to fabricate structures with intricate internal passages, such as TPMS. Moreover, these structures can be readily modeled using mathematical formulations, known as level-set equations, which are listed in Table 1.

Table 1 Trigonometric level-set equations utilized for each TPMS generation

Type of TPMS	Level-set equation
Gyroid	$sinXcosY + sinY\cos Z + sinZ\cos X = c$
Diamond	$\sin(X)\sin(Y)\sin(Z) + \sin(X)\cos(Y)\cos(Z) + \cos(X)\sin(Y)\cos(Z) + \cos(X)\cos(Y)\sin(Z) = c$
Koch	$cos2XsinYcosZ + cosXcos2YsinZ + sinXcosYcos2Z = c$
PMY	$2cosXcosY\cos Z + sin2XsinY + sinXsin2Z + sin2YsinZ = c$
Neovious	$3(cosX + cosY + \cos Z) + 4(cosXcosY\cos Z) = c$
IWP	$2(cosXcosY + cosY\cos Z + cosZcosX) - (cos2X + cos2Y + cos2Z) = c$
Primitive	$cosX + cosY + \cos Z = c$
FRD	$2cosXcosY\cos Z = c$

In a level set equation, 3-D coordinates x, y, and z are nondimensionalized by unit cell sizes α, β, and γ in x, y, and z directions respectively such that: $X = 2\pi x/\alpha$, $Y = 2\pi y/\beta$, and $Z = 2\pi z/\gamma$. The level-set constant, denoted as c, can be adjusted to regulate the relative porosity of the unit cell by varying the wall thickness. The specific relationship between the parameter c and porosity is illustrated in Figure 32.

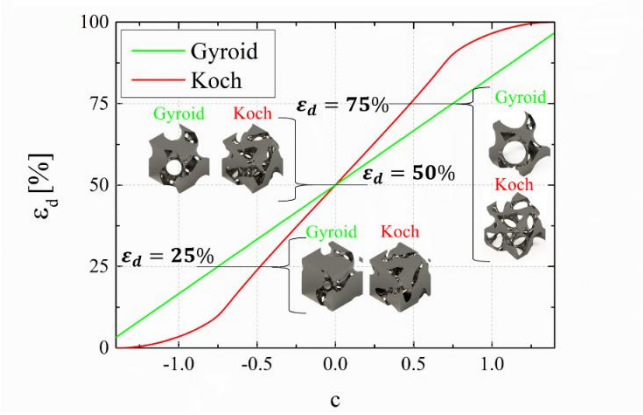

Figure 32 Porosity variation of TPMS lattices as a function of the level-set constant c.

TPMS-based lattices offer several potential advantages over conventional strut-based lattices, as summarized in Table 2. Strut-based lattices typically exhibit abrupt geometric transitions at their junctions, whereas TPMS-based lattices feature smooth, continuous surface transitions [94]. Previous studies have reported generally higher specific surface areas for sheet-based TPMS

architectures than for strut-based lattices at comparable relative densities [95] . Furthermore, strut junctions can promote local stress concentrations [94] , whereas the smooth transitions in TPMS-based lattices can alleviate such concentrations and improve load distribution. These geometric characteristics make TPMS structures promising candidates for addressing the previously discussed limitations of conventional porous media in transpiration cooling.

Table 2 Comparison of geometric characteristics and stress distribution between strut-based and TPMS-based lattices.

Feature	Strut-based lattices	TPMS
Representative unit-cell geometry	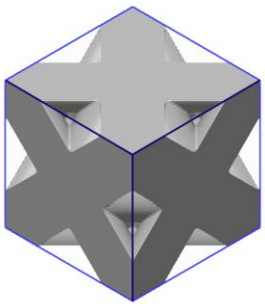 Octet truss	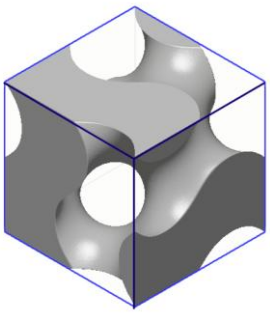 Gyroid
Surface continuity	Abrupt transitions at junctions	Smooth, continuous surfaces
Wetted surface area	Generally lower	Generally higher
Mechanical strength	Stress concentration at junctions	More uniform stress distribution

The iso(boundary)-surface, generated by the level set equation, is used to divide the volume into two distinct domains: the solid and the void domain, both enclosed by the iso-surface. Regions with values below the iso-surface threshold are designated as solid, while those exceeding this threshold are classified as voids. When c is set to zero, the level setting equation generates a porosity of 50%, thereby dividing the solid domain and void domain equally. The solid domain in this instance is defined by the following equation.

$$\emptyset(x, y, z) < c \tag{11}$$

The unit iso-surfaces and unit cell structures of each TPMS geometry listed in Table 1 are shown in Figure 33.

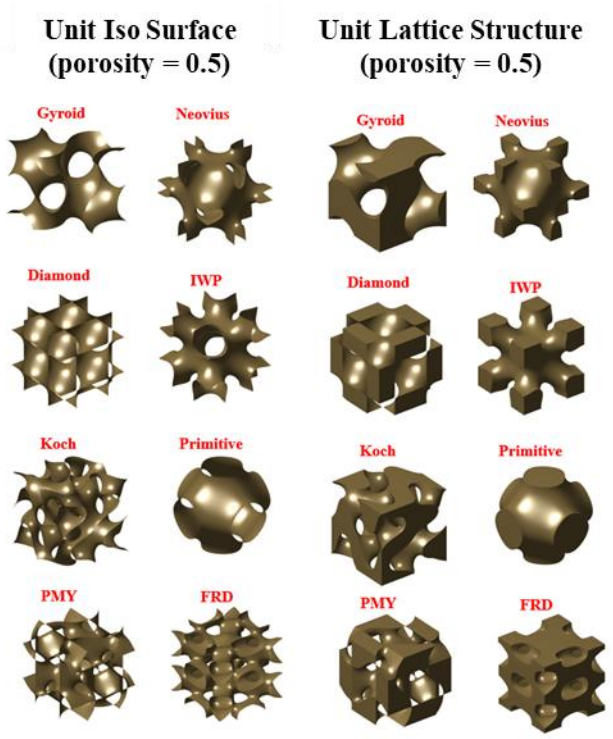

Figure 33 Unit iso-surfaces (left) and corresponding unit lattice structures (right) of various TPMS geometries at a porosity of 0.5.

As mentioned before, TPMS structures possess large wetted surface areas, making them well suited for cooling applications. Figure 34 presents the wetted surface area of the unit cells for various TPMS structures, which was theoretically calculated using an in-house MATLAB code.

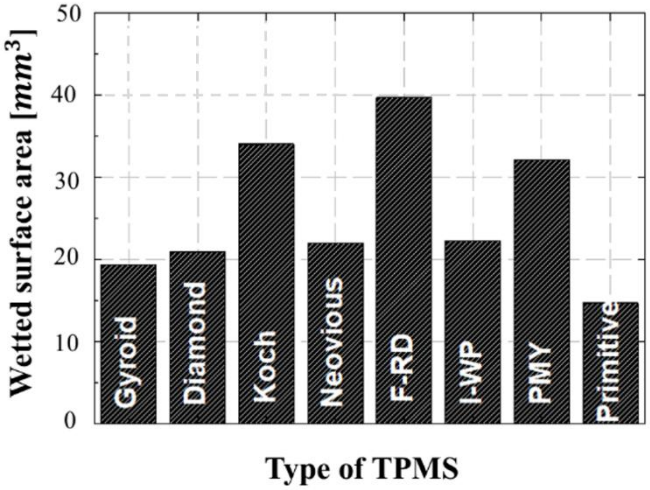

Figure 34 Wetted surface area of unit cells for various TPMS geometries at a porosity of 0.5. The wetted surface area was calculated for a unit cell volume of 2.5 × 2.5 × 2.5 mm³

Another key geometric parameter of TPMS structures influencing cooling performance is the pore diameter. The pore diameter, D_p, is defined as the diameter of the largest inscribed sphere that can pass through the narrowest constriction within the porous channel [96]. Figure 35 illustrates this definition for a gyroid-type unit cell. The pore diameter is governed by both the TPMS morphology and the porosity of the structure. Figure 36 shows the pore diameter as a function of porosity for Koch and Gyroid TPMS structures.

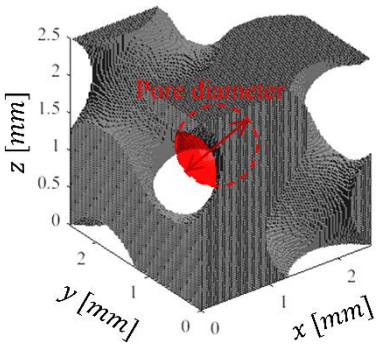

Figure 35 Unit cell cube of a Gyroid type TPMS structure with 50% porosity

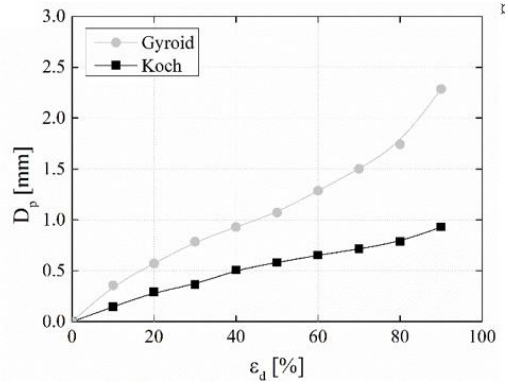

Figure 36 Pore diameter D_p as functions of porosity εd, for different TPMS geometries.

4.2 Fabrication of TPMS Test Coupons

In this study, the test coupons are fabricated using a commercial SLA (stereolithography) 3D printer (Form 3, Formlabs Inc., USA). This printer employs a single violet diode laser source with a wavelength of 405 nm and a laser power of 250 mW. The printing resolution is set to 25 µm in all three axes. In conjunction with the 3D printer, a high-temperature resin, capable of achieving a heat deflection temperature (HDT) of 238°C at 0.45 MPa after curing, was employed.

Figure 37 shows the active area within a test coupon featuring the Diamond type TPMS lattices. The total active area was measured to be 6.6 cm × 7.1 cm, however, only the center portion was used for measuring film cooling effectiveness to minimize the influences from edges of the test coupon. The observation area for making film cooling effectiveness measurement is of the dimensions of 2.5 cm × 7.1 cm, as indicated by the blue area in Figure 37. All measured 2D film cooling effectiveness distributions reported correspond to the observation area.

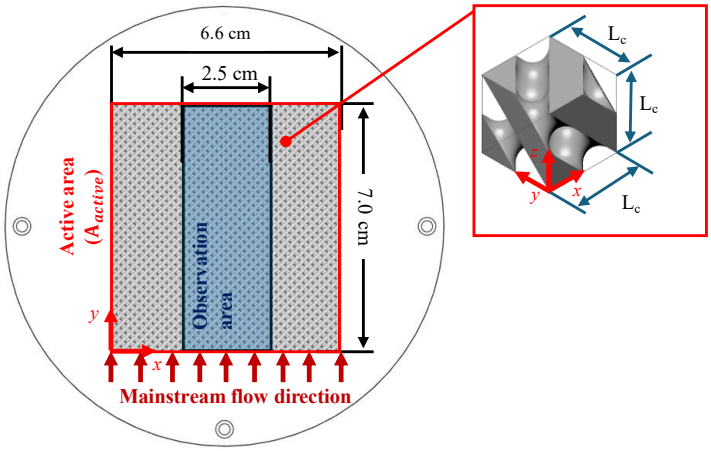

Figure 37 Schematic of test coupon with an active area featuring TPMS lattices.

To maintain a consistent porosity level across all test coupons in the final product, it is important to precisely control the 3D printing process. However, even when both the 3D printing process and the design parameters in the CAD model are controlled as precisely as possible, it is almost impossible to obtain exactly the design porosity after fabrication. This is a well-known challenge in additive manufacturing, where discrepancies often occur between designed geometries and actual end products [97].

Figure 38 conceptually illustrates the reduction of the internal void caused by excess material deposition during additive manufacturing of a TPMS unit cell. This void reduction is particularly pronounced at finer feature sizes, where unintended overcuring (i.e., excessive material deposition caused by excess laser energy input) partially fills the designed void regions, thereby reducing the final actual porosity.

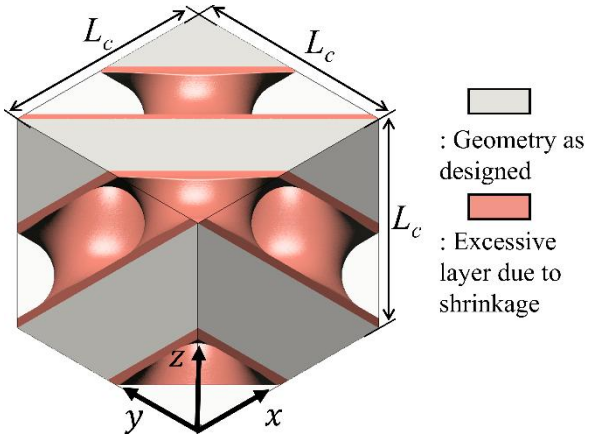

Figure 38 Unit cell cube of the Diamond type TPMS structure with 50% porosity illustrating excess printed layer formation during additive manufacturing.

Figure 39 compares the computer-aided design (CAD)-designed top surface profile with a microscopic image of the printed top surface, captured using a KEYENCE VHX-2000 digital microscope. The pitch $S_{x,d}$ is defined as the horizontal distance between adjacent solid boundaries in the CAD design. The designed profile (Figure 39 (a)) shows distinct boundaries between solid and void regions with a constant $S_{x,d}$. However, the microscopic image (Figure 39 (b)) reveals a wider boundary pitch than the designed $S_{x,d}$, which can be attributed to the deposition of an additional printed layer during fabrication.

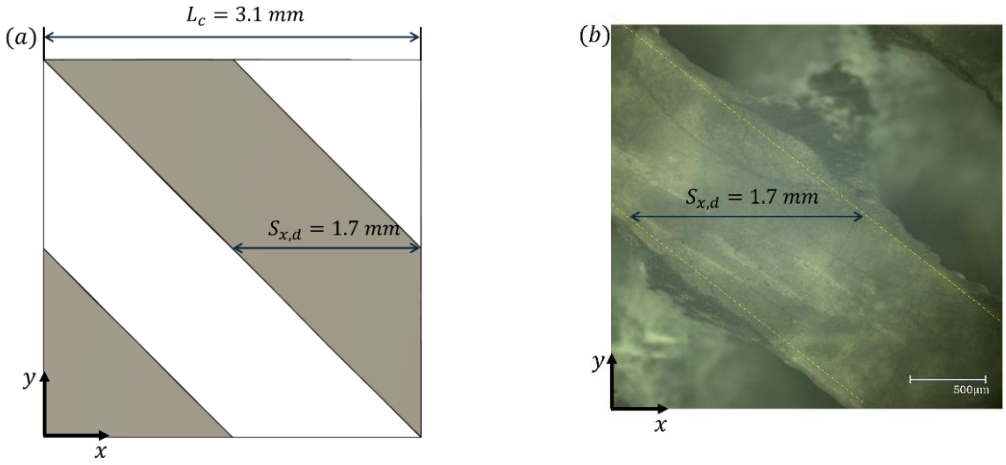

Figure 39 Profile of the solid–void boundary at the top surface of a Diamond-type TPMS structure with L_c=3.1 mm and 44% design porosity: (a) CAD-designed top surface profile (b) microscopic image of the printed top surface.

The geometrical discrepancies are attributed to excess material deposition during the additive manufacturing process, resulting in a reduction of the internal pore size relative to the original design. This poses a challenge to designing and fabricating TPMS lattices on millimeter scales. This reduction of the internal void is particularly challenging as the pore diameters of the TPMS structure D_p approaches the limit of 3D printer resolutions; in other words, printability issue arises. The additive manufacturing process involves a progressive deposition of layers, with the 3D CAD model being sliced into 2D layers that are subsequently built upon to form 3D parts. However, for curved surfaces, this slicing results in a stair-like profile. Using a smaller layer thickness can mitigate the stair-case effect, though this will inevitably prolong the build time. This issue can cause discrepancies between the actual and designed porosity. It is common for the porosity observed in TPMS structures produced via additive manufacturing to be lower than the designed value [25,98]. If the energy supplied by the laser exceeds the required amount, the wall thickness may become oversized, particularly near fine features such as edges.

In the present study, the layers thickness was set to 25µm, the smallest size compatible with the 3D printer used, with the objective of minimizing the stair-like profile within the TPMS structures. However, even with the best printer resolution setting, the reduction of the internal void becomes significant as the TPMS lattices approach printability limits. This is quantified by comparing design porosity (ε_d) of the lattice and the actual measured porosity (ε_a). The actual porosity was estimated based on the measured weight of the printed sample. The design porosity

can be inferred directly from the level-setting equation of the TPMS lattice, whereas the actual porosity can be inferred from the mass of final print product as follows.

$$\varepsilon_a = (1 - \frac{M_a}{M_s}) \times 100 \tag{12}$$

where M_a is the mass of the fabricated TPMS lattice structure and M_s is the mass of a fabricated solid piece of the same outer dimensions as the target TPMS lattice structure. Figure 40 summarizes how actual porosity deviates from design values with varying unit cell size, as primary findings from printability tests.

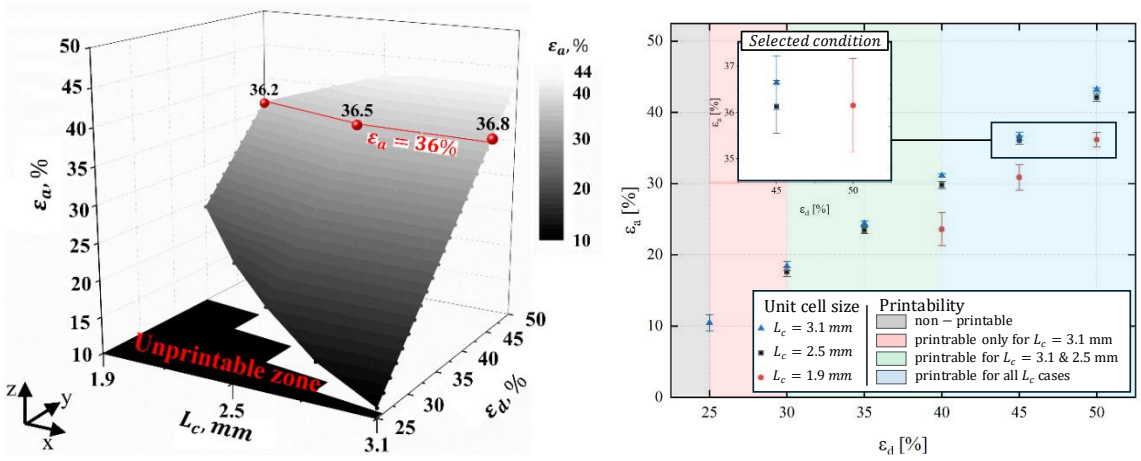

(a) (b)

Figure 40 Actual porosity as a function of unit cell size and design porosity presented as (a) a 3D surface plot and (b) a 2D representation of the same data.

The actual porosity values were measured using a precision electronic scale (Scientech SA-80) with a resolution of 0.1 mg, allowing determinations of actual porosity on a mass basis. As Figure 40 (a) illustrates, x and y axes represent the unit cell size and design porosity, respectively. The actual porosity is indicated by the grayscale color map and the *z*-axis, determined by Equation (12). The black-colored area on the *x*-*y* plane represents the unprintable region, where the pore diameter was closer to 0.6 mm. In this unprintable region, the pores of the TPMS structure experience stochastic clogging during the 3D printing process, resulting in uneven coolant distribution and a loss of interconnectivity of the lattice's internal channels, as the pore size approaches printability limits as compounded by decreasing unit cell size and porosity. Figure 40(b) further illustrates the printability map. At a design porosity below 25%, none of the unit cell sizes are printable, as indicated by the black region. Between 25% and 30%, only the largest unit cell ($L_c = 3.1$ mm) is

printable (red region). Between 30% and 40%, both the large and medium unit cell sizes ($L_c = 3.1$ and 2.5 mm) are printable (green region). Above 40%, all unit cell sizes become printable (blue region). It is also noteworthy that the standard deviation, calculated from five printed samples, increases near the printability boundaries, indicating reduced manufacturing consistency. Therefore, the experimental condition was selected away from the printability boundaries. As shown in the enlarged view, the selected design condition exhibits a maximum standard deviation of only ±1%, demonstrating good repeatability of the additive manufacturing process.

4.3 Overview of Experiment Setup

The transpiration cooling investigations are carried out in an open-loop low-speed wind tunnel located at the Gas Turbine Laboratory of the National Research Council Canada. Figure 41 shows a schematic of the experimental setup.

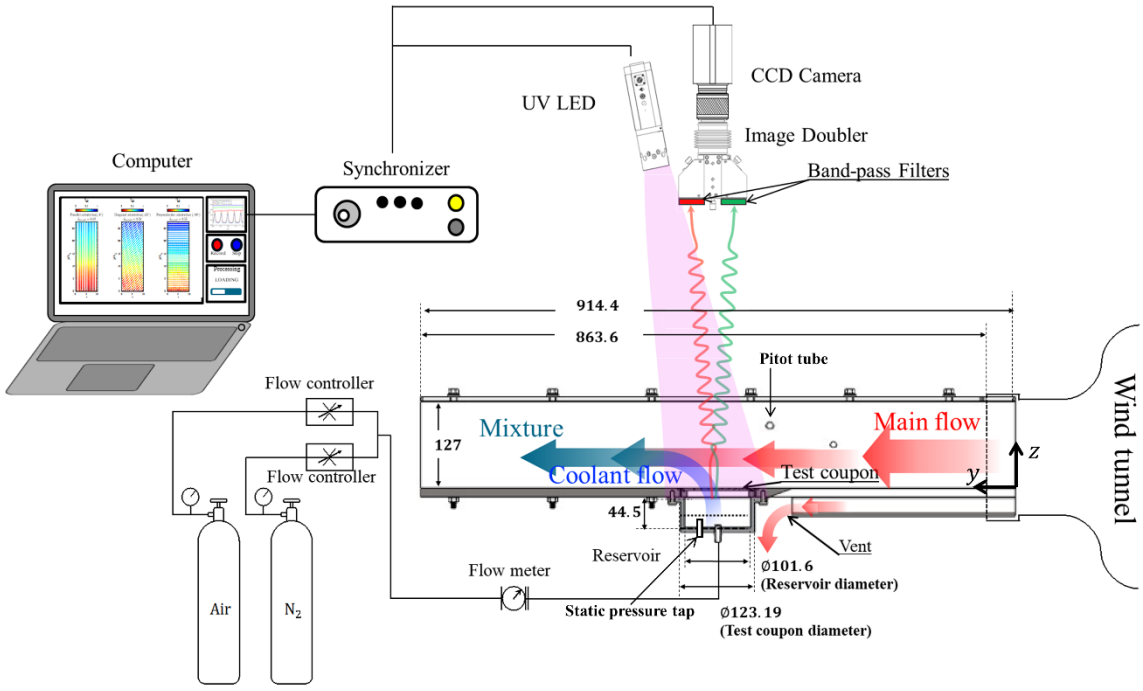

Figure 41 Schematic of the experimental setup

The main airflow is driven by a 30kW fan, capable of achieving a maximum mass flow rate of approximately 2.5kg/s at a pressure rise of 5kPa. In the test section, which has a 127 mm × 127 mm square cross-section, the mainstream airflow velocity was maintained at 33 m/s. The corresponding Reynolds number is approximately 256,000, representing typical airflow conditions

found in a gas turbine combustor. The turbulence intensity (TI) within the test section is estimated to be approximately 3% based on the empirical Reynolds number correlation, $TI = 0.16Re^{-1/8}$. The mainstream flow velocity is measured using a pitot tube, located at the leading edge of the test coupon. Nitrogen (N_2) is used as the coolant proxy, supplied through compressed gas bottles. The flow of the coolant is controlled by a FMA 5400A/5500A series flow meter from OMEGA, capable of adjusting the flow rate between 0 and 200 standard liters per minute (SLPM). The coolant is first sent to a reservoir and was conditioned by the combination of a honeycomb screen and a perforated plate to ensure a uniform distribution of coolant flow to the test coupon. The location of the honeycomb screen and perforated plate combination is indicated by the dashed line inside the reservoir in Figure 41. The reservoir has an internal diameter of 101.6 mm and a height of 44.5 mm. In addition, a ventilation system was implemented to control boundary-layer development upstream of the test coupon. Its effectiveness was validated by comparing the baseline configuration with a non-vented setup. The results confirm that the vent system plays a critical role in achieving the desired aerodynamic conditions by regulating boundary-layer thickness. The vented and non-vented configurations are shown in Figure 42(a) and Figure 42(b), respectively.

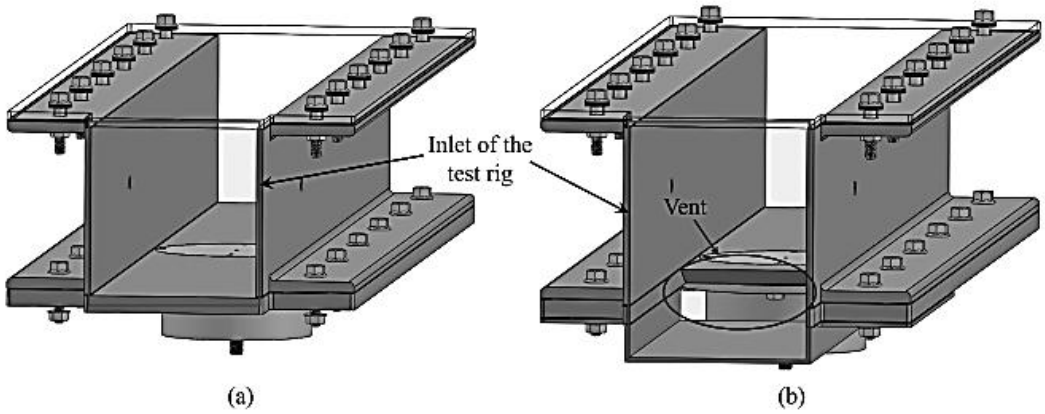

Figure 42 3D CAD model of the test rig: (a) without the vent system and (b) with the vent system.

A vent was designed and installed near the leading edge of the test coupons to control the boundary layer thickness, as shown in Figure 43(a). The boundary layer thickness was measured using a hot-wire anemometer positioned at the leading edge of the test coupon and centered across the width of the test section. The hot-wire probe was traversed vertically up to a height of 63.5 mm from the bottom wall to obtain the velocity profile. The measured velocity profile was compared with the CFD prediction, showing good agreement, and the momentum boundary layer thickness was determined from the velocity profile, as illustrated in Figure 43(b).

A vent was designed and installed near the leading edge of the test coupon to control the boundary layer thickness, and Figure 43(a) shows an enlarged view of the vent together with the hot-wire measurement arrangement used to measure the boundary layer thickness. The hot-wire probe was traversed vertically up to a height of 63.5 mm from the bottom wall to obtain the velocity profile. The measured velocity profile was compared with the CFD prediction, showing good agreement as illustrated in Figure 43(b).

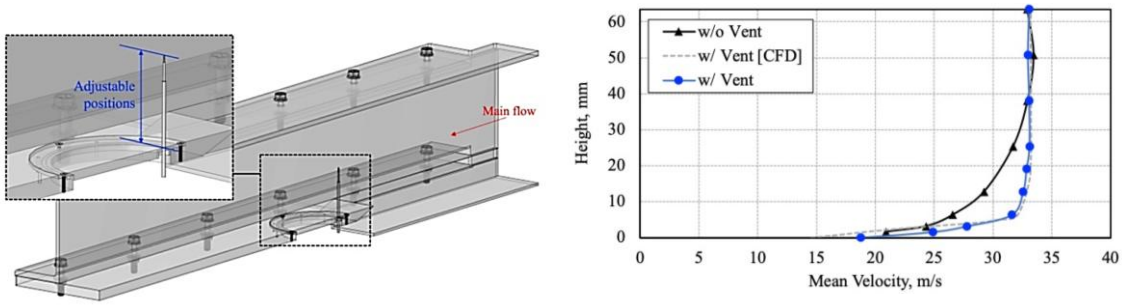

(a) (b)

Figure 43 (a) Cutaway view of the CAD model of the test section, illustrating the boundary layer control vent and the hot-wire measurement arrangement. (b) Comparison of the measured velocity profiles with and without the vent, together with the corresponding CFD predictions.

The operating conditions for all cases are shown in Table 2. As described earlier in section 2.2, the injection ratio was introduced to ensure a more appropriate evaluation of transpiration cooling performance. The corresponding blowing ratios, defined based on conventional effusion cooling for comparison.

Table 3 Summary of test conditions.

Injection ratio, %	**Corresponding Blowing ratio**	**Coolant flow rate, SLPM**	**Main air flow velocity, m/s**
0.68	0.6	66	33.0
1.14	1.0	110	33.0
1.60	1.4	153	33.0

In this study, the binary or dual-luminophore pressure-sensitive paint (PSP) and temperature-sensitive paint (TSP), both supplied by ISSI (Integrated Silicon Solution Inc.), were employed to evaluate the adiabatic film cooling effectiveness (AFE) and overall film cooling effectiveness (OFE), respectively.

A PSP advantage in studying film cooling is that the paint allows an in-situ determination of 2D distribution of adiabatic film cooling effectiveness. This capability makes the PSP method uniquely suited for studying detailed features of film cooling effectiveness across 2D surfaces, providing an intuitive understanding of film cooling performances. The fundamental principle of the PSP technique is luminescence decays of excited dye molecules is a function of non-radiative quenching by molecular oxygen within the paint, thereby the paint can function as distributed optical sensors for oxygen partial pressures. Binary PSP comprises two luminophores that interact with oxygen (see Figure 44 (top)), and a polymer binder that allows for oxygen permeation. Luminophore molecules absorb UV light, and transition to an excited state.

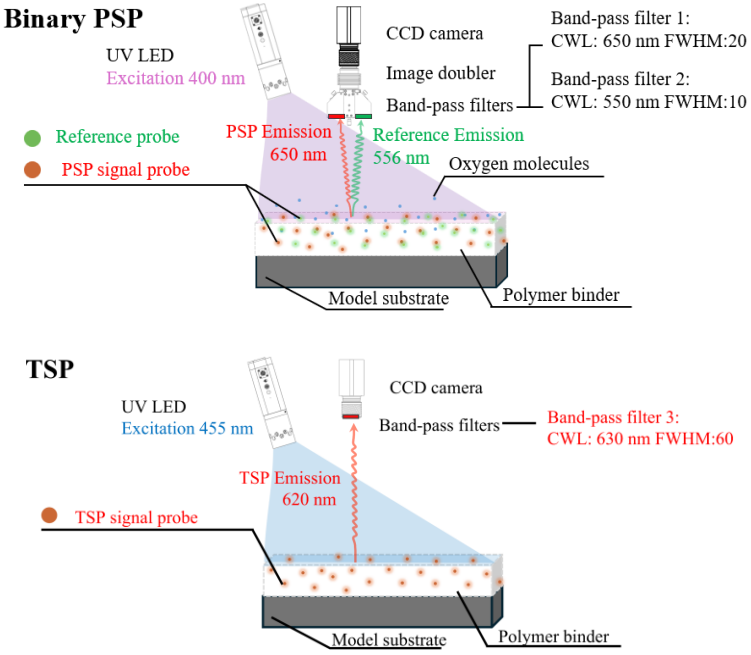

Figure 44 Schematic of binary pressure sensitive paint (top) and temperature sensitive paint (bottom).

These excited-state molecules either emit light about a specific wavelength or revert to the ground state through oxygen quenching. When the partial pressure of surrounding oxygen is high, the increased molecular presence of oxygen enhances the number of molecules transitioning back to the ground state via oxygen quenching, consequently reducing the number of excited-state molecules emitting light at a specific wavelength. Thus, the luminescent intensity emitted by PSP is inversely proportional to the oxygen partial pressure. In experiments utilizing PSP, the intensity of light emitted is recorded and analyzed to determine the two-dimensional (2D) oxygen pressure

distribution across the test surface. The paint consists of two different luminophores: a phosphor that is sensitive to both oxygen partial pressure and temperature variations has an emission spectrum centered at 650nm, and the other being sensitive only to temperature variations has an emission spectrum centered at 550nm. An air-cooled UV LED array (ISSI LM2X-DM-400) emitting UV radiation centered at 400nm is used for uniform and stable UV excitation of the PSP paint. A CCD camera (Lavision Image ProX 2M) with an image doubler (LaVision) attached in front was used to record luminescence from the PSP at 550nm and 650nm simultaneously. The two lenses of the image doubler were spectrally conditioned with bandpass filters, each centered at different wavelengths: the first filter at 650 nm with a 20 nm FWHM (full-width at half-maximum), and the second filter at 550 nm with a 10 nm FWHM. The image doubler juxtaposes the two wavelength-filtered images, allowing the CCD camera to record a single composite image containing the pixel-by-pixel light intensity at both wavelengths. The detailed measurement principle is described in the following section.

In contrast to PSP, TSP consists of a luminophore dispersed in an oxygen-impermeable polymer binder (see bottom panel of Figure 44). The luminophore absorbs blue excitation light and transitions to an excited state, from which it returns to the ground state by emitting fluorescence or through non-radiative thermal quenching. Unlike PSP, oxygen quenching does not occur because the polymer binder is impermeable to oxygen. Instead, the emission intensity is governed solely by temperature. As the temperature increases, the probability of non-radiative thermal quenching increases, reducing the luminescence intensity. Consequently, the emitted luminescence intensity is inversely proportional to the surface temperature. In TSP measurements, the spatial distribution of luminescence intensity is recorded and analyzed to reconstruct the two-dimensional (2D) surface temperature distribution, which is subsequently used to determine the overall film cooling effectiveness (OFE). A Royal Blue LED array (Thorlabs, M455L4) emitting light centered at 455 nm was employed to provide uniform and stable excitation of the TSP coating. The emitted fluorescence, centered at approximately 620 nm, was captured using a CCD camera (LaVision Image ProX 2M) equipped with a band-pass filter centered at 630 nm with a full width at half maximum (FWHM) of 60 nm. The camera records the pixel-by-pixel luminescence intensity to generate a spatially resolved temperature map. The detailed measurement principle is described in the following section.

4.4 Fundamentals of Pressure Sensitive Paint

In this research, Pressure Sensitive Paint (PSP) is utilized as a tool for examining heat/mass transfer mechanisms [99] particularly in the realm of film cooling studies[100–103]. To begin, the governing equation describing heat transfer in a two-dimensional turbulent boundary layer, expressed in the x–y coordinate system for a homogeneous fluid, is given as follows:

$$G_x \frac{\partial T}{\partial x} + G_y \frac{\partial T}{\partial y} = \rho(\alpha_\mathrm{t} + \alpha) \frac{\partial^2 T}{\partial y^2} \tag{13}$$

Here, α and G represent the thermal diffusivity and mass flux, respectively, and the subscript t denotes turbulent quantities. Under the assumption of an adiabatic boundary condition, the corresponding boundary conditions are as follows:

$$at\ y = 0\ (interface): \frac{\partial T}{\partial y} = 0, T = T_\mathrm{aw} \tag{14}$$

$$at\ y = \delta_\mathrm{f}\ (outside\ of\ the\ coolant\ film): T = T_\infty \tag{15}$$

$$at\ y = 0\ (coolant\ temperature):\ T = T_\mathrm{c} \tag{16}$$

Consider an analogous case in which the hot mainstream flow (T_∞) contains a tracer concentration C_∞, and the coolant discharged through the film-cooling holes (T_C) has a tracer concentration C_C. The corresponding governing equation for mass transfer, where C denotes the mass fraction of either a tracer element or a constituent gas, is given as follows:

$$G_x \frac{\partial C}{\partial x} + G_y \frac{\partial C}{\partial y} = \rho(D_\mathrm{t} + D) \frac{\partial^2 C}{\partial y^2} \tag{17}$$

Here, D represents the mass diffusivity. Under the assumption of an impermeable wall, the corresponding boundary conditions are as follows:

$$at\ y = 0\ (interface): \frac{\partial C}{\partial y} = 0, C = C_\mathrm{aw} \tag{18}$$

$$at\ y = \delta_\mathrm{f}\ (outside\ of\ the\ coolant\ film): C = C_\infty \tag{19}$$

$$at\ y = 0\ (coolant\ temperature):\ C = C_\mathrm{c} \tag{20}$$

It can be observed that Equations (13) and (17), along with their respective boundary conditions, share a similar structure. When the turbulent Lewis number, $Le_t = \frac{\alpha_t+\alpha}{D_t+D}$, equals unity, the governing equations and corresponding boundary conditions indicate that the properly nondimensionalized solutions for temperature and mass concentration become identical. Based on the findings of Rigby et al[104]., the approximation $Le_T \approx 1$ is valid for turbulent gaseous flow fields, including those typically encountered in gas turbine engines. Therefore, the adiabatic film cooling effectiveness,η_{ad}, can be as follows:

$$\eta_{ad} = \frac{T_{aw} - T_\infty}{T_C - T_\infty} \approx \frac{C_{aw} - C_\infty}{C_C - C_\infty} \tag{21}$$

The adiabatic film cooling effectiveness can be obtained through Equation (21). By invoking the analogy between heat and mass transfer, a direct correlation can be established between the PSP fluorescence intensity and the adiabatic film cooling effectiveness.

The relationship between fluorescence intensity and oxygen concentration is described by the Stern–Volmer equation as follows:

$$\frac{I_{max}(T)}{I(T)} = 1 + K(T) \cdot S(T,p) \cdot p \tag{22}$$

where I is the measured PSP fluorescence intensity, I_{max} is the maximum fluorescence intensity in the absence of oxygen, K is the Stern–Volmer constant depending on temperature, S is Henry's law coefficient (a function of both temperature and pressure), and p is the local oxygen partial pressure at the surface. In most aerodynamic applications, it is challenging to establish oxygen-free conditions because wind tunnels generally operate with air containing about 21% oxygen. Consequently, wind-off (zero-flow) conditions are commonly used as the reference state. Based on this approach, a second-order polynomial calibration relationship can be expressed as follows:

$$\frac{p}{p_{ref}} = A(T) + B(T)\left(\frac{I_{ref}}{I}\right) + C(T)\left(\frac{I_{ref}}{I}\right)^2, where \frac{I_{ref}}{I} = \frac{I_{ref} - I_{dark}}{I - I_{dark}} \tag{23}$$

The subscript *ref* denotes the reference condition corresponding to standard air with UV excitation, and I_{ref} represents the corrected PSP fluorescence intensity measured under these standard air conditions. In contrast, the subscript *dark* refers to the images obtained without UV excitation, which may include background light or sensor noise. To correct background light noise, both the

raw PSP fluorescence intensity I and the reference intensity I_{ref} are adjusted by subtracting the dark image intensity I_{dark}, yielding the corrected fluorescence intensities. And where A(T), B(T), and C(T) represent coefficients for each coefficient for polynomial curve fitting, but it also depends on temperature. Such fluctuations in the illumination intensity and temperature variations during calibration and data collection can impact the accuracy of deriving local oxygen partial pressures from PSP fluorescence. The effect of temperature on PSP fluorescence intensity is shown in Figure 45.

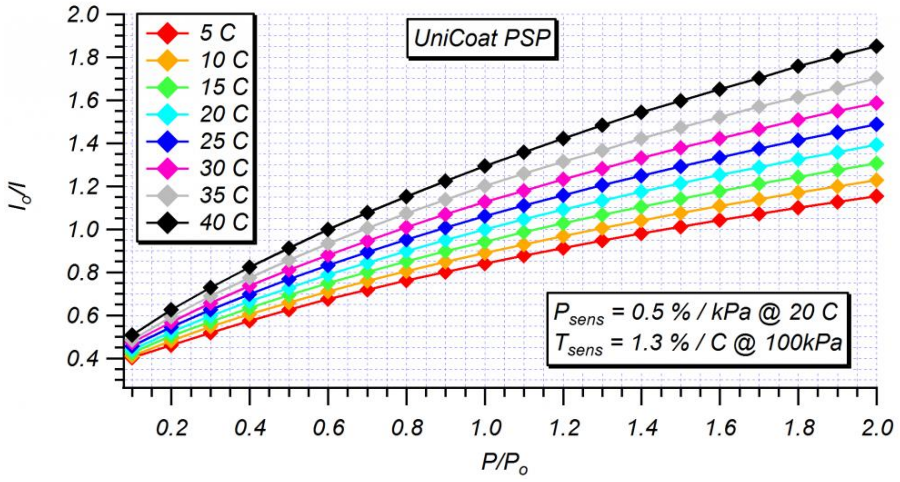

Figure 45 PSP calibration curve for single luminophore PSP [100]

To mitigate these uncertainties, a binary PSP is employed. As mentioned in previous chapter, the binary PSP is composed of two different luminophores: one is a phosphorescent dye that is sensitive to both oxygen partial pressure and temperature variations, the other is a fluorescent dye sensitive only to temperature variations. The binary PSP enables compensation for temperature-induced errors in the PSP signal using the following equation:

$$\frac{p}{p_{ref}} = A + B\left(\frac{r_{ref}}{r}\right) + C\left(\frac{r_{ref}}{r}\right)^2 \tag{24}$$

where

$$\frac{r_{ref}}{r} = \frac{\left(\frac{I_{ref} - I_{dark}}{I - I_{dark}}\right)_{PT}}{\left(\frac{I_{ref} - I_{dark}}{I - I_{dark}}\right)_{T}} \tag{25}$$

The subscripts PT and T denote the pressure- and temperature-sensitive emission (650 nm) and the temperature-sensitive reference emission (550 nm), respectively. By using a binary PSP, the temperature dependency during measurement can be neglected. The calibration curve for the binary PSP under various temperatures is shown in Figure 46.

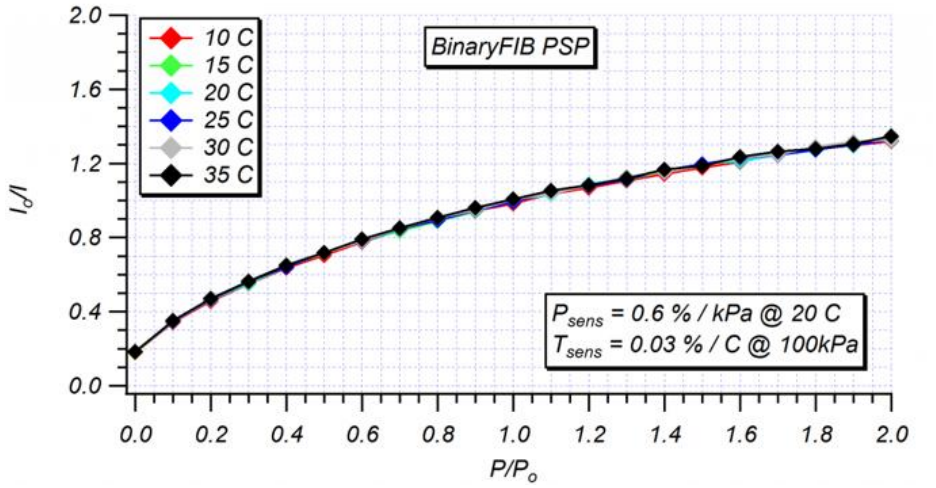

Figure 46 PSP calibration curve for binary PSP[103]

In this study, nitrogen is used as a coolant proxy. By adopting PSP, the adiabatic film cooling effectiveness (η_{ad}), defined in Equation (21), can be expressed as a ratio of the oxygen partial pressure measured by PSP as follows:

$$\eta_{ad} \approx \frac{C_{\mathrm{O2,air}} - C_{\mathrm{O2,mix}}}{C_{\mathrm{O2,air}}} = 1 - \frac{1}{1 + \frac{MM_{\mathrm{c}}}{MM_{\mathrm{air}}}\left[\frac{\left(X_{\mathrm{o_2,air}}\right)}{\left(X_{\mathrm{o_2,mix}}\right)} - 1\right]} = 1 - \frac{1}{1 + \frac{MM_{c}}{MM_{air}}\left[\frac{p}{p_{ref}} - 1\right]} \tag{26}$$

where $C_{\mathrm{O2,air}}$ and $C_{\mathrm{O2,mix}}$ represent the oxygen mass concentration in the mainstream flow (air) and the air-nitrogen mixture on the test surface, respectively, while $X_{\mathrm{O2,air}}$, and $X_{\mathrm{O2,mix}}$ denote the corresponding mole fractions. MM_{c} and MM_{air} are the molecular weights of air and coolant.

Chapter 5

Results

This chapter presents the results of seven systematic investigations conducted to advance transpiration cooling for next-generation gas turbines through the application of additively manufactured TPMS (Triply Periodic Minimal Surface) lattice structures. The primary objective of this research is to optimize the TPMS-based cooling architecture by systematically evaluating the influence of key design parameters on transpiration cooling performance.

To achieve this objective, the study defines the following research tasks to comprehensively assess the thermal performance of TPMS-based transpiration cooling structures:

---

1. The Influence of TPMS Unit Cell Size on Transpiration Cooling Performance
2. The Influence of TPMS Porosity on Transpiration Cooling Performance
3. The Influence of TPMS Orientation Angle on Transpiration Cooling Performance
4. The Influence of TPMS Morphology on Transpiration Cooling Performance
5. The Influence of Internal Tangential Flow on Transpiration Cooling
6. Porosity Optimization of TPMS Structures for Uniform Coolant Distribution
7. Comparison of Cooling Mechanisms Between Effusion and TPMS-Based Transpiration Cooling

---

The first four studies focus on the systematic isolation and independent evaluation of key TPMS design parameters—porosity (Diamond TPMS), unit cell size (Diamond TPMS), orientation angle (Diamond, Gyroid, and Koch TPMS), and morphological variation (Diamond, Gyroid, and Koch TPMS)—to quantify their isolated effects on transpiration cooling performance. The fifth and sixth studies shift the focus toward understanding and mitigating internal tangential flow. The fifth study (Diamond TPMS) elucidates the influence of internal tangential flow on transpiration cooling performance, whereas the sixth study (Gyroid and Koch TPMS) investigates porosity optimization as a design strategy to accelerate coolant-film formation by suppressing the adverse

effects of internal tangential flow. The final study (Koch TPMS) provides a fundamental assessment of the cooling mechanisms by simultaneously evaluating adiabatic film effectiveness (AFE) and overall film effectiveness (OFE), thereby distinguishing the relative contributions of coolant-film protection and conjugate heat transfer in TPMS-based transpiration cooling.

5.1 The Influence of TPMS Unit Cell Size on Transpiration Cooling Performance

This study investigates the influence of TPMS unit cell size on transpiration cooling effectiveness under three different blowing ratios. The primary focus is to quantitatively evaluate the effect of unit cell size on adiabatic film cooling effectiveness (η_{ad}) while maintaining a constant porosity level in the additively manufactured structures.

Through experimental measurements using binary pressure-sensitive paint (PSP), the study systematically examines the distinct effects of three different unit cell sizes on adiabatic film cooling effectiveness (AFE) at an identical porosity level. The results provide insight into how variations in unit cell size contribute to changes in cooling performance.

The results demonstrate that, even at a constant porosity, reducing the unit cell size improves the AFE. Smaller unit cells promote a more uniform coolant discharge and enhance coolant coverage over the cooled surface, resulting in a more continuous protective coolant film. These findings indicate that unit cell size is a critical design parameter for TPMS-based transpiration cooling and should be optimized together with porosity to maximize cooling performance.

Smaller unit cell sizes were found to produce smaller pore diameters (D_p) and larger wetted surface areas at a constant porosity level, resulting in higher pressure drop. Therefore, understanding the interrelationship between unit cell size, cooling effectiveness, pressure drop, and printability provides valuable guidance for the development of TPMS-based transpiration cooling strategies for next-generation gas turbine engines.

This study is written as a research article and published as a peer-reviewed journal paper, The Journal of Thermophysics and Heat Transfer.

JOURNAL OF THERMOPHYSICS AND HEAT TRANSFER
Vol. , No. ,

Impact of Triply Periodic Minimal Surface Structure Unit Cell Size on Transpiration Cooling

Juchan Son,[*] Yeongmin Pyo,[†] Patrick Richer,[‡] Bertrand Jodoin,[§] and Zekai Hong[¶]
University of Ottawa, Ottawa, Ontario K1N 6N5, Canada

https://doi.org/10.2514/1.T7212

Transpiration cooling is a highly promising technology for use in thermal management in modern gas-turbine-based aeroengines, providing superior cooling effectiveness compared to state-of-the-art effusion cooling methods. However, conventional porous media such as metallic foams and sintered metals, when used for transpiration cooling, face challenges in achieving desired engineering properties, such as surface texture, mechanical strength, and porosity profile. To achieve the full potential of transpiration cooling by overcoming the challenges inherent in conventional porous media, a precisely engineered deterministic porous medium is desirable. Recent advancements in additive manufacturing have enabled the fabrication of porous media with highly precise lattice structures. Among candidate lattice structures, triply periodic minimal surface (TPMS) structures are considered ideal due to their superior mechanical strengths and fully interconnected, periodic internal channels and external texture patterns to facilitate cooling film development. This study aims to investigate the impact of unit cell size of TPMS lattices on adiabatic film cooling effectiveness using binary pressure-sensitive paint (PSP). Diamond-type TPMS lattices of a fixed actual porosity (36%) but of three distinct unit cell sizes (1.9, 2.5, and 3.1 mm) were examined at three injection ratios (F = 0.68%, 1.14%, and 1.60%). Results show that smaller unit cell sizes lead to more effective and more uniform cooling films. Enhanced transpiration cooling effectiveness at smaller unit sizes might be attributed to shallower surface voids and reduced lateral flow within the porous medium. The findings are expected to guide the design of TPMS-based transpiration cooling systems.

Nomenclature

A	=	first-order coefficient of the polynomial fitting curve
A_{active}	=	active area, m^2
A_w	=	internal wetted area, m^2
B	=	second-order coefficient of the polynomial fitting curve
BR	=	blowing ratio
C	=	third-order coefficient of the polynomial fitting curve
C_{O2}	=	oxygen mass concentration, kg/m^3
c	=	TPMS level set constant
D_p	=	pore diameter of TPMS structure, m
d_c	=	effusion cooling hole diameter, m
F	=	injection ratio
I	=	intensity of PSP
L_c	=	unit cell length, m
MM	=	molecular weight, kg/kmol
M_a	=	mass of 3D printed TPMS lattices, kg
M_s	=	mass of 3D printed solid blocks, kg
P	=	pressure, kPa
$\dot{Q}_c$	=	coolant volumetric flow rate, m^3/s
r	=	intensity ratio for binary PSP
$S_{s,d}$	=	horizontal pitch between adjacent solid boundaries in the computer-aided design, mm
u	=	velocity, m/s
V	=	volume of porous medium, m^3
X	=	mole fraction
α	=	unit cell constant for x direction, m
β	=	unit cell constant for y direction, m
γ	=	unit cell constant for z direction, m
ΔP	=	percentage pressure drop
Δz	=	distance to the saddle void point, m
ϵ	=	porosity, %
η_{ad}	=	adiabatic film cooling effectiveness
λ	=	ratio of wetted surface area to volume, cm^2/cm^3
ϕ	=	level-set equation

Presented as Paper 2025-0329 at the AIAA SciTech 2025 Forum, Orlando, FL, January 6–10, 2025; received 18 February 2025; accepted for publication 20 June 2025; published online XX epubMonth XXXX. Copyright © 2025 by National Research Council of Canada. Published by the American Institute of Aeronautics and Astronautics, Inc., with permission. All requests for copying and permission to reprint should be submitted to CCC at www.copyright.com; employ the eISSN 1533-6808 to initiate your request. See also AIAA Rights and Permissions https://aiaa.org/publications/publish-with-aiaa/rights-and-permissions/.

[*]Ph.D. Candidate, affiliated with both the National Research Council of Canada and the University of Ottawa, 75 Laurier Ave E; also Aerospace Research Center, National Research Council of Canada, 1200 Montreal Road, Ottawa, Ontario K1A 0R6, Canada.

[†]Research Associate, affiliated with both the National Research Council of Canada and the University of Ottawa, 75 Laurier Ave E; also Aerospace Research Center, National Research Council of Canada, 1200 Montreal Road, Ottawa, Ontario K1A 0R6, Canada.

I. Introduction

TO IMPROVE overall engine efficiency, the turbine inlet temperature (TIT) has been gradually increased to above 2000 K [1,2]. However, this temperature exceeds the temperature limits of nickel-based superalloys, such as Inconel (Ni-Cr-Fe based) [3]. Given the extreme temperatures of gas turbines' hot-gas path, implementing effective thermal protection for crucial components, such as combustor liners, is essential to meet performance requirements and overcome metallurgical challenges [4].

Thermal management methods for gas turbine liners include convection [5], impingement [6], and effusion cooling [7,8]. Among these, effusion cooling is considered a state-of-the-art technology, extensively used in gas turbine liners, often in conjunction with thermal barrier coatings [9].

Over the past few decades, substantial efforts have been devoted to optimizing and enhancing the cooling effectiveness of effusion cooling. Andreini et al. [10] investigated the impact of hole injection angle (20°, 30°, and 90°) on the performance of effusion cooling under realistic swirling flow conditions. The results demonstrated that a more tilted injection angle (20 deg) provided the best film protection, enhancing adiabatic film cooling effectiveness and optimizing the stability of the coolant layer and its interaction with the mainstream

flow. Pyo et al. [7] investigated the impact of nonzero compound angles with constant pitch on adiabatic film cooling effectiveness. They found that a compound angle between 30° and 60° optimizes jet penetration and mixing, enhancing cooling effectiveness, with 45° recommended as an ideal starting point for future designs. In addition, extensive research was conducted to optimize various design parameters, inclination angle [11], pitch spacing [12], hole size [13], and shape [14,15], and fluid dynamic parameters, including blowing ratio (BR) [16,17] and density ratio [18].

To enhance the cooling effectiveness of stand-alone effusion cooling, recent studies explored the combination of jet impingement and film cooling, often applied to double-walled configurations for combined effects. Cho and Rhee [19] demonstrated that impingement/effusion cooling systems significantly increase surface mass transfer rates—approximately 6–10 times higher than effusion cooling alone. Jung et al. [20] examined conjugate heat transfer on full-coverage film cooling plates with varying Biot numbers, emphasizing the critical role of material conductivity.

However, effusion cooling consumes a significant amount of high-pressure compressor discharge air as coolant, creating a strong demand for advanced cooling methods that achieve high cooling effectiveness while reducing cooling air usage. From this perspective, transpiration cooling is considered the most ideal and promising cooling method for gas turbine hot-gas path components. Initially proposed in the early 1950s, transpiration cooling is recognized for its superior heat sink capability and its ability to promote coolant film formation over a broad surface—known as boundary-layer heat-blocking—without causing coolant film liftoff [21–23]. In transpiration cooling, coolant was transpired through a porous medium, such as sintered powder [24], woven mesh wires [25], melt casting [26], perforated plates [27], and composite porous materials [28], generating a coolant film that effectively blocks thermal penetration onto the surface.

Liu et al. [24] investigated the flow and heat transfer characteristics of transpiration cooling through sintered porous flat plates with different particle diameters (40 and 90 μm). Their results demonstrated that even a small amount of coolant injection significantly reduces heat transfer from hot gases, with cooling effectiveness increasing as the injection ratio rises and particle diameter decreases. Ma et al. [25] examined the performance of transpiration cooling using double and triple laminated sintered woven wire mesh structures with varying porosities. The study found that porosity and layer arrangement significantly influence fluid flow, heat transfer characteristics, and film coverage. Hinse et al. [26] conducted numerical and experimental studies to evaluate the film cooling effectiveness of transpiration cooling using melt-cast porous materials. Their findings showed that transpiration cooling could reduce the total surface heat flux by two to three times and deliver 15% to 30% higher film cooling effectiveness compared to multihole effusion cooling.

Over the past few decades, substantial efforts have been made to adapt transpiration cooling for practical applications [29,30]. However, despite these extensive efforts, transpiration cooling has not matured for engine applications, partly due to manufacturing challenges [31]. Primarily, conventional porous media have stochastic pore distributions, which can lead to uneven coolant mass flow distribution, resulting in localized hot spots and reduced mechanical strength. Additionally, it is impractical to ensure uniform pore sizes, and smaller pores are particularly vulnerable to clogging from contaminants in incoming air. Huang and He [32] investigated the impact of inhomogeneous porosity, caused by manufacturing tolerances and combustion gas contaminants, on cooling holes. Their study found that while inhomogeneous porosity significantly affects local film cooling effectiveness, it has a minimal effect (less than 1%) on overall cooling effectiveness due to heat conduction within the solid matrix.

Recent advancements in additive manufacturing technologies, commonly known as 3D printing, have made it feasible to fabricate lattice structures as deterministic porous media. Among these, the family of triply periodic minimal surfaces (TPMS) has gained significant attention as one of the most ideal lattice structures across various engineering fields [33]. This is due to their highly desirable characteristics, including periodic interconnected channels without abrupt edges and a high wetted surface-to-volume ratio. These unique features make TPMS structures widely applicable not only in heat sinks but also in transpiration cooling. [34–36].

Conversely, only a limited number of studies have been conducted on transpiration cooling using TPMS lattice structures. Zhou et al. [37] conducted a pore-scale investigation of transpiration cooling using TPMS structures. Their study revealed that the shape and size of the pore throat significantly influence coolant flow resistance and cooling effectiveness. Broumand et al. investigated transpiration cooling using TPMS structures with three different porosities (30%, 40%, and 50%) by comparing them with conventional effusion cooling methods under the same injection ratio (F) [38]. The results revealed that TPMS-based transpiration cooling does not suffer from cooling jet liftoff that is common to effusion cooling and can achieve an adiabatic film cooling effectiveness approaching unity when fully developed, while improving overall adiabatic film cooling effectiveness by more than five times at the highest injection ratio. Moreover, the authors of this study previously investigated the effect of the orientation angle of TPMS structures on transpiration cooling using three different geometries [39]. It was found that the Koch type of TPMS lattice exhibits insensitivity to the orientation of surface textures while maintaining the highest overall film cooling effectiveness, making it an ideal choice for transpiration cooling on complex surface geometries exposed to highly directional, localized flows. Although these prior investigations demonstrated great promise of TPMS-based transpiration cooling, a systematic investigation aimed at gaining a comprehensive understanding of TPMS-based transpiration cooling and optimizing its performance for engine conditions is still lacking. As part of a planned effort to systematically engineer optimal TPMS-based transpiration cooling, this study is focused on evaluating how an essential geometric parameter of lattice structures—unit cell size—impacts the performance of TPMS-based transpiration cooling.

There are many types of TPMS lattices within the family: Diamond type, Koch type, Gyroid type, to name a few. Therefore, it is impractical to investigate the effects of unit cell size on transpiration cooling performance for each type. The Diamond type is one of the simplest yet most extensively studied and applied TPMS structures in engineering. Therefore, without loss of generality, the present study aims to investigate the effects of unit cell size on transpiration cooling performance in the case of Diamond-type TPMS lattices. Three different Diamond-type TPMS test specimens with varying unit cell sizes were examined, while the porosity across all specimens was maintained. Consequently, unit cell size was the only geometric parameter to be evaluated in transpiration cooling performance in this study. The results of this study are expected to contribute to a comprehensive understanding of the interaction between the topological parameters of TPMS structures and cooling performance.

II. TPMS Structures and Experimental Setup

A. TPMS Lattice

The Diamond type of TPMS lattice was first proposed by Schwarz in 1865 [40], and it is selected as a representative TPMS type for studying effects of unit cell size on transpiration cooling performances, as discussed earlier in the Introduction section. The Diamond type of TPMS can be mathematically defined by level-setting equations in Cartesian coordinates [41], as shown below:

$$\varnothing(x,y,z) = \sin(X)\sin(Y)\sin(Z) + \sin(X)\cos(Y)\cos(Z) + \cos(X)\sin(Y)\cos(Z) + \cos(X)\cos(Y)\sin(Z) = c \tag{1}$$

where the capital letters (X, Y, and Z) are coordinates in three-dimensional space (x, y, z) nondimensionalized by unit cell lengths in three axial directions (α, β, and γ) respectively, such that $X = 2\pi x/\alpha$, $Y = 2\pi y/\beta$, and $Z = 2\pi z/\gamma$. Isotropic TPMS lattices

are most commonly engineered to take full advantage of the geometry's inherent benefits; therefore, the unit cell sizes in all directions are set as equal ($\alpha = \beta = \gamma = L_c$) in this study. The iso-(boundary)-surface is defined as a 3D surface where the level-setting equation is satisfied for a given constant c. For TPMS families, an isosurface divides the volume into two subdomains. A solid network can be derived from the isosurface by simply setting a subdomain on one side of the isosurface to be solid and the other subdomain to be void. In particular, when c is set as zero, the two subdomains have equal volumes, resulting in a 50% porosity (ε) of the derived solid network. In this study, the solid network is defined as follows:

Type of TPMS	1x1x1 unit cell cube ($\emptyset(x, y, z) < 0$)
Diamond	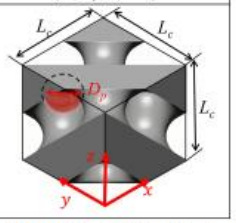

Fig. 1 Unit cell cube of the Diamond-type TPMS solid network with 50% porosity.

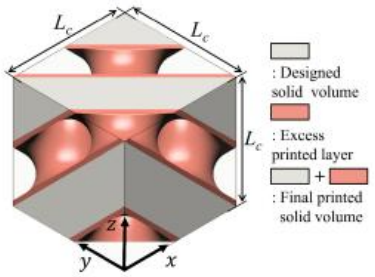

Fig. 2 Unit cell cube of a Diamond-type TPMS structure at 50% design porosity. The additional layer in color approximates the shrinkage of internal void due to additive manufacturing process.

$$\emptyset(x, y, z) < c \tag{2}$$

Figure 1 illustrates a solid network derived from the Diamond-type TPMS isosurface by setting $c = 0$, showing a unit cell cube. D_p in Fig. 1 represents the pore diameter of the TPMS structure, which is quantified as the diameter of the largest sphere that can pass through the narrowest channel of the structure [42].

B. Printability Test and Actual Porosity

It is a well-known challenge in additive manufacturing that discrepancies occur between design geometries and actual end products [43]. Figure 2 conceptually illustrates the effects of internal void shrinkage due to additive manufacturing processing in fabricating a TPMS unit cell. This shrinkage is particularly pronounced at finer feature sizes, where unintended overcuring (i.e., excessive material deposition caused by excess laser energy input) partially fills the designed void regions, thereby reducing the final actual porosity. Figure 3 compares the computer-aided design (CAD)-designed top surface profile with a microscopic image of the printed top surface, captured using a KEYENCE VHX-2000 digital microscope. The pitch $S_{x,d}$ is defined as the horizontal distance between adjacent solid boundaries in the CAD design. The designed profile (Fig. 3a) shows distinct boundaries between solid and void regions with a constant $S_{x,d}$. However, the microscopic image (Fig. 3b) reveals a wider boundary pitch than the designed $S_{x,d}$, which can be attributed to the deposition of an additional printed layer during fabrication.

The geometrical discrepancies are attributed to shrinkage, which is caused by uneven cooling of building materials and contraction as the materials solidify. This poses a challenge to designing and fabricating TPMS lattices on millimeter scales. This shrinkage is particularly challenging as the pore diameters of the TPMS structure D_p approaches the limit of 3D printer resolutions; in other words, the printability issue arises.

The additive manufacturing process involves a progressive deposition of layers, with the 3D CAD model being sliced into 2D layers that are subsequently built upon to form 3D parts. However, for curved surfaces, this slicing results in a stair-like profile. Using a smaller layer thickness can mitigate the staircase effect, though this will inevitably prolong the build time. Another issue that arises during the 3D printing process is a discrepancy between the actual and designed porosity. It is common for the porosity observed in TPMS structures produced via additive manufacturing to be less than the designed value [44,45]. If the energy supplied by the laser exceeds the required amount, the wall thickness may become oversized, particularly near fine features such as edges.

In the present study, the layer thickness was set to 25 μm, the smallest size compatible with the 3D printer used, with the objective of minimizing the stair-like profile within the TPMS structures. The

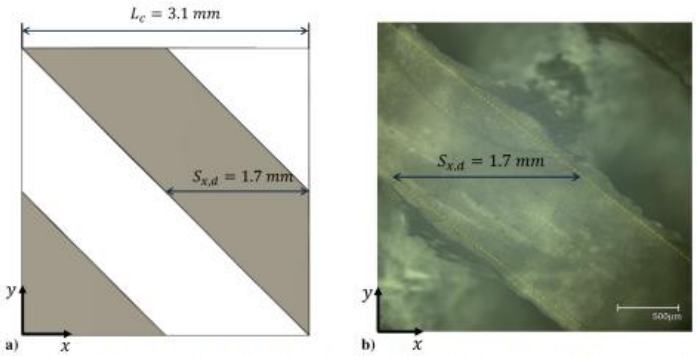

Fig. 3 Profile of the solid–void boundary at the top surface of a Diamond-type TPMS structure with $L_c = 3.1$ mm and 44% design porosity: a) CAD-designed top surface profile b) microscopic image of the printed top surface.

details of the 3D printer will be discussed later in the section. However, even with the best printer resolution setting, the shrinkage of internal voids becomes significant as the TPMS lattices approach printability limits, as indicated by pronounced deviations between the design porosity ε_d of the lattice and the actual porosity ε_a. Moreover, it is physically impractical to capture the entire porous geometry—particularly internal features—using optical microscopy, as the structure consists of multiple stacked layers of unit cells, obstructing visual access to inner regions. Therefore, in this study, the actual porosity was estimated based on the measured weight of the printed sample. The design porosity can be inferred directly from the level-sitting equation of the TPMS lattice, whereas the actual porosity can be inferred from the mass of the final print product as follows:

$$\varepsilon_a = \left(1 - \frac{M_a}{M_s}\right) \times 100 \tag{3}$$

where M_a is the mass of the fabricated TPMS lattice structure and M_s is the mass of a fabricated solid piece of the same outer dimensions as the target TPMS lattice structure. Figure 4 summarizes how actual porosity deviates from design values with varying unit cell size, as primary findings from printability tests. The actual porosity values were measured using a precision electronic scale (Scientech SA-80) with a resolution of 0.1 mg, allowing determinations of actual porosity on a mass basis. As Fig. 4 illustrates, the x and y axes represent the unit cell size and design porosity, respectively. The actual porosity is indicated by the grayscale color map and the z-axis, determined by Eq. (3). The black-colored area on the x-y plane represents the unprintable region, where the pore diameter was closer to 0.6 mm. In this unprintable region, the pores of the TPMS structure experience stochastic clogging during the 3D printing process, resulting in uneven coolant distribution and a loss of interconnectivity of the lattice's internal channels, as the pore size approaches printability limits as compounded by decreasing unit cell size and porosity.

Figure 5 illustrates pore diameter by design (D_p) as a function of design porosity (ε_d) and unit cell size (L_c). The red dashed line represents the printability threshold as estimated to be D_p = 0.6 mm; TPMS geometries of pore diameters below the threshold value were consistently observed with clogged pores due to deformations and shrinkage of internal voids from the additive manufacturing process. Geometries of pore diameters above this threshold value are deemed printable. The specific threshold design porosities for all three unit cell sizes were identified as follows:

1) Threshold design porosity $\varepsilon_d = 40\%$ at $L_c = 1.9$ mm to achieve $D_p = 0.61$ mm and an actual porosity $\varepsilon_a \approx 24\%$.

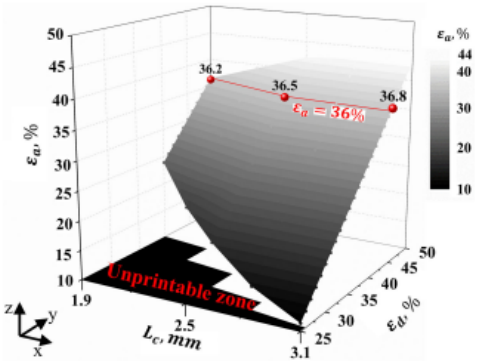

Fig. 4 Actual porosity as a function of unit cell size and design porosity. The red line marks the 36% actual porosity level.

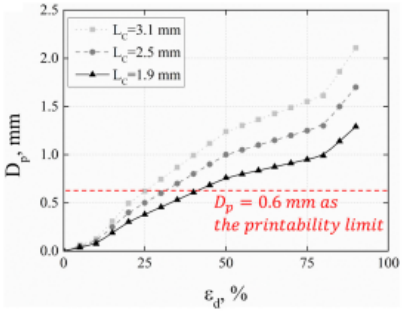

Fig. 5 Designed pore diameter (D_p) as a function of design porosity (ε_d) and unit cell size (L_c).

2) Threshold design porosity $\varepsilon_d = 30\%$ at $L_c = 2.5$ mm to achieve $D_p = 0.6$ mm and an actual porosity $\varepsilon_a \approx 18\%$.

3) Threshold design porosity $\varepsilon_d = 25\%$ at $L_c = 3.1$ mm to achieve $D_p = 0.6$ mm and an actual porosity $\varepsilon_a \approx 11\%$.

In the present study, three unit cell sizes were studied, while maintaining the same actual porosity, to focus on the effects of unit cell size on transpiration film cooling effectiveness. The design point was deliberately selected by matching the TPMS structure's pore size (D_p) with a typical effusion cooling hole diameter (d_e = 0.78 mm) [46]. If D_p was much smaller than 0.78 mm, the cooling air passage would be more susceptible to clogging due to contaminations, leading to degradation in long-term cooling performance [44]. The unit cell size of the baseline case ($L_{c,\text{base}}$) was determined to be 2.5 mm to achieve a 0.80 mm D_p at an actual porosity of 36%. These selected D_p values were sufficiently higher than the estimated printability threshold, preventing internal passages of the TPMS structures from clogging.

The unit cell size of two comparison cases was achieved by increasing and decreasing the baseline unit cell size by 25% to L_c = 3.1 mm and L_c = 1.9 mm, respectively. The 36% actual porosity is represented by the red line in Fig. 4, while the design porosities to achieve the identical actual porosity at all three unit cell sizes are indicated by the red points. The D_p values of actual printed samples were estimated to range from 0.61 mm at L_c = 1.9 mm to 0.99 mm at L_c = 3.1 mm. These selected unit cell sizes are within printability limits while ensuring that the pore sizes are comparable to conventional effusion cooling hole diameters.

To evaluate the repeatability of additively manufactured TPMS lattices, each TPMS geometry was 3D printed five times, and the actual porosity values of all five samples were independently determined. The mean and standard deviations of actual porosity measurements are summarized in Table 1. TPMS geometries of smaller unit cell sizes exhibit larger standard deviations in actual porosity, indicating that small unit cell sizes are more susceptible to inconsistencies in the 3D printing process, largely due to smaller pore diameters (see Fig. 5). It should be pointed out that all TPMS geometries investigated in this study, with actual porosity above 36%, showed relatively low standard deviations (<1%), indicating good repeatability in additive manufacturing processes.

C. Test Coupon Design

Three TPMS test coupons of the Diamond-type solid network were designed and fabricated at different unit cell sizes (L_c = 3.1 mm, 2.5 mm, and 1.9 mm) using a stereolithography (SLA) 3D printer. Liquid photopolymer solidifies by exposure to localized high-intensity UV illumination through a process known as photopolymerization. A commercial SLA 3D printer from Formlabs, Form3, was used for fabricating the test coupon, which features a 405 nm UV laser to achieve a resolution of 25 μm in all directions. In conjunction with the aforementioned 3D printer, a high-temperature resin, capable of achieving a heat deflection

Table 1 Mean and standard deviation values of actual porosity of printed TPMS structures[a]

Design porosity, %	Unit cell size = 3.1 mm		Unit cell size = 2.5 mm		Unit cell size = 1.9 mm	
	Actual porosity mean, %	Actual porosity standard deviation, %	Actual porosity mean, %	Actual porosity standard deviation, %	Actual porosity mean, %	Actual porosity standard deviation, %
25	10.43	1.13	Unprintable	— —	Unprintable	— —
30	18.42	0.64	17.60	0.64	Unprintable	— —
35	24.40	0.58	23.44	0.57	Unprintable	— —
40	31.12	0.37	29.82	0.56	23.60	2.30
45	36.75	0.25	36.46	0.50	30.87	1.78
50	43.21	0.24	42.13	0.45	36.15	1.01

[a]The TPMS structures are of varying unit cell sizes and design porosities.

temperature (HDT) of 238°C at 0.45 MPa after curing [47], was employed. Figure 6 shows the active area within a test coupon featuring the Diamond-type TPMS lattices. The total active area was measured to be 6.6 cm × 7.1 cm; however, only the center portion was used for measuring film cooling effectiveness to minimize the influences from nonactive edges of the test coupon. The observation area for making film cooling effectiveness measurements is of the dimensions of 2.5 cm × 7.1 cm, as indicated by the blue area in Fig. 6. All measured 2D film cooling effectiveness distributions that will be reported later in this article correspond to the observation area.

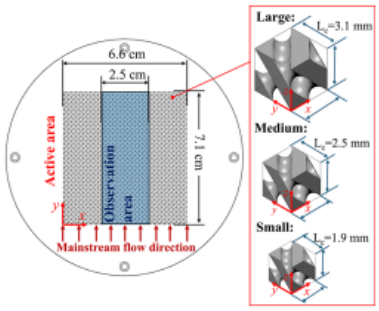

Fig. 6 Schematic of test coupon with an active area featuring TPMS lattices of three unit cell sizes.

Figure 7 presents the top surface texture of the observation area for all three test coupons. The blue regions represent solid surface, while the white regions denote surface grooves. The x and y axes in Fig. 7 are nondimensionalized by the unit cell size of the baseline case ($L_{c,base}$ = 2.5 mm). The thickness of the active area of the test coupons was identically set at 7.5 mm; therefore, the number of layers for each test coupon varies as the unit cell size changes. A schematic illustrating the variation in the number of layers is shown in Fig. 8.

Furthermore, top surface texture varies as a result of changing unit cell size, which alters how cooling flow interacts with the mainstream [39]. In particular, the depth of the top layer saddle points from the top surface, denoted as Δz, varies with unit cell size, as indicated in Fig. 8. Coolant enters the void near the top surface through pores located near the saddle points at the bottom of the void. The coolant initially accumulates in the void before gradually rising to the top surface. The coolant flow path is depicted by curved arrows in Fig. 9, illustrating how the fluid navigates through the porous structure. The Δz decreased from 0.35 mm at L_c = 3.1 to 0.24 mm at L_c = 1.9 mm. These values were calculated based on the actual porosity previously determined from mass measurements (see Fig. 4).

Figure 10 presents a 3D surface scan used to evaluate the actual Δz of the printed TPMS structure. Overall, the scanned geometry aligns reasonably well with the intended design. The designed Δz value was 388 μm, while the measured values were 341 and 330 μm at two different cross-sections. This observation further supports the presence of additional material deposited during printing. However, the measured Δz values are slightly smaller than the inferred value of 0.35 mm at L_c = 3.1, which was calculated based on actual porosity measurements. This discrepancy can be attributed to surface polishing

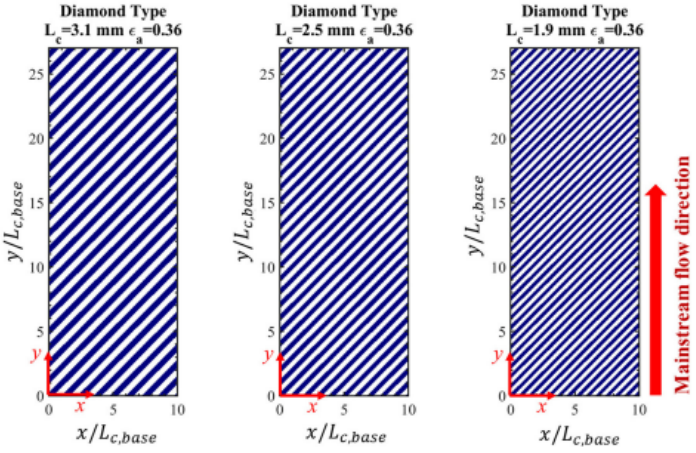

Fig. 7 Top surface texture of test coupons of varying unit cell sizes. The white areas denote void and the blue areas indicate solid surface areas.

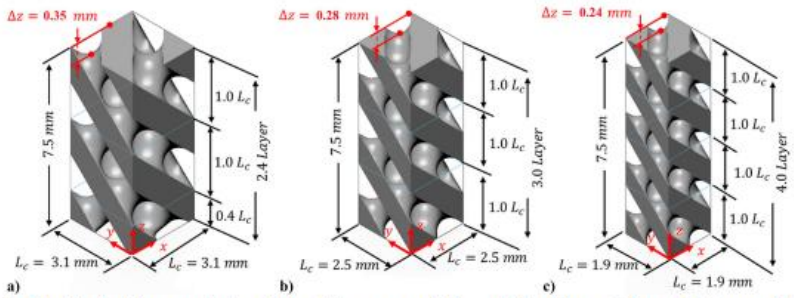

Fig. 8 Number of unit cell layers varies to maintain a 7.5 mm coupon thickness. Unit cell sizes: a) 3.1 mm, b) 2.5 mm, and c) 1.9 mm.

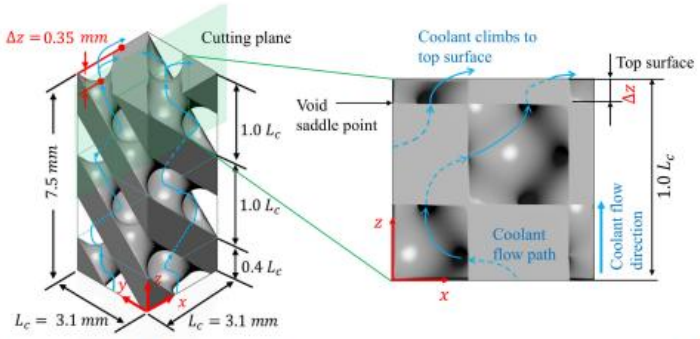

Fig. 9 Schematic of coolant flow paths in the TPMS lattice, emerging from internal passages and exiting at the top.

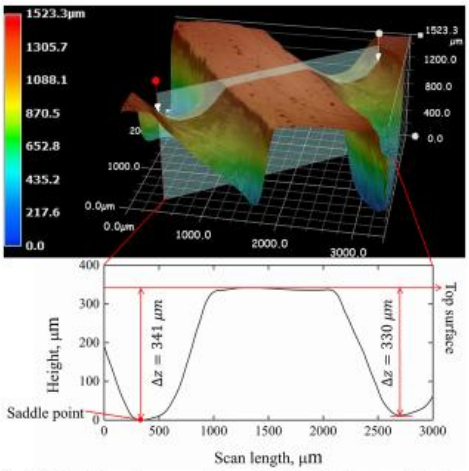

Fig. 10 The 3D surface scan of the printed TPMS structure with L_c = 3.1 mm and 36% actual porosity. The top image shows the surface height map, and the bottom plot presents the cross-sectional profile along the scan direction.

performed after printing, which may have reduced the top surface height. Additionally, as shown in Fig. 3b, the extra printed layer is not uniformly distributed, introducing local variation. Despite these deviations, the discrepancy is minor, and the porosity estimation derived from mass remains reliable. Key geometrical parameters are summarized in Table 2.

Table 2 Test coupon parameters

Parameter	Diamond-type TPMS		
Unit cell size, mm	3.1	2.5	1.9
Design porosity, %	44	45	48
Actual porosity, %	36	36	36
Actual pore size, mm	0.99	0.80	0.61
Number of layers	2.4	3.0	4.0
Depth of top layer saddle point from the top surface, mm	0.35	0.28	0.24
Wetted surface-area-to-volume ratio, cm^2/cm^3	18.7	23.7	30.5

D. Test Rig

An open-loop low-speed wind tunnel was used for studying TPMS-based transpiration cooling. Figure 11 shows the schematic of the test setup. The main flow is fed by a 30 kW fan capable of at 2.5 kg/s at a pressure rise of 5 kPa; the details are described in literature [48]. The test section has a cross-section of 127 mm × 127 mm. The mainstream flow velocity was set at 33 m/s, which was determined using a pitot tube in the center of the cross-section of the test section located at the leading edge of the test coupon. The corresponding Reynolds number is 256,000, which resembles the flow conditions inside a typical gas turbine combustor. Additionally, the turbulence intensity within the test section is estimated to be approximately 3%. The coolant proxy was inert nitrogen (N2), supplied through compressed gas bottles. The coolant flow was regulated by an OMEGA FMA 5400A/5500A series flow controller, capable of adjusting the flow rate between 0 and 200 standard liters per minute (SLPM). The coolant flow was initially directed to a

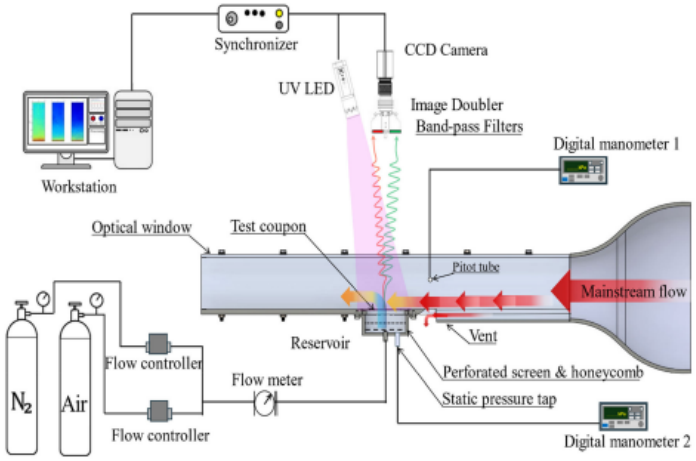

Fig. 11 Schematic of the experimental setup.

coolant reservoir, where it was conditioned by a honeycomb screen and a perforated plate to ensure uniform distribution to the active area of the test coupon. The dashed and dotted lines inside the reservoir in Fig. 11 indicate the locations of the perforated plate and honeycomb, respectively. The reservoir has an internal diameter of 101.6 mm and a height of 44.5 mm.

In the present study, a binary pressure-sensitive paint (PSP) from ISSI was used to measure adiabatic film cooling effectiveness. The application of PSP for studying film cooling effectiveness has been extensively discussed in our previous work [35,36]. The PSP was sprayed onto the top surface of the test coupon without clogging the internal channels. The thickness of the paint is estimated to be less than 20 μm, including the PSP and base coating [49]. Therefore, the application of PSP on the test coupon surface only induces insignificant alterations to the geometries of the TPMS lattices near the top surface of a test coupon. A significant advantage of adopting binary PSP is that 1) it allows for in-situ evaluation of the 2D distribution of film cooling effectiveness with high resolution, and 2) it eliminates temperature dependency by taking the ratio of two signals: one measures oxygen partial pressure, and the other serves as the reference. The fluorescence from the oxygen-sensitive molecule near 650 nm and the reference emission near 550 nm can be spectrally filtered to be free of each other. Details of the methodology of making film cooling effectiveness measurements using PSP are provided in the next section. An air-cooled UV LED array (ISSI LM2X-DM-400) centered at 400 nm was used to provide UV excitation to the PSP. The luminescent intensity of the excited PSP was recorded using a charge-coupled-device camera (Lavision Image ProX 2M) equipped with an image doubler (LaVision) conditioned with bandpass filters for each lens. The bandpass filters are one centered at 550 nm with a 10 nm full-width at half-maximum (FWHM) and the other one centered at 650 nm with a 20 nm FWHM.

III. Methodology

A. PSP Methodology

The adiabatic film cooling effectiveness (AFE), η_{ad}, is evaluated using the following equation:

$$\eta_{ad} = (T_m - T_{ad})/(T_m - T_c) \tag{4}$$

where T_m, T_{ad}, and T_c are the mainstream, adiabatic wall, and coolant temperatures, respectively. By adopting PSP to measure the η_{ad}, Eq. (4) can be expressed as a ratio of oxygen mass concentrations measured by PSP.

$$\eta_{ad} \approx \frac{C_{O2,air} - C_{O2,mix}}{C_{O2,air}} = 1 - \frac{1}{1 + \frac{MM_c}{MM_{air}}\left[\frac{(X_{O_2,air})}{(X_{O_2,mix})} - 1\right]} = 1 - \frac{1}{1 + \frac{MM_c}{MM_{air}}\left[\frac{(P_{O_2})_{air}}{(P_{O_2})_{mix}} - 1\right]} \tag{5}$$

where $C_{O2,air}$ and $C_{O2,mix}$ represent the oxygen mass concentration in the mainstream flow (air) and the air–nitrogen mixture on the test surface, respectively, while $X_{O2,air}$ and $X_{O2,mix}$ denote the corresponding mole fractions. MM_c and MM_{air} are the molecular weights of air and coolant; in this study, nitrogen was used as a coolant proxy. Further details can be found in [50]. The adiabatic film cooling effectiveness can be expressed as a ratio of the partial pressures of oxygen in the air ($(P_{O2})_{air}$) to the partial pressures of oxygen in the air–nitrogen mixture ($(P_{O2})_{mix}$) on the test surfaces, which can be determined by PSP [51].

PSP was applied in two layers: i) a basecoat layer that prepares the surface for binding, and 2) a PSP layer containing active luminescent molecules, including both oxygen-sensitive and reference molecules. These active luminescent molecules are uniformly distributed within a synthetic polymer binder. UV light excites oxygen-sensitive luminescent molecules within the binary PSP, causing them to emit light with an intensity inversely proportional to the partial pressure of oxygen near the paint surface. This phenomenon, known as oxygen quenching, occurs as higher oxygen partial pressure reduces the emitted light intensity. The relationship between oxygen partial pressure and the intensity of emission from oxygen-sensitive luminescent molecules can be approximated as a second-order polynomial, as follows [52]:

$$\frac{(P_{O2})_{mix}}{(P_{O2})_{air}} = \frac{p}{p_{ref}} = A(T)\left(\frac{I_{ref} - I_{dark}}{I - I_{dark}}\right)^2 + B(T)\left(\frac{I_{ref} - I_{dark}}{I - I_{dark}}\right) + C(T) \tag{6}$$

where I represent the intensity of the PSP fluorescence signal from oxygen-sensitive luminescent molecules. The subscript *ref* refers to reference fluorescence intensity with UV excitation when the coolant flow is off, while the subscript *dark* indicates background light intensity without UV excitation. The reference intensity condition is taken by having the PSP-coated test coupon exposed to ambient air, and the dark intensity is a result of background light and camera

offset. $A(T)$, $B(T)$, and $C(T)$ are temperature-dependent polynomial coefficients.

However, uncertainties introduced by temperature variations can be problematic when using the single-luminophore PSP. Therefore, dual-luminophore (binary) PSP was adopted to minimize uncertainties induced by temperature dependency of PSP fluorescence signal from oxygen-sensitive luminescent molecules. As discussed in prior studies, the temperature dependency can be removed by taking the ratio of the intensity of the pressure-sensitive fluorescence and that of the reference fluorescence near 650 and 550 nm, respectively. Equation (6) then can be rewritten as follows:

$$\frac{p}{p_{\text{ref}}} = A\left(\frac{r_{650}}{r_{550}}\right)^2 + B\left(\frac{r_{650}}{r_{550}}\right) + C \tag{7}$$

$$\left(\frac{r_{650}}{r_{550}}\right) = \frac{\left(\frac{I_{\text{ref}} - I_{\text{dark}}}{I - I_{\text{dark}}}\right)_{650\,\text{nm}}}{\left(\frac{I_{\text{ref}} - I_{\text{dark}}}{I - I_{\text{dark}}}\right)_{550\,\text{nm}}} \tag{8}$$

where r is the ratio of fluorescence intensities due to ambient air and under the influence of coolant proxy, both with dark background subtracted. By adopting the binary PSP, the polynomial coefficients A, B, and C became temperature-independent. The detailed calibration process for the binary PSP was reported in previous studies [7,8].

B. Repeatability of 3D Printing Processes

Shrinkage of internal voids is commonly observed in additively manufactured parts. Specific to porous structures, such shrinkages result in discrepancies between design and actual porosities of a porous geometry. To minimize the influence of such shrinkages, the TPMS geometries were selected so that their pore diameters are well above the estimated printability threshold ($D_p \approx 0.6$ mm as shown in Fig. 4). The uncertainty in 3D printing was quantified using Eq. (3), and the propagation of uncertainty was performed as follows:

$$\delta\varepsilon_a = \sqrt{\left(\frac{\partial\varepsilon_a}{\partial M_a}\delta M_a\right)^2 + \left(\frac{\partial\varepsilon_a}{\partial M_s}\delta M_s\right)^2} \tag{9}$$

The relative uncertainty of actual porosity for all TPMS geometries of this study was ±1.57% for unit cell size $L_c = 1.9$ mm, ±1.10% for $L_c = 2.5$ mm, and ±0.30% for $L_c = 3.1$ mm, respectively.

C. Measurement Uncertainty

Measuring adiabatic film cooling effectiveness using the binary PSP requires an accurate in-situ calibration. With a careful in-situ calibration, the measurement uncertainty can be derived from Eq. (5) through uncertainty propagation analysis [53,54].

$$\delta\eta_{\text{ad}} = \sqrt{\left(\frac{\partial\eta_{\text{ad}}}{\partial(P_{O_2})_{\text{mix}}}\delta(P_{O_2})_{\text{mix}}\right)^2 + \left(\frac{\partial\eta_{\text{ad}}}{\partial(P_{O_2})_{\text{air}}}\delta(P_{O_2})_{\text{air}}\right)^2} \tag{10}$$

For cases where the adiabatic film cooling effectiveness is $\delta\eta_{\text{ad}} = 0.8$ and $\delta\eta_{\text{ad}} = 0.2$, the relative measurement uncertainties were estimated to be $\delta\eta_{\text{ad}} = \pm 1.34\%$ and $\delta\eta_{\text{ad}} = \pm 5.46\%$, respectively. Sources of measurement errors include flow meters (OMEGA FMA5400A/5500A-series, ±1.5%), pressure transducers (Druck DPI 142, ±0.01%), and electronic scales (Scientech SA-80, ±0.1 mg).

IV. Results and Discussion

A. Operating Conditions and Pressure Drops

The operating conditions in this study were selected to match coolant usage over the same area under typical modern aeroengine conditions at blowing ratios (BR) of 0.6, 1.0, and 1.4 [7,8]. BR can be defined as follows:

$$BR = (\rho u)_c/(\rho u)_m \tag{11}$$

where ρ and u represent density and velocity, respectively. Meanwhile, the subscripts c and m denote coolant and mainstream flow. The mainstream flow velocity was maintained at 33 m/s, and the coolant velocity was determined from coolant volumetric flow rates $\dot{Q}_c$ active area A_{active}, as illustrated in Fig. 6, and the surface porosity $\varepsilon_{\text{surface}}$ of the test coupon.

$$u_c = \frac{\dot{Q}_c}{A_{\text{active}}\varepsilon_{\text{surface}}} \tag{12}$$

Due to much higher surface porosity in transpiration cooling cases in comparison with the state-of-the-art effusion cooling scenarios, BRs for transpiration cooling are significantly lower than corresponding effusion cooling cases (see Table 2). Consequently, the traditional BR is less suitable for describing test conditions in transpiration cooling studies. Alternatively, the injection ratio (F) is defined for describing transpiration cooling studies. The definition of F is as follows:

$$F = \frac{\dot{m}_c}{(\rho u)_m A_{\text{active}}} \tag{13}$$

where $\dot{m}_c$ is the coolant mass flow rate. In the present study, the active area ($A_{\text{active}} = 6.6\text{ cm} \times 7.1\text{ cm}$) was consistent with previous transpiration and effusion cooling studies [7,38]. The injection ratio was selected as $F = 0.68\%$, 1.14%, and 1.60%, by matching the coolant flow rates of baseline effusion cooling cases of the same A_{active} at BRs of 0.6, 1.0, and 1.4, respectively.

The percentage pressure drop (ΔP) across the porous TPMS structure was evaluated by taking the ratio of the absolute pressure drop across the test coupon and the static pressure immediately upstream to the transpiration test coupon. The upstream and downstream static pressures were measured by the pressure ports on the sidewalls of the coolant reservoir and the test section. The locations of each pressure port are illustrated in Fig. 11. ΔP is defined in Eq. (14), with Fig. 12 presenting the percentage pressure drops as functions of injection ratio F for all three test coupons.

$$\Delta P = \frac{P_{\text{reservoir}} - P_{\text{mainstream}}}{P_{\text{mainstream}}} \tag{14}$$

It is expected from Fig. 12 that ΔP monotonically increases with increasing F. A more illustrative observation is that ΔP sharply increases as the unit cell size decreases from 3.1 to 1.9 mm while maintaining the injection ratio. For example, ΔP is 0.42% with $L_c = 1.9$ mm, and ΔP drops to 0.09% when L_c increases to 3.1 mm with the injection ratio $F = 1.60\%$. The observation can

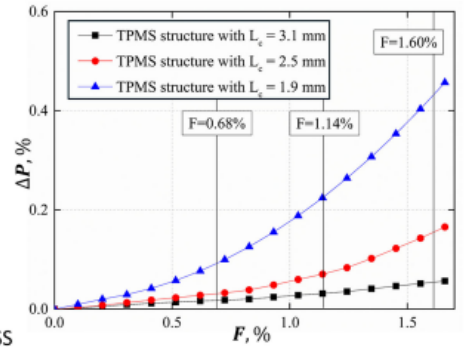

Fig. 12 Percentage pressure drops across transpiration cooling test coupons as functions of injection ratio.

be attributed to the fact that the wetted surface-area-to-volume ratio ($\lambda = A_W/V$) increases as unit cell size decreases [42]. The greater the λ, the more intricate the internal flow paths within TPMS lattice structures, making it more restrictive for the coolant to pass through. As summarized in Table 2, it can be seen that while the actual porosity is maintained, the pore sizes D_p are proportional to unit cell sizes. Upon more detailed examination, it is found that the decrease in pore sizes can be fully compensated by the increase in the number of unit cells per layer, leading to a constant throat area among all three test coupons of varying unit cell sizes. However, although the throat areas are invariant as unit cell size changes, as discussed earlier in the article, the number of layers increases as the unit cell size decreases, making the number of throats that the coolant needs to pass through the lattice structures inversely proportional to the unit cell size. It should be pointed out that the increase in throat area alone does not explain the changes in ΔP. For example, when the unit cell size reduces from $L_c = 3.1$ mm to $L_c = 2.5$ mm, the number of throats of internal flow passage increases by 25%; however, the increase in ΔP is more than 2X, as illustrated by Fig. 12. Therefore, the internal flow, and the subsequent ΔP, is strongly influenced by the viscosity of the internal flow, which can be represented by the wetted surface-area-to-volume ratio λ. It should also be pointed out that the ΔP obtained for the Diamond type of TPMS lattices is smaller compared to corresponding effusion cooling designs, largely due to the substantially higher porosity of the TPMS lattices. Conventional effusion-cooled liners are typically exposed to a ΔP ranging from 0.5% to 2.5% [55]. It is beneficial to maintain a low ΔP budget for reducing the work required for compressing air [56]. In the current study, the highest percentage pressure drop achieved was 0.44%, comparable to the lower limit of the pressure drops in effusion cooling.

B. Two-Dimensional Distributions of Film Cooling Effectiveness

The 2D distributions of adiabatic film cooling effectiveness, η_{ad}, for all three unit cell sizes with Diamond-type TPMS test coupons are shown in Fig. 13 for all three injection ratios (F). As mentioned earlier, the actual porosity was kept constant at 36% across all test coupons so that unit cell size is the sole variable. The color bar represents η_{ad} levels, where red denotes lower film cooling effectiveness and blue denotes higher film cooling effectiveness. The observation area, with dimensions of 2.5 cm × 7.1 cm, was used for visualization, and the x and y axes in Fig. 13 were nondimensionalized by the unit cell size of the baseline case ($L_{c,\text{base}} = 2.5$ mm), as indicated in Fig. 7. The mainstream flow direction is indicated by the red arrow in Fig. 13, aligned with the y-direction from left to right. Figure 13 shows a clear evolution of cooling film along the mainstream flow direction. The adiabatic film cooling effectiveness is significantly higher downstream (trailing edge) than upstream (leading edge) due to the accumulation of coolant, which leads to the thickening of the cooling film and more efficient heat shielding. Secondly, the film cooling effectiveness increases with injection ratio, monotonically rising from $F = 0.68\%$ to $F = 1.60\%$ for all unit cell sizes. In contrast, in generic effusion cooling, increased cooling air injections ironically result in less efficient film cooling effectiveness at blowing ratios beyond 0.6, due to undesirable effusion jet liftoffs, losing more coolant to mainstream flow [8].

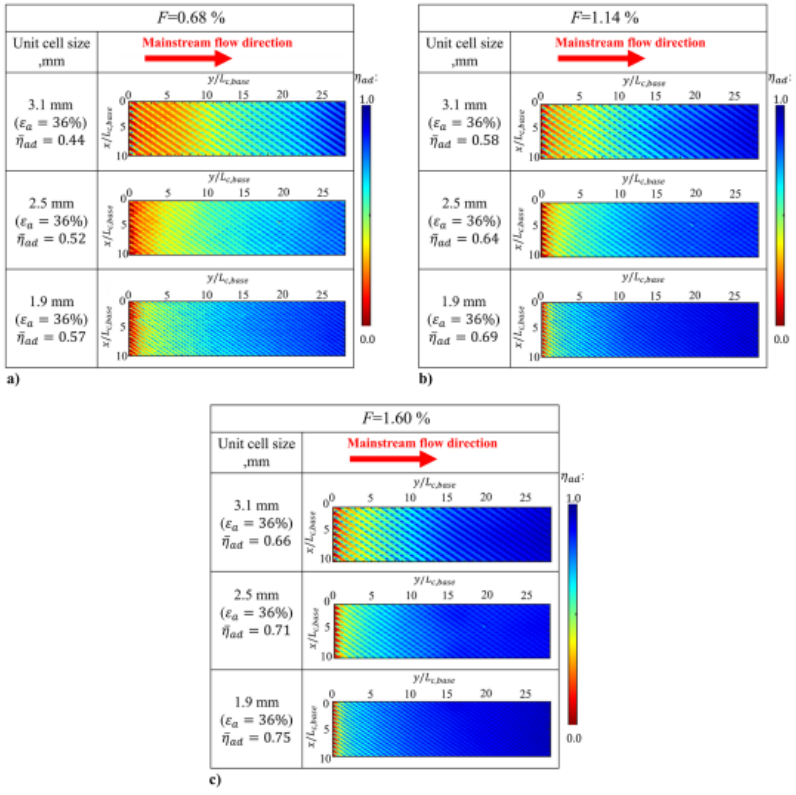

Fig. 13 The 2D distribution of adiabatic film cooling effectiveness of the Diamond-type TPMS achieved at combinations of unit cell sizes and injection ratios.

The trend of achieving better cooling with more cooling air is much more compatible with engine operations, as usually when the engines need more cooling at higher power settings, naturally more cooling air is supplied as a result of high percentage pressure drops across liners.

The most important observation of this study is that film cooling effectiveness increases as the unit cell size decreases. Across all injection ratios, the smallest unit cell size ($L_c = 1.9$ mm) exhibits the highest film cooling effectiveness. The overall averaged adiabatic film cooling effectiveness ($\bar{\eta}_{ad}$) was calculated by averaging over the entire observation area. The calculated values are shown in Fig. 13. The increases in $\bar{\eta}_{ad}$ from $L_c = 3.1$ mm to $L_c = 1.9$ mm are 0.13, 0.11, and 0.09 at $F = 0.68\%$, $F = 1.14\%$, and $F = 1.60\%$, respectively. The enhancement can be attributed to the following factors:

1) The voids are recessed by Δz from the top surface and fully interconnected, allowing them to act as channels that direct coolant downstream with the mainstream flow rather than allowing it to rise to the top surface. This channeled coolant delays the formation of cooling films on the top surface [39]. However, reducing the unit cell size decreases the depth of the saddle points of the top-layer voids (Δz), facilitating the coolant's ascent to the top surface. Conversely, a larger unit cell size results in deeper voids (larger Δz), causing the coolant to remain within the voids and limiting its ability to rise to the surface to form cooling films.

2) A smaller unit cell size also increases the number of unit cell layers (Fig. 8) and the wetted surface area-to-volume ratio while causing pore diameter to shrink (Fig. 5) of a TPMS structure. This leads to a higher pressure drop, which facilitates coolant accumulation on the surface by overcoming interruptions from the mainstream flow, particularly at the leading edge. If the pressure drop across a transpiration cooling test coupon is too low, the uniform distribution of the coolant may be interrupted by the mainstream [37,57]. The study finds that the mainstream outside of the porous structure induces a lateral flow of the coolant inside the porous structure. As a result, the coolant becomes unevenly distributed in a way that is very undesirable, as the internal lateral flow of the coolant transports coolant toward the trailing edge of the transpiration cooling coupon, whereas the evolution of cooling film benefits from a completely opposite distribution: more cooling air toward the leading edge, as the study finds.

C. Spanwise-Averaged Film Cooling Effectiveness

Spanwise averaging of film cooling effectiveness was performed to evaluate the development of film cooling over the surface of the TPMS-based transpiration cooling coupon quantitatively, as shown in Fig. 14. The spanwise averages were computed by excluding the surface void, as those areas are expected to be submerged in coolant. To precisely filter out the void on the surface of the test coupons when performing spanwise averages, the measured 2D film cooling effectiveness distributions are masked by the mathematical expressions of the solid areas on the top surface that are derived from the defining level-setting equations. The $\eta_{ad,span}$ reliably increases as the injection ratio F increases. The improvement was more pronounced when the injection ratio increased from $F = 0.68\%$ to 1.14% than from $F = 1.14\%$ to 1.60%, indicating that the enhancements in film cooling effectiveness do not correlate linearly with coolant flow rates and that returns diminish at higher injection ratios [58].

On the other hand, the comparisons of spanwise averages confirm that film cooling effectiveness improves as TPMS unit cell size decreases when the actual porosity is maintained. As discussed earlier, this improvement can be attributed to more favorable texture on the top surface, such as shallower voids near the top surface for collecting coolant and distributing it to the surface. The shallower void near the top surface also allows the coolant to rise more easily to the top surface to form cooling films.

The lattice with the largest unit cell size ($L_c = 3.1$ mm) exhibits an unusual slow initial rise in film cooling effectiveness near the leading edge compared to smaller unit cell size cases ($L_c = 2.5$ mm and $L_c = 1.9$ mm) at low injection ratio ($F = 0.68\%$), although the largest unit cell size coupon can reach the identical final film cooling

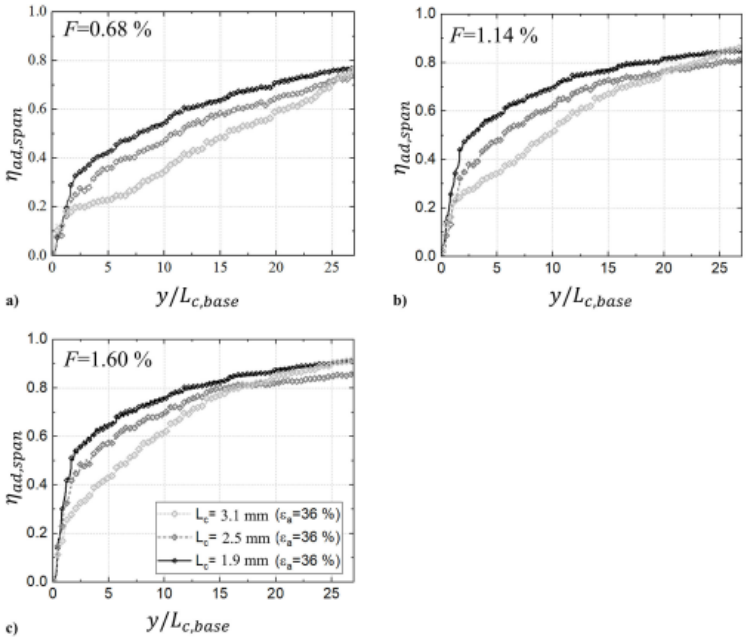

Fig. 14 Spanwise averages of adiabatic film cooling effectiveness.

effectiveness at the trailing edge of the test coupon, as shown in Fig. 14a. This observation supports the hypothesis that lateral flow can develop inside a porous medium of high permeability at low percentage pressure drops across the test coupons. As the lateral flow develops inside the large unit cell size TPMS lattice at a low injection ratio, the coolant was transported downstream internally, depriving the leading edge of the test coupon of much-needed cooling air supply, causing a delayed development of cooling film. However, toward the trailing edge, coolant that is being internally transported downstream emerges to the top surface, converging to the small level of film cooling effectiveness as smaller unit cell size cases under the same injection ratio. The lateral flow of coolant inside the lattice that is most pronounced at large unit cell sizes and low injection ratios is particularly unfavorable for quickly establishing the cooling film.

D. Overall Trends

As discussed in the previous section, the injection ratio and unit cell size, which serve as independent variables in this study, significantly affect film cooling effectiveness. Therefore, the overall averaged adiabatic film cooling effectiveness ($\bar{\eta}_{ad}$) can be expressed as a function of unit cell size and injection ratio, as shown below:

$$\bar{\eta}_{ad}(F, L_c) \tag{15}$$

Figure 15 shows $\bar{\eta}_{ad}$ as a function of unit cell size and injection ratio. The red dots represent the experimental measurements, with unit cell sizes being $L_c = 1.9, 2.5$, and 3.1 mm and injection ratios being $F = 0.68\%$, 1.14%, and 1.60%. The 3D surface in the figure was fitted through the experimental data. It visualizes the trend that film cooling effectiveness increases with decreasing unit cell size and increasing injection ratio. As discussed earlier, increasing the injection ratio enhances cooling performance, but the return diminishes at higher injection ratios ($F = 1.60\%$) due to coolant film saturation [58]. It was also observed that film cooling effectiveness improves by reducing unit cell size. However, further reductions in unit cell size hit printability limits and can lead to random blockages to narrow passages inside the lattice structures. In particular, as D_p decreases with unit cell sizes, the risk of clogging increases. In comparison with typical effusion hole diameters ranging from 0.25 to 1.00 mm [44], and the pore size D_p values investigated in this study range from 0.6 to 1.0 mm as a precaution for preventing clogging due to contaminations. The performance of transpiration cooling was compared to that of a state-of-the-art effusion cooling arrangement with an optimized compound angle developed by our group [7], under identical flow conditions. The effusion cooling achieved $\bar{\eta}_{ad}$ of 0.41, 0.39, and 0.38 at $F = 0.68\%$, 1.14%, and 1.60%, respectively. In contrast, transpiration cooling with a smaller unit cell size achieved significantly higher film cooling effectiveness values of 0.57, 0.69, and 0.75 at $F = 0.68\%$, 1.14%, and 1.60%, respectively.

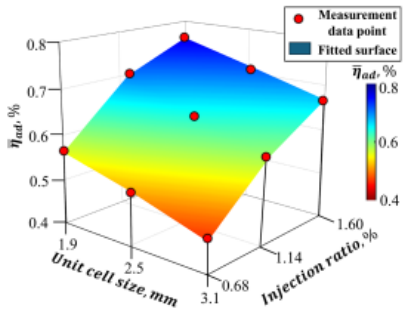

Fig. 15 Overall adiabatic film cooling effectiveness comparison and a fitted 3D surface as a function of unit cell size and injection ratio.

V. Conclusions

The influences of varying unit cell size of TPMS structures on transpiration cooling performance were experimentally examined using three different cell sizes ($L_c = 1.9, 2.5,$ and 3.1 mm). By maintaining an identical actual porosity across all test coupons and by focusing on one common TPMS type, the Diamond type of the TPMS family, the article represents a part of a systematic effort to understand how TPMS lattices can be best engineered for transpiration cooling by isolating the unit cell size effects from other geometrical parameters of TPMS lattices. Consistent trends between unit cell size and transpiration film cooling effectiveness were found.

Film cooling effectiveness increases along the mainstream direction in all studied cases as the coolant accumulates and a cooling film develops. A fully developed cooling film resulting from TPMS-based lattices can very efficiently protect the hot gas path components from high-temperature gases. The film cooling effectiveness of a fully developed cooling film resulting from transpiration cooling was found to be approaching 90%.

Increasing the injection ratio reliably results in enhancements in film cooling effectiveness. Unlike in effusion cooling, where the coolant film can experience liftoff at higher blowing ratios and results in reductions in film cooling effectiveness at higher cooling air flow rates, transpiration cooling effectively forms a continuous film that remains near the surface. The increase in effectiveness was more pronounced when transitioning from a low injection ratio ($F = 0.68\%$) to a medium injection ratio ($F = 1.14\%$). At medium injection ratios, the cooling film can be reasonably established and additional cooling air usage has diminishing gains in overall film cooling effectiveness.

Film cooling performance significantly increases with a reduction in unit cell size. Smaller unit cell sizes lead to shallower surface void, allowing the coolant easily arise to the top surface and form a cooling film. In addition, larger unit cell sizes ($Lc = 3.1$ mm) exhibit lower film cooling effectiveness in the early stage of cooling film development, particularly at low injection ratios. The phenomenon was attributed to undesirable lateral coolant flow internal to the porous lattice, unfavorably distributing more cooling air to the trailing edge of the test coupon. It should be pointed out that, although the effects of TPMS unit cell size on transpiration cooling were investigated with a relatively simple TPMS type—the Diamond type, the trends observed in this study are not TPMS-type dependent and are expected to be universal for all TPMS types. Therefore, it is most favorable to use TPMS lattices of the smallest unit cell size that is within printability limits to achieve the highest and most uniform film cooling effectiveness.

Lastly, a comparison of the overall averaged adiabatic film cooling effectiveness was conducted. Overall film cooling effectiveness can be represented as a function of unit cell size and injection ratio. The results demonstrated that increasing the injection ratio improves cooling performance, though returns diminish at higher flow rates due to coolant film saturation. Reducing the unit cell size further enhances performance, but excessively small sizes can lead to pore blockage due to 3D printing limitations and/or clogging from contaminations, highlighting the importance of selecting an appropriate unit cell size for practical applications. The highest performance in this study was achieved with a unit cell size of 1.9 mm and an injection ratio of 1.6% ($\bar{\eta}_{ad} = 0.76$). Compared to the overall film cooling effectiveness of our advanced effusion cooling design implemented with an optimized compound angle [7], this represents approximately a twofold enhancement under the condition of $F = 1.60\%$ (with the same air consumption per unit area as $BR = 1.4$). Future work to characterize flow internal to TPMS lattices is warranted due to the impact of internal flow on overall transpiration cooling effectiveness, as has been suggested by some observations of the present study.

Acknowledgments

The work is supported by the National Research Council of Canada's National Program Office under a Postdoctoral Fellowship Program grant (PDF2024-TM-AF). NRC Aerospace Research

Centre's Low-Emission Aviation Program also sponsored the work under Project A1-024514.

References

[1] Goldstein, R. J., Ibele, W. E., Patankar, S. V., Simon, T. W., Kuehn, T. H., Strykowski, P. J., Tamma, K. K., Heberlein, J. V. R., Davidson, J. H., Bischof, J., et al., "Heat Transfer—A Review of 2003 Literature," *International Journal of Heat and Mass Transfer*, Vol. 49, Nos. 3–4, 2006, pp. 451–534. https://doi.org/10.1016/j.ijheatmasstransfer.2005.11.001

[2] Reed, R. C., *The Superalloys: Fundamentals and Applications*, Cambridge Univ. Press, Cambridge, England, U.K., 2008. https://doi.org/10.1017/cbo9780511541285.006

[3] Khan, M. A., Sundarrajan, S., Natarajan, S., Parameswaran, P., and Mohandas, E., "Oxidation and Hot Corrosion Behavior of Nickel-Based Superalloy for Gas Turbine Applications," *Materials and Manufacturing Processes*, Vol. 29, No. 7, 2014, pp. 832–839. https://doi.org/10.1080/10426914.2014.901530

[4] Krewinkel, R., "A Review of Gas Turbine Effusion Cooling Studies," *International Journal of Heat and Mass Transfer*, Vol. 66, 2013, pp. 706–722. https://doi.org/10.1016/j.ijheatmasstransfer.2013.07.071

[5] Bailey, J. C., Intile, J., Fric, T. F., Tolpadi, A. K., Nirmalan, N. V., and Bunker, R. S., "Experimental and Numerical Study of Heat Transfer in a Gas Turbine Combustor Liner," *Journal of Engineering for Gas Turbines and Power*, Vol. 125, No. 4, 2003, pp. 994–1002. https://doi.org/10.1115/1.1615256

[6] Fan, X., Li, L., Zou, J., and Zhou, Y., "Cooling Methods for Gas Turbine Blade Leading Edge: Comparative Study on Impingement Cooling, Vortex Cooling and Double Vortex Cooling," *International Communications in Heat and Mass Transfer*, Vol. 100, 2019, pp. 133–145. https://doi.org/10.1016/j.icheatmasstransfer.2018.12.017

[7] Pyo, Y., Son, J., Richer, P., Jodoin, B., Broumand, M., Yun, S., and Hong, Z., "Isolating Influences of Varying Pitch from the Effects of Non-Zero Compound Angles on Effusion Cooling," *Aeronautical Journal*, Vol. 129, No. 1331, 2025, pp. 63–83. https://doi.org/10.1017/aer.2024.108

[8] Paitich, L. C., Richer, P., Jodoin, B., Pyo, Y., Yun, S., and Hong, Z., "Directional Effects of Effusion Cooling on the Cooling Film Effectiveness," *AIAA Journal*, Vol. 60, No. 1, 2022, pp. 423–434. https://doi.org/10.2514/1.J060625

[9] Nelson, W. A., Orenstein, R. M., DiMascio, P. S., and Johnson, C. A., "Development of Advanced Thermal Barrier Coatings for Severe Environments," *Proceedings of the ASME International Gas Turbine and Aeroengine Congress and Exposition*, Vol. 4, ASME, Houston, TX, June 1995. https://doi.org/10.1115/95-GT-270

[10] Andreini, A., Becchi, R., Facchini, B., Picchi, A., and Peschiulli, A., "The Effect of Effusion Holes Inclination Angle on the Adiabatic Film Cooling Effectiveness in a Three-Sector Gas Turbine Combustor Rig with a Realistic Swirling Flow," *International Journal of Thermal Sciences*, Vol. 121, 2017, pp. 75–88. https://doi.org/10.1016/j.ijthermalsci.2017.07.003

[11] Park, S., Jung, E. Y., Kim, S. H., Sohn, H. S., and Cho, H. H., "Enhancement of Film Cooling Effectiveness Using Backward Injection Holes," *International Journal of Thermal Sciences*, Vol. 110, 2016, pp. 314–324. https://doi.org/10.1016/j.ijthermalsci.2016.08.001

[12] Andrews, G. E., Alikhanizadeh, M., Tehrani, F. B., Hussain, C. I., and Azari, M. S. K., "Small Diameter Film Cooling Holes: The Influence of Hole Size and Pitch," *International Journal of Turbo and Jet Engines*, Vol. 5, Nos. 1–4, 1988, pp. 61–72. https://doi.org/10.1515/TJJ.1988.5.1-4.61

[13] Zhou, J., Wang, X., and Li, J., "Influences of Effusion Hole Diameter on Impingement/Effusion Cooling Performance at Turbine Blade Leading Edge," *International Journal of Heat and Mass Transfer*, Vol. 134, 2019, pp. 1101–1118. https://doi.org/10.1016/j.ijheatmasstransfer.2019.02.054

[14] Wang, C., Zhang, J., and Zhou, J., "Optimization of a Fan-Shaped Hole to Improve Film Cooling Performance by RBF Neural Network and Genetic Algorithm," *Aerospace Science and Technology*, Vol. 58, 2016, pp. 18–25. https://doi.org/10.1016/j.ast.2016.08.004

[15] Wang, W., Cui, J., and Qu, S., "Effects of Hole Arrangement and Trenched Hole on Multirow Film Cooling," *AIP Advances*, Vol. 12, No. 4, 2022. https://doi.org/10.1063/5.0082980

[16] Facchini, B., Tarchi, L., Toni, L., and Ceccherini, A., "Adiabatic and Overall Effectiveness Measurements of an Effusion Cooling Array for Turbine Endwall Application," *Journal of Turbomachinery*, Vol. 132, No. 4, 2010, pp. 1–11. https://doi.org/10.1115/1.3213555

[17] Wang, G., Ledezma, G., Delancey, J., and Wang, A., "Experimental Study of Effusion Cooling with Pressure-Sensitive Paint," *Journal of Engineering for Gas Turbines and Power*, Vol. 139, No. 5, 2017. https://doi.org/10.1115/1.4034943

[18] Bazdidi-Tehrani, F., and Andrews, G. E., "Full-Coverage Discrete Hole Film Cooling: Investigation of the Effect of Variable Density Ratio," *Journal of Engineering for Gas Turbines and Power*, Vol. 116, No. 3, July 1994, pp. 587–596. https://doi.org/10.1115/1.2906860

[19] Cho, H. H., and Rhee, D. H., "Local Heat/Mass Transfer Measurement on the Effusion Plate in Impingement/Effusion Cooling Systems," *Journal of Turbomachinery*, Vol. 123, No. 3, 2001, pp. 601–608. https://doi.org/10.1115/1.1344904

[20] Jung, E. Y., Chung, H., Choi, S. M., Woo, T. K., and Cho, H. H., "Conjugate Heat Transfer on Full-Coverage Film Cooling with Array Jet Impingements with Various Biot Numbers," *Experimental Thermal and Fluid Science*, Vol. 83, 2017, pp. 1–8. https://doi.org/10.1016/j.expthermflusci.2016.12.008

[21] Eckert, E. R. G., and Livingood, J. N. B., "Comparison of Effectiveness of Convection-, Transpiration-, and Film-Cooling Methods with Air as Coolant," Lewis Flight Propulsion Lab. NACA TR 1182, Cleveland, OH, 1954.

[22] Curry, D., Gomez, A., and Johnston, C., "Radiative, Ablative, and Active Cooling Thermal Protection Studies for the Leading Edge of a Fixed-Straight Wing Space Shuttle," *AIAA 6th Thermophysics Conference*, AIAA Paper 1971-0445, April 1971. https://doi.org/10.2514/6.1971-445

[23] Weinbaum, S., and Wheeler, H. L., "Heat Transfer in Sweat-Cooled Porous Metals," *Journal of Applied Physics*, Vol. 20, No. 1, 1949, pp. 113–122. https://doi.org/10.1063/1.1698226

[24] Liu, Y. Q., Jiang, P. X., Xiong, Y. Bin, and Wang, Y. P., "Experimental and Numerical Investigation of Transpiration Cooling for Sintered Porous Flat Plates," *Applied Thermal Engineering*, Vol. 50, No. 1, 2013, pp. 997–1007. https://doi.org/10.1016/j.applthermaleng.2012.08.028

[25] Ma, J., Luo, X., Li, H., and Liu, Y., "An Experimental Investigation on Transpiration Cooling Based on the Multi Laminated Sintered Woven Wire Mesh Structures," *Journal of Thermal Science and Engineering Applications*, Vol. 8, No. 3, 2016. https://doi.org/10.1115/1.4032921

[26] Hinse, M., Richer, P., Jodoin, B., Yildiz, K., Yun, S., and Hong, Z., "Numerical and Experimental Studies of Transpiration Cooling Film Effectiveness over Porous Materials," *Journal of Thermophysics and Heat Transfer*, Vol. 36, Feb. 2022. https://doi.org/10.2514/6.2020-3947

[27] Huang, Z., Xiong, Y. Bin, Liu, Y. Q., Jiang, P. X., and Zhu, Y. H., "Experimental Investigation of Full-Coverage Effusion Cooling through Perforated Flat Plates," *Applied Thermal Engineering*, Vol. 76, 2015, pp. 76–85. https://doi.org/10.1016/j.applthermaleng.2014.11.056

[28] Li, X., Liao, Z., Li, H., Jiang, P., and Xu, R., "Phase-Change Transpiration Cooling in Heterogeneous Composite Porous Plates: Heat Transfer Characteristics and Their Prediction," *International Journal of Heat and Mass Transfer*, Vol. 224, 2024, Paper 125290. https://doi.org/10.1016/j.ijheatmasstransfer.2024.125290

[29] Wu, N., Wang, J., Dong, W., and Ding, R., "An Experimental Investigation on Combined Sublimation and Transpiration Cooling for Sintered Porous Plates," *International Journal of Heat and Mass Transfer*, Vol. 116, 2018, pp. 685–693. https://doi.org/10.1016/j.ijheatmasstransfer.2017.09.062

[30] Yang, Y., Mao, J., Chen, P., Zhang, H., and Tang, H., "Numerical Investigation on Transpiration Cooling Performance with Different Porosities and Mainstream Pressure Gradients," *International Journal of Thermal Sciences*, Vol. 184, 2023, Paper 107991. https://doi.org/10.1016/j.ijthermalsci.2022.107991

[31] Mi, Q., Yi, S. H., Gang, D. D., Lu, X. G., and Liu, X. L., "Research Progress of Transpiration Cooling for Aircraft Thermal Protection," *Applied Thermal Engineering*, Vol. 236, 2024, Paper 121360. https://doi.org/10.1016/j.applthermaleng.2023.121360

[32] Huang, G., and He, L., "Influence of Inhomogeneous Porosity on Effusion Cooling," *International Journal of Heat and Mass Transfer*, Vol. 144, 2019, Paper 118675. https://doi.org/10.1016/j.ijheatmasstransfer.2019.118675

[33] Al-Ketan, O., Rowshan, R., and Abu Al-Rub, R. K., "Topology-Mechanical Property Relationship of 3D Printed Strut, Skeletal, and Sheet Based Periodic Metallic Cellular Materials," *Additive Manufacturing*, Vol. 19, 2018, pp. 167–183. https://doi.org/10.1016/j.addma.2017.12.006

[34] Reynolds, B. W., Fee, C. J., Morison, K. R., and Holland, D. J., "Characterisation of Heat Transfer Within 3D Printed TPMS Heat Exchangers," *International Journal of Heat and Mass Transfer*, Vol. 212, 2023, Paper 124264. https://doi.org/10.1016/j.ijheatmasstransfer.2023.124264

[35] Li, W., Li, W., and Yu, Z., "Heat Transfer Enhancement of Water-Cooled Triply Periodic Minimal Surface Heat Exchangers," *Applied Thermal Engineering*, Vol. 217, 2022, Paper 119198. https://doi.org/10.1016/j.applthermaleng.2022.119198

[36] Iyer, J., Moore, T., Nguyen, D., Roy, P., and Stolaroff, J., "Heat Transfer and Pressure Drop Characteristics of Heat Exchangers Based On Triply Periodic Minimal and Periodic Nodal Surfaces," *Applied Thermal Engineering*, Vol. 209, 2022, Paper 118192. https://doi.org/10.1016/j.applthermaleng.2022.118192

[37] Zhou, Z., Lv, Y., He, F., Liu, T., and Wang, J., "Pore-Scale Investigation of Transpiration Cooling Based on Triply Periodic Minimal Surface," *International Journal of Thermal Sciences*, Vol. 201, 2024, Paper 109019. https://doi.org/10.1016/j.ijthermalsci.2024.109019

[38] Broumand, M., Son, J., Pyo, Y., Yun, S., and Hong, Z., "TPMS-Based Transpiration Cooling for Film Cooling Enhancement," *International Journal of Heat and Mass Transfer*, Vol. 231, 2024, Paper 125824. https://doi.org/10.1016/j.ijheatmasstransfer.2024.125824

[39] Son, J., Brouman, M., Pyo, Y., Richer, P., Jodoin, B., and Hong, Z., "Effects of Lattice Orientation Angle on TPMS-Based Transpiration Cooling," *Journal of Engineering for Gas Turbines and Power*, Vol. 147, No. 9, 2025, Paper 091013. https://doi.org/10.1115/1.4067378

[40] Schwarz, H. A., *Gesammelte Mathematische Abhandlungen*, Springer, Berlin, 1890. https://doi.org/10.1007/978-3-0348-4118-4

[41] Al-Ketan, O., and Abu Al-Rub, R. K., "Multifunctional Mechanical Metamaterials Based on Triply Periodic Minimal Surface Lattices," *Advanced Engineering Materials*, Vol. 21, No. 10, 2019. https://doi.org/10.1002/adem.201900524

[42] Al-Ketan, O., Ali, M., Khalil, M., Rowshan, R., Khan, K. A., and Abu Al-Rub, R. K., "Forced Convection Computational Fluid Dynamics Analysis of Architected and Three-Dimensional Printable Heat Sinks Based on Triply Periodic Minimal Surfaces," *Journal of Thermal Science and Engineering Applications*, Vol. 13, No. 2, 2021. https://doi.org/10.1115/1.4047385

[43] Lu, Y., Cui, Z., Cheng, L., Li, J., Yang, Z., Zhu, H., and Wu, C., "Quantifying the Discrepancies in the Geometric and Mechanical Properties of the Theoretically Designed and Additively Manufactured Scaffolds," *Journal of the Mechanical Behavior of Biomedical Materials*, Vol. 112, 2020, Paper 104080. https://doi.org/10.1016/j.jmbbm.2020.104080

[44] Yan, C., Hao, L., Hussein, A., and Raymont, D., "Evaluations of Cellular Lattice Structures Manufactured Using Selective Laser Melting," *International Journal of Machine Tools and Manufacture*, Vol. 62, 2012, pp. 32–38. https://doi.org/10.1016/j.ijmachtools.2012.06.002

[45] Al-Ketan, O., Rowshan, R., and Abu Al-Rub, R. K., "Topology-Mechanical Property Relationship of 3D Printed Strut, Skeletal, and Sheet Based Periodic Metallic Cellular Materials," *Additive Manufacturing*, Vol. 19, 2018, pp. 167–183. https://doi.org/10.1016/j.addma.2017.12.006

[46] Woodcock, G. O., Ertz, T., and Koch, B., "Thermal Protection System," U.S. Patent 8,104,288, issued Jan. 31, 2012, https://patents.google.com/patent/US8104288B2.

[47] Formlabs, Materials Library, Formlabs Inc., July 2019, https://formlabs-media.formlabs.com/filer_public/ac/89/ac8963db-f54a-4cac-8fe9-fb740a7b06f1/formlabs-materials-library.pdf.

[48] Lei, Z., Mahallati, A., Cunningham, M., and Germain, P., "Influence of Inlet Swirl on the Aerodynamics of a Model Turbofan Lobed Mixer," *Proceedings of the ASME. 2010 International Mechanical Engineering Congress and Exposition*, Vol. 7, 2010, pp. 807–819. https://doi.org/10.1115/IMECE2010-39116

[49] Moon, K.-J., Mori, H., and Furukawa, M., "Simultaneous Measurement Method of Pressure and Temperature Using Dual-Layer PSP/TSP with Lifetime-Based Method," *Measurement Science and Technology*, Vol. 29, No. 12, 2018, Paper 125301. https://doi.org/10.1088/1361-6501/aae408

[50] Ahn, J., Mhetras, S., and Han, J. C., "Film-Cooling Effectiveness on a Gas Turbine Blade Tip Using Pressure-Sensitive Paint," *Journal of Heat Transfer*, Vol. 127, No. 5, 2005, pp. 521–530. https://doi.org/10.1115/1.1909208

[51] Liu, T., Sullivan, J. P., Asai, K., Klein, C., and Egami, Y., *Pressure and Temperature Sensitive Paints*, Springer, Berlin, 2005. https://doi.org/10.1007/3-540-26644-5_10

[52] Han, J. C., and Rallabandi, A. P., "Turbine Blade Film Cooling Using PSP Technique," *Frontiers in Heat and Mass Transfer*, Vol. 1, No. 1, 2010. https://doi.org/10.5098/hmt.v1.1.3001

[53] Natsui, G., Little, Z., Kapat, J. S., Dees, J. E., and Laskowski, G., "A Detailed Uncertainty Analysis of Adiabatic Film Cooling Effectiveness Measurements Using Pressure-Sensitive Paint," *Journal of Turbomachinery*, Vol. 138, No. 8, 2016. https://doi.org/10.1115/1.4032674

[54] Johnson, B., and Hu, H., "Measurement Uncertainty Analysis in Determining Adiabatic Film Cooling Effectiveness by Using Pressure Sensitive Paint Technique," *Journal of Turbomachinery*, Vol. 138, No. 12, 2016. https://doi.org/10.1115/1.4033506

[55] Chen, X., Krawciw, J., Xia, H., Denman, P. A., Bonham, C., and Carrotte, J. F., "Study of an Effusion-Cooled Plate with High Level of Upstream Fluctuation," *Applied Thermal Engineering*, Vol. 184, 2021, Paper 116126. https://doi.org/10.1016/j.applthermaleng.2020.116126

[56] Maurer, M. T., Benz, U., Swiatek, S., Konradt, O., and Mallm, M., "Heat-Resistant Coating System," U.S. Patent Application 14/445,413, filed July 29, 2015, https://patents.google.com/patent/US20150322219A1.

[57] Huang, G., Zhu, Y., Liao, Z. Y., Huang, Z., and Jiang, P. X., "Transpiration Cooling with Bio-Inspired Structured Surfaces," *Bioinspiration and Biomimetics*, Vol. 15, No. 3, 2020, Paper 036016. https://doi.org/10.1088/1748-3190/ab6bdf

[58] Otsu, H., Fujita, K., and Ito, T., "Application of the Transpiration Cooling Method for Reentry Vehicles," *45th AIAA Aerospace Sciences Meeting and Exhibit*, AIAA Paper 2007-1209, 2007. https://doi.org/10.2514/6.2007-1209

J. Burt
Associate Editor

5.2 The Influence of TPMS Porosity on Transpiration Cooling Performance

This study investigates the influence of TPMS porosity on transpiration cooling performance by examining three different porosity levels while maintaining a constant unit cell size. The primary objective is to quantitatively evaluate the effect of porosity on adiabatic film cooling effectiveness (η_{ad}).

In addition, a baseline effusion cooling configuration is considered for comparison. Accordingly, a secondary objective of this study is to compare the performance of the TPMS-based transpiration cooling configuration with the preferred porosity—identified as exhibiting the best performance under the investigated conditions—with that of the baseline effusion cooling case.

The comparative evaluation reveals that TPMS-based transpiration cooling substantially outperforms the baseline effusion cooling configuration. By suppressing the jet lift-off phenomenon typically observed in discrete-hole effusion cooling, the TPMS structure enables more uniform and continuous coolant coverage over the surface. As a result, near-unity adiabatic film cooling effectiveness is achieved in downstream regions, leading to an overall enhancement in cooling performance of more than fivefold relative to the effusion baseline case.

Furthermore, cooling performance generally improves with increasing porosity due to enhanced coolant distribution; however, excessively high porosity introduces performance limitations, particularly in leading edge. At high porosity levels, particularly under low injection ratios, insufficient film formation is observed in the upstream region. Although increasing the porosity enlarges the total discharge area and reduces the coolant exit velocity under a constant coolant mass flow rate, the dominant effect at excessively high porosity is the enhancement of internal tangential flow. This increased internal coolant transport redistributes the coolant toward the downstream region, delaying coolant discharge and the formation of a continuous coolant film near the leading edge. Consequently, the upstream cooling performance is reduced.

These findings demonstrate that porosity should be selected by balancing cooling effectiveness, coolant distribution, and structural integrity, rather than simply maximizing porosity.

This study is written as a research article and published as a peer-reviewed journal paper, The International Journal of Heat and Mass Transfer.

International Journal of Heat and Mass Transfer 231 (2024) 125824

Contents lists available at ScienceDirect

International Journal of Heat and Mass Transfer

journal homepage: www.elsevier.com/locate/ijhmt

TPMS-based transpiration cooling for film cooling enhancement

Mohsen Broumand *, Juchan Son, Yeongmin Pyo, Sean Yun, Zekai Hong

Aerospace Research Center, National Research Council of Canada, 1200 Montreal Road, K1A 0R6, Ottawa, Ontario, Canada

ARTICLE INFO

Key words:
Gas turbine cooling
Transpiration cooling
Effusion cooling
Pressure sensitive paint
Additive manufacturing
Triply periodic minimal surface (TPMS)

ABSTRACT

The present study experimentally evaluates the adiabatic film cooling effectiveness of a gaseous transpiration cooling concept based on a family of nature-inspired triply periodic minimal surface (TPMS) lattices that are enabled by additive manufacturing. The performances of TPMS-based transpiration cooling designs are directly compared to those of a typical effusion cooling design featuring an array of discrete cooling holes, the state-of-the-art cooling technology for aerospace gas turbines. Specifically, three solid-network TPMS lattice structures with porosities at 30, 40, and 50% are additively manufactured and their adiabatic film cooling effectiveness values are determined using a dual-luminophore pressure sensitive paint (PSP) method based on heat and mass transfer analogy. The experimental results indicate that, as the cooling film grows downstream, the adiabatic film cooling effectiveness of the TPMS lattice structure of 50% porosity approaches 0.77, 0.88, and 0.91 at low, medium, and high coolant flow rates, respectively. The adiabatic film cooling effectiveness values achieved with the TPMS-based transpiration cooling designs of this work reach five times those of conventional effusion cooling under corresponding coolant consumption rates. The findings of the present study suggest that TPMS-based transpiration cooling as a promising alternative to effusion cooling could bring significant efficiency gains to gas turbine engines by reducing cooling air consumptions, since it offers a higher adiabatic film cooling effectiveness, creates a more complete and uniform film coverage, and mitigates the film lift-off propensity at high blowing ratios. Furthermore, the distinctive features of TPMS lattices enable efficient interior cooling, provide high mechanical strengths, and facilitate additive manufacturing.

1. Introduction

Improving the efficiency of energy conversion systems is crucial for sustainability and addressing environmental concerns. More specifically, reducing cooling air consumption for gas turbine hot-gas path components, such as combustor liner, transition ducts, and turbine blades/vanes, can significantly improve the overall engine efficiency. This is because cooling air has to be compressed to the highest-pressure point of the entire engine, leading to excess energy consumption by the compressor. On the other hand, enhancing the efficiency of future gas turbines necessitates a rise in their overall pressure ratio (OPR) and thus turbine inlet temperature (TIT), which in turn requires a larger amount of compressed air for cooling purposes. These constraints and requirements highlight the need for a disruptive cooling technology capable of protecting gas turbine hot-gas path components from severe thermal stresses and premature failures with the least possible air consumption, see e.g., [1,2]. The cooling of hot gas path components is particularly important in a gas turbine with large pressure ratios as the air discharged from its compressor is at higher temperatures, making a less effective coolant.

In general, the progression of gas turbine efficiencies and concurrent reduction of cooling air consumption face two major impediments—material thermal limitations and thermal protection constraints. Concerning the latter, a variety of active and passive cooling techniques are currently employed in gas turbines. Component interiors can be cooled through internal flow convection [3,4] and impingement jet methods [5,6], and exterior/exposed surfaces can be protected from hot gasses using discrete hole effusion cooling [7,8] and thermal barrier coating [9,10]. Among them, using a series of discrete pin-holes fabricated within components for injecting coolant and creating a protective thin-layer of low-temperature gas, also-called cooling film, over exposed surfaces is deemed as one of the most effective cooling strategies extensively adopted in gas turbines, see e.g., [11,12].

However, two main drawbacks limit the effectiveness of discrete hole effusion cooling. First, instead of achieving a more effective cooling film, a higher coolant consumption rate usually leads to undesirable lift-off of

* Corresponding author.

https://doi.org/10.1016/j.ijheatmasstransfer.2024.125824
Received 15 February 2024; Received in revised form 26 May 2024; Accepted 5 June 2024
Available online 18 June 2024
0017-9310/Crown Copyright © 2024 Published by Elsevier Ltd. All rights are reserved, including those for text and data mining, AI training, and similar technologies.

miniature effusion cooling jets as a result of increased coolant blowing ratio (BR). The lift-off of effusion jets, also referred to as blow-off, subsequently promotes turbulent mixing and the entrainment of hot gasses into the near-wall region, leading to further deteriorated cooling film effectiveness. Second, achieving a complete and uniform film coverage is highly challenging with effusion cooling. The cooling film effectiveness is relatively high only in narrow streaks along the trajectories of discrete effusion jets, leaving under-protected gaps between these narrow streaks over hot surfaces. It is noteworthy that the effusion film cooling effectiveness and film coverage can be enhanced through a variety of methods, such as optimizing the size and number of holes per unit area [13–15], changing the shape and type of holes [16–18], altering the location and pattern of holes [19–21], and using directional effusion cooling through varying the inclination angle [22,23] and compound angle of holes [24,25]. However, the maximum achievable level of cooling effectiveness and thus the maximum ranges of OPR and TIT in gas turbines are still limited after applying such modifications which can also compromise the structural integrity of the components.

In this regard, extensive research efforts have been dedicated to the development of advanced cooling techniques for gas turbines, see e.g., [26,27]. Transpiration cooling is one of these techniques which works by passing a coolant, either gas or liquid, through a porous medium and creating a cooling film over its surface as the coolant emanates from the porous medium and interacts with the mainstream flow [28]. As such, transpiration cooling serves to enhance both the thermal protection (i.e., film cooling) of exposed surfaces and the inner-cooling (i.e., convective cooling) efficiency of structures. While early studies on porous medium-based transpiration cooling date back to the mid-twentieth century, see e.g., [29–31], it has found limited applications in gas turbines due to the concerns regarding structural strength and manufacturability [26]. There are also approximations to porous medium-based transpiration cooling in the form of a double-wall effusion cooling design combining porous structures or straight micro holes with effusion holes [32–37], though special attention must be given to thermal stresses caused by significant temperature variations across the walls [38–42].

Most recently, additive manufacturing (AM) advancements have enabled the precise fabrication of intricate porous/lattice structures as solid bodies featuring high mechanical strengths [43–45]. One study [46] reported that the cooling effectiveness of additively manufactured plates comprising straight micro holes with a high density approached to that of a sintered porous plate with the value of 0.7 when coolant blowing ratio was set to 2%. Another study [47] shown that the overall average cooling effectiveness of the blood vessel-shaped transpiration cooling structure fabricated through powder bed selective laser metal sintering (SLMS) could reach to a maximum value of 0.57 at high coolant injection ratios. A separate study on turbine blades [48] demonstrated that a transpiration cooling using a sintered porous surface could reach to the cooling effectiveness of about 0.6, which is 25% and 34% higher than that of internal flow convection and effusion cooling methods, respectively. More recently, a study from the present research group showed that a transpiration cooling using aluminum foams can provide adiabatic film cooling effectiveness on average 40% higher than an effusion cooling [49].

Among various types of porous and lattice structures, the nature-inspired triply periodic minimal surface (TPMS) lattice structures which are enabled by and uniquely well-suited for AM offers several advantages [50–52]. Concerning random (stochastic) porous media, such as sintered ceramic/metal and ceramic/metal foam, the arbitrarily distributed pores and solids in such structures can give rise to the creation of random hot spot zones and structural weak points, which can be effectively addressed by using mathematically defined/generated TPMS lattices featuring deterministic (non-stochastic) architecture. This deterministic design approach enables precise control over pore characteristics that can be intelligently designed to prevent the creation of non-uniform pressure fields and ensure a more uniform coolant flow, thereby minimizing the risk of clogging. The smooth/continuous transition of TPMS internal channels with seamless (no self-intersection) patterns and large surface area to volume ratios offer superior thermo-fluidic performances and elevated mechanical strengths in comparison with those of manually defined/generated structures with sharp edges and corners like conventional strut-and-node based lattices. Moreover, AM technologies enable the employment of advanced metal-based and ceramic-based materials in the fabrication of a porous medium with high thermal and chemical stability that are not achievable through traditional additive manufacturing techniques.

In general, TPMS structural attributes, including total nodes in a unit cell, the number of struts per node (interconnectivity), and strut angles, can be chosen from over 100 TPMS topologies. When combined with the TPMS customization capabilities, such as mathematical hybridization and grading, these characteristics enable the development of high-performance porous media for diverse practical applications, see e.g., [53,54]. In the available literature reports, the fluid flow and heat and mass transfer within TPMS lattices are fundamentally investigated in several experimental and numerical studies [55–58]. Their performances are also evaluated for various engineering applications, such as enhancing heat and mass transfer in membrane distillation [59], improving the efficiency of supercritical carbon dioxide (sCO_2) cycles [60], thermal management of batteries [61], and liquid-phase transpiration cooling of supersonic vehicles [62]. Amidst their widespread applications in diverse engineering fields, additively manufactured TPMS structures stand out for their large wetted area, exceptional mechanical robustness, and high design flexibility, stemming from their unique geometry with an intricate network of interconnected surfaces. These inherent characteristics of TPMS lattice structures offer distinct advantages that can surpass even those of effusion cooling plates featuring densely packed straight micro holes.

Given the benefits associated with porous medium-based transpiration cooling in thermal protection applications and the desirable features of additively manufactured TPMS lattices, the present study explores their practical applicability in enhancing film cooling for gas turbine hot gas path components. In doing so, a gaseous coolant proxy is forced through a number of solid-network lattices with different porosities which are additively manufactured based on triply periodic minimal surfaces. The 2-D distribution and averaged adiabatic film cooling effectiveness of the designed TPMS-based transpiration cooling is experimentally evaluated under subsonic flow conditions and the results are then compared with those of a conventional discrete pin-hole effusion cooling to get more insights into the viability of deploying the present technique in real gas turbines.

2. Methodology

2.1. TPMS lattice design and fabrication

A triply periodic minimal surface is a smooth 3D surface repeated in $\mathbb{R}^3$, where its local surface area is minimized and is free of self-intersections. It can be described by the nodal surface of a function defined in terms of Fourier series as [63,64]:

$$\Psi(\mathbf{r}) = \sum_{\mathbf{k}} F(\mathbf{k}) \cos[2\pi \mathbf{k}\cdot\mathbf{r} - \alpha(\mathbf{k})] = 0, \quad (1)$$

where $\alpha(\mathbf{k})$ is a phase shift and $F(\mathbf{k})$ is an amplitude factor associated with a given reciprocal vector, $\mathbf{k}$. TPMS topologies can be approximated by truncating the Fourier series to the leading term, giving various level-set equations in the form of $f(x,y,z) = c$ in the Cartesian coordinates. The level-set isovalue c controls the offsetting from the zero level-set surface that splits the space into two interpenetrating subdomains of equal volumes. Some of the simplest forms of TPMS level-set equations, corresponding to Schwarz-Primitive, Schoen-Gyroid, and Schwarz–Diamond surfaces are respectively expressed as [65,66]:

$$\cos X + \cos Y + \cos Z = c, \tag{2}$$

$$\sin X \cos Y + \sin Y \cos Z + \sin Z \cos X = c, \tag{3}$$

$$\cos X \cos Y \cos Z - \sin X \sin Y \sin Z = c, \tag{4}$$

where $X = 2\pi x/l_x$, $Y = 2\pi y/l_y$, $Z = 2\pi z/l_z$, and l_x, l_y, and l_z are unit cell sizes in the x, y, and z directions, respectively.

The defined triply periodic minimal surfaces can then be used to generate TPMS lattice structures based on two different lattice networks, namely solid-network lattice and sheet-network lattice [54,67]. When one of the subdomains divided by a minimal surface at a level-set constant, c, is considered as a solid and the other subdomain is considered as a void space, it results in a solid-network lattice. On the other hand, a sheet-network lattice is generated when the volume bounded by two minimal surfaces evaluated at two different level-set constants, e.g., $\pm c$, is considered as a solid, which separates the two void spaces created. In the both types of lattice networks, porosity (or solid volume fraction) is controlled by the value of c. In the present study, solid-network lattices, which consists of a solid subdomain and a void subdomain, are used for transpiration cooling purposes. Fig. 1 demonstrates how the porosities, ε, of the solid-network TPMS lattices obtained from Eqs. (2-4) can be altered by changing the level-set constant, c.

In the present study, three basic solid-network TPMS lattices with porosities of $\varepsilon =$ 30, 40, and 50% are designed using the Schwarz–Diamond topology. They consist of three layers at a constant unit cell size of $l = 2.54$ mm. In addition, a generic effusion cooling test coupon with staggered holes is designed as a baseline. The effusion holes have a constant diameter of $d = 0.79$ mm, a constant inclination angle of $\alpha = 20°$, and fixed spanwise and streamwise pitches of $\delta_x = 7d$ and $\delta_y = 9d$, respectively. These dimensions and arrangement of effusion cooling holes are commonly adopted for gas turbine cooling purposes, as seen in references [68,69]. All the designed test coupons are then fabricated employing a stereolithography (SLA) 3D printer which has a high resolution for the manufacturing of thin layers. The SLA printer is equipped with a 250 mW and 405 nm violet diode laser source and features a high resolution of 25 μm in each of the x, y, and z directions. Regarding the test coupon materials, a high-temperature resin with a maximum resistance temperature of 238 °C, from Formlabs [70], is employed to withstand the curing process of the dual-luminophore pressure sensitive paint (PSP) used for adiabatic film cooling effectiveness measurements. Fig. 2 depicts the schematic of the circular test coupon used in the present experiments, along with illustrating the selected measurement

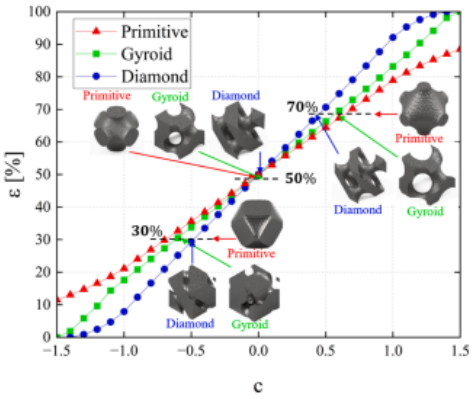

Fig. 1. Porosity variation of solid-network TPMS lattices as a function of the c value.

area with the dimensions of L_x=25 mm × L_y=70 mm and its excluded spanwise margins that is taken to ensure the continuity in measurements.

It is common for there to be some variation in the sizes of additively manufactured structures compared to the original designs after 3D printing. This variation can be attributed to factors such as material shrinkage, printing resolution, and post-processing techniques. To evaluate the tolerance of the printed designs, both the design porosity (ε_d) and the actual porosity (ε_a) of the test coupons are quantified respectively using [47]:

$$\varepsilon_d = \left(1 - \frac{V_d}{V_s}\right) \times 100\%, \tag{5}$$

$$\varepsilon_a = \left(1 - \frac{M_a}{M_s}\right) \times 100\%, \tag{6}$$

where V and M represent volume and mass values, respectively, and the subscripts s, d, and a represent the design properties of a solid plate with the same dimensions as the test coupons, the design properties of the test coupons, and the actual (measured) properties of the test coupons, respectively. Table 1 summarizes both the design and actual porosity values of the test coupons, indicating a maximum reduction in the porosity of the TPMS lattice structures of around 12%. A much smaller change in porosity is observable for the effusion cooling test coupon, with approximately 0.21%. The design and actual surface open area ratios are also provided in Table 1. It is seen that the actual diameter of the effusion cooling holes experienced approximately an 18% shrinkage. These holes underwent post-printing machining operations to drill them to their final dimensions, maintaining a hole diameter of 0.79 mm in the present study. The surface open area ratios of the TPMS lattice structures, estimated to be equal to their corresponding porosities, were kept as the as-built values.

2.2. Experimental setup and measurements

The main components of the experimental setup consist of an open-loop subsonic wind tunnel with a square test section of 127 × 127 mm^2, a reservoir with multiple internal flow straighteners for the uniform injection of coolant through the test coupon installed directly above it and flush with the test section bottom-wall, and an optical setup for adiabatic film cooling effectiveness measurements through the test section top-wall which is made of polycarbonate. The schematic of the experimental setup is shown in Fig. 3.

In the present experiments, the main airstream is delivered to the test section at a velocity of 33 m/s (Reynolds number of ~256,000) and the turbulence intensity of 5% under atmospheric temperature and pressure conditions. Compressed gas bottles are used for the injection of Nitrogen (N_2) as the coolant proxy at three different flow rates, $\dot{m}_c = 1.32$, 2.16, and 3 g/s, that are controlled by an OMEGA FMA 5400A/5500A series flow meter. In effusion cooling, these flow rates correspond to blowing ratios (BR=$\rho_c u_c/\rho_m u_m$) of 0.6, 1.0, and 1.4, respectively, where ρ_c and u_c represent the density and velocity of the coolant and ρ_m and u_m represent the density and velocity of the mainstream, respectively. Similar BR ranges are commonly adopted during the actual development phase in the gas turbine industry. At equivalent mainstream and coolant flow rates, however, transpiration cooling exhibits significantly lower blowing ratios due to the much higher surface open area ratios of TPMS lattice structures, see Table 1. Consequently, the injection ratio, F, defined based on the active area, A_{active}, is employed as an alternative to the blowing ratio. The injection ratio is defined as:

$$F = \dot{m}_c / \left((\rho u)_m A_{active}\right), \tag{7}$$

where $A_{active} = 66$ mm × 70 mm is the area of the PSP coated surface shown in Fig. 2, which is consistent across both effusion and transpiration cooling experiments. As such, the performances of all the test

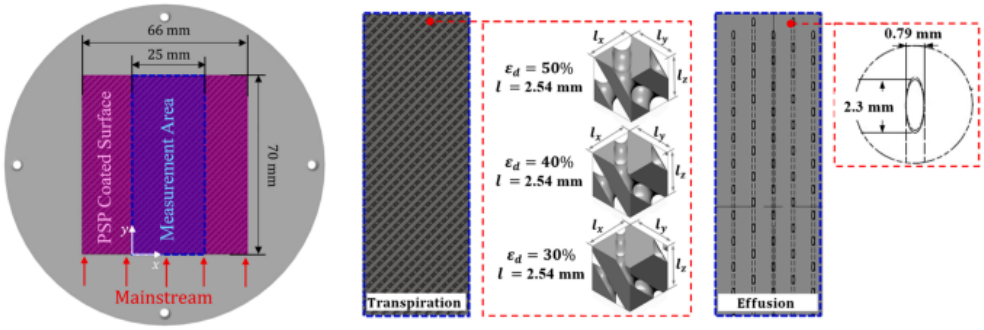

Fig. 2. Schematics of the circular test coupon and its PSP coated region (left) and the corresponding measurement areas associated with the transpiration and effusion cooling structures (right).

Table 1
Manufacturing tolerance of test coupons from SLA resin 3D printing.

Test coupon	Design porosity, (ε_d)	Actual porosity, (ε_a)	Design surface open area ratio	Actual surface open area ratio
Discrete hole plate ($d = 0.79$ mm, $\alpha = 20°$, $\delta_x = 7d$ and $\delta_y = 9d$)	1.35%	1.14%	4.10%	3.46%
TPMS lattice structure (Topology = Schwarz–Diamond; solid-network, $l = 2.54$ mm)	30% 40% 50%	18.34% 30.52% 42.48%	30% 40% 50%	18.34% 30.52% 42.48%

coupons are compared in terms of the injection ratio while the mainstream flow rate (velocity) is kept unchanged throughout the experiments. The test conditions employed in the current effusion and transpiration cooling experiments are summarized in Table 2.

Fig. 4 shows the pressure drop percentages of the transpiration and effusion test coupons as a function of the coolant flow rate, which are obtained through the simultaneous measurement of pressures in the mainstream and the reservoir using a pitot tube. According to Fig. 4, the TPMS based transpiration cooling shows a much smaller pressure drop than the effusion cooling due to the high porosities of TPMS lattice structures and their low internal flow resistances.

The adiabatic film cooling effectiveness of the test coupons is estimated through coating the test coupon surfaces with dual-luminophore pressure sensitive paint (PSP), exciting them with a UV illumination, and then recording the emitted signals using a photodetector. The fundamental principle of this technique is based on luminescence quenching by oxygen within the paint materials, which enables the measurement of local oxygen (O_2) partial pressure over the PSP coated surfaces. The information can then be correlated to adiabatic film cooling effectiveness through the calibration of PSP [71–74]. The dual-luminophore PSP used in the present study is named BinaryFIB PSP, from ISSI [75], which includes two distinct luminescent dyes to compensate the errors associated with temperature variations in small pressure gradients (low-speed flows). It has a single UV excitation peak between 380 and 520 nm and two emission peaks; one associated with a pressure-sensitive signal with a peak emission intensity between 620 and 750 nm and the other related to a reference signal with a peak emission intensity between 550 and 600 nm. An air-cooled LED light source also from ISSI (model LM2X-DM) is used to provide a stable UV excitation at 400 nm. Two sets of fluorescence intensity images are acquired by a Lavision ImagerProX 2 M camera equipped with a Lavison Image Doubler with two bandpass filters, where the first one has a center wavelength of 650 nm with a tolerance of 20 nm and the second one has a center wavelength of 560 nm with a tolerance of 10 nm.

2.3. Data reduction and PSP calibration

The cooling film effectiveness, η, quantifies the proximity of the wall temperature to the coolant temperature and can be defined in terms of the temperature of mainstream, T_m, and the temperature of coolant, T_c, as:

$$\eta = \frac{T_m - T_w}{T_m - T_c}, \tag{8}$$

where T_w is the surface temperature of the coolant injection wall. In PSP film effectiveness measurements, the main airstream adjacent to the PSP coated surface is expected to greatly diluted when the foreign gas as a coolant is emanated from the test coupons. Therefore, through applying heat and mass transfer analogy, a new parameter named adiabatic film cooling effectiveness, η_{ad}, which indicates the coolant effectiveness in covering the wall exposed surfaces, can be defined as:

$$\eta_{ad} = \frac{X_{O_2,air} - X_{O_2,f}}{X_{O_2,air} - X_{O_2,c}}, \tag{9}$$

where X_{O_2} is the mole fraction of oxygen in different streams and the subscripts *air*, *c*, and *f* denote the main airstream, the coolant stream, and the wall-adjacent film layer, respectively. Noted that the considered heat and mass transfer analogy is valid under two fundamental assumptions, see e.g., [76]. First, it is assumed that boundary conditions are analogous, where surfaces are considered adiabatic in heat transfer and impermeable in mass transfer. Second, it is assumed that the turbulent Lewis number is close to unity because of the highly turbulent flow-field. Following these assumptions and since the value of X_{O_2} is zero in the coolant (N_2) stream, as well as considering the similar molecular weights of nitrogen and air, the adiabatic film cooling effectiveness equation can be further simplified and expressed solely as a function of oxygen partial pressure as:

$$\eta_{ad} = 1 - \frac{X_{O_2,f}}{X_{O_2,air}} = 1 - \frac{P_{O_2,f}}{P_{O_2,air}}. \tag{10}$$

Herein, a data reduction approach is followed in order to transform the PSP images collected in the experiments into pressure maps, thereby estimating the adiabatic film cooling effectiveness of test coupons employing Eq. (10). The relation between the measured fluorescence intensity, I, and the oxygen partial pressure (or oxygen mole fraction) can be expressed using the Stern-Volmer equation as [77]:

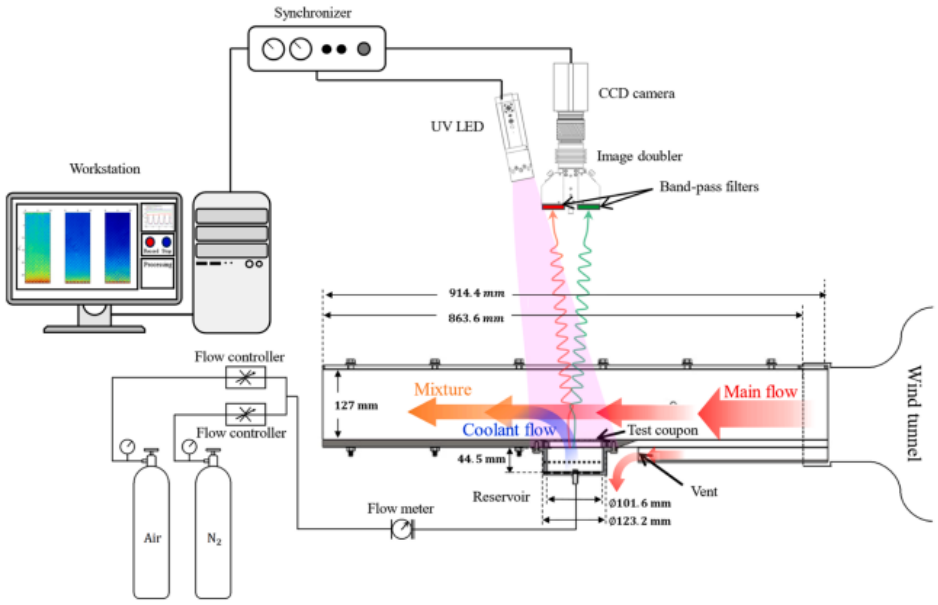

Fig. 3. Schematic of the experimental setup and its components.

Table 2
The coolant flow rates and injection ratios used in the present experiments.

	Effusion cooling	Transpiration cooling
$\dot{m}_c$ [g/s]	1.32	1.32
	2.16	2.16
	3.00	3.00
F [%]	0.68	0.68
	1.14	1.14
	1.60	1.60

$$\frac{I_0(T)}{I(T)} = 1 + K(T)\cdot S(T,P)\cdot X_{O_2}\cdot P, \tag{11}$$

where I_0 is the fluorescence intensity at the zero-oxygen condition, K is the temperature-dependent Stern-Volmer coefficient, S is Henry's law coefficient which is a function of both air temperature, T, and air pressure, P. Because of the difficulties to provide zero-oxygen condition in the experiments, the fluorescence intensity at a zero speed (wind-off) condition, I_{ref}, with a known pressure, P_{ref}, is considered as a reference and Eq. (11) is normalized using them. Then, for PSP measurements, the oxygen partial pressure can be estimated using a second-order polynomial equation as:

$$\frac{P_{O_2}}{P_{O_2,ref}} = C_1(T)\left(\frac{r_{ref}}{r}\right)^2 + C_2(T)\left(\frac{r_{ref}}{r}\right) + +C_3(T), \tag{12}$$

where C_1, C_2, and C_3, are the temperature-dependent coefficients which are determined through the calibration of PSP and $r\ /r_{ref}$ is the normalized ratio of fluorescence intensities corrected for nonhomogeneous luminophore concentrations and variations in the paint thickness that is defined as:

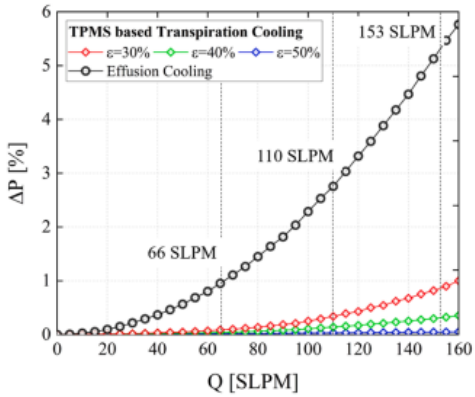

Fig. 4. Pressure drop percentages of the test coupons as a function of coolant flow rate; the coolant flow rates used in the present study are shown by the vertical dashed lines.

$$\frac{r}{r_{ref}} = \frac{(I - I_{dark})_{PT}/(I - I_{dark})_T}{(I_{ref} - I_{dark})_{PT}/(I_{ref} - I_{dark})_T}, \tag{13}$$

where the subscript *dark* denotes the camera reading in the absence of (switched-off) UV excitation to correct any background noises. The subscript *PT* is associated with the pressure-sensitive signal peak of 650 nm that depends on both pressure and temperature and the subscript *T* is related to the reference signal peak of 560 nm that depends on tem-

perature only.

In the present experiments, the dual-luminophore PSP applied on a test coupon is calibrated at a zero speed (wind-off) condition through exposing the PSP coated surfaces with known oxygen partial pressures and then performing pixel-wise calibrations in order to find a relation between the local PSP fluorescence intensity ratios and the local oxygen partial pressure ratios based on Eq. (12). In doing so, a calibration gas comprised of neat N_2 and air at different volumetric fractions, 0%, 20%, 40%, 60%, 80%, 100%, are purged through a shroud which isolates the test coupons from the rest of the wind tunnel test section, see Fig. 5 (left). As shown in Fig. 5 (right), the PSP calibration curve obtained in the present study exhibits a good agreement with the ones published in the literature and also by the manufacturer [74,75]. After finishing the calibration of each PSP-coated test coupon, the calibration shroud is removed from the test section and wind tunnel is turned on for real PSP measurements with pure N_2 as the coolant proxy.

2.4. Uncertainty quantification

Various sources of uncertainty and error can be identified in the present experiments, including the errors associated with measuring and controlling devices along with image acquisition and calibration errors. The uncertainty associated with the PSP measurement technique is mainly attributed to the combination of temperature nonuniformities and photodegradation effects, which is estimated to be less than 2.2% under a careful experimental procedure [78]. Applying the propagation of uncertainty formula, Eq. (14), to Eq. (10), the uncertainty in the local adiabatic film cooling effectiveness can be estimated based on Eq. (15).

$$\delta f = \sqrt{\sum \left(\frac{\partial f}{\partial x_i}\right)^2 \delta x_i^2}. \tag{14}$$

$$\delta\eta_{ad} = \sqrt{\left(\frac{\partial\eta_{ad}}{\partial\left(P_{O_2}/P_{O_2\,ref}\right)_{air}}\right)^2 \delta\left(P_{O_2}/P_{O_2\,ref}\right)_{air}^2 + \left(\frac{\partial\eta_{ad}}{\partial\left(P_{O_2}/P_{O_2\,ref}\right)_{f}}\right)^2 \delta\left(P_{O_2}/P_{O_2\,ref}\right)_{f}^2}. \tag{15}$$

According to Eq. (12), the pressure ratios are correlated with the camera recorded light intensity ratios based on the calibration constants, C_1, C_2, and C_3. As such, the uncertainty in adiabatic film cooling effectiveness is linked to the uncertainty in pressure measurements during the PSP calibration and the maximum signal-to-noise ratio of the camera. The maximum uncertainty in the local adiabatic film cooling effectiveness is estimated to be 5.37% at η_{ad}= 0.1 in the present experiments.

3. Results and discussion

3.1. Distributions of film effectiveness over TPMS lattices

The 2-D distributions of adiabatic film cooling effectiveness, η_{ad}, over the three TPMS lattices designed with porosities of ε = 30, 40, and 50% are shown in Fig. 6 for the three defined injection ratios of 0.68%, 1.14%, and 1.60% and the selected mainstream velocity of 33 m/s. The mainstream direction is aligned with the y direction in Fig. 2, from bottom to top. In all the cases here, a nonuniform distribution is evident along the mainstream direction, where the adiabatic film cooling effectiveness is significantly higher in the downstream region at the trailing edge compared to the upstream region at the leading edge. This is primarily attributed to the downstream accumulation of the coolant. The results also show that the adiabatic film cooling effectiveness is improved with increasing the lattice porosity from 30% to 50% at all the coolant flow rates studied, indicating a better distribution of the coolant over the TPMS lattices with higher porosities. Furthermore, it is observed that the adiabatic film cooling effectiveness of a lattice structure with a defined porosity is increased with rising the injection ratio from 0.68% to 1.14% and 1.60%. This highlights the negligible effects of lift-off phenomenon on the film coverage over the TPMS lattices, even at the highest coolant flow rate studied herein.

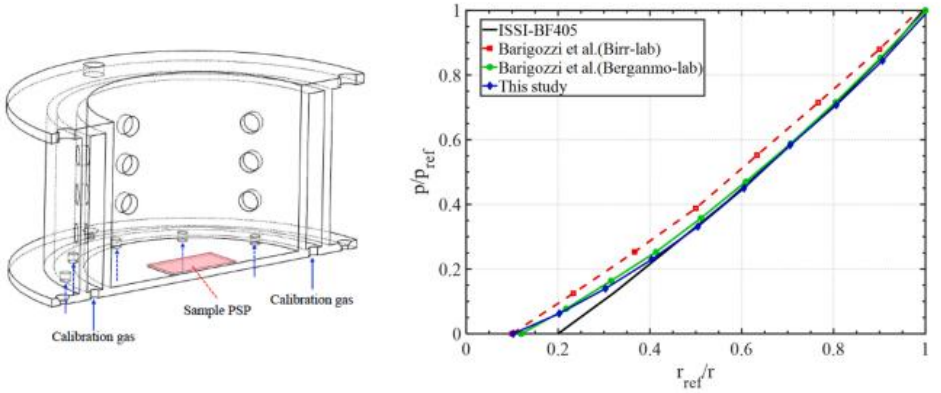

Fig. 5. Cross-section of the calibration shroud (left) and comparison between the PSP calibration curves of ISSI [75], Birr and Bergamo Laboratories [74], and the present study (right).

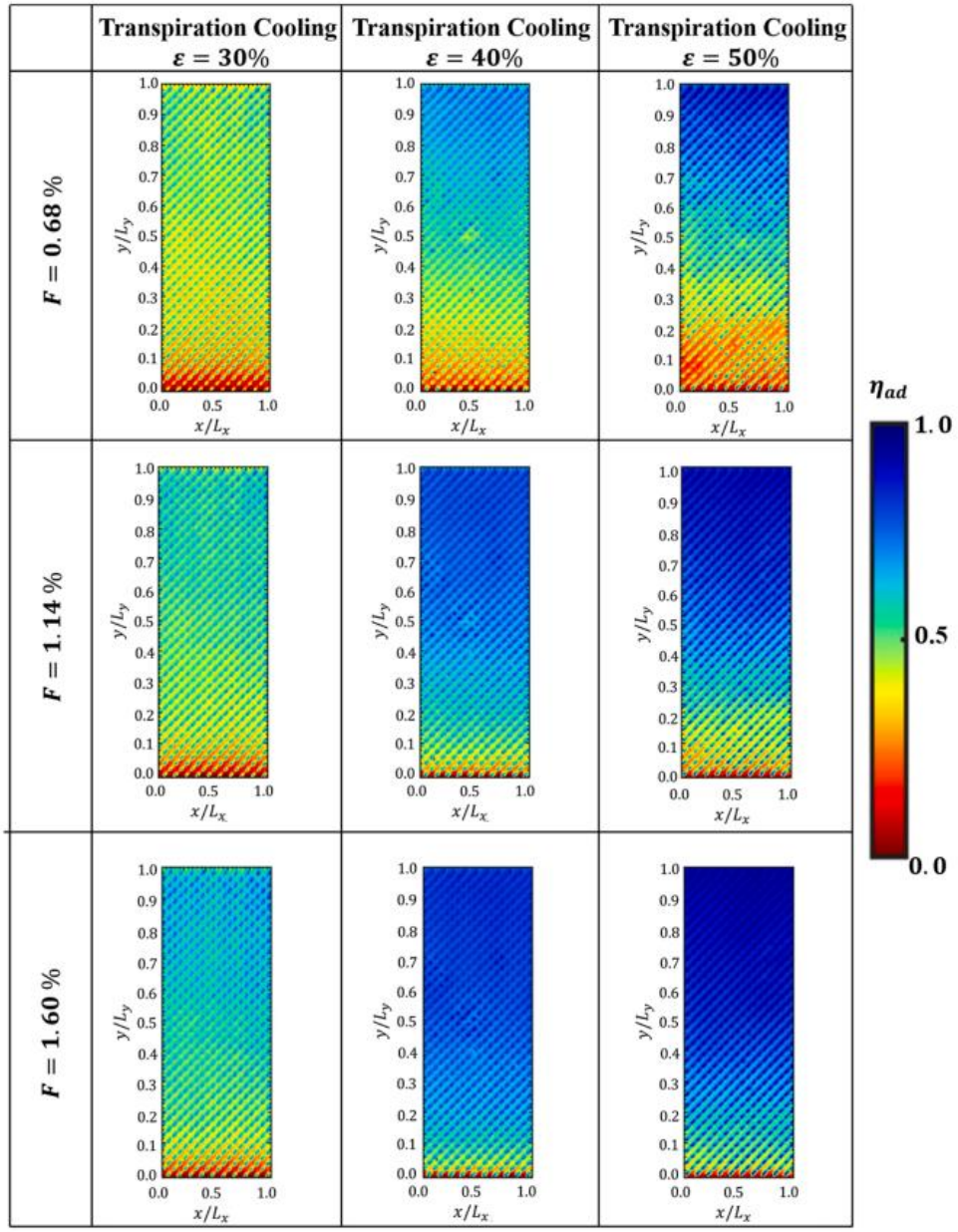

Fig. 6. The 2-D distributions of adiabatic film cooling effectiveness over the TPMS lattices with three different porosities at the injection ratios of 0.68% (top), 1.14% (middle), and 1.60% (bottom).

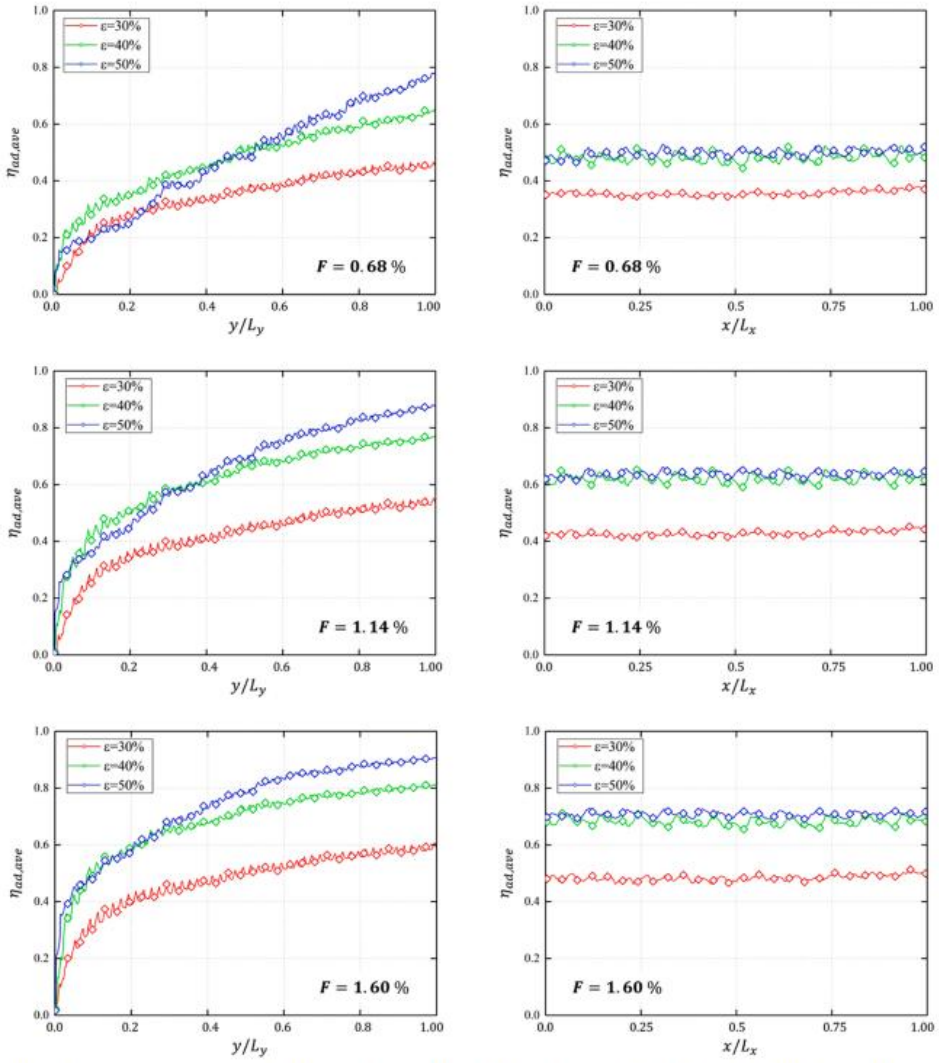

Fig. 7. The variations of spanwise-averaged (left) and streamwise-averaged (right) adiabatic film cooling effectiveness over the TPMS lattices with three different porosities at the injection ratios of 0.68% (top), 1.14% (middle), and 1.60% (bottom).

3.2. Variations of averaged film effectiveness along and across TPMS lattices

In Fig. 7, the variations of spanwise-averaged and streamwise-averaged adiabatic film cooling effectiveness, $\eta_{ad.\ ave}$, are shown, respectively, along the y and x directions of the TPMS lattices with porosities of ε = 30, 40, and 50% at the three defined injection ratios of 0.68%, 1.14%, and 1.60% and the selected mainstream velocity of 33 m/s. It should be noted that displaying the averaged adiabatic film cooling effectiveness values of the transpiration cooling cases with including surface open areas can lead to overestimation, especially when compared with the effusion cooling case due to its much lower surface open area, as shown in Table 1. This is because surface open areas have unity film cooling effectiveness by definition, as they represent no heat deposited on a solid surface. Therefore, the spanwise and streamwise averaged plots are depicted with surface open areas excluded.

The nonuniformity of the adiabatic film cooling effectiveness along the y direction, as previously indicated in Fig. 6, becomes more apparent when examining the spanwise-averaged adiabatic film cooling effectiveness depicted in Fig. 7. Interestingly, it is observed that with

increasing porosity, the spanwise-averaged adiabatic film cooling effectiveness slightly decreases in upstream regions near the leading edge, while it increases more rapidly as one approaches the trailing edge downstream. The deficiency of the cooling film in the initial stages of the lattice structure with higher porosity can be ascribed to the relatively lower velocity of the coolant at the same flow rate, caused by the larger open areas of the test coupon with high porosity. This phenomenon may even give rise to undesirable hot-gas ingestion into a porous medium with very high porosity [49,79]. However, the upstream deficit is rapidly compensated by the accumulation of coolant downstream. This trend is particularly pronounced in cases with 50% porosity and low injection ratios. According to Fig. 7, the values of the streamwise-averaged adiabatic film cooling effectiveness also show similar overall trends as those of the spanwise-averaged one, where the effectiveness improves with increasing porosity, though with lower magnitudes for the streamwise-averaged cases as they are averaged along the nonuniform y-direction profile. In addition, there is no significant fluctuations observed in the streamwise-averaged adiabatic film cooling effectiveness profiles along the x direction, as expected for porous structures. Overall, the both spanwise- and streamwise-averaged adiabatic film cooling effectiveness values increase with rising the coolant flow rate. For example, as illustrated in Fig. 7, the spanwise-averaged adiabatic film cooling effectiveness of the 50% porosity TPMS structure approaches 0.77, 0.88, and 0.91 at the trailing edge in downstream with increasing the injection ratio from 0.68% to 1.14% and 1.60%, respectively.

3.3. Comparison between transpiration and effusion cooling methods

A comparison between the 2-D distributions of adiabatic film cooling effectiveness, η_{ad}, over the TPMS lattice structure with 50% porosity and the designed discrete hole effusion cooling test coupon are shown in Fig. 8 for the same injection ratios of 0.68%, 1.14%, and 1.60% and the mainstream velocity of 33 m/s. At all studied coolant flow rates, transpiration cooling demonstrates a high adiabatic film cooling effectiveness over the majority of the measurement area, except for upstream regions near the trailing edge. On the other hand, the effusion cooling is unable to provide a sufficient adiabatic film cooling effectiveness over almost the entire area of its coverage with the exception of hole exits, which exhibit large adiabatic film cooling effectiveness values. This serves as a significant indication of the greater capability of the transpiration cooling method to provide more complete film coverage, which is highly beneficial in preventing the creation of hot spot zones over exposed surfaces in real applications.

In Fig. 9, a comparison between the variations of spanwise-averaged and streamwise-averaged adiabatic film cooling effectiveness, $\eta_{ad,\ ave}$, are shown, respectively, along the y and x directions of the TPMS lattice structure with 50% porosity and the discrete hole effusion cooling test coupon for the same injection ratios of 0.68%, 1.14%, and 1.60% and the mainstream velocity of 33 m/s. The spanwise and streamwise averaged plots are depicted with surface open areas excluded, as explained in Section 3.2. At all the coolant flow rates studied, the transpiration cooling offers much higher spanwise- and streamwise-averaged adiabatic film cooling effectiveness values compared to the effusion cooling method. Of particular interest, while increasing the coolant flow rate enhances both the spanwise- and streamwise-averaged adiabatic film cooling effectiveness of the transpiration cooling cases, it has an adverse effect on the performance of the effusion cooling method. The reduction of both the spanwise- and streamwise-averaged adiabatic film cooling effectiveness of the effusion cooling with increasing the coolant flow rate could be attributed to the occurrence of film lift-off at high blowing ratios that promotes the turbulent mixing and entrain the mainstream air into the near-wall region, thereby reducing the concentration of the coolant proxy, i.e., Nitrogen, over the exposed surfaces. Another interesting observation is pertaining to the high-amplitude fluctuations of the profiles associated with effusion cooling method, which are more pronounced in the streamwise-averaged adiabatic film cooling effectiveness profiles, see Fig. 9 (right). This is because of the fact that adiabatic film cooling effectiveness is high at the hole exit and drops immediately with distancing from the injection location until reaching the next hole, which could yield hot spot zones over exposed surfaces in real applications. However, much smoother adiabatic film cooling effectiveness profiles are observable in the transpiration cooling method, highlighting the capability of it in providing a more complete film coverage.

3.4. Overall adiabatic film cooling effectiveness

In order to achieve a single parameter for evaluating and comparing the performances of all the cases studied in the present study, the local solid-surface adiabatic film cooling effectiveness of each case is averaged over the entire measurement area (i.e., solid surface averaging), resulting in overall adiabatic film cooling effectiveness values, $\eta_{ad,\ overall}$, as presented in Table 3. The findings indicate that the adiabatic film

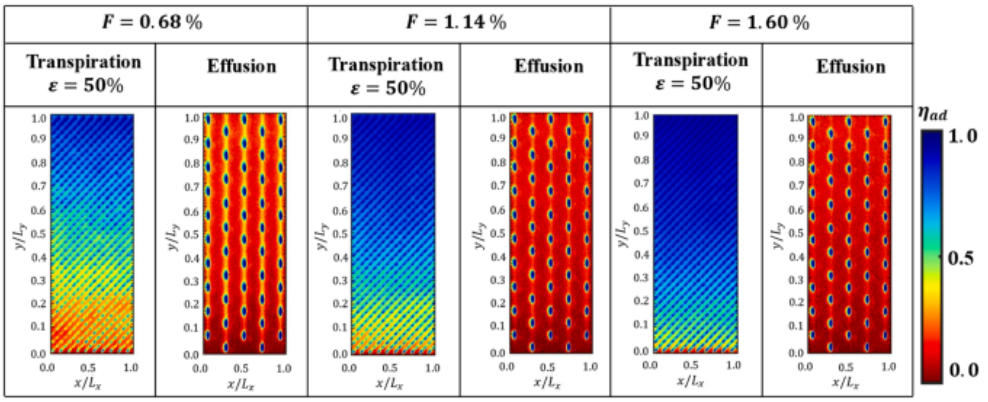

Fig. 8. Comparison between the 2-D distributions of adiabatic film cooling effectiveness over the TPMS lattice structure with 50% porosity and the discrete hole effusion cooling test coupon at the injection ratios of 0.68% (left), 1.14% (middle), and 1.60% (right).

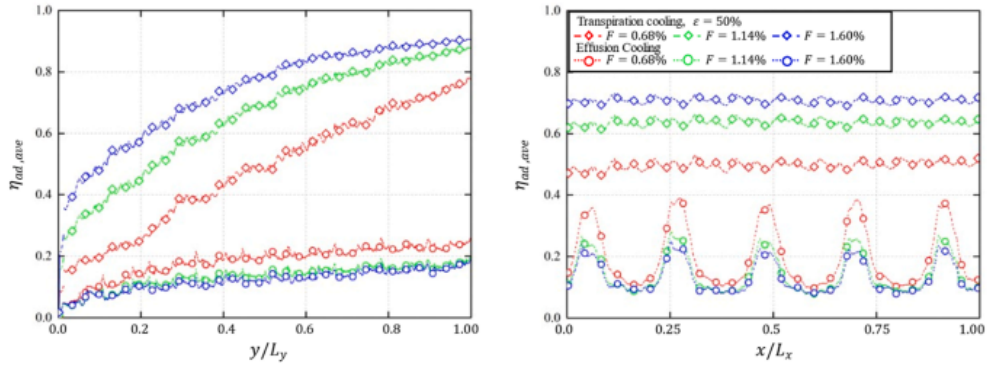

Fig. 9. Comparison between the variations of spanwise-averaged (left) and streamwise-averaged (right) adiabatic film cooling effectiveness over the TPMS lattice structure with 50% porosity and the discrete hole effusion cooling test coupon at the injection ratios of 0.68%, 1.14%, and 1.60%.

Table 3
Overall adiabatic film cooling effectiveness of both the effusion and transpiration cooling cases with surface open areas excluded.

Film cooling method	ε_d	F [%]	$\eta_{ad,\ overall}$
Discrete hole effusion cooling	1.35%	0.68	0.20
		1.14	0.14
		1.60	0.13
TPMS-based transpiration cooling	30%	0.68	0.36 (1.80↑)
		1.14	0.43 (2.87↑)
		1.60	0.49 (3.50↑)
	40%	0.68	0.49 (2.45↑)
		1.14	0.63 (4.20↑)
		1.60	0.69 (4.92↑)
	50%	0.68	0.51 (2.55↑)
		1.14	0.67 (4.47↑)
		1.60	0.75 (5.36↑)

cooling effectiveness of TPMS-based transpiration cooling can exceed five times that of discrete hole effusion cooling, particularly at the highest values of porosity and coolant flow rate investigated in this study. This is attributed to the greater adiabatic film cooling effectiveness and more thorough film coverage achieved by TPMS-based transpiration cooling, as discussed in earlier sections. Note that unlike conventional porous media, which often suffer from uneven air distribution and potential mechanical and clogging issues, TPMS lattice structure enables a more uniform distribution of coolant, significantly enhancing film cooling performance. From Table 3, it is also observed that as the values of porosity and coolant flow rate decrease, the differences between the $\eta_{ad,\ overall}$ values of the transpiration and effusion cooling methods diminish. Nonetheless, even at the lowest values of porosity and coolant flow rate studied herein, the transpiration cooling method still exhibits a noticeable (i.e., two-fold) improvement in $\eta_{ad,\ overall}$ compared to the effusion cooling method. The contrasting impacts of coolant flow rate increasing on the $\eta_{ad,\ overall}$ values of the transpiration and effusion cooling methods are also apparent in Table 3, where the effusion cooling exhibits a decreasing trend. This could be ascribed to the undesirable film lift-off phenomenon observed in the effusion cooling method at high blowing ratios, a problem alleviated by TPMS-based transpiration cooling.

4. Conclusion

The performances of a transpiration cooling method employing additively manufactured TPMS lattice structures were evaluated and compared with those of the state-of-the-art discrete hole effusion cooling method widely used for cooling gas turbine hot-gas path components, where TPMS lattice structures were defined mathematically through their level-set equations. TPMS lattices can be precisely engineered for both global and local control of their characteristics, such as structure type/topology, porosity, and unit cell size, in order to achieve optimal fluid flow and heat transfer performances in engineering applications. A dual-luminophore pressure sensitive paint measurement was performed to compare the adiabatic film cooling effectiveness between TPMS-based transpiration cooling and conventional effusion cooling. The results showed that the TPMS-based transpiration cooling does not suffer from the undesirable cooling jet lift-off effects that plague effusion cooling and is capable of approaching an adiabatic film cooling effectiveness of unity in downstream along with improving the overall adiabatic film cooling effectiveness by more than five times. The TPMS-based transpiration cooling also showed a more complete and uniform film coverage than the effusion cooling, mainly due to an even and almost continuous distribution of coolant by TPMS lattices. Overall, TPMS-based transpiration cooling not only can increase the thermal protection of exposed surfaces, but also can improve the inner-cooling efficiency of structures. The performance benefits of TPMS-based transpiration cooling call for future comprehensive investigations to evaluate mechanical strength, fatigue resistance, and clogging prevention methods of TPMS lattice structures for longevity under harsh environments. In the end, it is important to acknowledge that while the effusion and transpiration cooling designs used in the present study offer valuable insights, there may be more efficient design configurations for both cooling techniques. Future research should focus on comparing the effectiveness of different types of effusion and TPMS structures and exploring optimization techniques to enhance their efficiencies further.

CRediT authorship contribution statement

Mohsen Broumand: Writing – original draft, Methodology, Investigation, Formal analysis, Data curation, Conceptualization. **Juchan Son:** Methodology, Investigation, Formal analysis, Data curation, Conceptualization. **Yeongmin Pyo:** Methodology, Investigation, Formal analysis, Data curation, Conceptualization. **Sean Yun:** Resources, Project administration, Funding acquisition. **Zekai Hong:** Writing – review & editing, Supervision, Resources.

Declaration of competing interest

The authors declare that they have no known competing financial

interests or personal relationships that could have appeared to influence the work reported in this paper.

Data availability

Data will be made available on request.

Acknowledgments

The work is supported by the National Research Council of Canada (NRC) National Program Office under the Ideation New Beginnings Program (No. 577) and Postdoctoral Fellowship Program (PDF2021–06). Additional funding for the work is provided by the NRC's Aerospace Research Center under the LEAP Program (LEAP-012).

References

[1] Han J.-C., Dutta S., Ekkad S., Gas Turbine Heat Transfer and Cooling Technology (2nd ed.), 2013. https://doi.org/10.1201/b13616.
[2] D.G. Wilson, T. Korakianitis, The design of high-efficiency turbomachinery and gas turbines, (2014). https://doi.org/10.7551/mitpress/9940.001.0001.
[3] J.H. Wagner, B.V. Johnson, R.A. Graziani, F.C. Yeh, Heat transfer in rotating serpentine passages with trips normal to the flow, ASME J. Turbomach. 114 (1992) 847–857, https://doi.org/10.1115/1.2928038.
[4] J. Armstrong, D. Winstanley, A review of staggered array pin fin heat transfer for turbine cooling applications, ASME J. Turbomach. 110 (1988) 94–103, https://doi.org/10.1115/1.3262173.
[5] J.R. Taylor, Heat transfer phenomena in gas turbines, (1980). https://doi.org/10.1115/80-GT-172.
[6] L. Yang, J. Ren, H. Jiang, P. Ligrani, Experimental and numerical investigation of unsteady impingement cooling within a blade leading edge passage, Int. J. Heat Mass Transf. 71 (2014) 57–68, https://doi.org/10.1016/j.ijheatmasstransfer.2013.12.006.
[7] P. Grootenhuis, The mechanism and application of effusion cooling, Aeronaut. J. 63 (1959) 73–89, https://doi.org/10.1017/S0368393100070632.
[8] R.J. Goldstein, E.R.G. Eckert, F. Burggraf, Effects of hole geometry and density on three-dimensional film cooling, Int. J. Heat Mass Transf. 17 (1974) 595–607, https://doi.org/10.1016/0017-9310(74)90007-6.
[9] C.A.J.W.A. Nelson, R.M. Orenstein, P.S. DiMascio, Development of Advanced Thermal Barrier Coatings for Severe Environments, Turbo Expo Power Land, Sea, Air, 1995, 95-GT-270V004T10A011.
[10] K. Mondal, L. Nuñez, C.M. Downey, L.J. van Rooyen, Recent advances in the thermal barrier coatings for extreme environments, Mater. Sci. Energy Technol. 4 (2021) 208–210, https://doi.org/10.1016/j.mset.2021.06.006.
[11] D.G. Bogard, K.A. Thole, Gas turbine film cooling, J. Propuls. Power. 22 (2006) 249–270, https://doi.org/10.2514/1.18034.
[12] R. Krewinkel, A review of gas turbine effusion cooling studies, Int. J. Heat Mass Transf. 66 (2013) 706–722, https://doi.org/10.1016/j.ijheatmasstransfer.2013.07.071.
[13] Andrews G.E., Alikhanizadeh M., T.F. Bazdidi, Hussain C.I., A.M.S. Koshkbar, Small diameter film cooling holes: the influence of hole size and pitch, 5 (1988) 61–72. https://doi.org/10.1515/TJJ.1988.5.1-4.61.
[14] H.H. Cho, D.H. Rhee, R.J. Goldstein, Effects of hole arrangements on local heat/mass transfer for impingement/effusion cooling with small hole spacing, J. Turbomach. (2008) 130, https://doi.org/10.1115/1.2812325.
[15] Z. Huang, Y.-B. Xiong, Y.-Q. Liu, P.-X. Jiang, Y.-H. Zhu, Experimental investigation of full-coverage effusion cooling through perforated flat plates, Appl. Therm. Eng. 76 (2015) 76–85, https://doi.org/10.1016/j.applthermaleng.2014.11.056.
[16] Y. Lu, A. Dhungel, S.V. Ekkad, R.S. Bunker, Effect of trench width and depth on film cooling from cylindrical holes embedded in trenches, J. Turbomach. (2008) 131, https://doi.org/10.1115/1.2950057.
[17] H. Wei, J.L. Ai, Y.Q. Zu, L. Ding, Heat transfer characteristics of fan-shaped hole effusion cooling for a constant hole exit width – Numerical simulation and experimental validation, Appl. Therm. Eng. 160 (2019) 113978, https://doi.org/10.1016/j.applthermaleng.2019.113978.
[18] L. Fischer, D. James, S. Jeyaseelan, M. Pfitzner, Optimizing the trench shaped film cooling design, Int. J. Heat Mass Transf. 214 (2023) 124399, https://doi.org/10.1016/j.ijheatmasstransfer.2023.124399.
[19] A.C. Shrager, K.A. Thole, D. Mongillo, Effects of effusion cooling pattern near the dilution hole for a double-walled combustor liner—part 1: overall effectiveness measurements, J. Eng. Gas Turbines Power. 141 (2018), https://doi.org/10.1115/1.4041148.
[20] M. Courtis, A. Murray, B. Coulton, P. Ireland, I. Mayo, Influence of spanwise and streamwise film hole spacing on adiabatic film effectiveness for effusion-cooled gas turbine blades, Int. J. Turbomachin. Propuls. Power. 6 (2021), https://doi.org/10.3390/ijtpp6030037.
[21] Q. Wang, Y. Li, J. Lou, L. Yang, A decision-making design approach to optimize the hole arrangement of effusion cooling plates under non-uniform heat load conditions, Appl. Therm. Eng. 235 (2023) 121417, https://doi.org/10.1016/j.applthermaleng.2023.121417.
[22] R.J. Goldstein, L.D. Stone, Row-of-holes film cooling of curved walls at low injection angles, J. Turbomach. 119 (1997) 574–579, https://doi.org/10.1115/1.2841160.
[23] V. Venkatesh, S. J, B. Vignesh, D. S. K, R.K. Velamati, S. A.R, B. Ramakrishnananda, S. Batchu, Studies on effusion cooling: impact of geometric parameters on cooling effectiveness and coolant consumption, Aerosp. Sci. Technol. 77 (2018) 58–66, https://doi.org/10.1016/j.ast.2017.12.044.
[24] V. Aga, R.S. Abhari, Influence of flow structure on compound angled film cooling effectiveness and heat transfer, J. Turbomach. (2011) 133, https://doi.org/10.1115/1.4002420.
[25] L.C. Paitich, P. Richer, B. Jodoin, Y. Pyo, S. Yun, Z. Hong, Directional effects of effusion cooling on the cooling film effectiveness, AIAA J 60 (2021) 423–434, https://doi.org/10.2514/1.J060625.
[26] R.S. Bunker, Evolution of Turbine Cooling, (2017). https://doi.org/10.1115/GT2017-63205.
[27] W. Wang, Y. Yan, Y. Zhou, J. Cui, Review of advanced effusive cooling for gas turbine blades, Energies (2022) 15, https://doi.org/10.3390/en15228568.
[28] Q. Mi, S.H. Yi, D.D. Gang, X.G. Lu, X.L. Liu, Research progress of transpiration cooling for aircraft thermal protection, Appl. Therm. Eng. 236 (2024) 121360, https://doi.org/10.1016/j.applthermaleng.2023.121360.
[29] W. Rannie, A Simplified Theory of Porous Wall Cooling, Tech. Rep. Jet Propulsion Laboratory, Pasadena, CA, 1947.
[30] P.O.L. DUWEZ, H.L. WHEELER, Experimental study of cooling by injection of a fluid through a porous material, J. Aeronaut. Sci. 15 (1948) 509–521, https://doi.org/10.2514/8.11640.
[31] E.R.G. Eckert, N.B. Livingood, Comparison of Effectiveness of convection-, transpiration-, and Film-Cooling Methods With Air As coolant, Tech. Rep. 1182, NACA, Lewis Flight Propulsion Laboratory, Cleveland, OH, 1954.
[32] G.C. Ngetich, A.V. Murray, P.T. Ireland, E. Romero, A three-dimensional conjugate approach for analyzing a double-walled effusion-cooled turbine blade, J. Turbomach. (2018) 141, https://doi.org/10.1115/1.4041379.
[33] W. Li, X. Lu, X. Li, J. Ren, H. Jiang, On improving full-coverage effusion cooling efficiency by varying cooling arrangements and wall thickness in double wall cooling application, J. Heat Transfer. (2019) 141, https://doi.org/10.1115/1.4042772.
[34] A.V. Murray, P.T. Ireland, E. Romero, Experimental and computational methods for the evaluation of double-wall, effusion cooling systems, J. Turbomach. (2020) 142, https://doi.org/10.1115/1.4047384.
[35] M. Courtis, C. Skamniotis, A. Cocks, P. Ireland, Coupled aerothermal-mechanical analysis in single crystal double wall transpiration cooled gas turbine blades with a large film hole density, Appl. Therm. Eng. 219 (2023) 119329, https://doi.org/10.1016/j.applthermaleng.2022.119329.
[36] H. Gu, D. Zhou, K. Du, W. Li, Overall cooling characteristics of double-wall effusion system considering material selections and hole arrangements, Int. J. Heat Mass Transf. 216 (2023) 124599, https://doi.org/10.1016/j.ijheatmasstransfer.2023.124599.
[37] E.Y. Jung, H. Chung, S.M. Choi, T. Woo, H.H. Cho, Conjugate heat transfer on full-coverage film cooling with array jet impingements with various Biot numbers, Exp. Therm. Fluid Sci. 83 (2017) 1–8, https://doi.org/10.1016/j.expthermflusci.2016.12.008.
[38] C. Skamniotis, A.C.F. Cocks, Designing against severe stresses at compound cooling holes of double wall transpiration cooled engine components, Aerosp. Sci. Technol. 116 (2021) 106856, https://doi.org/10.1016/j.ast.2021.106856.
[39] C. Skamniotis, A.C.F. Cocks, 2D and 3D thermoelastic phenomena in double wall transpiration cooling systems for gas turbine blades and hypersonic flight, Aerosp. Sci. Technol. 113 (2021) 106610, https://doi.org/10.1016/j.ast.2021.106610.
[40] C. Skamniotis, M. Courtis, A.C.F. Cocks, Multiscale analysis of thermomechanical stresses in double wall transpiration cooling systems for gas turbine blades, Int. J. Mech. Sci. 207 (2021) 106657, https://doi.org/10.1016/j.ijmecsci.2021.106657.
[41] C. Skamniotis, A.C.F. Cocks, Creep-plasticity-fatigue calculations in the design of porous double layers for new transpiration cooling systems, Int. J. Fatigue. 151 (2021) 106304, https://doi.org/10.1016/j.ijfatigue.2021.106304.
[42] C. Skamniotis, A.C.F. Cocks, Minimising stresses in double wall transpiration cooled components for high temperature applications, Int. J. Mech. Sci. 189 (2021) 105983, https://doi.org/10.1016/j.ijmecsci.2020.105983.
[43] J.R. McDonough, A perspective on the current and future roles of additive manufacturing in process engineering, with an emphasis on heat transfer, Therm. Sci. Eng. Prog. 19 (2020) 100594, https://doi.org/10.1016/j.tsep.2020.100594.
[44] I. Kaur, P. Singh, Critical evaluation of additively manufactured metal lattices for viability in advanced heat exchangers, Int. J. Heat Mass Transf. 168 (2021) 120858, https://doi.org/10.1016/j.ijheatmasstransfer.2020.120858.
[45] K.A. Thole, S.P. Lynch, A.J. Wildgoose, Chapter Five - Review of Advances in Convective Heat Transfer Developed Through Additive Manufacturing, in: J.P. Abraham, J.M. Gorman, W.B.T.-A. in H.T. Minkowycz (Eds.), Elsevier, 2021: pp. 249–325. https://doi.org/10.1016/bs.aiht.2021.06.004.
[46] G. Huang, Z. Min, L. Yang, P.-X. Jiang, M. Chyu, Transpiration cooling for additive manufactured porous plates with partition walls, Int. J. Heat Mass Transf. 124 (2018) 1076–1087, https://doi.org/10.1016/j.ijheatmasstransfer.2018.03.110.
[47] Z. Min, G. Huang, S.N. Parbat, L. Yang, M.K. Chyu, Experimental Investigation on Additively Manufactured Transpiration and Film Cooling Structures, J. Turbomach. (2019) 141, https://doi.org/10.1115/1.4042009.
[48] M. Kim, D.H. Shin, J.S. Kim, B.J. Lee, J. Lee, Experimental investigation of effusion and transpiration air cooling for single turbine blade, Appl. Therm. Eng. 182 (2021) 116156, https://doi.org/10.1016/j.applthermaleng.2020.116156.
[49] M. Hinse, K. Yildiz, P. Richer, B. Jodoin, M. Bourmand, S. Yun, Z. Hong, Numerical and Experimental Studies of Transpiration Cooling Film Effectiveness over Porous

Materials, J. Thermophys. Heat Transf. (2022) 1–15, https://doi.org/10.2514/1.T6510.
[50] M. Helou, S. Kara, Design, analysis and manufacturing of lattice structures: an overview, Int. J. Comput. Integr. Manuf. 31 (2018) 243–261, https://doi.org/10.1080/0951192X.2017.1407456.
[51] F. Tamburrino, S. Graziosi, M. Bordegoni, The design process of additively manufactured mesoscale lattice structures: a review, J. Comput. Inf. Sci. Eng. 18 (2018), https://doi.org/10.1115/1.4040131.
[52] T. Maconachie, M. Leary, B. Lozanovski, X. Zhang, M. Qian, O. Faruque, M. Brandt, SLM lattice structures: properties, performance, applications and challenges, Mater. Des. 183 (2019) 108137, https://doi.org/10.1016/j.matdes.2019.108137.
[53] N. Yang, S. Wang, L. Gao, Y. Men, C. Zhang, Building implicit-surface-based composite porous architectures, Compos. Struct. 173 (2017) 35–43, https://doi.org/10.1016/j.compstruct.2017.04.004.
[54] O. Al-Ketan, R.K. Abu Al-Rub, Multifunctional mechanical metamaterials based on triply periodic minimal surface lattices, Adv. Eng. Mater. 21 (2019) 1900524, https://doi.org/10.1002/adem.201900524.
[55] Z. Cheng, R. Xu, P.-X. Jiang, Morphology, flow and heat transfer in triply periodic minimal surface based porous structures, Int. J. Heat Mass Transf. 170 (2021) 120902, https://doi.org/10.1016/j.ijheatmasstransfer.2021.120902.
[56] Z. Cheng, X. Li, R. Xu, P. Jiang, Investigations on porous media customized by triply periodic minimal surface: heat transfer correlations and strength performance, Int. Commun. Heat Mass Transf. 129 (2021) 105713, https://doi.org/10.1016/j.icheatmasstransfer.2021.105713.
[57] O. Al-Ketan, M. Ali, M. Khalil, R. Rowshan, K.A. Khan, R.K. Abu Al-Rub, Forced convection computational fluid dynamics analysis of architected and three-dimensional printable heat sinks based on triply periodic minimal surfaces, J. Therm. Sci. Eng. Appl. 13 (2020), https://doi.org/10.1115/1.4047385.
[58] J. Iyer, T. Moore, D. Nguyen, P. Roy, J. Stolaroff, Heat transfer and pressure drop characteristics of heat exchangers based on triply periodic minimal and periodic nodal surfaces, Appl. Therm. Eng. 209 (2022) 118192, https://doi.org/10.1016/j.applthermaleng.2022.118192.
[59] N. Thomas, N. Sreedhar, O. Al-Ketan, R. Rowshan, R.K. Abu Al-Rub, H. Arafat, 3D printed triply periodic minimal surfaces as spacers for enhanced heat and mass transfer in membrane distillation, Desalination 443 (2018) 256–271, https://doi.org/10.1016/j.desal.2018.06.009.
[60] W. Li, G. Yu, Z. Yu, Bioinspired heat exchangers based on triply periodic minimal surfaces for supercritical CO2 cycles, Appl. Therm. Eng. 179 (2020) 115686, https://doi.org/10.1016/j.applthermaleng.2020.115686.
[61] Z. Fan, R. Gao, S. Liu, A novel battery thermal management system based on P type triply periodic minimal surface, Int. J. Heat Mass Transf. 194 (2022) 123090, https://doi.org/10.1016/j.ijheatmasstransfer.2022.123090.
[62] Z. Cheng, R. Xu, P. Jiang, Transpiration cooling with phase change by functionally graded porous media, Int. J. Heat Mass Transf. 205 (2023) 123862, https://doi.org/10.1016/j.ijheatmasstransfer.2023.123862.
[63] J. Klinowski, A.L. Mackay, H. Terrones, J. Klinowski, A.L. Mackay, Curved surfaces in chemical structure, Philos. Trans. R. Soc. London. Ser. A Math. Phys. Eng. Sci. 354 (1997) 1975–1987, https://doi.org/10.1098/rsta.1996.0086.
[64] P.J.F. Gandy, S. Bardhan, A.L. Mackay, J. Klinowski, Nodal surface approximations to the P,G,D and I-WP triply periodic minimal surfaces, Chem. Phys. Lett. 336 (2001) 187–195, https://doi.org/10.1016/S0009-2614(00)01418-4.
[65] H.A. Schwarz, Gesammelte Mathematische Abhandlungen, Springer-Verlag Berlin Heidelberg, 1890, https://doi.org/10.1007/978-3-642-50665-9.
[66] A.H. Schoen, Infinite periodic minimal surfaces without self-intersections, (1970).
[67] L. Han, S. Che, An overview of materials with triply periodic minimal surfaces and related geometry: from biological structures to self-assembled systems, Adv. Mater. 30 (2018) 1705708, https://doi.org/10.1002/adma.201705708.
[68] B. Woodcock, G. O., Ertz, T., and Koch, Effusion cooling techniques for combustors in engine assemblies, U.S. Patent No. 8,104,288, 2012.
[69] J.M. Dai, Z., Pearson, M.R., .and Cohen, Combustor liner effusion cooling holes, U. S. Patent No. 14/618,087, 2016.
[70] Formlabs Material Library, Everything You Need to Start Printing., (n.d.).
[71] T.V. Jones, Theory for the use of foreign gas in simulating film cooling, Int. J. Heat Fluid Flow. 20 (1999) 349–354, https://doi.org/10.1016/S0142-727X(99)00017-X.
[72] A. Andreini, B. Facchini, A. Picchi, L. Tarchi, F. Turrini, Experimental and theoretical investigation of thermal effectiveness in multiperforated plates for combustor liner effusion cooling, J. Turbomach. 136 (2014) 91003, https://doi.org/10.1115/1.4026846.
[73] L. Andrei, A. Andreini, C. Bianchini, G. Caciolli, B. Facchini, L. Mazzei, A. Picchi, F. Turrini, Effusion cooling plates for combustor liners: experimental and numerical investigations on the effect of density ratio, Energy Procedia 45 (2014) 1402–1411, https://doi.org/10.1016/j.egypro.2014.01.147.
[74] G. Barigozzi, C. Mucignat, H. Abdeh, D. Scandella, G. Dolci, Assessment of binary PSP technique for film cooling effectiveness measurement on nozzle vane cascade with cutback trailing edge, Exp. Therm. Fluid Sci. 97 (2018) 431–443, https://doi.org/10.1016/j.expthermflusci.2018.05.015.
[75] Innovative scientific solutions inc. binary pressure-sensitive paint, (n.d.). https://innssi.com/(accessed October 31, 2023).
[76] J.-C. Han, A. Rallabandi, Turbine blade film cooling using PSP technique, Front. Heat Mass Transf. 1 (2010), https://doi.org/10.5098/hmt.v1.1.3001.
[77] T. Liu, J.P. Sullivan, Pressure and Temperature Sensitive Paints, Springer Berlin Heidelberg, 2006. https://books.google.ca/books?id=9wIoSOr0FcMC.
[78] G. Natsui, Z. Little, J.S. Kapat, J.E. Dees, G. Laskowski, A detailed uncertainty analysis of adiabatic film cooling effectiveness measurements using pressure-sensitive paint, J. Turbomach. (2016) 138, https://doi.org/10.1115/1.4032674.
[79] S.A. Showkat Ali, M. Azarpeyvand, M. Szoke, C.R. Ilário Da Silva, Boundary layer flow interaction with a permeable wall, Phys. Fluids. (2018) 30, https://doi.org/10.1063/1.5043276.

5.3 The Influence of TPMS Orientation Angle on Transpiration Cooling Performance

While unit cell size and porosity are well-established geometric parameters influencing cooling performance, additional variables may also significantly affect transpiration cooling behavior.

When coolant is discharged through a porous structure, it forms a coolant film on the surface as the mainstream flow passes over it. In such cases, the relative orientation between the coolant flow path (i.e., surface void direction) and the mainstream flow can substantially influence film cooling effectiveness.

Under swirling mainstream conditions—characteristic of gas turbine operations—the flow field becomes highly directional and complex. Consequently, the interaction between the mainstream flow and the coolant discharge becomes a critical factor governing cooling performance. In effusion cooling, this phenomenon is well documented and commonly referred to as the compound angle effect.

However, the influence of such directional flow effects has not yet been systematically investigated in the context of transpiration cooling. The present study aims to examine the effect of the orientation angle of TPMS surface voids relative to the mainstream flow direction. The surface voids considered here refer to the troughs or recessed channels inherently formed on the surface of TPMS lattice structures. The objective of this work is to identify TPMS structural features that (a) maximize adiabatic film cooling effectiveness and (b) exhibit minimal sensitivity to variations in mainstream flow direction.

In this experimental investigation, the effects of surface void orientation on cooling effectiveness were evaluated for three TPMS solid-network morphologies—Diamond, Koch, and Gyroid. This study established that TPMS lattices should be designed with surface voids oriented perpendicular to the mainstream and with sufficiently high surface tortuosity to minimize orientation sensitivity. Among the geometries investigated, the Koch TPMS exhibited the highest overall cooling effectiveness and the lowest orientation sensitivity owing to its high surface tortuosity, making it the preferred design for practical transpiration cooling applications.

This study is written as a research article and published as a peer-reviewed journal paper, ASME Journal of Engineering for Gas Turbines and Power.

ASME Journal of Engineering for Gas Turbines and Power
Online journal at:
https://asmedigitalcollection.asme.org/gasturbinespower

Juchan Son
Department of Mechanical Engineering,
University of Ottawa,
161 Louis-Pasteur Private,
Ottawa, ON K1N 6N5, Canada;
Aerospace Research Center,
National Research Council of Canada,
1200 Montreal Road,
Ottawa, ON K1A 0R6, Canada

Mohsen Brouman
Aerospace Research Center,
National Research Council of Canada,
1200 Montreal Road,
Ottawa, ON K1A 0R6, Canada

Yeongmin Pyo
Department of Mechanical Engineering,
University of Ottawa,
161 Louis-Pasteur Private,
Ottawa, ON K1N 6N5, Canada

Patrick Richer
Department of Mechanical Engineering,
University of Ottawa,
161 Louis-Pasteur Private,
Ottawa, ON K1N 6N5, Canada

Bertrand Jodoin
Department of Mechanical Engineering,
University of Ottawa,
161 Louis-Pasteur Private,
Ottawa, ON K1N 6N5, Canada

Zekai Hong[1]
Department of Mechanical Engineering,
University of Ottawa,
161 Louis-Pasteur Private,
Ottawa, ON K1N 6N5, Canada;
Aerospace Research Center,
National Research Council of Canada,
1200 Montreal Road,
Ottawa, ON K1A 0R6, Canada

Effects of Lattice Orientation Angle on TPMS-Based Transpiration Cooling

Establishing a continuous cooling film is an effective way to thermally protect hot-gas path components of gas turbines. For aero-engines, effusion cooling is the state-of-the-art method for developing cooling films. However, the cooling film generated by this method is far from ideal, as discrete miniature cooling air jets exiting from effusion cooling holes leave large gaps between cooling holes without adequate cooling film protection. Furthermore, effusion cooling jets can experience strong liftoff from component surfaces and are subsequently diluted due to mixing with the main flow. Recent advances in additive manufacturing (AM) technologies have enabled the fabrication of porous materials with precisely engineered lattice structures, significantly enhancing the film cooling effectiveness of hot-gas path components through transpiration cooling. A prior study has demonstrated highly promising transpiration cooling results by using a family of lattice geometries referred to as triply periodic minimal surface (TPMS) lattices. The present study experimentally investigates the influence of various TPMS lattice orientations on the film cooling effectiveness. Three types of TPMS structures, namely, diamond, Koch, and gyroid, are compared to demonstrate that the TPMS lattice orientation angle affects transpiration cooling performance, with different levels of sensitivity according to the TPMS structure. The TPMS lattice structures studied in this investigation are fabricated by stereolithography (SLA) three-dimensional printing. The adiabatic cooling film effectiveness (AFE) is measured using pressure sensitive paint (PSP). [DOI: 10.1115/1.4067378]

[1]Corresponding author.
Turbo Expo, June 24–28, 2024. GT2024.
Manuscript received August 23, 2024; final manuscript received September 9, 2024; published online January 29, 2025. Editor: Jerzy T. Sawicki.
This work was prepared while under employment by the Government of Canada as part of the official duties of the author(s) indicated above, as such copyright is owned by that Government, which reserves its own copyright under national law.

1 Introduction

In recent decades, gas turbines have faced a dual challenge: meeting environmental regulations while maintaining high efficiency [1]. The drive for enhancing thermal efficiency has resulted in a consistent elevation in turbine inlet temperatures (TIT),

Copyright © 2025 by ASME and His Majesty the King in Right of Canada

surpassing the melting thresholds of conventional Nickel-based superalloys [2]. High thermal loads of gas turbines make hot-gas path components vulnerable, including combustor liners and turbine blades [3]. Advanced cooling technologies allow the lifespan of crucial components of gas turbine engines to be greatly extended while boosting engine efficiency.

Among various cooling methods, effusion cooling represents the state-of-the-art technology [4,5]. Effusion cooling employs an array of discrete microsized cooling holes that discharge cooling air to create a thin insulating film over exposed surfaces, acting as a barrier against hot mainstream gases. To optimize the cooling effectiveness of effusion cooling, various parameters, including hole diameter [6], hole shape [7], hole arrangement [8], inclination angle [9], hole-to-hole pitch [10] and directional effects [11] have been explored extensively. These collective efforts have led to the optimization of effusion cooling.

However, the ever-increasing demand for rising TIT highlights the need for more advanced cooling methods. Transpiration cooling holds the promise of meeting cooling needs of the next-generation gas turbines. In transpiration cooling, coolant passes through many internal micro lia before exiting from the surface of the porous media. Transpiration cooling is superior to effusion cooling due to its capability of providing extensive internal heat transfer areas and uniform distributions of coolant, resulting in more effective coolant films [12,13]. In transpiration cooling, the coolant ejected through porous media forms a cooling gas layer on the wall, a phenomenon known as boundary layer heat-blocking [14] boundary layer, modifying temperature and velocity profiles near the wall, and significantly reduces heat transfer from the hot mainstream to the combustor liner. Therefore, due to these benefits, transpiration cooling has been studied since it was first proposed in the 1940s [15]. In pursuit of optimizing the transpiration cooling, various types of porous media, including open-cell foam [16], woven wire mesh [17], and sintered met for transpiration cooling applications. While these studies have highlighted the superior performances of transpiration cooling, the stochastic nature of porous structures investigated in previous studies poses practical challenges. In fact, since pore sizes and distributions are not precisely controlled during the manufacturing process, it can lead to variations in cooling effectiveness and potentially creating localized hots nts. Therefore, precisely engineered porous media is needed for the successful implementation of transpiration cooling.

With recent advancements in additive manufacturing, it has now become feasible to fabricate purposely engineered porous media [19,20]. In particular, gas turbine cooling designs featuring additive manufacturing is being actively pursued. For example, Kim et al. [21] to compare the cooling effectiveness of additively manufactured effusion and transpiration cooling designs. Huang et al. [22] proposed the addition of partition walls to reinforce the mechanical strength of a plate with densely populated cooling holes. More recently, Min et al. [23] fabricated six types of transpiration cooling structures and explored the film effectiveness values of their designs with complex geometries. The findings of the aforementioned studies have emphasized the substantial influence of porous medium geometrical parameters on the effectiveness of a transpiration cooling method. Transpiration cooling based on deterministic lattice structures fabricated by add s to address drawbacks of stochastic porous media for transpiration cooling. Among various types of deterministic lattice structures, the structures designed based on triply periodic minimal surfaces (TPMS), inspired by the nanocell scale structure found in nature, have gained considerable attention in various engineering and scientific applications due to their well-defined mathematical properties and periodic characteristics [24,25]. TPMS-based lattice structures offer advantageous morphological properties, including a large surface area-to-volume ratio, smooth edges and corners, a reciprocal structure, and interconnected void networks. For example, TPMS lattices have been employed across a spectrum of engineering fields, including soft robotics [26], structure weight reductions [27] and medical devices [28]. More specifically, they are extensively utilized for heat sinks and heat exchangers due to their convoluted internal channels, with a very high surface area-to-volume ratio, which can lead to significant enhancements in the efficiency of heat exchangers/sinks [29,30].

The use of additively manufactured TPMS lattice structures for transpiration cooling was proposed in a recent study [31] by demonstrating the approach's superior film cooling effectiveness over a generic effusion cooling design. Building upon the previous conceptual study, the present work is aimed at understanding the effects of the orientation angle of surface voids of TPMS lattice structures with respect to the mainstream flow. The surface voids referred to here are troughs or recessed channels intrinsic to the surface of TPMS lattice structures.

The cooling surfaces of a gas turbine combustor are subject to highly directional flows resulting from swirling main flow and other localized flow patterns. A conceptual gas turbine combustor that features transpiration cooling is illustrated in Fig. 1.

The goal of the present study is to identify features of TPMS lattice structures that (a) optimize film cooling effectiveness and (b) have minimal sensitivity to flow directions for transpiration cooling. In this experimental study, effects of surface void orientation on cooling effectiveness are investigated for three different TPMS solid-network types, namely, diamond, Koch, and gyroid, which will be discussed in Sec. 3.

2 Experiment Setup

2.1 Triply Periodic Minimal Surface Structure. In this study, three distinct TPMS structure types, namely, diamond, Koch, and gyroid, are being investigated for their potential as porous media for transpiration cooling purposes. Each TPMS structure is characterized by a level set equation, as presented in Table 1. In a level set equation, 3-D coordinates x, y, and z are nondimensionalized by unit cell sizes α, β, and γ in x, y, and z directions respectively such that: $X = 2\pi x/\alpha$, $Y = 2\pi y/\beta$, and $Z = 2\pi z/\gamma$. In this study, the cell size is identical in all three directions, i.e., $\alpha = \beta = \gamma = L_c$. The level set constant, referred to as c, is subject to adjustment to regulate the unit cell relative porosity. The porosity is controlled by adjusting the wall thickness through parameter c. The iso(boundary)-surface, generated by the level set equation, is used to divide the volume into two distinct domains: the solid and the void domain, both enclosed by the isosurface. Regions with values below the isosurface threshold are designated as solid, while those exceeding this threshold are classified as voids. When c is set to zero, the level setting equation generates a porosity of 50%, thereby dividing the solid domain and void domain equally. The solid domain in this instance is defined by the following equation:

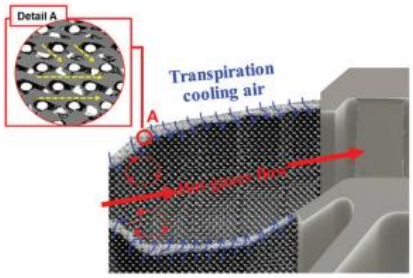

Fig. 1 Conceptual design of a gas turbine combustor featuring TPMS lattice-based transpiration cooling

Table 1 Level set equation

Type	Level set equation
Diamond	$\varnothing(x,y,z) = \sin(X)\sin(Y)\sin(Z) + \sin(X)\cos(Y)\cos(Z) + \cos(X)\sin(Y)\cos(Z) + \cos(X)\cos(Y)\sin(Z) = c$
Koch	$\varnothing(x,y,z) = \cos(2X)\sin(Y)\cos(Z) + \cos(2Y)\sin(Z)\cos(X) + \cos(2Z)\sin(X)\cos(Y) = c$
Gyroid	$\varnothing(x,y,z) = \cos(X)\sin(Y) + \cos(Y)\sin(Z) + \cos(Z)\sin(X) = c$

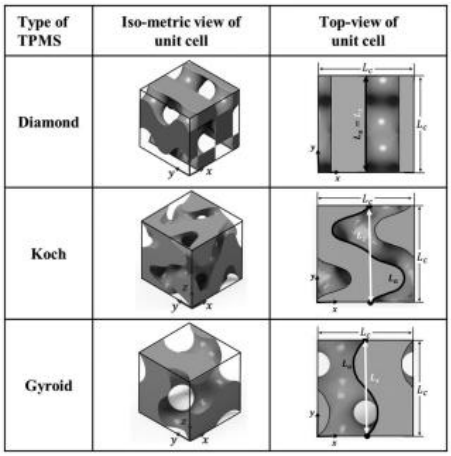

Fig. 2 Unit cells of diamond, Koch, and gyroid types of TPMS geometries with $c = 0$ ($\varepsilon = 50\%$)

$$\varnothing(x,y,z) < c \tag{1}$$

Graphic illustrations of unit cells of the TPMS structures used in this study are presented in Fig. 2 in the unmodified forms as defined in Table 1. It should be pointed out that a rotation of TPMS geometries can be achieved by linear operations, for example, an anticlockwise rotation of angle θ about the z axis can be achieved by the following linear operation

$$\begin{bmatrix} x \\ y \\ z \end{bmatrix}_{\text{rotated}} = \begin{bmatrix} \cos\theta & -\sin\theta & 0 \\ \sin\theta & \cos\theta & 0 \\ 0 & 0 & 1 \end{bmatrix} \begin{bmatrix} x \\ y \\ z \end{bmatrix}_{\text{original}} \tag{2}$$

We investigate the impact of orientation angles on cooling effectiveness by rotating the TPMS lattices about the z axis.

2.2 Test Coupon Design. In this study, a total of seven distinct test coupons were designed and fabricated for three TPMS types (diamond, Koch, and gyroid). All circular test coupons are 123.2 mm in diameter with a rectangular active area of 66.1 × 70.9 mm centered in coupon. The unit cell length L_c and porosity (ε) are identical for all test coupons at 2.54 mm and 50% ($c = 0$), respectively. As shown in Fig. 3, a 25.4 mm × 70.9 mm rectangle at the center of the active area, as highlighted by the yellow dashed line, is used as the observation area. To minimize influences from the solid areas peripheral to the active area and to ensure continuity in measurements, only this center portion was used for measuring film cooling effectiveness. The top views of the observation areas of all seven test coupons are shown in Fig. 4 with the blanks indicating voids on the surface while the areas in black are solids on the surface. The orientation angle is defined as follows: a cooling void pattern aligned parallel to the mainstream

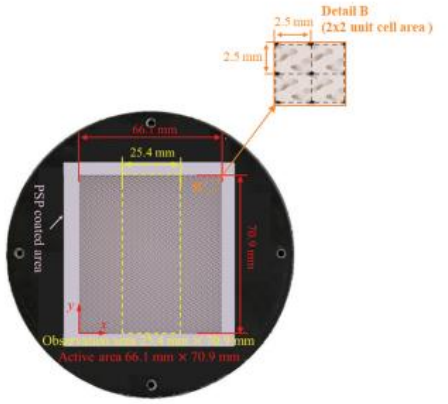

Fig. 3 Three-dimensional printed test coupon of koch type in parallel orientation. The center portion of the active area is used for measurements.

flow is defined as Parallel orientation, similarly, Perpendicular orientation and Diagonal orientation are defined. Each test coupon's orientation angle was depicted in Fig. 4.

Another geometric characteristic considered in this study is the two-dimensional (2D) tortuosity on the top surface, which is commonly used as a criterion to characterize geometrical properties of porous structures [32,33].

Surface tortuosity (τ) is defined as the ratio between the arc length L_a, which represents the actual curving path of each structure, and the chord L_x, the straight-line distance between the endpoints, as illustrated in Fig. 2. In this study, surface tortuosity was offset by one so that a straight line has a zero surface tortuosity. Thus, τ can be calculated as follows:

$$\tau = \frac{L_a}{L_x} - 1 \tag{3}$$

As seen in Fig. 2, for the diamond type, the boundaries between solid and void areas are straight lines at all orientation angles. In this case, the diamond type exhibits zero tortuosity (due to its straight boundary lines). Similarly for the Koch type, the solid and void areas are divided by meandering boundaries for all orientation angles. The Koch type demonstrates the largest tortuosity of 1.1 of all three TPMS geometries investigated in this study. For the gyroid type, the solid and void areas are divided by boundaries of moderate tortuosity of 0.17.

In this study, the test coupons were fabricated using an SLA (stereolithography) three-dimensional (3D) printer. This printer utilizes a single violet diode laser source with a wavelength of 405 nm and a laser power of 250 mW. The printer's resolution was set to 25 μm for all three directions. A high-temperature resin was employed. Detailed material information of high-temperature resin can be found in Ref. [34].

2.3 Experiment Setup. The transpiration cooling studies of TPMS lattice geometries were carried out in an open-loop low-speed

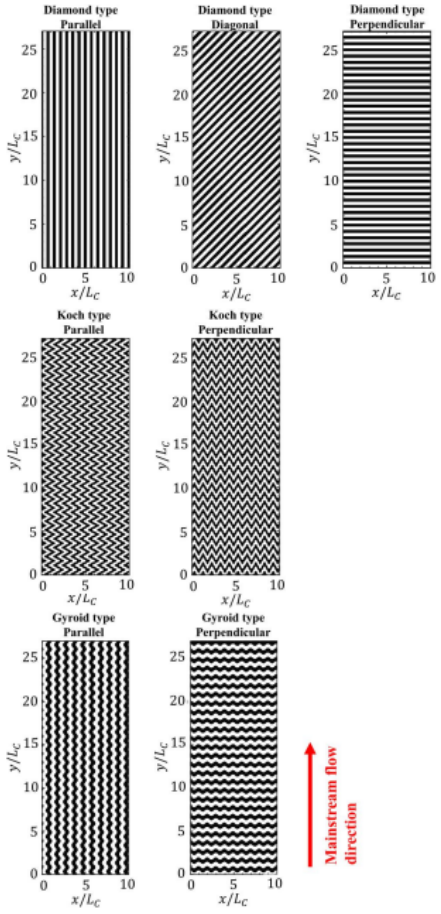

Fig. 4 Top surfaces of the observation areas of all seven test coupons with blanks (white area) representing voids at the sample surface. The direction of the main flow is upwards in the figure.

wind tunnel located at the Gas Turbine Laboratory of the National Research Council Canada. Figure 5 shows a schematic of the experiment setup, with technical details reported in a previous study [35]. The main airflow is driven by a 30 kW fan, capable of achieving a maximum mass flowrate of approximately 2.5 kg/s at a pressure rise of 5 kPa. In the test section, which has a 127 mm × 127 mm square cross section, the mainstream airflow velocity was maintained at 33 m/s. The corresponding Reynolds number is approximately 256,000, representing typical airflow conditions found in a gas turbine combustor. The turbulence intensity within the test section is estimated to be approximately 5% [35]. The velocity of the mainstream flow was measured using a pitot tube, located at the leading edge of the test coupon.

Neat nitrogen (N2) was used as the coolant proxy, supplied through compressed gas bottles. The flow of the coolant was controlled by a FMA 5400 A/5500A series flowmeter from OMEGA, capable of adjusting the flowrate between 0 and 200 standard liters per minute (SLPM). The coolant flow was first sent to a reservoir and was conditioned by the combination of a honeycomb screen and a perforated plate to ensure a uniform distribution of coolant flow to the active area of a test coupon. The location of the honeycomb screen and perforated plate combination is indicated by the dashed line inside the reservoir in Fig. 5. A CFD simulation indicates that the coolant leaving the reservoir has less than 2% variation in local flux across the entire active area of the test coupon. The reservoir has an internal diameter of 101.6 mm and a height of 44.5 mm.

In this study, the binary or dual-luminophore pressure-sensitive paint (PSP) from ISSI was employed to evaluate film cooling effectiveness. A PSP advantage in studying film cooling is that the paint allows an in situ determination of 2D distribution of film cooling effectiveness. This capability makes the PSP method uniquely suited for studying detailed features of film cooling effectiveness across 2D surfaces, providing an intuitive understanding of film cooling performances. The fundamental principle of the PSP technique is luminescence decays of excited dye molecules competes with nonradiative quenching by molecular oxygen within the paint, thereby the paint can function as distributed optical sensors for oxygen partial pressures. Binary PSP comprises two luminophores that interact with oxygen, and a polymer binder that allows for oxygen permeation. Luminophore molecules absorb UV light, and transition to an excited state. These excited-state molecules either emit light about a specific wavelength or revert to the ground state through oxygen quenching. When the partial pressure of surrounding oxygen is high, the increased molecular presence of oxygen enhances the number of molecules transitioning back to the ground state via oxygen quenching, consequently reducing the number of excited-state molecules emitting light at a specific wavelength. Thus, the luminescent intensity emitted by PSP is inversely proportional to the oxygen partial pressure. In experiments utilizing PSP, the intensity of light emitted is recorded and analyzed to determine the 2D pressure distribution across the test surface. The paint consists of two different luminophores: a phosphor that is sensitive to both oxygen partial pressure and temperature variations has an emission spectrum centered at 650 nm, and the other being sensitive only to temperature variations has an emission spectrum centered at 550 nm. An air-cooled UV LED array (ISSI LM2X-DM-400) emitting UV radiation centered at 400 nm is used for uniform and stable UV excitation of the PSP paint. A CCD camera (Lavision Image ProX 2 M) with an image doubler (LaVision) attached in front was used to record luminescence from the PSP at 550 nm and 650 nm simultaneously. The two lenses of the image doubler were spectrally conditioned with bandpass filters, each centered at different wavelengths: the first filter at 650 nm with a 20 nm FWHM (full-width at half-maximum), and the second filter at 550 nm with a 10 nm FWHM.

2.4 Pressure Sensitive Paint Methodology. Film cooling effectiveness is defined in Eq. (4) and can be calculated from adiabatic wall temperatures

$$\eta_{ad} = \frac{T_m - T_{ad}}{T_m - T_c} \tag{4}$$

However, in the study a heat-mass transfer analogy was adopted by measuring oxygen partial pressure near the surface with the PSP. The heat-mass transfer analogy is described in detail by Liu et al. [36]. Following the analogy, the adiabatic film cooling effectiveness can be referred from the following equation:

$$\eta_{ad} \approx \frac{CO_{air} - CO_{fg}}{CO_{air}} = \frac{(P_{O_2})_{air} - (P_{O_2})_c}{(P_{O_2})_{air}} \tag{5}$$

To determine the adiabatic film cooling effectiveness using Eq. (5), it is necessary to calibrate the correlation between the oxygen partial

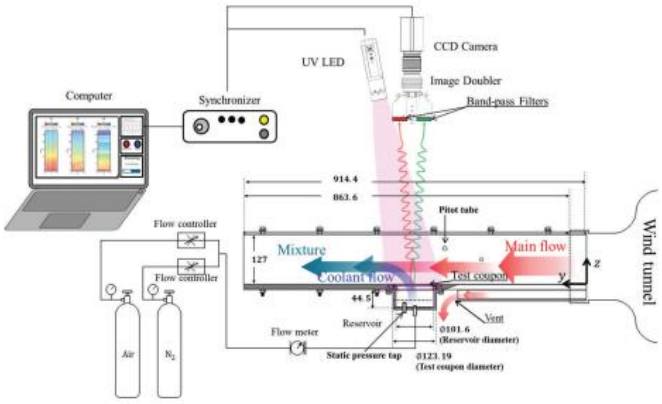

Fig. 5 Schematic of the experiment setup (unit: mm)

pressure and PSP luminescence signals [36]. The empirical correlation used for calibrating luminescence of binary PSP and oxygen partial pressure is the following equation:

$$\frac{(P_{O_2})_{fg}}{(P_{O_2})_{air}} = A + B\left(\frac{r_{ref}}{r}\right) + C\left(\frac{r_{ref}}{r}\right)^2 \tag{6}$$

where $\frac{r_{ref}}{r}$ represents the ratio between the 650 nm PSP luminescence intensity and the 550 nm one at the reference oxygen partial pressure, i.e., the oxygen partial pressure of ambient air; with the 550 nm signal being only temperature dependent and the 650 nm one depending on both temperature and oxygen partial pressure. $\frac{r_{ref}}{r}$ can be defined as follows:

$$\frac{r_{ref}}{r} = \frac{\left(\frac{I_{ref} - I_{dark}}{I - I_{dark}}\right)_{650}}{\left(\frac{I_{ref} - I_{dark}}{I - I_{dark}}\right)_{550}} \tag{7}$$

where I represent luminescent intensity, *ref* subscript denotes a condition when the PSP is subject to ambient air, and *dark* subscript denotes the background luminescent signal when the UV excitation was off, which allows for the correction of camera noise. A, B, and C are correction coefficients that are obtained from calibration process and can vary depending on PSP applications on a particular surface, UV excitation, and optical setup of the camera.

2.5 Measurement Uncertainty. An error propagation analysis was performed to quantify the measurement uncertainty. Based on the Stern-Volmer equation, Sajben et al. [37] analyzed various sources of uncertainty contributing to errors in PSP measurements, including: (1) paint degradation, (2) image registration errors, (3) variation in LED illumination spectrum and intensity, (4) photodetector noise, and (5) PSP calibration errors.

In this study, each PSP image was obtained by averaging 120 frames to reduce random noises in the data. Furthermore, the binary PSP method minimizes measurement errors due to temperature variations in the range of 5 °C to 45 °C [38]. In addition, the pixel-wise calibrations were performed in situ, further reducing measurement uncertainties. Following the procedure described in Ref. [39], the relative uncertainty of adiabatic cooling film effectiveness (AFE) was estimated to be ± 4.56% when $\eta = 0.1$; the value decreases to ± 1.8% when η increases to 0.8.

3 Results and Discussion

3.1 Testing Conditions. The operating conditions in this study were chosen to match the coolant flow rates between transpiration cooling and prior effusion cooling studies under typical engine conditions with Blowing Ratios (BR) at 0.6, 1.0, and 1.4 [31]. BR, a nondimensional parameter, is commonly used for effusion cooling studies and is defined as follows:

$$BR = \frac{\rho_c u_c}{\rho_m u_m} \tag{8}$$

where u_c and u_m represent velocities of effusion cooling jets and mainstream flow. In turn, u_c can be calculated from coolant volumetric flowrate $\dot{Q}_C$, active area A_{active} (shown in Fig. 3) and surface porosity of the test coupon $\varepsilon_{surface}$

$$u_c = \frac{\dot{Q}_c}{A_{active} * \varepsilon_{surface}} \tag{9}$$

However, a different nondimensional parameter, injection ratio F, is introduced for describing transpiration cooling due to the fact that transpiration cooling could have a surface porosity two orders of magnitude higher than that of typical effusion cooling. F is defined as follows:

$$F = \frac{\dot{m}_c}{\rho_m u_m A_{active}} \tag{10}$$

In this study, we matched the active area A_{active} (66 mm × 71 mm) with the previous effusion/transpiration cooling comparison study [31]. As mentioned earlier in the Subsection, the injection ratios F were determined by matching coolant flow rates to baseline effusion cooling cases at BRs of 0.6, 1.0, and 1.4 with the same A_{active}, respectively. In addition, the main flow velocity (u_m) was maintained and compared to the previous study [31]. Table 2 summarizes test conditions in comparison with corresponding effusion cooling studies.

3.2 Flow Characteristics Through Triply Periodic Minimal Surface Lattices. The Percentage pressure drop (ΔP) is defined as the ratio of pressure drop across the transpiration cooling test coupons and the upstream static pressure in the reservoir ($P_{reservoir}$) using the following equation:

Table 2 Testing conditions

Main flow velocity (m/s)		33	
Blowing ratio of the corresponding effusion cooling case	0.6	1.0	1.4
Coolant velocity exiting transpiration cooling coupon surface (m/s)	0.47	0.78	1.10
Injection ratio (%)	0.68	1.14	1.60
Coolant mass flow rate (g/s)	1.32	2.16	3.00

$$\Delta P = \frac{P_{\text{reservoir}} - P_{\text{testsection}}}{P_{\text{reservoir}}} * 100 \tag{11}$$

where the pressure drop is the pressure difference between two static pressures upstream and downstream to the test coupons. The upstream static pressure $P_{reservoir}$ is measured through a static pressure tap attached to the bottom of the reservoir, whereas the downstream static pressure $P_{testsection}$ is measure through the static pressure port of a Pitot tube. Both pressure port locations are indicated in Fig. 5.

The ΔP values for all three TPMS types as summarized in Fig. 6. The general trend is that pressure drop increases as coolant flowrate increases, however, it should be pointed out that the type of TPMS structure plays a more dominate role in controlling pressure drops.

In this case, the gyroid structure exhibits low ΔP. However, a pressure drop too low could pose potential challenges in supplying coolant uniformly over a large transpiration cooling surface in practical applications and it can lead to diminished film cooling effectiveness.

In comparison, the Koch type of TPMS has the highest ΔP, resulting in a reasonable pressure drop that's favorable for a more uniform coolant distribution. At the same time, the Koch type of TPMS was found to have the highest film cooling effectiveness of all three TPMS types investigated at all coolant flow rates considered in this study. The film cooling effectiveness of each coupon is discussed in detail in the corresponding subsection.

The Reynolds number for flow internal to TPMS lattices, Re_{TPMS}, can be evaluated using the following definition [40]:

$$\text{Re}_{\text{TPMS}} = (\rho_c u_c d_h)/\mu_c \tag{12}$$

where d_h and μ_c represent hydraulic diameter and viscosity of coolant, respectively. The hydraulic diameter d_h can be calculated with the volume of the lattice structure V and corresponding wetted surface area A_w using $d_h = 4V/A_w$. The wetted surface area for diamond, Koch, and gyroid types used in this study are determined to be 3.26, 5.26, and 2.94 times of the corresponding surface area A_{active}, respectively. Studies on flows internal to TPMS lattices show that the transition to turbulence begins at $Re_{TPMS} \approx 150$ [41]. The calculated Re_{TPMS} values across the types and operating conditions are significantly lower than critical value of Re_{TPMS} as summarized in Table 3.

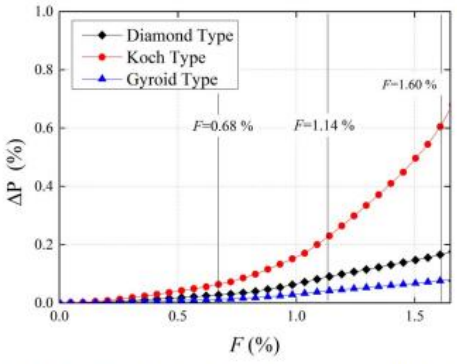

Fig. 6 Percentage pressure drop across transpiration test coupons as a function of injection ratio F. Veritival lines indicate the injection ratios used in the current study.

3.3 Surface Geometry Highly Sensitive to Orientation. This study found the top surface of diamond type of TPMS lattice structure is highly sensitive to orientation angles. Three orientation angles, the angle between main flow and the primary direction of the surface voids, were evaluated: parallel (0°), diagonal (45°), and perpendicular (90°). 2D distributions of adiabatic film cooling effectiveness of all three orientations that were measured at three coolant flow rates are presented and compared in Fig. 7, with subpanels (*a*) corresponding to $F = 0.68\%$, (*b*) $F = 1.14\%$, and (*c*) $F = 1.60\%$. In Fig. 7, the adiabatic film cooling effectiveness, denoted as η_{ad}, distributions are represented by 2D color maps, with red representing zero effectiveness and blue fully efficient cooling film.

Additionally, the overall averaged film cooling effectiveness, denoted as $\bar{\eta}$, is also evaluated. Although the PSP was applied to the entire surfaces of the TPMS lattices, the trough areas were expected to be largely covered by coolant and would skew film cooling effectiveness comparisons, therefore the voids were excluded from AFE evaluations so that only the exposed top surfaces were compared. The exclusion of the voids was achieved by filtering the measured AFE 2D maps with the mathematical expressions of the top surface contour of a TPMS lattice, as shown in Fig. 4. For example, white areas in Fig. 7 indicate voids that are excluded from 2D AFE distributions.

Film cooling effectiveness was calculated and was represented in the figure for the top surface areas only. A consistent pattern was observed: the orientation that features surface voids perpendicular to the main flow consistently demonstrates the highest film cooling effectiveness. However, the lowest film cooling effectiveness was observed when the surface voids are parallel to the main flow direction. The observed difference may be explained by the way that coolant exits from the TPMS lattice while interacting with the surface textures. The mean velocity of the coolant exiting the TPMS

Table 3 Summary of test coupon specifications and flow characteristics

Test coupon specifications								
Type	Diamond			Koch		Gyroid		
Orientation angle	0	45	90	0	90	0	90	
Volumetric porosity (%)	50							
Surface porosity (%)	50							
Internal wetted area (mm^2)	$3.26 \times A_{active}$			$5.26 \times A_{active}$		$2.94 \times A_{active}$		
Tortuosity	0			1.10		0.17		
Internal Flow Characteristic								
Type	Diamond			Koch		Gyroid		
Re_{TPMS} at $F = 0.68\%$	17.42			10.80		20.29		
Re_{TPMS} at $F = 1.14\%$	28.92			17.00		33.67		
Re_{TPMS} at $F = 1.60\%$	40.78			25.28		47.48		

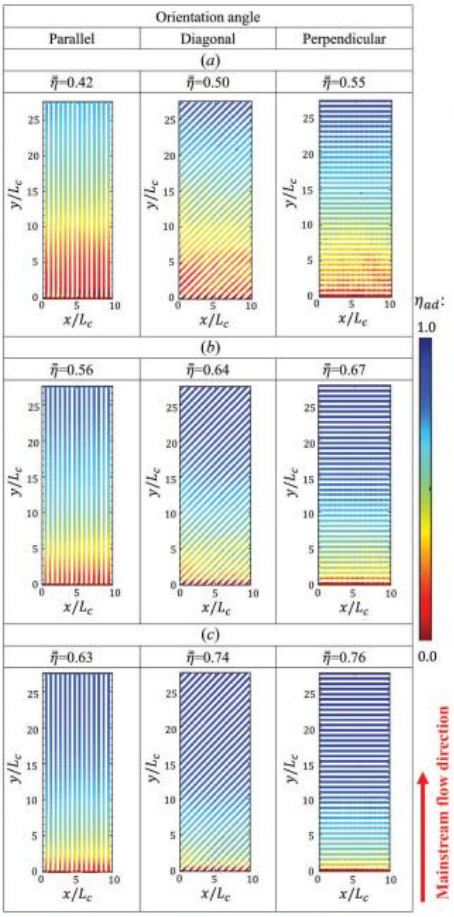

Fig. 7 2D distribution of film cooling effectiveness of the diamond type at varying orientation angles and injection ratios: (*a*) $F = 0.68\%$, (*b*) $F = 1.14\%$, and (*c*) $F = 1.60\%$. Red arrows indicate the mainstream flow direction.

lattice surface was 0.47 m/s at $F = 0.68\%$, $F = 1.14\%$, and $F = 1.60\%$, respectively. For such low coolant flow velocities, the coolant doesn't have enough momentum to experience the liftoff as effusion cooling jets do. Consequently, the transpiration cooling flow emerging from the top surface of the porous media may be characterized by low Reynolds number. In addition, unlike stochastic porous media such as metal foams, TPMS lattice structures are featured with highly patterned surface textures. The low Reynolds number coolant flow immediately interacts with the patterned surface textures after exiting the TPMS surface. For the case of diamond type of TPMS lattice investigated in this work, the surface troughs recess from the top surface by 0.08 mm. Although the amplitude of surface recessions was small, the low momentum coolant flow responds to the surface textures. Specifically, it is observed that the coolant flow was confined in the miniature troughs on the surfaces of diamond type TPMS lattices. When the orientation of the surface troughs (or surface voids) is parallel to the direction of the main flow, the troughs act as channels for discharging coolant downstream while sheltering the coolant from leaving the channels. The confinement is nonideal from the perspective of developing cooling film, as the surface troughs that are parallel to the main flows delays the development of cooling films by channeling the coolant to further downstream locations, as can be seen from the comparisons in Fig. 7. In contrast, surface troughs that are perpendicular to the main flow direction promote the formation of cooling films. Once the coolant is being discharged from the diamond type of TPMS lattices at the bottom of the troughs (refer to the unit cell model in Fig. 2), the coolant can flow downstream only by climbing out from the troughs and get to the top surface of the lattice, leading to efficient use of coolant in forming uniform cooling films. The increases in $\bar{\eta}$ (overall averaged film cooling effectiveness) from the Parallel troughs to Perpendicular ones are 0.09, 0.11, and 0.13 at $F = 0.68\%$, $F = 1.14\%$, and $F = 1.60\%$, respectively, where $\bar{\eta}_{avg}$ indicates the mean film cooling effectiveness for the entire observation area.

The diagonal orientation of the surface troughs with the main flow direction shows film cooling effectiveness between the parallel and perpendicular cases discussed above. It should be noted that the diagonal orientation of the surface troughs has overall performances close to those of the perpendicular trough orientation, which is a little surprising. A potential explanation is that although the diagonally orientated troughs provide paths for coolant to flow downstream, the diagonal orientation of the troughs also makes the effective slopes of the trough walls gentler, making it easier for the coolant to climb out the troughs to produce cooling films. Figure 8 shows the comparisons of film cooling effectiveness of three orientations of the diamond structures that are averaged in the spanwise direction. The spanwise mean is achieved by averaging film cooling effectiveness values derived from a row of pixels in a direction that is perpendicular to the main flow. The comparisons indicate that the differences among three orientations are most pronounced at the leading edge where the cooling film is initiated. The initial cooling film development was inhibited by parallel troughs that channel coolant away to downstream locations without promoting the formation of a cooling film.

3.4 Surface Geometry With Least Sensitivity to Orientation. The surface geometry of the Koch type of TPMS lattice demonstrated less sensitivity to orientation variations. Figure 9 shows comparisons of the film cooling effectiveness of the Koch type of TPMS when the surface voids are primarily parallel and perpendicular to the main flow direction.

Comparing to the diamond geometry, it is obvious that the surface geometry of the Koch type of TPMS demonstrates less sensitivity to orientation variations. This reduced sensitivity to surface orientation can be attributed to the meandering pattern of surface troughs. The sharp twists and turns of large tortuosity inhibit the coolant from being channeled downstream in the troughs regardless of the orientation of the troughs. Therefore, the coolant was forced to climb out from the trough. The numerous twists and directional changes within the troughs create several points where coolant is retained. Consequently, this obstruction compels the coolant to climb out from the troughs. Moreover, the pronounced tortuosity facilitates the uniform distribution of the coolant over an extended distance as it exits the troughs. This uniform distribution results from the restricted downstream movement of the coolant. Additionally, this retention reduces momentum, enabling the coolant to accumulate more efficiently on the surface without lifting. Consequently, the surface texture of the Koch type of TPMS hinders the dissipation of coolant due to mixing with the mainstream flow, leading to higher film cooling effectiveness values. This is particularly noticeable as the coolant flowrate increases, where at $F = 1.60\%$ in the parallel orientation, the Koch type shows a 0.09 increase in film cooling effectiveness averaged over the entire observation area ($\bar{\eta}$)

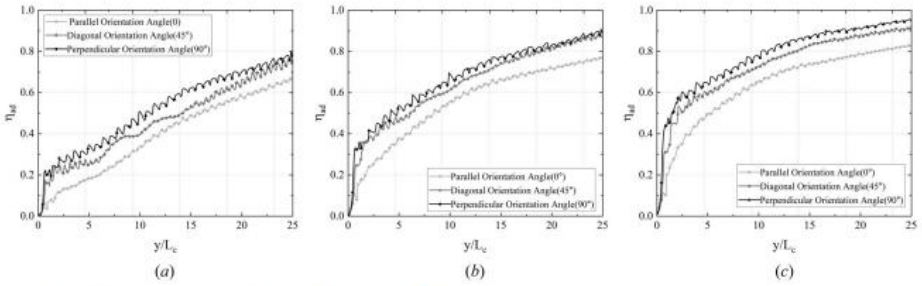

Fig. 8 Spanwise averaged film cooling effectiveness of the diamond type at varying orientation angles and injection ratios: (*a*) $F = 0.68\%$, (*b*) $F = 1.14\%$, and (*c*) $F = 1.60\%$

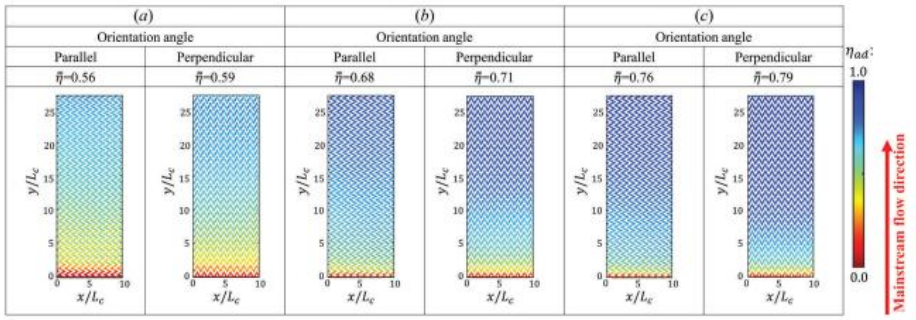

Fig. 9 Two-dimensional distribution of film cooling effectiveness of the Koch type at varying orientation angles and injection ratios: (*a*) $F = 0.68\%$, (*b*) $F = 1.14\%$, and (*c*) $F = 1.60\%$. Red arrows indicate the mainstream flow direction.

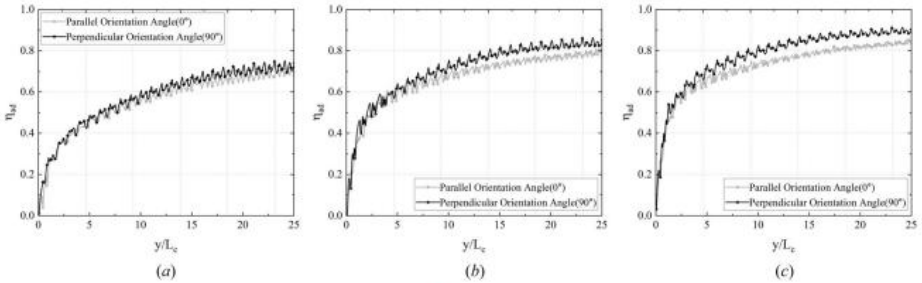

Fig. 10 Spanwise averaged film cooling effectiveness of the Koch type at varying orientation angles and injection ratios: (*a*) $F = 0.68\%$, (*b*) $F = 1.14\%$, and (*c*) $F = 1.60\%$

comparing to the diamond type (in parallel orientation). The comparisons of mean film cooling effectiveness along the spanwise direction shown in Fig. 10 confirm the insensitivity of the Koch type of TPMS surface texture to surface orientation.

3.5 Surface Geometry With Mixed Sensitivity to Orientation. Lastly, the cooling effectiveness of the gyroid type of TPMS of parallel and perpendicular orientations was evaluated and compared. The 2D distributions of cooling effectiveness are presented in Fig. 11 while the comparison of film cooling effectiveness averaged along the spanwise direction are shown in Fig. 12. The gyroid type of TPMS shows a mixed sensitivity to surface orientation, situated between those of the diamond and Koch types. The difference in $\bar{\eta}$ between the parallel and perpendicular orientations at $F = 0.68\%$, $F = 1.14\%$, and $F = 1.60\%$ were found to be 0.07, 0.09, and 0.09, respectively.

3.6 Orientation Sensitivity as a Function of Surface Tortuosity. Orientation sensitivity (OS) is defined using the difference in overall film effectiveness in two orthogonal orientations (perpendicular and parallel) as following equation:

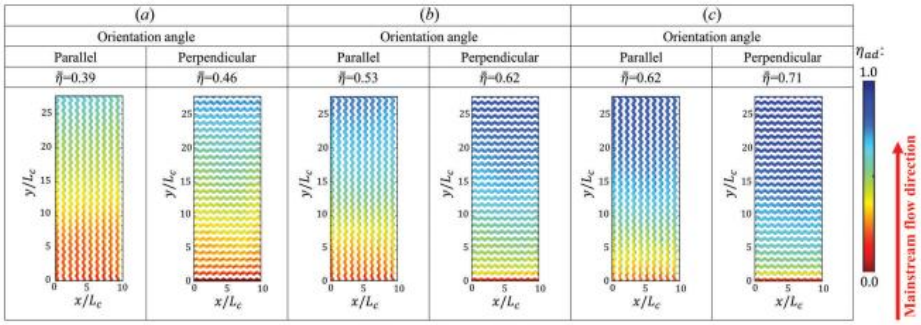

Fig. 11 Two-dimensional distribution of film cooling effectiveness of the gyroid type at varying orientation angles and injection ratios: (*a*) $F = 0.68\%$, (*b*) $F = 1.14\%$, and (*c*) $F = 1.60\%$. Red arrows indicate the mainstream flow direction.

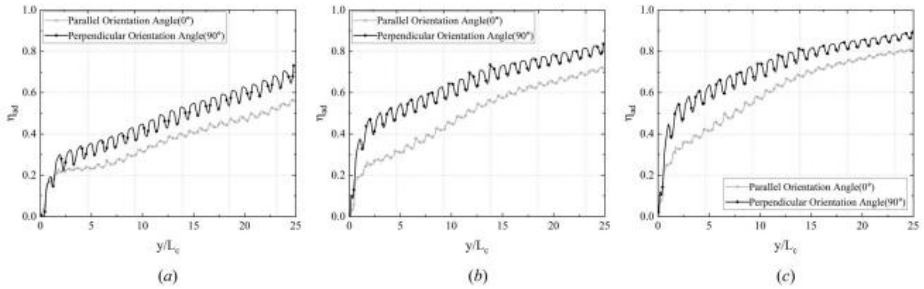

Fig. 12 Spanwise averaged film cooling effectiveness of the gyroid type at varying orientation angles and inection ratios: (*a*) $F = 0.68\%$, (*b*) $F = 1.14\%$, and (*c*) $F = 1.60\%$

$$OS = \frac{\bar{\eta}_{\text{perpendicular}} - \bar{\eta}_{\text{parallel}}}{\bar{\eta}_{\text{perpendicular}}} * 100 \qquad (13)$$

In this equation, $\bar{\eta}_{\text{perpendicular}}$ represents the mean film cooling effectiveness over the observation area when the TPMS lattice is in the optimal perpendicular orientation. Conversely, $\bar{\eta}_{\text{parallel}}$ denotes the mean film cooling effectiveness of the same TPMS lattice in the parallel orientation. Orientation sensitivity reveals the degree to which the orientation of TPMS lattice's surface textures impacts cooling film effectiveness. Figure 13 illustrates the correlations between surface tortuosity and orientation sensitivity for all three TPMS types investigated in this study at three injection ratios. It is observed that the orientation sensitivity almost linearly decreases with increasing surface tortuosity for all coolant flow rates. However, the directional sensitivity is more pronounced at lower coolant flow rates. While overall film cooling effectiveness increases with increasing coolant flow rates, a smaller portion of coolant could be channeled downstream by surface troughs parallel to the main flow, leading to diminished orientation sensitivity at higher flow rates [42]. The orientation sensitivity of the diamond type of TPMS at flowrate of $F = 0.68\%$ appears to be an outlier, which may be explained by the significant delay to cooling film development due to surface troughs that are parallel to the main flow direction. At this smallest coolant flowrate, a relatively large portion of coolant is being channeled downstream by these parallel surface troughs; the delay in cooling film is more pronounced for the smallest coolant flowrate as it does not allow a cooling film to be fully developed within the observation area.

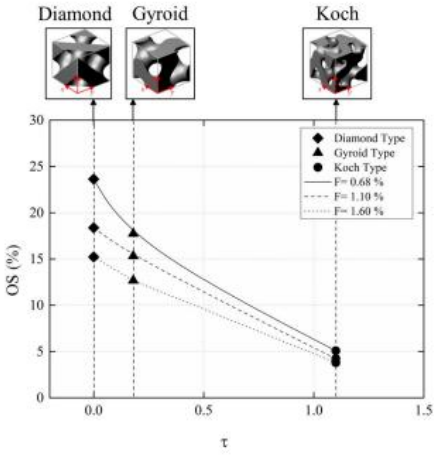

Fig. 13 Orientation sensitivity as a function of surface tortuosity

Table 4 Overall averaged adiabatic film cooling effectiveness

Type	Orientation angle	$\bar{\eta}$ $F=0.68\%$	$F=1.14\%$	$F=1.60\%$
Diamond	Parallel	0.42	0.56	0.63
	Perpendicular	0.55	0.67	0.76
Koch	Parallel	0.56	0.68	0.76
	Perpendicular	0.59	0.71	0.79
Gyroid	Parallel	0.39	0.53	0.62
	Perpendicular	0.46	0.62	0.71

3.7 Pressure Drop Effects on Overall Cooling Film Effectiveness. Table 4 summarizes overall adiabatic film cooling effectiveness ($\bar{\eta}$) values for all test configurations at various injection ratios, where the overall adiabatic film cooling effectiveness is computed by averaging local adiabatic film cooling effectiveness over the entire measurement area. The comparisons between the diamond type and the Koch type indicate that the overall cooling film effectiveness is comparable at all injection ratios when the diamond type is in its optimal orientation (perpendicular), despite the large discrepancy in pressure drops (refer to Fig. 6). However, when the diamond is compared to the gyroid at both types' optimal orientation (perpendicular), the discrepancy in overall cooling film effectiveness is pronounced, particularly at the lowest injection ratio ($F=0.68\%$).

Although the gyroid type was found to have an orientation sensitivity between the diamond type and the Koch type, one property that separates the gyroid type apart from the other two types is that the gyroid type has the lowest pressure drop while everything else being constant, due to the fact that gyroid type has internal structures allow straight passages for fluid to pass through (see Fig. 2). The pressure drop is related to the complexity of the internal channels, which can be reflected by internal wetted area A_w. Referring to Table 3, the gyroid type has the smallest internal wetted area A_w (2.94 times of surface area A_{active}) among the three TPMS types investigated in this study while it has the lowest ΔP value. Meanwhile, the Koch type with the most complex internal channels, as shown in Fig. 2, has the largest internal wetted area ($5.26\,A_{active}$), resulting in the highest ΔP value.

At the lowest injection ratio of ($F=0.68\%$), the percentage pressure drop across the test coupon was measured to be only 0.03%, 0.07, and 0.01% for the diamond, Koch, and gyroid types, respectively. At such low percentage pressure drops, the coolant distribution is very susceptible to the pressure distribution on the surface of the transpiration cooling coupon. In addition, early studies [12,43] suggest that coolant could flow laterally inside the lattice structures of low flow resistance. This internal coolant flow from the leading edge to the trailing edge side deprives the leading edge of much needed coolant supply, causing the delay in the development of cooling films. At higher injection ratios, the discrepancy in overall cooling film effectiveness between gyroid and Dimond types diminishes when both in the perpendicular orientation. Similarly, when the pressure drop is adequately to ensure a uniform cooling flow distribution and to inhibit internal lateral flow, the difference among TPMS types becomes insignificant in terms of optimal cooling film effectiveness, the comparison between the Koch type and the diamond type (in perpendicular orientation) as an example.

4 Results and Discussion

Three TPMS lattice geometries, namely, diamond, Koch, and gyroid, were experimentally investigated to understand the impact of the orientation and surface tortuosity on transpiration film cooling effectiveness. In general, surface troughs that are perpendicular to the main flow direction led to improved film cooling effectiveness compared to the parallel ones: The latter make poor utilization of coolant by confining the coolant inside troughs and subsequently channeling it downstream without promptly developing a cooling film. In contrast, coolant is less channeled downstream by surface troughs that are perpendicular to the main flow direction; instead, the coolant in the perpendicular troughs is driven out of the troughs and promptly forms a cooling film on the top surface.

Furthermore, the tortuosity of the troughs on the top surface of TPMS lattices was found to impact not only the overall film cooling effectiveness but also the orientation sensitivity of surface textures. As the tortuosity increases, a more uniform distribution of the coolant film is achieved regardless of the orientation of surface troughs, leading to reduced sensitivity to the orientation of the surface troughs relative to the main flow. For the test coupon of the diamond type of TPMS with zero tortuosity on the top surface, the orientation sensitivities at $F=0.68\%$, $F=1.14\%$, and $F=1.60\%$ were found to be 24%, 17%, and 15% , respectively. For the test coupon of the Koch type of TPMS with the highest tortuosity of 1.39, the orientation sensitivities at $F=0.68\%$, $F=1.14\%$, and $F=1.60\%$ were determined to be 5%, 4%, and 3% , respectively. The test coupon of the gyroid type of TPMS with a moderate tortuosity of 0.26 demonstrated less pronounced orientation sensitivities of 17%, 14%, and 12% respectively at $F=0.68\%$, $F=1.14\%$, and $F=1.60\%$.

It should be highlighted that a TPMS lattice type can exhibit the desirable low orientation sensitivity, however, it does not guarantee that the type of TPMS lattice also possesses a superior cooling film effectiveness. For instance, the diamond type overperforms the gyroid type in terms of cooling film effectiveness when the both types are at the optimal orientation, whereas the diamond type has higher orientation sensitivity. The observation can be rationalized that the orientation sensitivity of a TPMS type is primarily controlled by its surface textures. However, the overall cooling film effectiveness can be compounded by factors other than surface textures, for example, a less-ideal cooling flow distribution could impair the overall cooling film effectiveness, as in the case of gyroid type of TPMS under a low injection ratio. When the cooling flow can pass through the transpiration cooling at a low pressure drop, the distribution of cooling flow is susceptible to small pressure disturbances external to the lattice on both the hot side or the cold side. Therefore, a sizable percentage pressure-drop (on order of 1%) across the transpiration cooled liner is beneficial and should be maintained.

Of all three TPMS lattice types investigated by the current study, the Koch type was found to have minimal orientation sensitivity while maintaining the highest overall film cooling effectiveness. This makes the Koch type of TPMS geometry ideal for transpiration cooling on complex geometry surfaces exposed to highly directional flows.

Acknowledgment

The work was supported by the National Research Council of Canada (NRC)'s National Program Office under a Postdoctoral Fellowship Program grant (PDF2024-TM-AF). NRC Aerospace Research Centre's Low-Emission Aviation Program also sponsored the work under project A1-024514.

Funding Data

- National Research Council Canada (Award No. PDF2024-TM-AF; Funder ID: 10.13039/501100000046).

Data Availability Statement

The authors attest that all data for this study are included in the paper.

Nomenclature

A_{active} = active area (mm^2)
A_w = internal wetted area (mm^2)

A = first order coefficient of the polynomial fitting curve
B = second order coefficient of the polynomial fitting curve
C = third order coefficient of the polynomial fitting curve
CO = oxygen concentration
c = TPMS level set constant
d_h = the hydraulic diameter of TPMS (mm)
F = injection ratio (%)
I = intensity of PSP
L_C = unit cell length (mm)
P = pressure (Pa)
r = intensity ratio for binary PSP
T = temperature (K)

Greek Symbols

α = unit cell constant for x direction
β = unit cell constant for y direction
γ = unit cell constant for z direction
ε = porosity (%)
η = film cooling effectiveness
θ = rotation of angle
τ = tortuosity
$\varnothing$ = level-set equation

Subscripts

ad = adiabatic
c = coolant
dark = dark condition
m = mainstream
ref = reference

Acronyms

TPMS = triple periodic minimal surface
PSP = pressure sensitive paint
SLA = stereolithography
SLPM = standard liter per minute
AFE = adiabatic cooling film effectiveness
BR = blowing ratio

References

[1] Badran, O. O., 1999, "Gas-Turbine Performance Improvements," Appl. Energy, **64**(1–4), pp. 263–273.
[2] Caron, P., and Khan, T., 1999, "Evolution of Ni-Based Superalloys for Single Crystal Gas Turbine Blade Applications," Aerosp. Sci. Technol., **3**(8), pp. 513–523.
[3] Ligrani, P., 2013, "Heat Transfer Augmentation Technologies for Internal Cooling of Turbine Components of Gas Turbine Engines," Int. J. Rotating Mach., **2013**, pp. 1–32.
[4] Andrews, G. E., Alikhanizadeh, M., Tehrani, F. B., Hussain, C. I., and Azari, M. S. K., 1988, "Small Diameter Film Cooling Holes: The Influence of Hole Size and Pitch," Int. J. Turbo Jet Engines, **5**, pp. 61–73.
[5] Cerri, G., Giovannelli, A., Battisti, L., and Fedrizzi, R., 2007, "Advances in Effusive Cooling Techniques of Gas Turbines," Appl. Therm. Eng., **27**(4), pp. 692–698.
[6] Zhou, J., Wang, X., and Li, J., 2019, "Influences of Effusion Hole Diameter on Impingement/Effusion Cooling Performance at Turbine Blade Leading Edge," Int. J. Heat Mass Transf., **134**, pp. 1101–1118.
[7] Wei, H., Ai, J. L., Zu, Y. Q., and Ding, L., 2019, "Heat Transfer Characteristics of Fan-Shaped Hole Effusion Cooling for a Constant Hole Exit Width – Numerical Simulation and Experimental Validation," Appl. Therm. Eng., **160**(2019), p. 113978.
[8] Yang, L., Dai, W., Rao, Y., and Chyu, M. K., 2019, "Optimization of the Hole Distribution of an Effusively Cooled Surface Facing Non-Uniform Incoming Temperature Using Deep Learning Approaches," Int. J. Heat Mass Transf., **145**(2019), p. 118749.
[9] Andreini, A., Becchi, R., Facchini, B., Picchi, A., and Peschiulli, A., 2017, "The Effect of Effusion Holes Inclination Angle on the Adiabatic Film Cooling Effectiveness in a Three-Sector Gas Turbine Combustor Rig With a Realistic Swirling Flow," Int. J. Therm. Sci., **121**, pp. 75–88.
[10] Cho, H. H., Rhee, D. H., and Goldstein, R. J., 2008, "Effects of Hole Arrangements on Local Heat/Mass Transfer for Impingement/Effusion Cooling With Small Hole Spacing," ASME J. Turbomach., **130**(4), p. 041003.
[11] Paitich, L. C., Richer, P., Jodoin, B., Pyo, Y., Yun, S., and Hong, Z., 2021, "Directional Effects of Effusion Cooling on the Cooling Film Effectiveness," AIAA J., **60**(1), pp. 1–11.
[12] Hinse, M., Richer, P., Jodoin, B., Yildiz, K., Yun, S., and Hong, Z., 2020, "Numerical and Experimental Studies of Transpiration Cooling Film Effectiveness Over Porous Materials," J. Thermophys. Heat Transf., **36**(4), pp. 803–817.
[13] Eckert, E. R. G., and Livingood, J. N. B., 1953, "Comparison of Effectiveness of Convection, Transpiration, and Film Cooling Methods With Air as Coolant," National Advisory Committee for Aeronautics Technical Note, p. 3010, Report No. NACA-TR-1182.
[14] Curry, D., Gomez, A., and Johnston, C., 1971, "Radiative, Ablative and Active Cooling Thermal Protection Studies for the Leading Edge of a Fixed-Straight Wing Space Shuttle," AIAA Paper No. 1971-445.
[15] Weinbaum, S., and Wheeler, H. L., 1949, "Heat Transfer in Sweat-Cooled Porous Metals," J. Appl. Phys., **20**(1), pp. 113–122.
[16] Krittacom, B., Amatachaya, P., and Sangchot, R., 2014, "Energy Balance in Al-Co Open-Celled Foam of Transpiration Cooling," *Applied Mechanics and Materials*, **575**(2014), pp. 41–45.
[17] Ma, J., Luo, X., Li, H., and Liu, Y., 2016, "An Experimental Investigation on Transpiration Cooling Based on the Multilaminated Sintered Woven Wire Mesh Structures," ASME J. Therm. Sci. Eng. Appl., **8**(3), p. 031005.
[18] Huang, G., Liao, Z., Xu, R., Zhu, Y., and Jiang, P. X., 2020, "Self-Pumping Transpiration Cooling With a Protective Porous Armor," Appl. Therm. Eng., **164**(2020), p. 114485.
[19] McDonough, J. R., 2020, "A Perspective on the Current and Future Roles of Additive Manufacturing in Process Engineering, With an Emphasis on Heat Transfer," Therm. Sci. Eng. Prog., **19**, p. 100594.
[20] Ngo, T. D., Kashani, A., Imbalzano, G., Nguyen, K. T. Q., and Hui, D., 2018, "Additive Manufacturing (3D Printing): A Review of Materials, Methods, Applications and Challenges," Compos. B Eng., **143**, pp. 172–196.
[21] Kim, M., Shin, D. H., Kim, J. S., Lee, B. J., and Lee, J., 2021, "Experimental Investigation of Effusion and Transpiration Air Cooling for Single Turbine Blade," Appl. Therm. Eng., **182**(2021), p. 116156.
[22] Huang, G., Min, Z., Yang, L., Jiang, P. X., and Chyu, M., 2018, "Transpiration Cooling for Additive Manufactured Porous Plates With Partition Walls," Int. J. Heat Mass Transf., **124**, pp. 1076–1087.
[23] Min, Z., Huang, G., Parbat, S. N., Yang, L., and Chyu, M. K., 2019, "Experimental Investigation on Additively Manufactured Transpiration and Film Cooling Structures," ASME J. Turbomach., **141**(3), p. 031009.
[24] Al-Ketan, O., and Abu Al-Rub, R. K., 2019, "Multifunctional Mechanical Metamaterials Based on Triply Periodic Minimal Surface Lattices," Adv. Eng. Mater., **21**(10), p. 1900524.
[25] Qureshi, Z. A., Elnajjar, E., Al-Ketan, O., Al-Rub, R. A., and Al-Omari, S. B., 2021, "Heat Transfer Performance of a Finned Metal Foam-Phase Change Material (FMF- PCM) System Incorporating Triply Periodic Minimal Surfaces (TPMS)," Int. J. Heat Mass Transf., **170**(2021), p. 121001.
[26] Hussain, I., Al-Ketan, O., Renda, F., Malvezzi, M., Prattichizzo, D., Seneviratne, L., Abu Al-Rub, R. K., and Gan, D., 2020, "Design and Prototyping Soft–Rigid Tendon-Driven Modular Grippers Using Interpenetrating Phase Composites Materials," Int. J. Rob. Res., **39**(14), pp. 1635–1646.
[27] Maskery, I., Sturm, L., Aremu, A. O., Panesar, A., Williams, C. B., Tuck, C. J., Wildman, R. D., Ashcroft, A., and Hague, R. J. M., 2018, "Insights Into the Mechanical Properties of Several Triply Periodic Minimal Surface Lattice Structures Made by Polymer Additive Manufacturing," Polymer, **152**, pp. 62–71.
[28] Han, C., Li, Y., Wang, Q., Wen, S., Wei, Q., Yan, C., Hao, L., Liu, J., and Shi, Y., 2018, "Continuous Functionally Graded Porous Titanium Scaffolds Manufactured by Selective Laser Melting for Bone Implants," J. Mech. Behav. Biomed. Mater., **80**, pp. 119–127.
[29] Femmer, T., Kuehne, A. J. C., and Wessling, M., 2015, "Estimation of the Structure Dependent Performance of 3-D Rapid Prototyped Membranes," Chem. Eng. J., **273**, pp. 438–445.
[30] Li, W., Li, W., and Yu, Z., 2022, "Heat Transfer Enhancement of Water-Cooled Triply Periodic Minimal Surface Heat Exchangers," Appl. Therm. Eng., **217**, p. 119198.
[31] Broumand, M., Son, J., Pyo, Y., Yun, S., and Hong, Z., 2024, "TPMS-Based Transpiration Cooling for Film Cooling Enhancement," Int. J. Heat Mass Transf., **231**, p. 125824.
[32] Fu, J., Thomas, H. R., and Li, C., 2021, "Tortuosity of Porous Media: Image Analysis and Physical Simulation," Earth Sci. Rev., **212**, p. 103439.
[33] Grisan, E., Foracchia, M., and Ruggeri, A., 2003, "A Novel Method for the Automatic Evaluation of Retinal Vessel Tortuosity," Proceedings of the 25th Annual International Conference of the IEEE Engineering in Medicine and Biology Society, Vol. 1, Cancun, Mexico, Sept. 17–21, pp. 866–869.
[34] Formlabs, 2023, "Formlabs Material Library, Everything You Need to Start Printing," Formlabs, Somerville, MA, accessed Dec. 16, 2023, https://formlabs-media.formlabs.com/filer_public/ac/89/ac8963db-f54a-4cac-8fe9-fb740a7b06f1/formlabs-materials-library.pdf
[35] Lei, Z., Mahallati, A., Cunningham, M., and Germain, P., 2010, "Influence of Inlet Swirl on the Aerodynamics of a Model Turbofan Lobed Mixer," ASME Paper No. IMECE2010-39116.
[36] Liu, T., Sullivan, J. P., Asai, K., Klein, C., and Egami, Y., 2005, *Pressure and Temperature Sensitive Paints*, Springer, Berlin.
[37] Sajben, M., 1993, "Uncertainty Estimates for Pressure Sensitive Paint Measurements," AIAA J., **31**(11), pp. 2105–2110.
[38] Barigozzi, G., Mucignat, C., Abdeh, H., Scandella, D., and Dolci, G., 2018, "Assessment of Binary PSP Technique for Film Cooling Effectiveness

Measurement on Nozzle Vane Cascade With Cutback Trailing Edge," Exp. Therm. Fluid Sci., **97**, pp. 431–443.
[39] Natsui, G., Little, Z., Kapat, J. S., Dees, J. E., and Laskowski, G., 2016, "A Detailed Uncertainty Analysis of Adiabatic Film Cooling Effectiveness Measurements Using Pressure-Sensitive Paint," ASME J. Turbomach., **138**(8), p. 081007.
[40] Iyer, J., Moore, T., Nguyen, D., Roy, P., and Stolaroff, J., 2022, "Heat Transfer and Pressure Drop Characteristics of Heat Exchangers Based on Triply Periodic Minimal and Periodic Nodal Surfaces," Appl. Therm. Eng., **209**, p. 118192.
[41] Reynolds, B. W., Fee, C. J., Morison, K. R., and Holland, D. J., 2023, "Characterisation of Heat Transfer Within 3D Printed TPMS Heat Exchangers," Int. J. Heat Mass Transf., **212**, p. 124264.
[42] Xu, G., Liu, Y., Luo, X., Ma, J., and Li, H., 2015, "Experimental Investigation of Transpiration Cooling for Sintered Woven Wire Mesh Structures," Int. J. Heat Mass Transf., **91**, pp. 898–907.
[43] Zhou, Z., Lv, Y., He, F., Liu, T., and Wang, J., 2024, "Pore-Scale Investigation of Transpiration Cooling Based on Triply Periodic Minimal Surface," Int. J. Therm. Sci., **201**, p. 109019.

5.4 The Influence of TPMS Morphology on Transpiration Cooling Performance

Despite the promising potential of TPMS-based transpiration cooling, more comprehensive parametric investigations—including factors not addressed in the previous section—are required before this cooling strategy can be considered viable for practical engine applications. This necessity arises from the inherent difficulty of designing ideal TPMS lattice structures that are optimized for complex engine geometries and localized directional flow conditions.

For example, real gas turbine components feature varying surface curvatures, which can induce geometric distortion of the TPMS surface structure when mapped onto curved substrates. Such curvature-induced morphological variations may alter local pore orientation flow pathways, and orientation angle, thereby affecting cooling performance.

In the previous subsection, the effects of TPMS lattice orientation on transpiration cooling performance were examined. Although, in certain limiting cases, morphological variation may manifest as a simple reorientation of surface features, such instances represent special cases. In practical applications, morphological variations—particularly those induced by surface curvature in hot-gas path components—can alter lattice topology and flow pathways in a more complex manner.

The objective of the present study is to evaluate the influence of curvature-induced morphological variations on the transpiration-cooling performance of three representative TPMS lattice types—Diamond, Gyroid, and Koch—and to identify the morphology that provides the highest cooling performance with the lowest sensitivity to morphological variations. The study aims to establish design guidelines for selecting TPMS lattice configurations suitable for complex gas turbine components. To achieve these objectives, a combined experimental and numerical investigation was conducted. Based on this fundamental understanding, the study establishes that the Koch TPMS provides the highest tolerance to curvature-induced morphological variations while maintaining superior cooling effectiveness, making it the preferred lattice configuration for transpiration-cooled gas turbine liners with complex curved surfaces.

Experimental work prepared as a research article and published as a peer-reviewed technical paper in the proceedings of ASME Turbo Expo 2025.

5.4.1 Experimental study

Proceedings of ASME Turbo Expo 2025
Turbomachinery Technical Conference and Exposition
GT2025
June 16-20, 2025, Memphis, Tennessee

GT2025-151422

EFFECT OF MORPHOLOGICAL VARIATIONS IN TPMS LATTICE STRUCTURES ON TRANSPIRATION COOLING

Juchan Son
University of Ottawa,
Ottawa, Canada
National Research
Council of Canada,
Ottawa, Canada

Patrick Richer
University of Ottawa,
Ottawa, Canada

Bertrand Jodoin
University of Ottawa,
Ottawa, Canada

Zekai Hong
National Research
Council of Canada,
Ottawa, Canada
University of Ottawa,
Ottawa, Canada

ABSTRACT

The development of advanced cooling technologies for modern aero engines has become essential to protect critical gas turbine components, such as the combustion chamber, from increasing combustion temperatures and to extend their operational lifespan. Among cooling techniques, transpiration cooling stands out due to its notable merits, including efficient heat exchange on extensive internal surface areas between the porous solid networks and the cooling fluid, as well as the formation of an effective and uniform cooling film on the wall surface without lift-off. However, the performance of transpiration cooling relies on the precise control of pore size to ensure uniform film cooling distribution across the entire surface and to prevent the formation of localized hot spots. Recent advancements in additive manufacturing (AM), commonly known as 3D printing technology, have enabled the fabrication of lattice-based deterministic porous media with precisely controlled pore sizes and distributions. Among the various lattice structures used in transpiration cooling systems, Triply Periodic Minimal Surfaces (TPMS) have drawn significant attention due to their high performance and periodic characteristics, which can be precisely controlled. The potential of transpiration cooling using this family of lattice geometries has been demonstrated in our previous studies. However, optimizing transpiration cooling with TPMS lattice-based porous media in real gas turbine components remains challenging. Complex geometric features of engine components, including surface curvatures and variations in component thickness, lead to morphological variations in surface texture and the orientation of surface void patterns, which can significantly affect the performance of transpiration cooling. Given the geometry complexity of engine hot-gas path components, it is impractical to make location-specific variations to the TPMS lattices to precisely control the resulting surface texture of prescribed pattern and orientation. This study investigates experimentally how film cooling effectiveness is affected by the use of different types of TPMS lattices that expose varying cross-sections of a TPMS lattice as the top surface with changing surface texture pattern and orientation. The goal is to understand how these cross-section variations affect transpiration cooling performance and to identify TPMS geometries that are ideally insensitive to such variations. Three types of TPMS structures, namely Diamond, Koch, and Gyroid, were selected to develop a design principle for choosing TPMS types for transpiration cooling that are least sensitive to variation in surface texture resulting from complex geometries. The Pressure Sensitive Paint (PSP) technique was employed for assessing resulting film cooling effectiveness.

Keywords: Gas Turbine, Film Cooling, Transpiration Cooling, Additive Manufacturing, Triple Periodic Minimal Surface (TPMS)

NOMENCLATURE

A_{active}	Active area [cm^2]
A_w	Wetted surface area [cm^2]
Co_2	Oxygen mass concentration
D_P	The pore diameter of TPMS [mm]
F	Injection ratio [%]
I	PSP fluorescent intensity
L_C	Unit cell length $[mm]$
l	Arc length of a surface void $[mm]$
P	Pressure $[Pa]$
T	Temperature $[K]$
Δz	Distance between top surface to void saddle point $[mm]$

GREEKS

θ	Angle between arc and the mainstream flow
ε	Porosity [%]
η	Film cooling effectiveness

© 2025 by National Research Council of Canada

λ	Wetted surface area to volume ratio [cm^2/ cm^3]
τ	Tortuosity
τ_{eff}	Effective tortuosity
ω	Correcting factor

ACRONYMS

TPMS	Triple Periodic Minimal Surface
PSP	Pressure Sensitive Paint
SLA	Stereolithography
SLPM	Standard Liter Per Minute
AFE	Adiabatic Film Cooling Effectiveness
BR	Blowing Ratio

1. INTRODUCTION

Over the past few decades, the turbine inlet temperature (TIT) of gas turbines has consistently increased to achieve higher overall[1]. However, the gas temperature in the combustion chamber has risen far exceeding the temperature limits of advanced superalloys, such as Inconel (Ni-Cr-Fe) and Hastelloy (Ni-Mo-Fe)[2]. Given the extreme temperatures inside gas turbines hot-gas path, implementing effective thermal protection for critical components, such as combustor liners, is essential to meet performance requirements and extend the life [3].

Transpiration cooling is considered as a promising cooling method to meet ever challenging thermal management demands in developing the next-gen aero-engines, with two main advantages. First, it promotes a phenomenon known as boundary layer heat-blocking[4], by inducing a thickened boundary layer, which modifies the near-wall temperature and velocity gradients. Second, it enables effective cooling through efficient heat transfer between the coolant and the solid networks of the porous media, facilitated by a large wetted surface area[5]. The coolant that is discharged through a porous medium forms a cooling gas layer over the surface of the porous medium, thickening the boundary layer. This alteration of the temperature and velocity profiles near the wall significantly reduces heat transfer from the hot mainstream to the combustor liner[5]. Liu et al.[6] explored the effects of turbulent boundary layers in transpiration cooling using Particle Image Velocimetry (PIV) to acquire velocity field distributions and to visualize the boundary layer. Their findings conclusively demonstrated that a thickened turbulent boundary layer reduced convective heat transfer from the mainstream flow to the liner. In this vein, extensive research work has been conducted on transpiration cooling[5,7]. Weinbaum et al.[8] introduced the concept of transpiration cooling in rocket engines in the 1940s. Subsequently, research on transpiration cooling employing various forms of porous media has been conducted[9–13], including sintered powder[9], woven fiber[10], metal deposition[11], and laser perforation[12]. However, the aforementioned conventional porous media structures present notable drawbacks despite their superior performance, due to manufacturing challenges in precisely controlling pore sizes and distribution[14]. Inconsistencies in pore sizes and distributions can lead to uneven coolant flow and pressure distribution within the porous medium, potentially creating localized hot spots. Furthermore, smaller pore sizes are more vulnerable to clogging from contaminants[15]. This not only undermines the cooling effectiveness but also reduces the components life span[16]. Yang et al. [15] conducted numerical studies on the clogging effect in transpiration cooling systems and found that holes closer to the leading edge are highly susceptible to plugging. Although significant efforts have been made to prevent blockages and precisely control pore size in conventional porous media, it remains a persistent challenge. More recently, advancements in additive manufacturing (AM), commonly known as 3D printing, has enabled the fabrication of precisely controlled, deterministic porous media, expanding its potential for application in transpiration cooling[17]. Kim et al.[18] compared the cooling effectiveness of effusion cooling with that of transpiration cooling using a metal 3D-printed porous surface. Transpiration cooling achieved a nearly uniform coolant film over a broad area and demonstrated higher effectiveness compared to effusion cooling. Min et al.[19] conducted experiments to assess and compare the cooling effectiveness of an effusion cooling design with five transpiration cooling designs fabricated using SLS additive manufacturing. The results demonstrated that the transpiration cooling designs achieved superior cooling effectiveness compared to effusion cooling, which was attributed to the significantly increased wetted area.

Previous research has highlighted the advantages of transpiration cooling with porous media fabricated via 3D printing. Building on these findings, recent efforts have concentrated on optimizing deterministic porous media structures, which provide well-defined internal channels and a fully controlled, uniform pore structure, size, and distribution.

Among various lattice structures, Triply Periodic Minimal Surfaces (TPMS) exhibit superior properties as advanced deterministic porous structures. TPMS geometries were first defined in the 1860s [20]. Their defining characteristic of having zero mean curvature (minimal surface) results in a structure where every point on the surface is stable, effectively distributing fluid flow. Moreover, unlike other porous structures, which are stochastically distributed, TPMS lattices are defined mathematically, allowing for complete control and engineered distribution.

Recently, TPMS structures have attracted significant interest and have been utilized in various applied science fields, including soft robotics[21], medical devices[22], structure weight reductions[23], and heat exchangers/sinks[24,25]. However, their potential application in transpiration cooling is still in its infancy stage. Zhou et al.[26] conducted a pore-scale investigation of TPMS-based transpiration cooling, demonstrating that the shape and size of the throats of internal passages of the lattices play a crucial role in determining coolant flow resistance and cooling effectiveness. Broumand et al.[27] investigated 3D-printed TPMS lattice-based structures with varying porosity for transpiration cooling. Their results demonstrated significantly superior cooling effectiveness compared to the conventional baseline effusion cooling design, achieving a fivefold increase in film cooling effectiveness. The authors examined the impact of the orientation of TPMS lattice's texture on the top surface on transpiration cooling among three TPMS types. Their findings revealed that a surface void pattern

 © 2025 by National Research Council of Canada

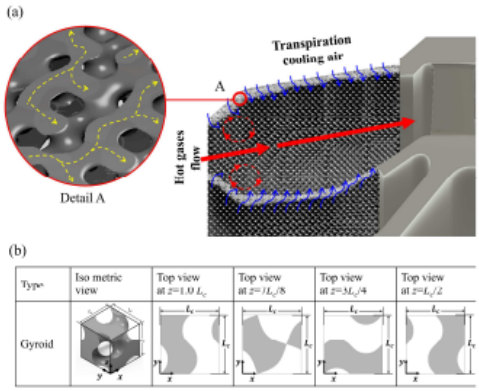

FIGURE 1: (a) A CONCETPUAL EMBODYMENT OF TPMS-BASED TRANSPRIATION COOLING FOR A GAS TURBINE COMBUSTOR. YELLOW ARROWS IN DETAIL A SHOW TEXTURE CHANGES DUE TO SURFACE CURVATURE. (b) PATTEN ON THE TOP SURFACE OF A GYROID-TYPE UNIT CELL CHANGES AS A RESUT OF morphological VARIATION.

oriented perpendicular to the main flow direction enhances cooling effectiveness more than a parallel void pattern. This improvement can be attributed to the fact that perpendicularly orientated voids facilitate the formation of a coolant film on the top surface by forcing coolant to rise up from the voids to from cooling film on the top surface [28,29]. Additionally, the authors focused on the effects of TPMS lattice unit cell sizes on transpiration cooling performance [30]. It was revealed that smaller unit cell sizes exhibit superior cooling performances while the actual porosity was hold as a constant, due to a more uniform distribution of coolant mass flow along the mainstream flow direction and a surface texture easier for developing the cooling film. In addition, if the pressure drop is too low due to large unit cell sizes, a lateral flow of coolant develops inside the porous medium, unfavorably distributing the coolant towards the tailing edge of the test coupon and undermining overall cooling efficiency. The study also highlights the importance of careful selection of TPMS pore sizes to mitigate the risk of clogging the coolant passages.

Despite great promises of TPMS-based transpiration cooling, more comprehensive parametric studies are needed before the cooling strategy can see engine applications. This is largely due to challenges in designing a robust TPMS lattice for transpiration cooling that has optimal performance for complex engine geometries and localized directional flows. For example, real gas turbine components have varying curvatures, resulting in changes in top surface textures when a uniform TPMS lattice is employed to construct the hot-gas path components, as illustrated in Fig. 1. The top surface texture undergoes significant alterations in patterns and orientations by varying the offset from the top surface of an unaltered unit cell (the iso-metric view of

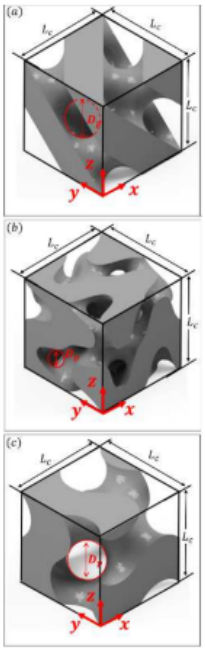

FIGURE 2: ISOMETRIC VIEWS OF UNIT CELL STRUCTURES OF FOLLOWING TPMS TYPES: (A) DIAMOND, (B) KOCH, AND (C) GYROID TPMS. AN IDENTICAL POROSITY IS CHOSEN (ε=50%).

Fig. 2) at steps of one-eighth of the unit cell length, as shown in Fig. 1 (b). Here, L_c in Fig. 1 (b) represents the unit cell size of the TPMS structure. These surface pattern and orientation variations can significantly impact local transpiration cooling performance. The objective of this study is to identify characteristics of a TPMS lattice structure that minimize sensitivity to morphological variations induced by surface curvature of the hot-gas path components while delivering near optimal cooling performance.

2. EXPERIMENT SET UP

2.1 TPMS structure

In this study, three types of TPMS structures, namely Diamond, Koch, and Gyroid, are selected to investigate the impacts of morphological variations of TPMS lattices on the performance of transpiration cooling. TPMS structures are defined by level-set equations. The detailed level-set equations for each TPMS structure are provided in [31]. The isometric views of unit cells of the selected TPMS latticed are illustrated in Fig. 2, with the porosity (ε) and unit cell size (L_c) of the unit cells set identically at 50% and 2.5 mm, respectively. Each unit cell structure is interconnected and repeated in the x, y, and z

 © 2025 by National Research Council of Canada

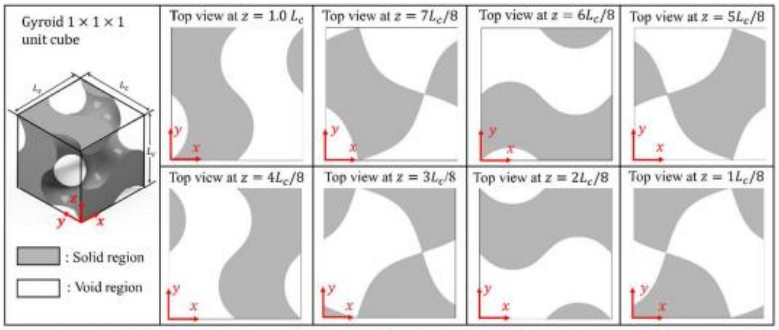

FIGURE 3: PROGRESSION OF CROSS-SECTION VARIATIONS IN A GYROID TYPE TPMS UNIT CELL AT INCREMENTS OF ONE EIGHTH OF A UNIT CELL LENGTH.

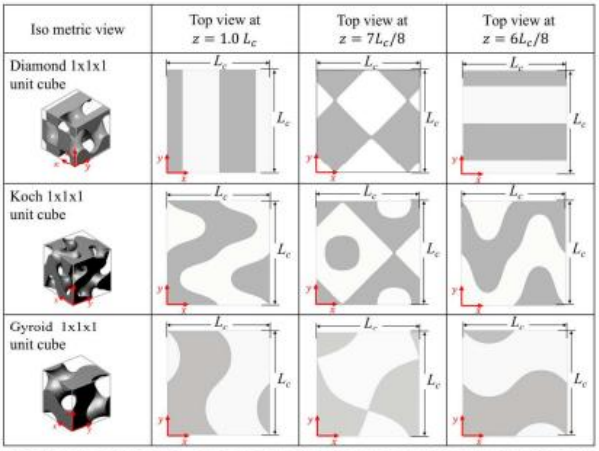

FIGURE 4: VISUALIZATION OF SELECTED CROSS-SECTION VARIATIONS FOR DIAMOND, KOCH, AND GYROID TPMS STRUCTURES

directions, enabling deterministic control of the pore size and distribution. In Fig. 2, D_p representing the pore diameter of the TPMS structure, is quantified as the diameter of the largest sphere that can pass through the narrowest channel of the structure [32], as indicated in Fig. 2.

As actual engine combustor liners curve and main flows inside the combustor swirl, the texture of the exposed surface of a combustor liner fabricated from a continuous TPMS lattice varies in patterns and changes in orientation relative to the flow on the surface. Fig. 3 illustrates how top surface pattern changes as a result of morphological variations in the Gyroid-type of TPMS unit cell. It is evident that the cross-sectional pattern changes distinctly at increments of one-eighth of the unit cell length. Initially, the surface pattern appears as a smooth wavy curve. After an offset of one-eighth unit cell length, the surface pattern transitions to a grid-like (or checkerboard) arrangement. With the next offset of one-eighth unit cell length, it shifts back to a wavy smooth curve, however, rotated 90 degrees from the very first pattern. The progression of unit cell cross-section variations in steps of one-eighth of the unit cell size for one-whole unit cell is shown in Fig. 3. The morphological variation repeats itself every unit cell length. Similar morphological variations in unit cell cross-sections can be observed in other TPMS types, including the other two TPMS structures to be evaluated of this study, Diamond and Koch-types. To investigate the effect of morphological variations in unit cell cross-sections on transpiration cooling, three representative textures generated by making cross-sections from each aforementioned TPMS type were selected to be the textures on the top-surface of transpiration cooling coupons, totaling nine test coupons, as

 © 2025 by National Research Council of Canada

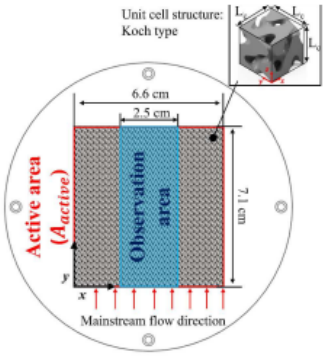

FIGURE 5: DIAGRAM OF CIRCULAR TEST COUPON SHOWING ACTIVE AREA FEATURING TPMS LATTICES. THE CENTRAL PORTION OF THE ACTIVE AREA WAS USED FOR MAKING PSP MEASUREMENTS (OBSERVATION AREA).

shown in Fig. 4. The representative textures can be categorized as grid-like patterns and patterns featuring non-intersecting voids. The orthogonal nature of functions defining the level-set equations dictates that the orientation of non-intersecting voids rotates 90 degrees by taking cross-sections one quarter of the unit cell length apart. When these patterns were selected to be the textures on the top surface of a transpiration cooling coupon, we can define the orientations of the surface voids with respect to the direction of the mainstream. When the orientation of the surface voids is aligned with the mainstream flow direction, the surface texture is defined as in parallel arrangement. Likewise, the perpendicular arrangement is defined when the orientation of the surface voids is perpendicular to the mainstream flow direction. Therefore, for each TPMS type, three extreme surface textures can be derived: parallel, perpendicular, and grid. Patterns that can be obtained at any other TPMS unit cell cross-sections is essentially a transition phase between two extreme surface patterns, and therefore the transpiration cooling performance of a test coupon based on such a transitional surface pattern will be bounded by the three extreme cases of the corresponding TPMS type that this study investigates.

2.2 Test coupon design

As discussed in previous sub-section, a total of nine circular test coupons were designed surrounding three TPMS types (Diamond, Koch, and Gyroid). All nine test coupons were fabricated using a stereolithography (SLA) 3D printer. This printer utilizes a 250 mW UV diode laser near 405 nm to solidify polymer resin. The printer's resolution was set to 25 micrometers in all three dimensions. A high-temperature resin was used; detailed material specifications of the resin can be found in [33]. The dimensions of the circular test coupons are depicted in Fig.5, where the mainstream flow direction is aligned with the y-axis. All circular test coupons are 12.3 cm in diameter, featuring an active area of 6.6 cm by 7.1 cm located in the center of the

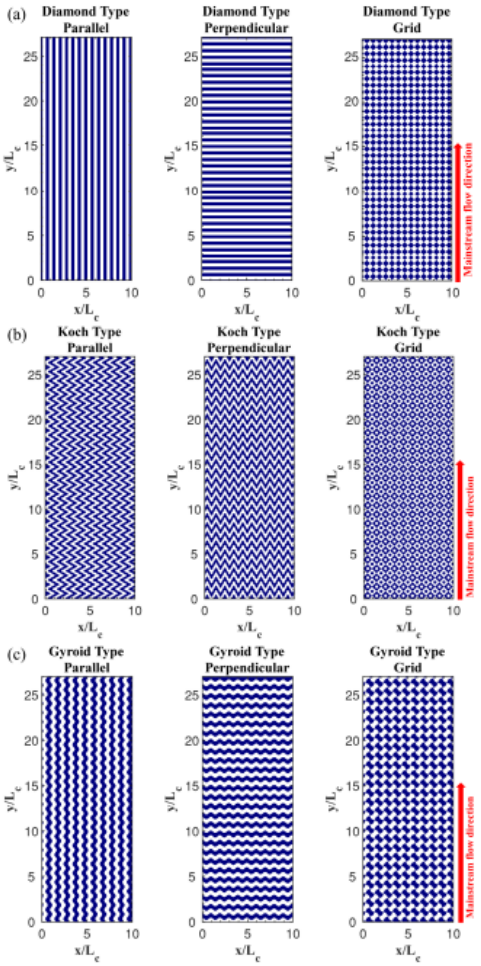

FIGURE 6: TOP VIEW OF OBSERVATION AREA OF ALL NINE TEST COUPONS: (a) DIAMOND, (b) KOCH, AND (c) GYROID. WHITE AREAS DENOTE VOID WHILE BLUE INDICATES SOLID. MAINSTREAM FLOW DIRECTION IS INDICATED BY THE RED ARROWS.

coupons and a thickness of 7.5 mm. The unit cell size (L_c) and porosity (ε) of all nine test coupons were uniformly set to 2.5 mm and 50%. Therefore, the thickness of the test coupon's active area is equal to three times of the unit cell size. To minimize influences from the solid wall adjacent to the active area, areas near both side edges of the active area were not included for

© 2025 by National Research Council of Canada

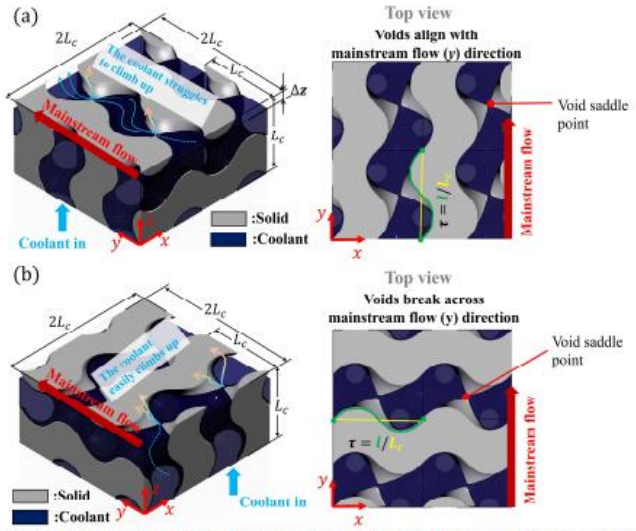

FIGURE 7: ORITENATIONS OF SURFACE VOIDS STONGLY AFFECT HOW COOLANT EVOLUES INTO COOLING FILM UPON EXITING THE TPMS LATTICES.

measurements. The observation area is highlighted in blue in Fig. 5.

Using the top surface textures that are discussed and defined in the previous sub-section, the top views of the observation area for all nine test coupons are summarized in Fig. 6, where the white areas represent the void sections of the top surface, and the dark blue areas indicate the solid sections. It is worth noting that the top surface porosity is identical for all test coupons at 50%.

A nondimensional parameter, tortuosity (τ), was previously defined to characterize the waviness of the voids on the top surface of a TPMS-based transpiration cooling test coupon [34]. The tortuosity (τ) within the unit cell can be calculated using the following expression:

$$\tau = l/L_c \quad (1)$$

where l represents the arc length of a surface void of a single unit cell, as illustrated by the green curve in Fig. 7. As defined earlier, L_c is the unit cell length, which is identical to the chord length. However, tortuosity (τ) alone is not adequate to characterize the surface texture. For example, as Fig. 7 illustrates, the tortuosity τ value is identical for surfaces voids that are parallel and perpendicular to the mainstream flow in the case of the Gyroid-type of TPMS structure. Instead, the orientation of the surface voids relative to the mainstream flow direction significantly impacts coolant behavior and, consequently, transpiration cooling performance. When the surface voids are parallel to the mainstream flow direction, as revealed in Fig. 7, the surface voids serve as natural channels for the coolant to flow downstream without forcing the formation of cooling film over the top surface. In contrast, in the case of surface voids perpendicular aligned with the mainstream flow, the coolant entering the surface voids has to raise up to the top surface to exit from the transpiration cooling coupon, promoting the formation of cooling film. Therefore, a change in orientation of surface texture can substantially affect transpiration cooling performance when the tortuosity is identical. For example, for a Gyroid-type TPMS lattice, the saddle points of the surface voids are recessed 0.31 mm from the top surface (Δz) with a unit cell size of 2.5 mm.

To account for the influence of the orientation of the surface voids relative to the mainstream flow, an effective tortuosity (τ_{eff}) is further introduced as follows:

$$\tau_{eff} = \omega \cdot \tau \quad (2)$$

where ω is a correcting factor to account for the orientation of the surface voids relative to the mainstream flow. It is computed as the integral of the projected length of an arc on the direction that's perpendicular to the main flow. The correcting factor (ω) is calculated as follows:

$$\omega = \frac{1}{L_c}\int_0^{L_c} |tan\,[\theta(y)]|dy \quad (3)$$

and θ is the location-specific angle between the arc and the mainstream flow. As expected, by correcting for the orientation factor of surface patterns, the grid patterns exhibit highest τ_{eff}, while the parallel patterns show lowest τ_{eff}. The computed values are summarized in Table 1.

© 2025 by National Research Council of Canada

Table. 1. SUMMARY OF PARAMETERS FOR TPMS STRUCTURES WITH VARIED CROSS-SECTIONAL PATTERNS

Type of TPMS	Diamond			Koch			Gyroid		
Variable \ Cross-sectional pattern	Parallel	Perpen-dicular	Grid	Parallel	Perpen-dicular	Grid	Parallel	Perpen-dicular	Grid
L_c [mm]	2.5								
ε [%]	50								
τ [-]	1.00	1.00	1.95	2.10	2.10	2.46	1.17	1.17	1.90
ω [-]	0	1.00	0.71	0.57	0.80	0.71	0.45	0.86	0.66
τ_{eff} [-]	0	1.00	1.38	1.20	1.68	1.75	0.53	1.01	1.26
λ [cm^2/cm^3]	13.0			21.1			11.6		
D_p [mm]	0.88			0.60			0.98		

Other geometrical characteristics of the test coupons are also summarized in Table 1, including wetted surface area to volume ratio ($\lambda=A_w/V$), and pore diameter D_p. The wetted surface area A_w is the total internal surface area within the TPMS lattice that interacts with the coolant gas.

2.3 Experiment setup

The effects of morphological variations in TPMS lattice structures on transpiration cooling were studied in an open-loop low-speed wind tunnel, as presented in Fig. 8. The experimental setup has been detailed in previous studies [27–30] and is briefly summarized here. The wind tunnel is driven by a 30kW fan capable of a maximum rate of 2.5 kg/s and a pressure rise of 5 kPa [35]. A mainstream flow velocity of 33 m/s was maintained in the test section of a 12.7 cm × 12.7 cm cross-section. The Reynolds number of the main flow is estimated to be 256,000 at the test section. The velocity of the mainstream flow was measured using a pitot tube positioned at the leading edge of the test coupon. At the same location, the static pressure downstream to the transpiration cooling coupon was determined. The turbulence intensity within the section is estimated to be approximately 3%. Neat nitrogen (N_2), used as the coolant proxy, was supplied from compressed gas bottles and was regulated by flow controller to reach flow rates between 0 and 200 standard liters per minute (SLPM). The static pressure in the coolant reservoir was measured as the pressure upstream to the transpiration cooling coupon. The reservoir's internal diameter and height are 10.2 cm and 4.5 cm, respectively.

A binary (dual-luminophore) Pressure-Sensitive Paint (PSP) from ISSI Inc. was adopted to evaluate film cooling effectiveness by evaluating local oxygen partial pressures. The PSP luminescence intensity was captured using a CCD camera (LaVision Image ProX 2M) with an image doubler under UV excitation (ISSI LM2X-DM-400, 400 nm), see [28,29,36].

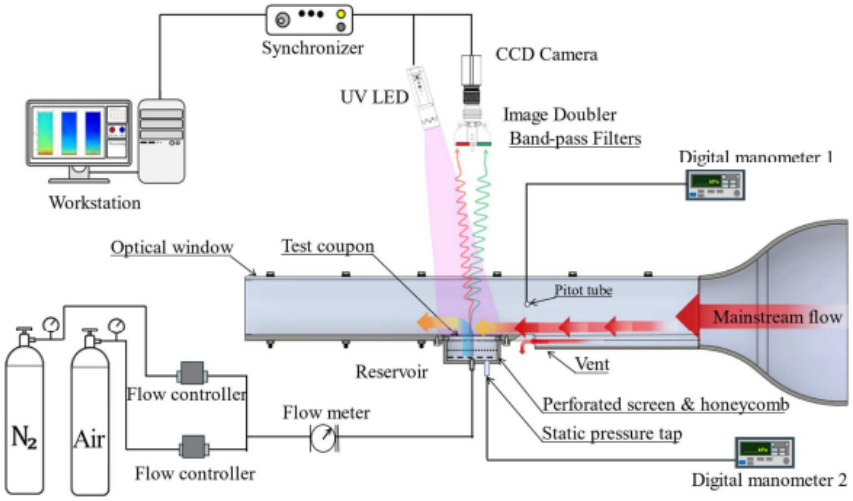

FIGURE 8: SCHEMATIC OF THE EXPERIMENT SETUP

© 2025 by National Research Council of Canada

2.4 Methodology

PSP measures oxygen partial pressures on film cooling surfaces to determine adiabatic film cooling effectiveness (η_{ad}) by invoking the heat and mass transfer analogy [37]:

$$\eta_{ad} = \frac{Co_{2,air} - Co_{2,mix}}{Co_{2,air}} = 1 - \frac{1}{1 + \frac{MM_c}{MM_{air}}\left[\frac{P_{o_2,air}}{P_{o_2,mix}} - 1\right]} \quad (4)$$

Here, Co_{air} is oxygen mass-concentration in main-stream air flow and Co_{mix} is oxygen mass-concentration in the mixture near the surface resulting from coolant mixing with the main-stream air. MM_c and MM_{air} are the molecular weight of air and coolant; in this study nitrogen is used as the coolant proxy. The oxygen mass concentration can be determined by measuring the intensity of PSP fluorescence. Therefore, the adiabatic film cooling effectiveness can be evaluated as a function of the partial pressures of oxygen in air $P_{o_2,air}$ and the partial pressures of oxygen in the near-wall mixture $P_{o_2,mix}$ [38]. Detailed discussions on data reduction and calibration processes have been reported in our previous studies [27–30].

2.5 Uncertainty quantification

The determination of adiabatic film cooling effectiveness using binary PSP relies on precise calibration and accurate image acquisition[39]. The uncertainty associated with PSP measurements is derived from Equation (4) using the uncertainty propagation [40]. The uncertainty in local adiabatic film cooling effectiveness is expressed as follows:

$$\Delta\eta_{ad} = \sqrt{\left(\frac{\partial\eta_{ad}}{\partial P_{o_2,mix}}\delta P_{o_2,mix}\right)^2 + \left(\frac{\partial\eta_{ad}}{\partial P_{o_2,ref}}\delta P_{o_2,ref}\right)^2} \quad (5)$$

In this study, each PSP image was generated by averaging 120 frames to minimize random noise in the data. The binary PSP method further reduces measurement errors caused by temperature variations within the range of 5°C to 45°C [41]. To enhance accuracy, pixel-wise calibrations were conducted in situ, effectively minimizing measurement uncertainties. The relative uncertainties of measured adiabatic film cooling effectiveness were estimated to be $\Delta\eta_{ad}$=±1.34% for η_{ad}=0.8 and $\Delta\eta_{ad}$=±5.46% for η_{ad}=0.2, respectively.

2.6 Test conditions

The blowing ratio (BR) is a fundamental non-dimensional parameter in film cooling studies, defined as follows:

$$BR = \frac{\rho_c u_c}{\rho_m u_m} \quad (6)$$

Here, u and ρ represent velocity and density, respectively, while the subscripts c and m denote coolant and mainstream flow. The coolant exit velocity (u_c) is calculated using the following equation.

$$u_c = \frac{\dot{Q}_c}{A_{active} * \varepsilon_{surface}} \quad (7)$$

Here, $\dot{Q}_c$ represents the coolant volumetric flow rate, while A_{active} and $\varepsilon_{surface}$ denote the active area, as illustrated in Fig. 5, and surface porosity of the test coupon, respectively. In this study, the values of $\dot{Q}_c$ were chosen to achieve BR of 0.6, 1.0, and 1.4 [36].

However, BRs for transpiration cooling are significantly lower due to the fact that surface porosity in the transpiration cooling could be two orders of magnitudes higher comparing to those in effusion cooling scenarios. As a result, conventional BR is ill-suited for evaluating the operating conditions of transpiration cooling when the coolant flow rate per unit area remains the same. To overcome this limitation, injection ratio (F) has been introduced as an alternative parameter in accessing transpiration cooling cases. F is defined as follows:

$$F = \frac{\dot{m}_c}{A_{active}} \cdot \frac{1}{(\rho u)_m} = BR \cdot \varepsilon \quad (8)$$

Here, $\dot{m}_c$ represents the mass flow rate of the coolant. The active area of this study (A_{active}=6.6 cm×7.1 cm) is consistent with previous transpiration and effusion cooling studies [27,36]. Three injection ratios, F = 0.68%, 1.14%, and 1.60%, were applied to each test coupon for this work.

3. RESULTS AND DISCUSSIONS

3.1 Flow characteristics through TPMS lattices

Percentage pressure drops (ΔP) across a test coupon is defined as the ratio of the pressure difference between the static pressure in the reservoir ($P_{reservoir}$) and the static pressure in the test section ($P_{mainstream}$). The ΔP can be expressed as follows:

$$\Delta P = \frac{P_{reservoir} - P_{mainstream}}{P_{reservoir}} \quad (9)$$

ΔP values for all three types of TPMS-lattices as a function of F are presented in Fig. 9. As indicated in Table 1, all three types of TPMS lattices are of identical unit cell size of 2.5 mm and porosity of 50%. The Koch-type of TPMS lattice has the highest ΔP when an identical injection ratio F was applied. This can be explained by the fact that the Koch-type TPMS structure have the highest wetted surface area-to-volume ratio (λ=A_W/V) and the smallest pore diameter (D_p) as defined in Section 2. High λ in lattice structures in combination with small pore sizes D_p results in an intricate internal flow path within a TPMS structure, reducing the structure's permeability and causing percentage pressure drops to increase [32]. Similarly, the Gyroid-type exhibits the smallest λ and the largest D_p, leading to the lowest percentage pressure drop. The percentage pressure drops are close between the Diamond- and the Gyroid-types, due to similar wetted surface area-to-volume ratios beween the two types: 11.6 cm²/cm³ for the Gyroid-type vs. 13.0 cm²/cm³ for the Diamond-type, comparing to a substantially larger value of 21.1 cm²/cm³ for the Koch-type.

It should be noted that the differences in top surface pattern for each type of TPMS lattice do not affect the percentage pressure drop, as the test coupons are of identical thickness and unit cell size. The repetitive nature of TPMS lattices guarantees that a fixed number of unit cells are stacked over the thickness of the test coupon.

Reducing ΔP can be beneficial, as compressing air consumes significant mechanical energy [42]. Conventional effusion-cooled liners typically exhibit ΔP values ranging from 0.5% to 2.5% [43]. In this study, the highest observed ΔP (ΔP =

© 2025 by National Research Council of Canada

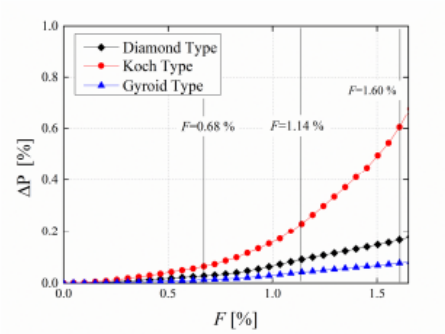

FIGURE 9: PERCENTAGE PRESSURE DROP ACROSS TEST COUPONS AS A FUNCTION OF INJECTION RATIO *F*.

0.6%) is observed with the Koch-type at F = 1.60%, comparable to the lower limit of percentage pressure drops in effusion cooling.

3.2 The Diamond-type TPMS highly sensitive to morphological variations

The Diamond-type TPMS lattice was found to be highly sensitive to morphological variations. Three distinctive cross-sectional patterns were experimentally investigated: parallel, perpendicular, and grid. The 2D distributions of adiabatic film cooling effectiveness (η_{ad}) for all three morphological patterns are compared in Fig. 10. The color bar represents the cooling effectiveness, with blue indicating η_{ad}=1 and red indicating η_{ad}=0. Subpanels (a), (b), and (c) correspond to F=0.68%, F=1.14%, and F=1.60%, respectively. Additionally, the overall averaged film cooling effectiveness, denoted as $\bar{\eta}_{ad}$, was also evaluated and represented in the figure. It should be noted that the voids were excluded from evaluating η_{ad} averages, allowing for a comparison focused solely on the exposed top surfaces. The voids were excluded by masking the measured 2D η_{ad} maps with mathematical expressions of top surface patterns. For instance, the white areas in Fig. 10 represent voids that are excluded from η_{ad} evaluations. As shown in Fig. 10, a distinct improvement in film cooling effectiveness along the mainstream flow direction is observed in all the cases presented in the figure. This evolution, commonly observed in film cooling, is attributed to the cumulative effect of the coolant film, which develops progressively as coolant is continuously being discharged along the streamwise direction. As a result, the adiabatic film cooling effectiveness is significantly higher at the trailing edge (downstream) compared to that at the leading edge (upstream).

Additionally, the film cooling effectiveness reliably increases with F. Unlike conventional effusion cooling, the coolant exit from the porous transpiration cooling surface does not experience coolant jet lift-off, even at the highest injection ratio (F=1.60%), due to low momentum of the coolant flow. A higher F introduces a greater volume of coolant over the top

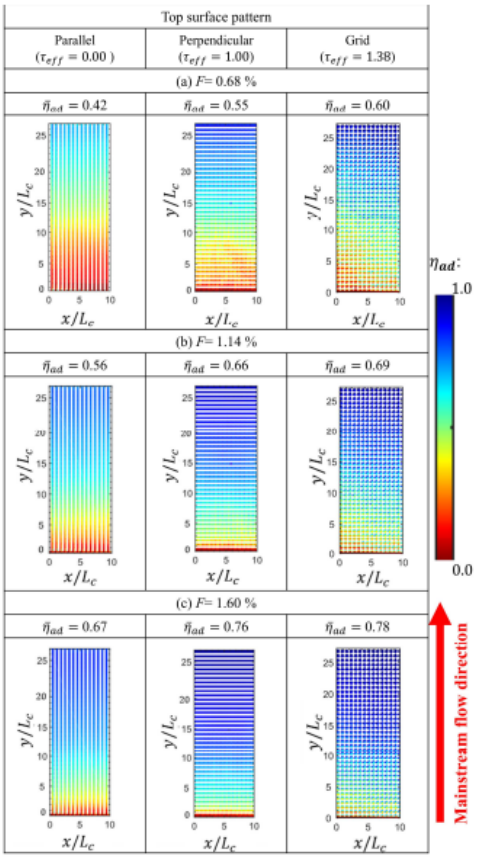

FIGURE 10: 2D DISTRIBUTION OF FILM COOLING EFFECTIVENESS OF THE DIAMOND-TYPE WITH MORPHOLOGICAL VARIATIONS. THREE INJECTION RATIOS WERE APPLIED: (a) F=0.68%, (b) F=1.14%, AND (c) F=1.60%. RED ARROWS INDICATE THE MAINSTREAM FLOW DIRECTION.

surface, facilitating the formation of a denser layer of coolant film. As a result, the mainstream flow is displaced from the surface, significantly reducing the gas temperature and flow velocity near wall, reducing heat fluxes from the hot mainstream flow. However, the benefits of increasing F were more pronounced when the cooling air was under-supplied and the injection ratio was low (F=0.68%). At F = 1.14%, the cooling film is adequately established shortly after the leading edge (within ~10 mm to reach η_{ad} above 0.4 in the worst case scenario) providing effective thermal protection. Further increases in

© 2025 by National Research Council of Canada

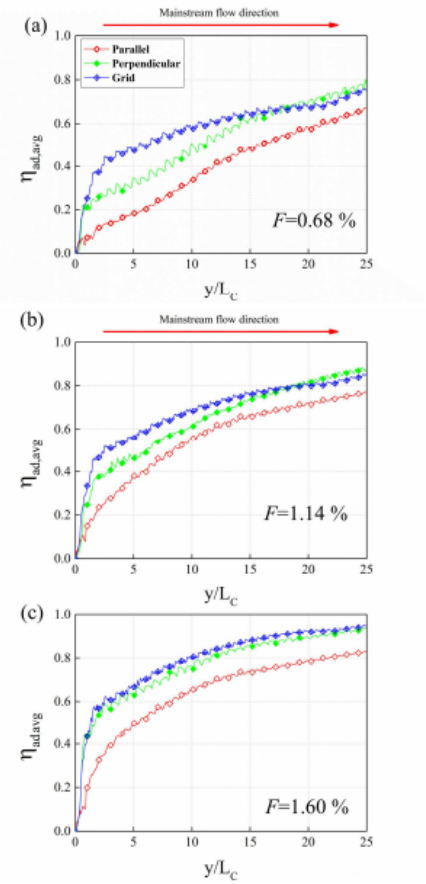

FIGURE 11: SPANWISE AVERAGED FILM COOLING EFFECTIVENESS AS A RESULT OF MORPHOLOGICAL VARIATIONS OF THE DIAMOND-TYPE OVER A RANGE OF INJECTION RATIOS.

coolant injection ratio yield diminishing returns in film cooling effectiveness as the surface has already been covered a dense cooling film [44]. A consistent trend observed with morphological variations of the Diamond-type of TPMS at all injection ratios is that the adiabatic effectiveness (η_{ad}) increases substantially as the top surface texture switches from parallel pattern to perpendicular or grid patterns. For all surface textures, the void channels are recessed from the top surface to the void saddle point by the same depth Δz (see Fig. 7). Although the recession is relatively small, the evolution of coolant flow was substantially altered once enters the surface void channel due to low coolant flow momentum. When the pattern on the top surface becomes parallel to the main flow direction as a result of the morphological variation, the voids act as channels for directing the coolant downstream and discouraging its upward movement to the top surface to form cooling films. As a result, the morphological variation of the Diamond-type resulting in top surface voids that are parallel to the mainstream direction pattern exhibited the lowest η_{ad} at all F, which can be quantified by the pattern's zero effective tortuosity (τ_{eff}). In contrast, when the morphological variation of the Diamond-type TPMS results in top surface voids being perpendicular to mainstream flow, the pattern on the top surface can be characterized by a unity effective tortuosity (τ_{eff}) which indicates a surface void pattern most favorable to the formation of cooling films. As the coolant enters the surface voids from the pores leading to the surface voids near saddle point (see Fig. 7b), the coolant must arise out of the voids to reach the top surface to flow downstream. This alignment facilitates efficient utilization of the coolant, allowing for the formation of uniform cooling films, as the void channels are constantly interrupted in the mainstream flow direction and are not directly interconnected. For the Diamond-type, the morphological variation results in an increase in η_{ad} from voids parallel to the mainstream flow to the perpendicular pattern of 0.13, 0.10, and 0.09 at F=0.68%, F=1.14%, and F=1.60%, respectively.

This alignment facilitates efficient utilization of the coolant, allowing for the formation of uniform cooling films, as the void channels are constantly interrupted in the mainstream flow direction and are not directly interconnected. For the Diamond-type, the morphological variation results in an increase in η_{ad} from voids parallel to the mainstream flow to the perpendicular pattern of 0.13, 0.10, and 0.09 at F=0.68%, F=1.14%, and F=1.60%, respectively.

The morphological variation of the Diamond-type that results in a grid pattern on the top surface can be characterized by the highest effective tortuosity value of 1.38. In this configuration, the surface voids are also perfectly interrupted in the mainstream direction, resembling a checkerboard pattern. The grid pattern has the highest AFE, which is corresponding to the highest effective tortuosity. The grid pattern not only prevents downstream transport of coolant by breaking up void channels but also makes the voids more distributed among solid surface, further promoting the formation of cooling film. For the Diamond-type, the $\bar{\eta}_{ad}$ increases from the Perpendicular to Grid morphological pattern by 0.05, 0.03, and 0.02 at F=0.68%, F=1.14%, and F=1.60%, respectively. The maximum difference in $\bar{\eta}_{ad}$ between the Parallel and Grid morphological patterns is 0.18, 0.13, and 0.11 at F=0.68%, F=1.14%, and F=1.60%, respectively.

Fig. 11 compares the spanwise-averaged film cooling effectiveness resulting from the three morphological variations of the Diamond-type of TPMS. This averaging is calculated by taking the mean film cooling effectiveness across a row of pixels perpendicular to the main flow. The results indicate that differences among the three morphological patterns are most pronounced at the leading edge, where the cooling film initiates.

 © 2025 by National Research Council of Canada

3.3 The Koch-type TPMS insensitive to morphological variations

The Koch-type of TPMS lattice demonstrated the least sensitivity to morphological variations among the three TPMS types investigated of this study. Fig. 12 presents the 2D distribution of film cooling effectiveness resulting from all three representative morphological variations of the Koch-type, highlighting insubstantial differences among the morphological variations. This insensitivity can be attributed to meandering void patterns on the top surface for all morphological variations, which results in uniformly high effective tortuosity. The sharp twists and turns associated with high effective tortuosity inhibit surface voids from channeling coolant downstream. This feature of the surface texture encourages the coolant to arise out of the void channels and to form uniform cooling films subsequently.

Similar to the Diamond-type, the observed trend was that the grid pattern has the highest cooling film effectiveness at all injection ratios, however, the differences between the gird pattern and perpendicular pattern is minimal: the cooling film effectiveness averaged over the entire measurement area, $\bar{\eta}_{ad}$, only differ by 0.02, 0.01, and 0.01 at $F = 0.68\%$, $F = 1.14\%$, and $F = 1.60\%$, respectively. The differences in $\bar{\eta}_{ad}$ between the perpendicular and parallel surface void patterns are also insignificant for the Koch-type: 0.04, 0.03, and 0.03 at $F = 0.68\%$, $F = 1.14\%$, and $F = 1.60\%$, respectively. Thus, the Koch-type is proved to be insensitive to morphological variations.

3.4 The Gyroid-type TPMS exhibits mixed sensitivity to morphological variations

Fig. 14 presents the 2D distributions of cooling film effectiveness of the Gyroid-type TPMS under morphological variations, while Fig. 15 shows the corresponding comparisons of spanwise-averaged film cooling effectiveness. Both figures demonstrate that the Gyroid-type has mixed sensitivity to morphological variations compared to the other TPMS types. Similar to the Koch-type, increases in $\bar{\eta}_{ad}$ were insignificant for the Gyroid-type when a morphological variation results in a grid pattern on the top surface, comparing to the one with the surface voids predominately perpendicular to the mainstream flow direction, differing only by 0.02, 0.01, and 0.01 at $F = 0.68\%$, $F = 1.14\%$, and $F = 1.60\%$, respectively. In addition, modest increases in $\bar{\eta}_{ad}$ were observed when a morphological variation of the Gyroid-type resulting a change in the direction of the surface voids from being predominantly parallel to the mainstream flow to being perpendicular: 0.07, 0.06, and 0.06 at $F = 0.68\%$, $F = 1.14\%$, and $F = 1.60\%$, respectively. The level of sensitivity of the Gyroid-type TPMS to morphological variations is higher comparing to the Koch-type but is certainly much lower when is compared to the Diamond-type.

3.5 TPMS sensitivity to morphological variations

The sensitivity of a TPMS lattice's effectiveness used for transpiration cooling to morphological variations can be evaluated by how much the effective tortuosity of the resulting top surface patterns vary, as illustrated in Fig. 16. A consistent trend was observed that transpiration cooling performance sees

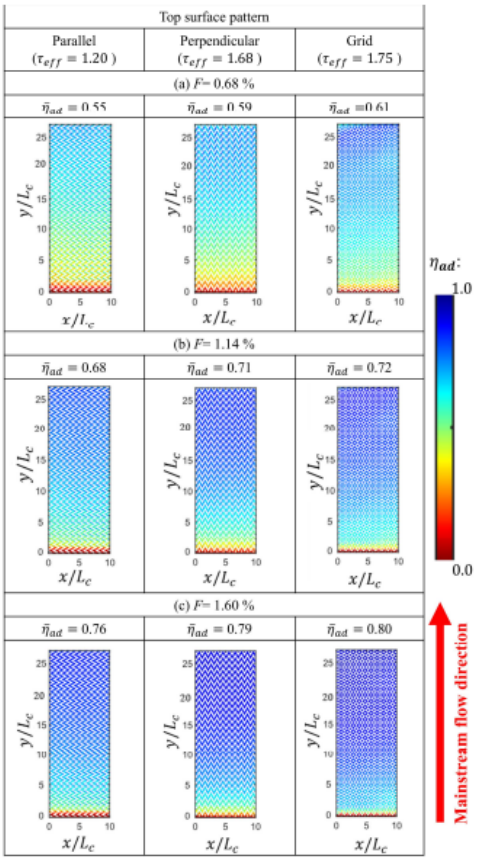

FIGURE 12: 2D DISTRIBUTION OF FILM COOLING EFFECTIVENESS OF THE KOCH-TYPE WITH MORPHOLOGICAL VARIATIONS. THREE INJECTION RATIOS WERE APPLIED: (a) F=0.68%, (b) F=1.14%, AND (c) F=1.60%. RED ARROWS INDICATE THE MAINSTREAM FLOW DIRECTION.

improvements as τ_{eff} Increases for all three TPMS types. The relationship between τ_{eff} and $\bar{\eta}_{ad}$ is nearly linear for all three TPMS types investigated of nearly identical slope. This observation suggests that the variance in effective tortuosity τ_{eff} of a TPMS lattice's top surface patterns can be a good indication of the lattice's sensitivity to morphological variations when used for transpiration cooling, although many other factors contribute to the performance of a TPMS. Practically, the sensitivity of a TPMS lattice to morphological variations can be quantified by the maximum difference in surface patterns' effective tortuosity.

© 2025 by National Research Council of Canada

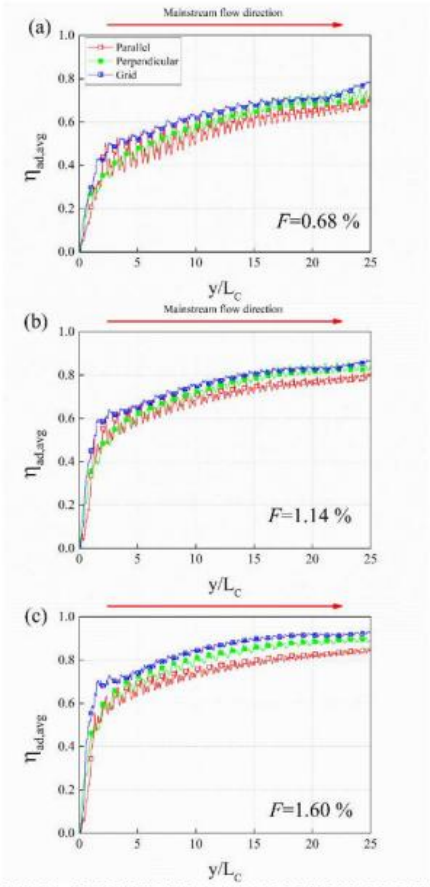

FIGURE 13: SPANWISE AVERAGED FILM COOLING EFFECTIVENESS AS A RESULT OF MORPHOLOGICAL VARIATIONS OF THE KOCH-TYPE OVER A RANGE OF INJECTION RATIOS.

The figure shows that the Diamond-type TPMS has the highest sensitivity to morphological variations due to a significant difference in τ_{eff} between the two extreme surface patterns. Specifically, the surface pattern with voids parallel to the mainstream flow direction exhibited a zero τ_{eff} while the grid pattern has a significantly increased τ_{eff} of 1.38. In contrast, the Koch-type exhibits the lowest sensitivity to morphological variations as indicated by the minimal variance in τ_{eff}.

3.6 Correlation between transpiration cooling effectiveness and percentage pressure drop

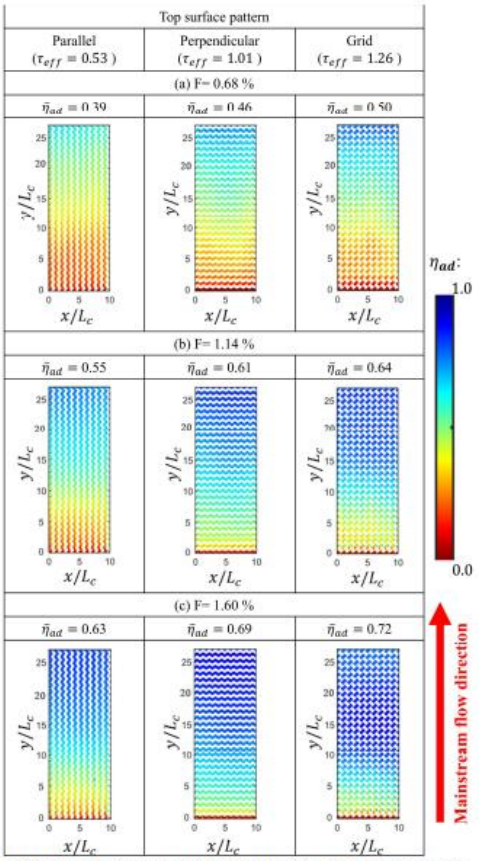

FIGURE 14: 2D DISTRIBUTION OF FILM COOLING EFFECTIVENESS OF THE GYROID-TYPE WITH MORPHOLOGICAL VARIATIONS. THREE INJECTION RATIOS WERE APPLIED: (a) F=0.68%, (b) F=1.14%, AND (c) F=1.60%. RED ARROWS INDICATE THE MAINSTREAM FLOW DIRECTION.

It is evident from Fig. 16 that there are other factors controlling the cooling film effectiveness other than the effective tortuosity. For example, when the voids on the top surface are parallel to the mainstream direction, the Diamond-type demonstrates higher overall cooling film effectiveness $\bar{\eta}_{ad}$ than the Gyroid-type, despite that the Gyroid-type has a higher effective tortuosity. This suggests that effective tortuosity is best-suited for evaluating a TPMS type's sensitivity to morphological variations. By itself, effective tortuosity cannot be used for comparing absolute transpiration cooling film effectiveness

© 2025 by National Research Council of Canada

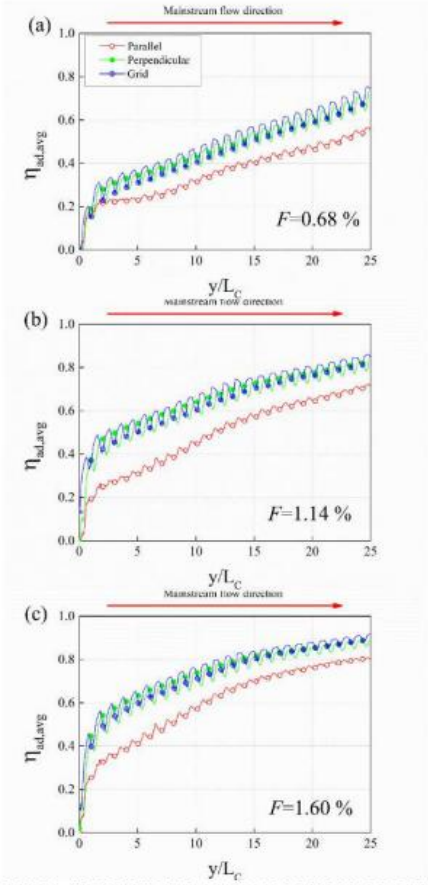

FIGURE 15: SPANWISE AVERAGED FILM COOLING EFFECTIVENESS AS A RESULT OF MORPHOLOGICAL VARIATIONS OF THE GYROID-TYPE OVER A RANGE OF INJECTION RATIOS.

between different TPMS types or lattices of the identical TPMS type but of different unit cell sizes or porosities.

The Gyroid-type demonstrates a significantly lower percentage pressure drop compared to other TPMS types under identical injection ratios, as shown in Fig. 9. The lower pressure drop of the Gyroid-type is attributed to the simplicity of its internal channel geometry and larger pore diameter. As shown in Table 1, the Gyroid-type has the smallest wetted surface-to-volume ratio and the largest pore diameter, resulting in the smallest ΔP. The effect of ΔP is illustrated in Fig. 17, which shows $\bar{\eta}_{ad}$ a function of ΔP at F=1.60%. Note that ΔP is

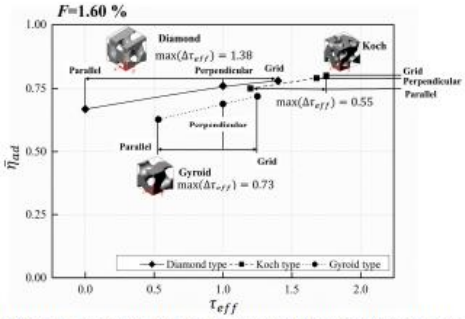

FIGURE 16: VARIANCE IN EFFECTIVE TORTUOSITY τ_{eff} OF A TPMS LATTICE'S TOP SURFACE PATTERNS INDICATES THE LATTICE'S SENSITIVITY TO MORPHOLOGICAL VARIATIONS.

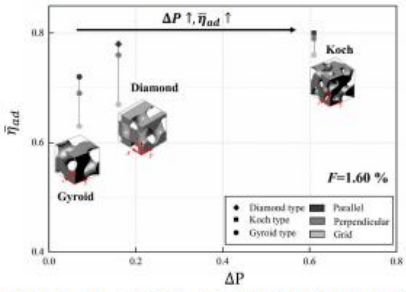

FIGURE 17: EFFECT OF PERCENTAGE PRESSURE DROP (ΔP) ON THE OVERALL FILM COOLING EFFECTIVENESS.

invariant under morphological variations if other parameters of a TPMS lattice are hold constant, as wetted surface area-to-volume ratios and pore diameters are the same.[46]

This observation supports the hypothesis that lateral flow may develop within porous media with high permeability under low pressure drop conditions. The internal lateral flow appears to be induced by the viscosity of the fluid of the mainstream. This internal flow disrupts the uniform distribution of coolant in porous media of high permeability, as discussed in the literature [13,28]. Such lateral flow inside porous media redirects the coolant downstream, depriving the leading edge of the test coupon of essential cooling air and delaying the formation of the cooling film [13]. Consequently, an increase in ΔP can improve cooling performance by forcing a more uniform distribution of cooling air. This study indicates that the Koch-type demonstrated the highest cooling performance and a ΔP within the typical range of conventional effusion-cooled liners (0.5% to 2.5%), making it an ideal candidate for transpiration cooling for optimal cooling film effectiveness.

© 2025 by National Research Council of Canada

4. CONCLUSIONS

This study is part of a systematic effort to understand how TPMS lattices can be optimized for transpiration cooling by focusing on the impact of morphological variations within a unit cell structure. Three TPMS lattice types, Diamond-type, Koch-type, and Gyroid-type, were chosen for carrying out this study in order to identify properties in a TPMS type that can indicate the structure's insensitivity to morphological variations so that one continuous TPMS lattice can be applied to design and fabricate a hot-gas path component of complex geometries.

Among the three TPMS types studied, the Diamond-type exhibits the highest sensitivity to morphological variations, with significant improvement in cooling effectiveness when the surface void patterns are transitioning from voids parallel to mainstream flow direction to a grid pattern. This sensitivity to morphological variations is undesirable for a robust cooling design and can be attributed to substantial changes in effective tortuosity τ_{eff} of the resulting top surface patterns. In contrast, the Koch-type demonstrates the least sensitivity to morphological variations, attributing to low τ_{eff} variation as a result of complex void patterns throughout the morphological variations.

However, it is important to note that insensitivity of in a TPMS type to morphological variations does not guarantee adequate film cooling effectiveness and other factors can strongly influence the overall transpiration cooling performance. For instance, while the Diamond-type outperforms the Gyroid-type in film cooling effectiveness for all top surface patterns resulting from morphological variations, it also exhibits greater sensitivity to morphological variations. The sensitivity of a TPMS type to morphological variations is primarily determined by the maximum variance in its effective tortuosity value. However, overall transpiration cooling film effectiveness depends on factors other than the effective tortuosity τ_{eff}. For example, large unit cell size or low porosity can cause a percentage pressure drop that's too low across the transpiration cooling coupon, leading to a non-ideal shift of coolant to downstream due to a lateral flow internal to the lattice, as observed in the case of the Gyroid-type.

Among the three TPMS types investigated in this study the Koch-type exhibited minimal morphological sensitivity while maintaining the highest overall film cooling effectiveness. This makes the Koch TPMS geometry ideal for designing transpiration-cooled gas turbine liners that are immune to variations in top surface when a continuous TPMS lattice is used to fabricate a component of curved surfaces.

ACKNOWLEDGEMENTS

The work is supported by the National Research Council of Canada (NRC)'s National Program Office under Postdoctoral Fellowship Program (PDF2024-TM-AF). The work is also supported by NRC's Low-Emission Aviation Program (LEAP) under project A1-024515.

REFERENCES

[1] Goldstein, R. J., Ibele, W. E., Patankar, S. V., Simon, T. W., Kuehn, T. H., Strykowski, P. J., Tamma, K. K., Heberlein, J. V. R., Davidson, J. H., Bischof, J., Kulacki, F. A., Kortshagen, U., Garrick, S., and Srinivasan, V., 2006, "Heat Transfer—A Review of 2003 Literature," *Int. J. Heat Mass Transf.*, 49(3–4), pp. 451–534.https://doi.org/10.1016/J.IJHEATMASSTRANSFER.2005.11.001.

[2] Khan, M. A., Sundarrajan, S., Natarajan, S., Parameswaran, P., and Mohandas, E., 2014, "Oxidation and Hot Corrosion Behavior of Nickel-Based Superalloy for Gas Turbine Applications," *Materials and manufacturing processes*, 29(7), pp. 832–839.

[3] Krewinkel, R., 2013, "A Review of Gas Turbine Effusion Cooling Studies," *Int. J. Heat Mass Transf.*, 66, pp. 706–722. https://doi.org/10.1016/J.IJHEATMASSTRANSFER.2013.07.071.

[4] Curry, D., A. Gomez, and C. Johnston., 1971, "Radiative, ablative, and active cooling thermal protection studies for the leading edge of a fixed-straight wing space shuttle." *6th Thermophysics Conference*.

[5] Terry, John E., and Gus J. Caras., 1966, "Transpiration and film cooling of liquid rocket nozzles." *Redstone Scientific Information Center, Redstone Arsenal, Alabama*.

[6] Liu, Y. Q., Jiang, P. X., Xiong, Y. Bin, and Wang, Y. P., 2013, "Experimental and Numerical Investigation of Transpiration Cooling for Sintered Porous Flat Plates," *Appl. Therm. Eng.*, pp. 997–1007. https://doi.org/10.1016/j.applthermaleng.2012.08.028.

[7] Mi, Q., Yi, S. H., Gang, D. D., Lu, X. G., and Liu, X. L., 2024, "Research Progress of Transpiration Cooling for Aircraft Thermal Protection," *Appl. Therm. Eng.*, 236. https://doi.org/10.1016/j.applthermaleng.2023.121360.

[8] Weinbaum, S., and Wheeler, H. L., 1949, "Heat Transfer in Sweat-Cooled Porous Metals," *J. Appl. Phys.*, 20(1), pp. 113–122. https://doi.org/10.1063/1.1698226.

[9] Nguyentat, T., Hayes, W. A., Meland, T. O., Veith, E. M., and Ellis, D. L., 2006, "Fabrication of a Liquid Rocket Combustion Chamber Liner of Advanced Copper Alloy GRCop-84 via Formed Platelet Liner Technology," *42nd AIAA/ASME/SAE/ASEE Joint Propulsion Conference & Exhibit.*

[10] Xu, G., Liu, Y., Luo, X., Ma, J., and Li, H., 2015, "Experimental Investigation of Transpiration Cooling for Sintered Woven Wire Mesh Structures," *Int J Heat Mass Transf*, 91, pp. 898–907. https://doi.org/10.1016/j.ijheatmasstransfer.2015.07.060.

[11] Wu, N., Wang, J., Dong, W., and Ding, R., 2018, "An Experimental Investigation on Combined Sublimation and Transpiration Cooling for Sintered Porous Plates," *Int. J. Heat Mass Transf.*, 116, pp. 685–693. https://doi.org/10.1016/j.ijheatmasstransfer.2017.09.062.

[12] Sun, H., Ma, H., Yan, L., Fu, H., Luan, Y., and Zunino, P., 2024, "Numerical Simulations on the Performance of Transpiration Cooling Implemented with Perforated Flat Plates," *Appl. Therm. Eng.*, 238, p. 121943. https://doi.org/10.1016/J.APPLTHERMALENG.2023.121943.

[13] Hinse, M., Yildiz, K., Richer, P., Jodoin, B., Yildiz, K., Yun, S., and Hong, Z., 2020, "Numerical and Experimental Studies of Transpiration Cooling Film Effectiveness over Porous Materials," *J. of Therm. and Heat Transf.*, pp. 1–20. https://doi.org/10.2514/1.T6510

[14] Lai, N., Qin, X., Ye, Z., Li, C., Chen, K., and Zhang, Y., 2013, "The Study on Permeability Reduction Performance of a Hyperbranched Polymer in High Permeability Porous Medium," J. Pet. Sci. Eng., 112, pp. 198–205. https://doi.org/10.1016/J.PETROL.2013.11.005.

 © 2025 by National Research Council of Canada

[15] Wassell, A. B., and J. K. Bhangu., 1980, "The development and application of improved combustor wall cooling techniques." *Turbo Expo: Power for Land, Sea, and Air*. Vol. 79658. American Society of Mechanical Engineers.

[16] Yang, L., Chen, W., and Chyu, M. K., 2018, "A Convolution Modeling Method for Pore Plugging Impact on Transpiration Cooling Configurations Perforated by Straight Holes," *Int. J. Heat Mass Transf.*, 126, pp. 1057–1066. https://doi.org/10.1016/j.ijheatmasstransfer.2018.06.068.

[17] Jakus, A. E., Geisendorfer, N. R., Lewis, P. L., and Shah, R. N., 2018, "3D-Printing Porosity: A New Approach to Creating Elevated Porosity Materials and Structures," *Acta Biomater*, 72, pp. 94–109. https://doi.org/10.1016/j.actbio.2018.03.039.

[18] Kim, M., Shin, D. H., Kim, J. S., Lee, B. J., and Lee, J., 2021, "Experimental Investigation of Effusion and Transpiration Air Cooling for Single Turbine Blade," *Appl. Therm. Eng.*, 182. https://doi.org/10.1016/j.applthermaleng.2020.116156.

[19] Min, Z., Huang, G., Parbat, S. N., Yang, L., and Chyu, M. K., 2019, "Experimental Investigation on Additively Manufactured Transpiration and Film Cooling Structures," *J. Turbomach.*, 141(3). https://doi.org/10.1115/1.4042009.

[20] Schwarz, H. A., 1972, *Gesammelte mathematische abhandlungen*. Springer, Berlin.

[21] Hussain, I., Al-Ketan, O., Renda, F., Malvezzi, M., Prattichizzo, D., Seneviratne, L., Abu Al-Rub, R. K., and Gan, D., 2020, "Design and Prototyping Soft–Rigid Tendon-Driven Modular Grippers Using Interpenetrating Phase Composites Materials," *Int. J. Robot. Res.*, 39(14), pp. 1635–1646. https://doi.org/10.1177/0278364920907697.

[22] Han, C., Li, Y., Wang, Q., Wen, S., Wei, Q., Yan, C., Hao, L., Liu, J., and Shi, Y., 2018, "Continuous Functionally Graded Porous Titanium Scaffolds Manufactured by Selective Laser Melting for Bone Implants," *J. Mech. Behav. Biomed. Mater.*, 80, pp. 119–127. https://doi.org/10.1016/j.jmbbm.2018.01.013.

[23] Maskery, I., Sturm, L., Aremu, A. O., Panesar, A., Williams, C. B., Tuck, C. J., Wildman, R. D., Ashcroft, I. A., and Hague, R. J. M., 2018, "Insights into the Mechanical Properties of Several Triply Periodic Minimal Surface Lattice Structures Made by Polymer Additive Manufacturing," *Polymer*, 152, pp. 62–71. https://doi.org/10.1016/j.polymer.2017.11.049.

[24] Li, W., Li, W., and Yu, Z., 2022, "Heat Transfer Enhancement of Water-Cooled Triply Periodic Minimal Surface Heat Exchangers," *Appl. Therm. Eng.*, 217, p. 119198.https://doi.org/10.1016/J.APPLTHERMALENG.2022.119198.

[25] Tang, W., Zhou, H., Zeng, Y., Yan, M., Jiang, C., Yang, P., Li, Q., Li, Z., Fu, J., Huang, Y., and Zhao, Y., 2023, "Analysis on the Convective Heat Transfer Process and Performance Evaluation of Triply Periodic Minimal Surface (TPMS) Based on Diamond, Gyroid and Iwp," *Int. J. Heat Mass Transf.*, 201, p. 123642. https://doi.org/10.1016/J.IJHEATMASSTRANSFER.2022.123642.

[26] Zhou, Z., Lv, Y., He, F., Liu, T., and Wang, J., 2024, "Pore-Scale Investigation of Transpiration Cooling Based on Triply Periodic Minimal Surface," *Int. J. Therm. Sci.*, 201.

[27] Broumand, M., Son, J., Pyo, Y., Yun, S., and Hong, Z., 2024, "TPMS-Based Transpiration Cooling for Film Cooling Enhancement," *Int. J. Heat Mass Transf.*, 231. https://doi.org/10.1016/j.ijheatmasstransfer.2024.125824.

[28] Son, J., Broumand, M., Pyo, Y., Richer, P., Jodoin, B., and Hong, Z., 2024, "Effects of Lattice Orientation Angle On Tpms-Based Transpiration Cooling," *J. Eng. Gas Turbine Power*, pp. 1–28. https://doi.org/10.1115/1.4067378.

[29] Son, J, Broumand, M, Pyo, Y, Richer, P, Jodoin, B, & Hong, Z. "Effects of Lattice Orientation Angle on TPMS-Based Transpiration Cooling." *Proceedings of the ASME Turbo Expo* 2024, London, United Kingdom. June 24–28, 2024. https://doi.org/10.1115/GT2024-126861

[30] Son, J., Pyo, Y., Richer, P., Jodoin, B., and Hong, Z., 2025, "Impact of TPMS Structure Unit Cell Size on Transpiration Cooling." *Proceedings of the AIAA/SCI TECH 2025*, Orlando, FL, January 6–10, 2025.

[31] Novak, N., Al-Ketan, O., Borovinšek, M., Krstulović-Opara, L., Rowshan, R., Vesenjak, M., and Ren, Z., 2021, "Development of Novel Hybrid TPMS Cellular Lattices and Their Mechanical Characterisation," *J. of Mater. Res. Technol.*, 15, pp. 1318–1329. https://doi.org/10.1016/j.jmrt.2021.08.092.

[32] Al-Ketan, O., Ali, M., Khalil, M., Rowshan, R., Khan, K. A., and Abu Al-Rub, R. K., 2021, "Forced Convection Computational Fluid Dynamics Analysis of Architected and Three-Dimensional Printable Heat Sinks Based on Triply Periodic Minimal Surfaces," *J. Therm. Sci Eng Appl*, 13(2). https://doi.org/10.1115/1.4047385.

[33] Formlabs, Formlabs Material Library, Everything You Need to Start Printing.

[34] Fu, J., Thomas, H. R., and Li, C., 2021, "Tortuosity of Porous Media: Image Analysis and Physical Simulation," *Earth. Sci. Rev.*, 212, p. 103439.

[35] Lei, Z., Mahallati, A., Cunningham, M., & Germain, P., 2010, "Influence of Inlet Swirl on the Aerodynamics of a Model Turbofan Lobed Mixer." *ASME International Mechanical Engineering Congress and Exposition*. pp. 807-819.

[36] Pyo, Y., Son, J., Richer, P., Jodoin, B., Broumand, M., Yun, S., and Hong, Z., 2024, "Isolating Influences of Varying Pitch from the Effects of Non-Zero Compound Angles on Effusion Cooling," *Aeronaut. J.*, pp. 1–21. https://doi.org/10.1017/aer.2024.108.

[37] Han, J.-C., and Rallabandi, A. P., 2010, "Turbine Blade Film Cooling Using PSP Technique," *Front. Heat Mass Tran.*, 1(1), p. 013001.

[38] Liu, T., Sullivan, J. P., Asai, K., Klein, C., and Egami, Y., 2005, Pressure and Temperature Sensitive Paints, Springer.

[39] Sajben, M., 1993, "Uncertainty Estimates for Pressure Sensitive Paint Measurements," *AIAA J.*, 31(11), pp. 2105–2110. https://doi.org/10.2514/3.11897.

[40] Natsui, G., Little, Z., Kapat, J. S., Dees, J. E., and Laskowski, G., 2016, "A Detailed Uncertainty Analysis of Adiabatic Film Cooling Effectiveness Measurements Using Pressure-Sensitive Paint," *J. Turbomach.*, 138(8). https://doi.org/10.1115/1.4032674.

[41] Barigozzi, G., Mucignat, C., Abdeh, H., Scandella, D., and Dolci, G., 2018, "Assessment of Binary PSP Technique for Film Cooling Effectiveness Measurement on Nozzle Vane Cascade with Cutback Trailing Edge," *Exp. Therm. Fluid Sci.*, 97, pp. 431–443. https://doi.org/10.1016/j.expthermflusci.2018.05.015.

[42] Maurer, M. T., Benz, U., Swiatek, S., Konradt, O., & Mallm, M. (2015). *U.S. Patent Application No. 14/445,413*.

[43] Chen, X., Krawciw, J., Xia, H., Denman, P. A., Bonham, C., and Carrotte, J. F., 2021, "Study of an Effusion-Cooled Plate with High Level of Upstream Fluctuation," *Appl. Therm. Eng.*, 184. https://doi.org/10.1016/j.applthermaleng.2020.116126.

[44] Otsu, H., Fujita, K., and Ito, T., 2007, "Application of the Transpiration Cooling Method for Reentry Vehicles," *45th AIAA Aerospace Sciences Meeting and Exhibit*, https://doi.org/doi:10.2514/6.2007-1209.

 © 2025 by National Research Council of Canada

5.4.2 Numerical study

From the experimental results discussed in the previous section, it was clearly demonstrated using Pressure Sensitive Paint (PSP) measurements that morphological variations significantly affect the transpiration cooling performance of TPMS structures. Increased film cooling effectiveness correlated well with enhanced effective tortuosity due to improved conditions for film formation across various surface morphologies.

However, PSP measurements are inherently limited to assessing film cooling effectiveness only at the exposed surfaces and do not directly provide insights into the detailed coolant flow behavior and film thickness development. Thus, computational fluid dynamics (CFD) simulations were conducted to gain a deeper understanding of the underlying coolant transport mechanisms. To systematically evaluate the isolated effect of morphological variations on transpiration cooling performance, numerical simulations were performed using a simplified computational domain composed of a 1 × 1 × 3 arrangement of Gyroid-type TPMS unit cells in the *x*, *y*, and *z* directions. The three morphological configurations—Parallel, Perpendicular, and Grid—were modeled to match the unit cell size and porosity used in the experimental setup. This domain enabled a focused investigation of how surface morphology influences coolant film formation and distribution under the same injection ratio conditions as the experiments. Additional details regarding the computational domain and boundary conditions are provided in the following section.

5.4.2.1 Computational domain and boundary conditions

Further numerical analyses were conducted to investigate the effect of morphological variations on transpiration cooling performance using the 3-dimensional, steady state computational model. Only the fluid domain was modeled in the present study to replicate the PSP-based determination of adiabatic film cooling effectiveness. Since the PSP methodology relies on the heat–mass transfer analogy ($Le_t \approx 1$), heat conduction and internal convection effects are not represented in the measurements. Therefore, the TPMS solid matrix was excluded from the computational domain, enabling the isolated assessment of coolant transport and mixing within the fluid domain, computational domain was illustrated in Figure 47. A constant velocity inlet ($u_\infty = 33\frac{m}{s}, T_\infty = 350\ K$) and a pressure outlet with zero gauge pressure (P_{gage}=0 Pa) were prescribed at the channel inlet and outlet, respectively. Periodic boundary conditions were imposed on the lateral surfaces. A symmetry boundary condition was applied to the top surface of the mainstream channel,

allowing only half of the experimental rig height to be modeled. This reduced the computational domain and the total number of mesh elements while preserving the flow physics. The bottom boundary of the reservoir was defined as a mass flux inlet supplying pure nitrogen, consistent with the experimental coolant flow rates. The coolant reservoir boundary was modeled as a mass flux inlet supplying pure nitrogen (T_c=300 K), with mass flow rates consistent with the injection ratios investigated experimentally: F=0.68%, 1.14%, and 1.60%.

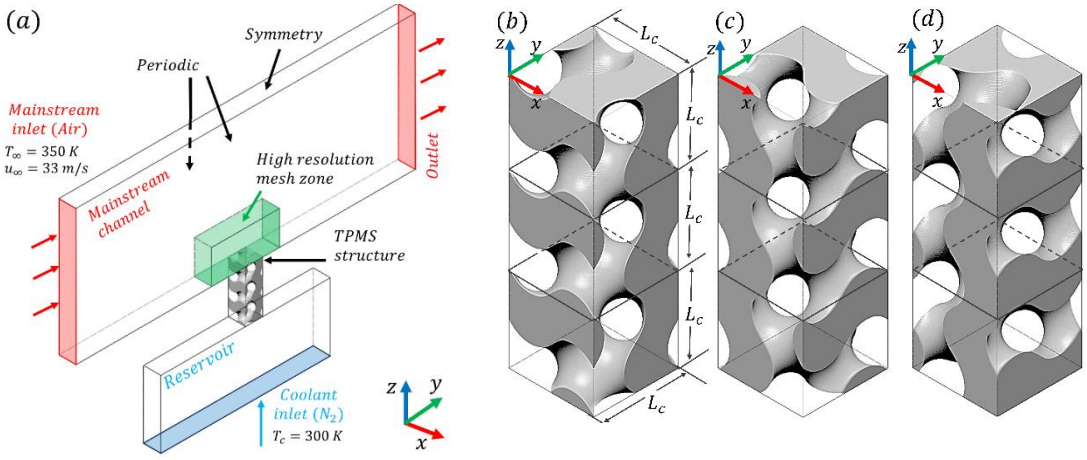

Figure 47 Geometry model used for simulation. (a) Computational domain, and (b) Parallel, (c) Perpendicular, and (d) Grid configurations of the TPMS structure.

The initial TPMS geometry was generated in MATLAB and exported as an STL (Stereo Lithography) file. As shown in Figure 48, the raw STL geometry (Step:1 STL scripting) contained an excessively large number of triangular faces, which not only increased computational cost and memory requirement and could adversely affect mesh generation quality [84].

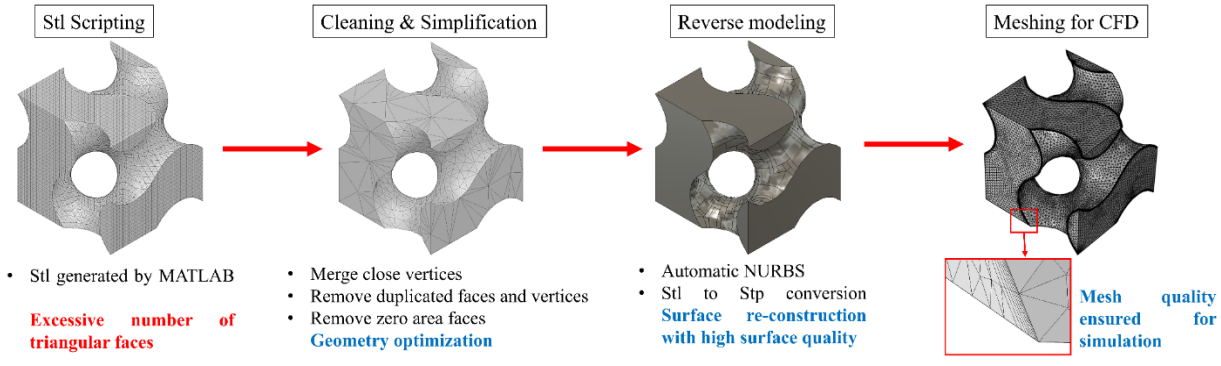

Figure 48 Workflow of STL based TPMS geometry conversion to STP for CFD analysis

To overcome these limitations, a reverse modeling workflow was employed to convert the STL geometry into a STEP (STP) format. During the Cleaning and Simplification stage (Step 2),

duplicate vertices, redundant entities, and degenerate (zero-area) faces were removed, while preserving the essential geometric and topological features of the TPMS structure. Subsequently, in the Reverse Modeling stage (Step 3), the cleaned STL surface was reconstructed into a high-quality NURBS (Non-Uniform Rational B-Splines)-based surface and STP format. Finally, in the Meshing for CFD stage (Step 4), the STP geometry was imported into the meshing environment, refined, and discretized into a computational mesh suitable for CFD analysis. This workflow improved geometric representation, reduced meshing effort, and facilitated CFD simulations of TPMS structures containing complex and small-scale features. The computational domain was discretized using an unstructured mesh generated in COMSOL Multiphysics. As shown in Figure. 49, eight boundary-layer (inflation) layers were applied at the channel–TPMS interface to ensure adequate resolution of near-wall flow and thermal gradients, while maintaining accurate representation of the complex TPMS geometry.

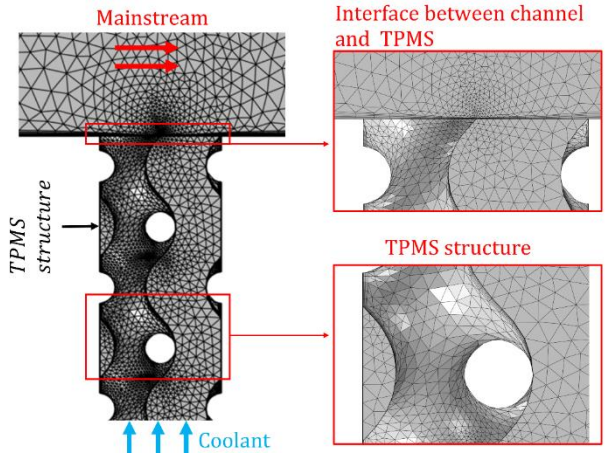

Figure 49 Computational mesh for the Gyroid-type structure, showing boundary-layer refinement near the channel–porous interface and internal surfaces.

5.4.2.2 Turbulent model verification

Accurate prediction of transpiration cooling performance depends on the selection of an appropriate turbulence model to capture the interaction between the mainstream flow and coolant emerging from the porous structure. Therefore, a turbulence model sensitivity study was conducted by comparing the numerical predictions with the PSP measurements. Numerical simulations were performed using the Standard k-ε, Realizable k-ε, and SST k-ω turbulence models, and the corresponding results are presented in Figure 50.

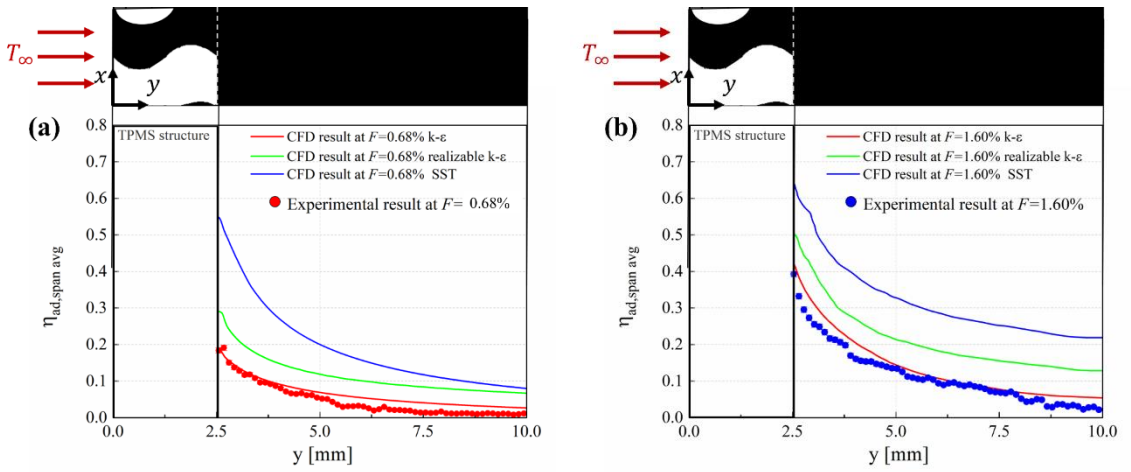

Figure 50 Comparison of spanwise-averaged AFE ($\eta_{ad,span\,avg}$) obtained from CFD and PSP measurements at injection ratios of (a) $F = 0.68\%$ and (b) $F = 1.60\%$.

Figure 50 compares the spanwise-averaged adiabatic film cooling effectiveness predicted by the CFD simulations with the corresponding PSP measurements. The test coupon used in the experiment is shown in Figure 51. As in Figure 47, the coupon contains a single unit cell in the streamwise direction and multiple unit cells arranged in the spanwise direction to approximate the periodic boundary conditions applied in the CFD simulations. The experimental results were obtained by averaging the PSP measurements over the ten unit cells within the observation area.

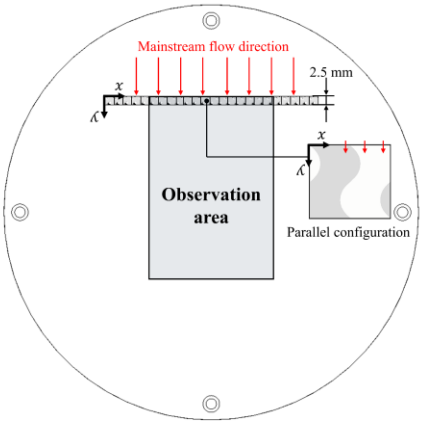

Figure 51 Schematic of the test coupon used for PSP measurements

Among the turbulence models evaluated, the Standard k-ε model provided the closest agreement with the experimental data for all injection ratios investigated. In contrast, both the Realizable k-ε and SST k-ω models consistently overpredicted the adiabatic film cooling

effectiveness throughout the downstream region. Therefore, the Standard k-ε model was selected for all subsequent numerical analyses.

Figure 52 presents a comparison of the adiabatic film cooling effectiveness distributions predicted using the selected standard k-ε model and those obtained from the PSP measurements.

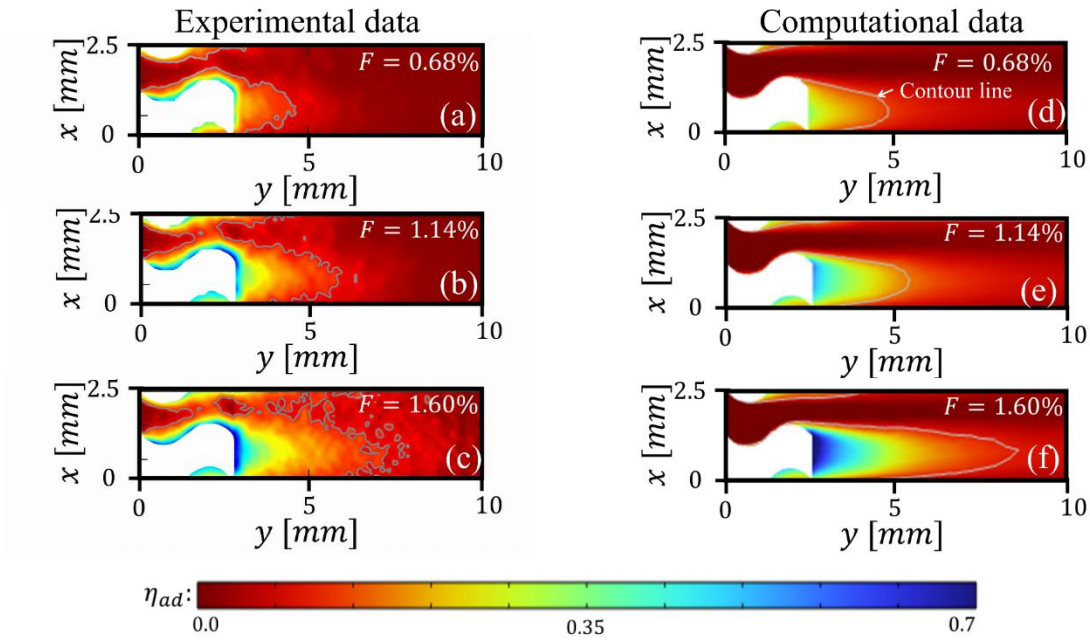

Figure 52 Comparison between experimentally measured and numerically predicted AFE distributions for injection ratios of $\boldsymbol{F = 0.68\%}$, $\boldsymbol{1.14\%}$, and $\boldsymbol{1.60\%}$. Panels (a)–(c) show PSP measurements, while panels (d)–(f) present CFD predictions obtained using the Standard $\boldsymbol{k\text{-}\varepsilon}$ turbulence model. The gray contour line represents $\boldsymbol{\eta_{ad} = 0.15}$, defining the boundary of the effective cooling region.

Overall, the numerical model captures the major features of the adiabatic film cooling effectiveness distribution and reproduces the coolant coverage observed in the experiments. However, the effectiveness in the downstream region is consistently overpredicted. This discrepancy may be attributed to the unmodeled surface roughness of the 3D-printed test coupon, experimental measurement uncertainties associated with the PSP measurements and coolant flow-rate measurement and adjustment. The present coupon required substantially lower coolant flow rates of 2.5, 4.2, and 5.9 SLPM at F = 0.68%, 1.14%, and 1.60%, respectively, compared with 66, 110, and 153 SLPM for the original coupon (Section 5.4.1). With the flow-rate display configured to show integer values, its finite resolution limited the precision with which these lower flow rates could be read and adjusted, potentially increasing the relative uncertainty in the coolant injection

ratio. The discrepancy may also reflect the limitations inherent to RANS (Reynolds-averaged Navier–Stokes) turbulence modeling. Nevertheless, the maximum relative error between the experimental and numerical results remained below 11.5% at $F = 1.60\%$.

To evaluate mesh independence, three grid resolutions were tested: Grid 1 (1.4 million cells), Grid 2 (2.3 million cells), and Grid 3 (3.0 million cells). The area-averaged AFE was evaluated at an injection ratio of F=1.60%. As shown in Figure 53, the results for Grid 2 and Grid 3 closely match, indicating convergence. Therefore, Grid 2 was selected for all subsequent simulations to balance computational cost and accuracy.

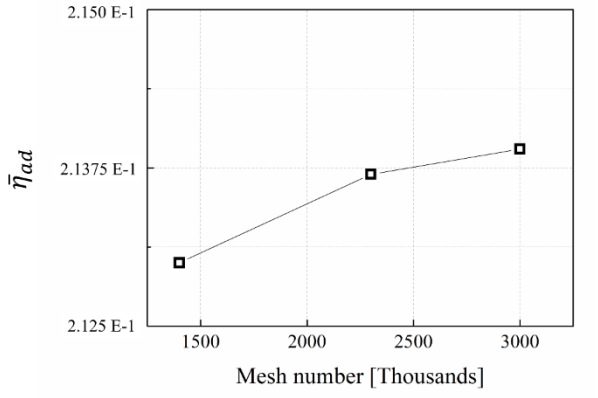

Figure 53 Area averaged AFE for three different grid resolutions at F=1.60%.

5.4.2.3 Results: Adiabatic film cooling effectiveness distribution at different morphological variations

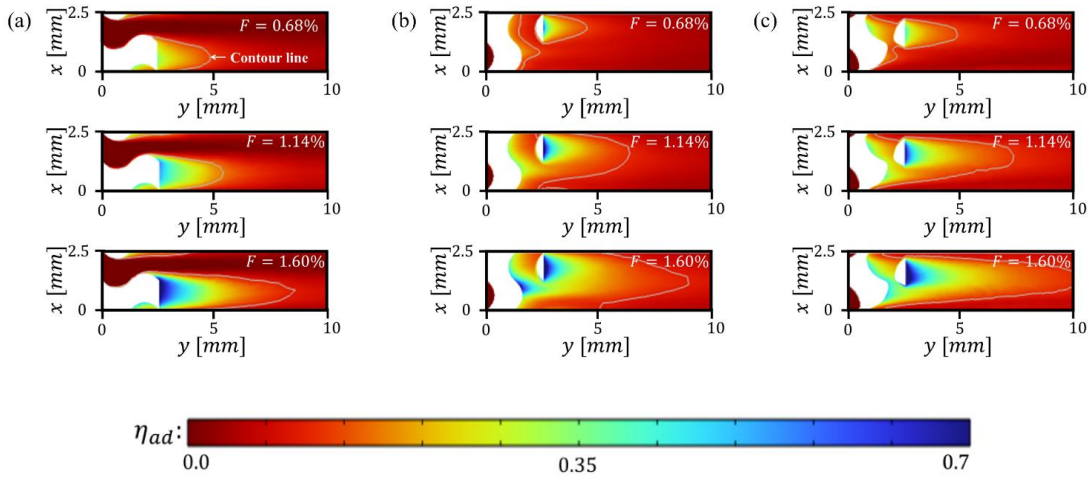

Figure 54 AFE distributions at the top surface for gyroid-type TPMS structures under three different configurations: (a) Parallel, (b) Perpendicular, and (c) Grid. Results are shown for three injection ratios (F=0.68%, 1.14%, and 1.60%). The effective cooling area is defined by the grey contour line corresponding to $\boldsymbol{\eta_{ad} = 0.15}$

Figure 54 presents the surface distributions of adiabatic film effectiveness (AFE) at different injection ratios (F) for three morphological configurations. The grey contour line denotes the effective cooling region, defined as the area where η_{ad}>0.15. This threshold was selected to clearly distinguish the penetration of the coolant film. As expected, the coolant film develops downstream due to the cumulative effect of the coolant injection, forming a protective layer along the streamwise direction [23]. Two clear trends can be observed. First, the surface AFE increases with higher injection ratios, which agrees with the experimental observations presented in Section 5.4.1. The increase in coolant mass flow leads to a thicker film without lift-off, even at the highest injection ratio. Second, AFE improves progressively from the Parallel to Perpendicular to Grid configurations. In the Parallel configuration (Figure 54 (a)), the cooling voids are aligned with the mainstream flow direction. As a result, a pronounced strip-like uncooled region persists between adjacent voids in the central portion of the surface (x≈1.5−2.3 mm). Even at the highest injection ratio (F=1.60%), this uncooled region is not completely covered by coolant. Because the voids are oriented parallel to the mainstream flow, the coolant preferentially forms streamwise streaks, while lateral spreading is significantly restricted. In contrast, the Perpendicular configuration (Figure 54 (b)) promotes greater lateral coolant dispersion because the cooling voids are oriented

perpendicular to the mainstream flow direction. Consequently, the coolant spreads more effectively across the surface, eliminating the persistent uncooled region observed in the Parallel configuration. This behavior is attributed to the increased effective tortuosity of the flow passages, resulting in a more uniform coolant distribution along the spanwise (x) direction. However, at the lowest injection ratio ($F = 0.68\%$), the coolant lacks sufficient momentum to penetrate downstream. As a result, the effective cooling area, defined by the $\eta_{ad} = 0.15$ contour, becomes discontinuous ($y \approx 1.5 - 2.5$ mm) downstream of the first void, producing a separated effective cooling area. As the injection ratio increases, this discontinuity disappears due to the enhanced coolant momentum, which improves downstream penetration and maintains a continuous effective cooling region.

The Grid configuration (Figure 54 (c)) provides the most uniform and effective coolant coverage among the three configurations. Compared with the Parallel and Perpendicular configurations, the cooling voids are distributed in both the spanwise and streamwise directions, resulting in a higher effective tortuosity. Consequently, both lateral spreading and downstream penetration of the coolant are enhanced, leading to a larger effective cooling area and a more continuous coolant film over the cooled surface. Unlike the Perpendicular configuration, the $\eta_{ad} = 0.15$contour remains continuous even at the lowest injection ratio ($F = 0.68\%$). In addition, the persistent uncooled region observed in the Parallel configuration is absent, demonstrating improved spanwise coolant coverage and downstream film development. This behavior indicates a more uniform distribution of coolant across the surface and demonstrates the superior cooling performance of the Grid configuration.

5.4.2.4 Results: Effect of injection ratio on coolant film thickness

Coolant discharged through the cooling voids forms a coolant film over the surface, creating a region of reduced temperature relative to the mainstream flow. This coolant film plays a critical role in protecting the surface from the high thermal loads encountered in combustion environments. Owing to the temperature difference between the coolant and mainstream flow, a thermal boundary layer develops, resulting in a distinct temperature gradient across the coolant–mainstream interface. To quantify the thermal boundary-layer thickness δ_t s at different streamwise locations, a dimensionless temperature parameter was introduced. Following the conventional boundary-layer thickness criterion [105], the thermal boundary-layer thickness $\delta_t$was defined as the location where $\theta(z) = 0.99$:

$$\theta(z) = \frac{(T(z) - T_c)}{(T_\infty - T_c)},\ \delta_t : 0.99\theta(z) \qquad (27)$$

Here, $\theta(z)$ represents the dimensionless temperature, where $T(z)$ is the local fluid temperature measured along the wall-normal direction at a specified streamwise location. Values of θ(z) range from 0 when $T(z)$ is equal to the coolant temperature (T_c) to 1 when $T(z)$ reaches the mainstream temperature (T_∞), with intermediate values describing the thermal mixing region between the coolant and mainstream flows. The thermal boundary-layer thickness, δ_t, is defined as the location where $\theta(z) = 0.99$, corresponding to a recovery of 99% of the mainstream temperature. However, the thermal boundary-layer thickness alone may not adequately capture variations in coolant-film development, as it primarily represents the outer extent of the thermal field. Therefore, following Chen et al. [106], an additional coolant-film thickness parameter, δ_{cf}, was introduced and defined at $\theta(y) = 0.85$. The coolant-film thickness,δ_{cf}, represents the region more strongly influenced by coolant flow than δ_t because it is located within the thermal boundary layer. Therefore, it provides a more sensitive indicator of coolant–mainstream flow interaction than the overall thermal boundary-layer thickness alone

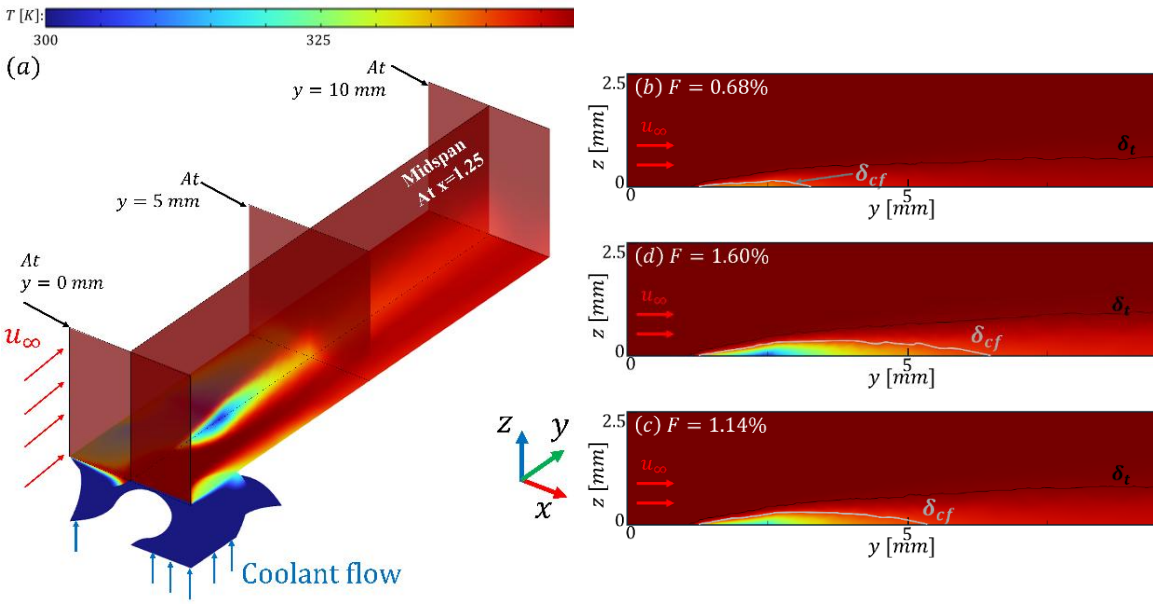

Figure 55 Temperature contours visualizing coolant film development at different injection ratios. (a) Isometric view. (b–d) Temperature contours at the mid-span plane for (b) F=0.68%, (c) F=1.14%, and (d) F=1.60%, with $\boldsymbol{\delta_t}$ (black contour) and $\boldsymbol{\delta_{cf}}$ (gray contour).

Figure 55 illustrates the coolant-film development for the Parallel configuration at different injection ratios on the midspan plane. The thermal boundary-layer thickness, δ_t, exhibits only a modest increase with increasing injection ratio, suggesting that the overall thermal field remains largely unchanged. However, the coolant-film thickness, δ_{cf}, increases substantially in both the wall-normal (z) and streamwise (y) directions. The growth of δ_{cf} with increasing injection ratio demonstrates the progressive enhancement of coolant-film formation. A more detailed investigation of the thermal boundary layer and coolant film thickness was conducted by comparing the profile at different injection ratios, as shown in Figure 56

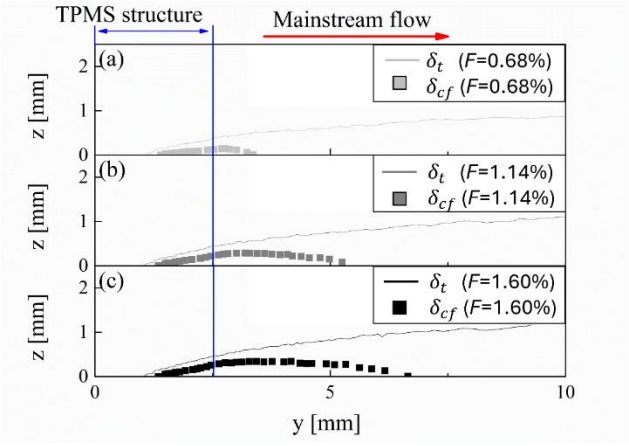

Figure 56 Streamwise distributions of the thermal boundary-layer thickness ($\boldsymbol{\delta_t}$) and coolant-film thickness ($\boldsymbol{\delta_{cf}}$) for the Parallel configuration at injection ratios of (a) $\boldsymbol{F = 0.68\%}$, (b) $\boldsymbol{F = 1.14\%}$, and (c) $\boldsymbol{F = 1.60\%}$.

The thermal boundary-layer thickness, δ_t, gradually increased along the streamwise direction, reaching z= 0.86 mm, 1.10 mm, and 1.19 mm at $y \approx 10$mm for $F = 0.68\%$, 1.14%, and 1.60%, respectively. The increase in δ_t is attributed to the greater amount of coolant supplied to the surface at higher injection ratios, which promotes the formation of a thicker coolant layer. Notably, the increase in δ_t is more pronounced between $F = 0.68\%$and $F = 1.14\%$ than between $F = 1.14\%$and $F = 1.60\%$, indicating that the enhancements in film cooling effectiveness do not correlate linearly with coolant flow rates and that returns diminish at higher injection ratios [107]

For δ_{cf}, the maximum coolant-film thickness occurred near the trailing edge of the TPMS structure ($y \approx 2.5$ mm), reaching 0.15 mm, 0.28 mm, and 0.39 mm for $F = 0.68\%$, 1.14%, and 1.60%, respectively. Downstream of the TPMS structure, δ_{cf} progressively diminished due to coolant–mainstream mixing and disappeared at approximately $y = 3.40$, 5.54, and 6.67 mm, respectively. The increase in both the maximum film thickness and persistence length indicates that higher injection ratios promote the formation of a thicker and more persistent coolant film, thereby enhancing downstream surface protection. Notably, no coolant-film detachment was observed throughout the investigated range.

5.4.2.5 Results: Effect of morphological variation on coolant film thickness

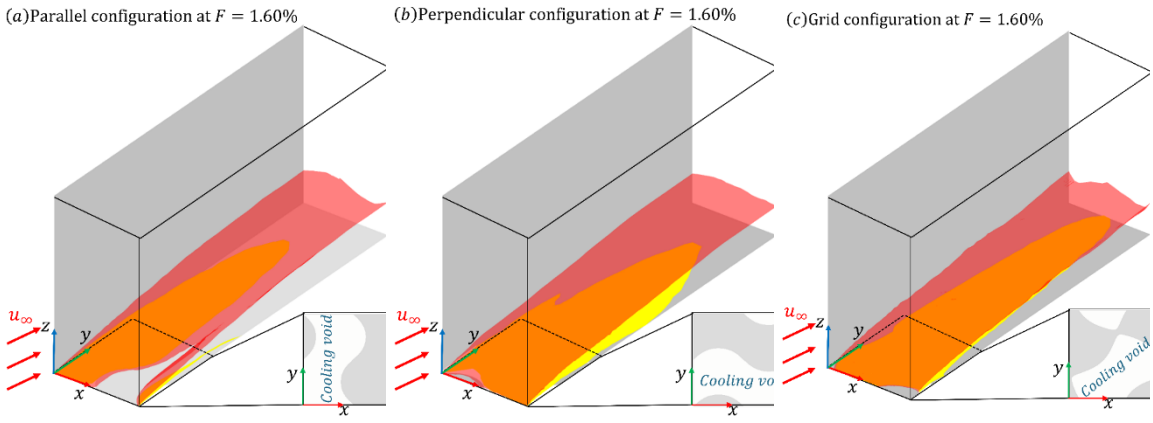

Figure 57 Isosurfaces visualizing of $\boldsymbol{\delta_t}$ (Red) and $\boldsymbol{\delta_{cf}}$ (Yellow) at an injection ratio of F=1.60%, for three different morphological configurations: (a) Parallel, (b) Perpendicular, and (c) Grid.

Figure 57 visualizes coolant-film development using temperature isosurfaces corresponding to δ_t (red) and δ_{cf} (yellow) at an injection ratio of $F = 1.60\%$ for the three morphological configurations. In the Parallel configuration (Figure 57 (a)), a persistent strip-like uncooled region is observed between adjacent cooling voids, even at $F = 1.60\%$. The alignment of the cooling voids with the mainstream flow causes the coolant to be transported predominantly in the streamwise direction while restricting lateral spreading, resulting in insufficient coolant coverage in the inter-void region. Consequently, persistent uncovered regions remain near the leading edge, indicating insufficient coolant coverage to establish both the thermal boundary layer (δ_t) and the coolant film (δ_{cf}).

In contrast, the Perpendicular configuration (Figure 57 (b)) exhibits complete spanwise coverage of both the thermal boundary-layer (δ_t) and coolant-film (δ_{cf}) isosurfaces across the entire surface width (x = 0–2.5 mm), eliminating the uncovered regions observed in the Parallel configuration. This improvement results from the reorientation of the cooling voids perpendicular to the mainstream flow direction and enables a more uniform distribution of coolant across the surface.

The Grid configuration (Figure 57 (c)) exhibits complete spanwise coverage and the greatest downstream extent of both the δ_t and δ_{cf} isosurfaces among the three configurations. Owing to its higher effective tortuosity, enhancing both lateral spreading and downstream film

development. As a result, it achieves the most uniform and persistent coolant-film coverage, indicating superior cooling performance relative to the Parallel and Perpendicular configurations. A more detailed investigation of the thermal boundary layer and coolant film thickness was conducted by comparing the profile at different injection ratios, as shown in Figure 58.

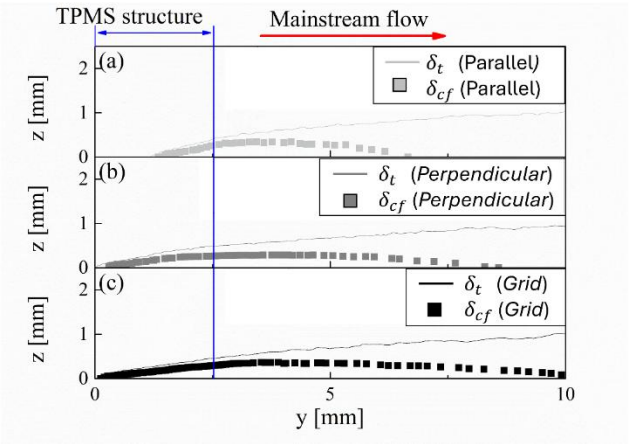

Figure 58 Streamwise distributions of the thermal boundary-layer thickness ($\boldsymbol{\delta_t}$) and coolant-film thickness ($\boldsymbol{\delta_{cf}}$) under different surface configurations at *F*=1.60%: (a) Parallel, (b) Perpendicular, and (c) Grid.

The thermal boundary-layer thickness, δ_t, exhibits no significant variation among the morphological configurations at the same injection ratio. In contrast, the coolant-film thickness, δ_{cf}, increases progressively with morphological complexity, reaching maximum values of 0.39 mm, 0.44 mm, and 0.47 mm for the Parallel, Perpendicular, and Grid configurations, respectively. Similarly, the downstream persistence length of δ_{cf} increases from approximately $y = 6.67$mm for the Parallel configuration to $y = 8.59$ mm and $y = 9.91$ mm for the Perpendicular and Grid configurations, respectively. These results indicate that morphological variations primarily influence coolant-film formation and persistence rather than the overall thermal boundary layer. Considering that practical gas-turbine combustors are exposed to highly directional mainstream flows generated by swirlers and complex geometric curvatures, the Grid morphology appears particularly attractive because it maintains uniform coolant distribution and sustained coolant-film development despite changes in surface texture.

5.4.2.6 Conclusion

This study aims to systematically investigate the influence of TPMS morphological variations on transpiration-cooling performance through combined experimental and numerical approaches. Three TPMS lattice types—Diamond, Koch, and Gyroid—were examined to identify morphological characteristics that minimize sensitivity to surface-texture variations and enable robust cooling performance in complex hot-gas path components. Experimental measurements were performed using the pressure-sensitive paint (PSP) technique, while numerical analyses were conducted using steady-state Reynolds-averaged Navier–Stokes (RANS) simulations.

The experimental results showed that the Diamond-type demonstrated the highest sensitivity to morphological variations, showing significant improvements in cooling effectiveness as surface void patterns transitioned from Parallel to a Grid configuration. This sensitivity is linked to substantial changes in effective tortuosity (τ_{eff}) on the top surface. Conversely, the Koch-type TPMS exhibited minimal sensitivity to morphological variations, maintaining consistently high τ_{eff} across different morphological variations, attributed to inherently complex and interconnected void structures. However, morphological insensitivity alone does not guarantee optimal cooling effectiveness, as transpiration cooling performance is influenced by additional factors such as pressure drop and internal flow distribution. For instance, the Diamond-type, despite its higher morphological sensitivity, consistently achieved superior cooling effectiveness compared to the Gyroid-type across morphological variations. The Gyroid-type TPMS, while displaying moderate morphological sensitivity, showed lower overall cooling effectiveness due to its relatively simple internal channels, resulting in too low percentage pressure drop and undesirable lateral coolant movement.

Numerical simulations provided further insight into the mechanisms underlying the experimental observations and supported the experimental trends. The results showed that increasing the injection ratio enhanced coolant-film development, leading to greater coolant-film thickness (δ_{cf}) and extended downstream persistence. This behavior was attributed to the increased coolant supply, which promoted the formation of a thicker coolant layer over the protected surface. The simulations also demonstrated that TPMS morphological variations significantly influence spanwise coolant-film coverage and coolant-film thickness. In the Parallel configuration, a persistent strip-like uncooled region remained between adjacent cooling voids because the cooling voids were aligned parallel to the mainstream flow direction, restricting lateral coolant spreading.

Transitioning from the Parallel to the Perpendicular configuration eliminated the uncovered region because the surface voids were reoriented perpendicular to the mainstream flow direction, enabling more uniform coolant discharge across the spanwise direction and enhancing lateral coolant dispersion. The Grid configuration provided the greatest enhancement in both spanwise coverage and downstream persistence, resulting in the most effective coolant-film formation among the investigated TPMS morphologies. This superior cooling performance is attributed to its highest effective tortuosity, which increases the degree of misalignment between the surface-void pattern and the mainstream flow direction, thereby promoting more uniform coolant distribution and sustained coolant-film development.

A combined evaluation of the experimental and numerical results confirms that the Koch-type TPMS is the most suitable candidate for transpiration cooling in gas-turbine components, offering both minimal sensitivity to morphological variations and the highest overall cooling effectiveness. Owing to its inherently complex and highly interconnected void network, the Koch-type TPMS maintains high effective tortuosity across different morphological configurations, promoting uniform coolant distribution and sustained coolant-film development. Consequently, it represents a promising solution for transpiration-cooled turbine liners operating under highly directional mainstream flows and complex surface curvatures, where morphology-induced surface-texture variations are unavoidable.

5.5 The Influence of Internal Tangential Flow on Transpiration Cooling

Despite systematic efforts in previous studies to optimize TPMS-based transpiration cooling, several unresolved challenges remain. As reported by Hinse et al. [108], when a high-speed mainstream flow (33 m/s) passes over a porous medium, viscous shear at the porous surface entrains the coolant inside the TPMS through its interconnected internal channels toward the downstream region. A similar mechanism may occur in TPMS structures, given their fully interconnected internal channels. Such internal tangential flow can promote downstream coolant migration inside the TPMS, leading to non-uniform coolant distribution and the formation of localized hot spots, particularly near the leading-edge region.

Although various mitigation strategies have been proposed in the literature [90–92], a systematic investigation providing both quantitative and qualitative insights into the impact of internal tangential flow on cooling performance remains lacking. In response, the present study examines the influence of internal tangential flow in TPMS-based transpiration cooling systems by introducing partition walls perpendicular to the mainstream flow direction to suppress internal tangential fluid motion.

The primary objective of this study is to verify the existence of internal tangential flow by comparing TPMS configurations with and without partition walls, and to evaluate its influence on transpiration-cooling performance through experiments and pore-scale numerical simulations. The results establish that TPMS structures should be designed to suppress internal tangential flow, for example by incorporating partition walls or other flow-interruption features, to promote earlier coolant-film formation and more uniform coolant distribution.

This study is currently under review as a full-length research article in the International Journal of Heat and Mass Transfer.

International Journal of Heat and Mass Transfer

Confirming Internal Tangential Flow in Porous Media in Diminishing Transpiration Cooling Film Effectiveness

Juchan Son, first author

University of Ottawa, Ottawa, Canada

Department of Mechanical Engineering, University of Ottawa, 161 Louis-Pasteur Private, K1N 6N5, Ottawa, Ontario, Canada

National Research Council of Canada, Ottawa, Canada

Aerospace Research Center, National Research Council of Canada, 1200 Montreal Road, K1A 0R6, Ottawa, Ontario, Canada

Sina Kashanj, second author

National Research Council of Canada, Ottawa, Canada

Aerospace Research Center, National Research Council of Canada, 1200 Montreal Road, K1A 0R6, Ottawa, Ontario, Canada

Patrick Richer, third author

University of Ottawa, Ottawa, Canada

Department of Mechanical Engineering, University of Ottawa, 161 Louis-Pasteur Private, K1N 6N5, Ottawa, Ontario, Canada

Bertrand Jodoin, fourth author

University of Ottawa, Ottawa, Canada

Department of Mechanical Engineering, University of Ottawa, 161 Louis-Pasteur Private, K1N 6N5, Ottawa,

International Journal of Heat and Mass Transfer

Ontario, Canada

Mohsen Brouman, fifth author

National Research Council of Canada, Ottawa, Canada

Aerospace Research Center, National Research Council of Canada, 1200 Montreal Road, K1A 0R6, Ottawa, Ontario, Canada

Zekai Hong[1], sixth author

University of Ottawa, Ottawa, Canada

Department of Mechanical Engineering, University of Ottawa, 161 Louis-Pasteur Private, K1N 6N5, Ottawa, Ontario, Canada

National Research Council of Canada, Ottawa, Canada

Aerospace Research Center, National Research Council of Canada, 1200 Montreal Road, K1A 0R6, Ottawa, Ontario, Canada

ABSTRACT

Transpiration cooling is a promising technique for cooling gas turbine hot-gas path components, offering enhanced cooling film effectiveness compared to state-of-the-art effusion cooling. Traditional porous media, including metallic foams and sintered metals have been studied for transpiration cooling in the past. However, recent developments in additive manufacturing have allowed more accurate and replicable fabrication of porous structures, featuring precisely engineered lattice geometries, such as Triply Periodic Minimal Surface (TPMS) structures. In previous studies, we proposed to use TPMS lattice structures for transpiration cooling focusing on TPMS structure design for

[1] Corresponding author

optimized transpiration cooling performance. However, it was hypothesized that internal tangential flow could develop inside the porous structures, leading to unintended transportation of coolant to downstream areas, resulting in localized and overall reduction of cooling film effectiveness at the leading edge vicinity In this study, a TPMS lattice with thin partition walls designed to obstruct this detrimental internal flow is studied and results are compared to to those obtained when using an identical, non-partitioned TPMS lattice transpiration structure. The influence of the partition walls was evaluated both qualitatively and quantitatively through experimental testing and computational fluid dynamics (CFD) simulations to confirm the hypothesis that this internal flow is responsible for unintended detrimental downstream transportation of coolant.

1. INTRODUCTION

Raising the turbine inlet temperature (TIT) in aero-engines is a key strategy for enhancing power output and thermal efficiency [1,2]. To meet increasing performance demands, TIT has been progressively raised, reaching values as high as 2100 K [3], significantly above the melting point of nickel-based superalloys such as Inconel (Ni-Cr-Fe based) [4]. Accordingly, key gas turbine components such as the combustion liner and turbine blades are exposed to severe thermal loads, and effective thermal management has become a critical focus, not only to extend the lifespan of these components but also to improve overall turbine efficiency. Various thermal management techniques have been developed, including internal cooling[5], impingement cooling [6], and effusion cooling [7–10]. Among these, effusion cooling is regarded as a state-of-the-art technology and is widely implemented, often in combination with thermal barrier coatings [11].

In recent decades, considerable efforts have been directed toward improving the cooling performance of effusion cooling systems. Andreini et al. [12] investigated the effect of injection angle (20°, 30°, and 90°) on the performance of effusion cooling under realistic swirling flow conditions. Their findings showed that a more inclined injection angle (20°) offered superior film coverage, resulting in higher adiabatic film cooling effectiveness and improved stability of the coolant layer. Schmidt et al. [13] conducted an experimental study on film cooling effectiveness using a flat-plate facility under zero pressure gradient conditions. The investigation focused on single-row, inclined injection holes supplied with cryogenically cooled air, comparing streamwise-aligned round holes with compound-angle holes (60°) featuring either round or diffusing exits. By varying hole spacing, blowing ratio, and momentum flux ratio, they found that compound-angle holes, particularly those with diffusing exits, achieved higher overall effectiveness and more

uniform coolant distribution at elevated momentum flux ratios. Furthermore, Pyo et al. [7] investigated the effect of non-zero compound angles with constant pitch on adiabatic film cooling effectiveness using a multi-row cooling hole configuration. Their results indicated that compound angles between 30° and 60° optimized jet penetration and coolant distribution, thereby enhancing cooling performance [8].

In addition, extensive research has been undertaken to optimize both geometric and fluid dynamic parameters influencing cooling performance. Geometric parameters include injection direction [7], pitch spacing [14], hole size [15], and hole shape [16–18], while fluid dynamic parameters such as blowing ratio (BR) [16,17] and density ratio [19,20] have also been extensively studied. Furthermore, a conjugate cooling scheme integrating impingement and effusion cooling has been introduced to maximize cooling performance [21–24]. Cho and Rhee [22] reported that this combined approach significantly enhances surface mass transfer rates, yielding values approximately six to ten times higher than those achieved with effusion cooling alone.

However, turbine inlet temperatures (TIT) are projected to increase further in next-generation aero-engines [25], imposing greater thermal loads on turbine components and potentially reducing their operational lifespan [26]. Consequently, there is growing interest in advanced thermal management strategies capable of withstanding these more extreme conditions. For instance, methods that can maintain high cooling effectiveness across a wide range of conditions, including high blowing ratios, where conventional effusion cooling often suffers from issues such as jet lift-off. In this context, transpiration cooling has emerged as one of the most promising solutions. Transpiration cooling is not a new concept as it was originally proposed in the early 1950s [27,28]. Transpiration cooling operates by discharging coolant through a porous medium. The coolant forms a broad and stable film over the surface, which protects it from the hot mainstream flow by modifying the boundary layer thickness without experiencing film lift-off. At the same time, heat is removed from the porous structure through convection into the coolant flow [27–29]. A variety of stochastically manufactured porous materials, such as sintered powder [30,31], woven mesh wires [32], melt casting [33], perforated plates [34], and composite porous materials [35], have been employed in transpiration cooling systems. Considerable research efforts have been devoted to evaluating their cooling performance [36].

Early applications of powder-sintered porous metals were demonstrated by NASA, where copper was used as the base material to fabricate porous structures with porosities ranging from 25% to 50% for cooling injection panels and combustion chambers in rocket engines through powder sintering[31]. Liu et al. [34] investigated transpiration cooling using a micro-perforated plate under low-temperature and low-speed mainstream conditions. The velocity field was

measured through Particle Image Velocimetry (PIV). The results indicated that coolant injection led to boundary layer thickening and a reduction in the near-wall velocity gradient. An increase in injection rate further augmented the boundary layer thickness.

Despite its demonstrated performance and potential, the practical application of transpiration cooling has remained limited due to inherent challenges associated with conventional porous materials manufacturing. The stochastic nature of pore distribution in traditionally manufactured media often results in local hot spots and structural weaknesses. Furthermore, achieving precise control over pore size and spatial distribution to mitigate these issues remains extremely difficult, if not unfeasible with traditional fabrication techniques [37].

Recent advances in additive manufacturing, particularly 3D printing, have addressed some of these limitations by enabling the fabrication of deterministic porous structures with uniform and repeatable lattice geometries. Among various architectures, triply periodic minimal surface (TPMS) structures have garnered significant attention due to their highly regular geometry, mechanical robustness, and favorable flow characteristics. As a result, TPMS-based porous media are increasingly being explored across a wide range of engineering applications [38]. TPMS structures possess fully interconnected internal channels with smooth, continuous surfaces, and their high surface-area-to-volume ratio makes them particularly well-suited for applications involving heat transfer and cooling [39–41].

Broumand et al. [42] investigated transpiration cooling using TPMS structures with three different porosity levels (30%, 40%, and 50%), comparing their performance to that of conventional effusion cooling under identical injection ratios (F). The study showed that TPMS-based transpiration cooling mitigates cooling jet lift-off, a common issue in effusion cooling, and can achieve adiabatic film cooling effectiveness values approaching unity when fully developed. Moreover, at the highest injection ratio, it demonstrated more than a fivefold improvement in overall adiabatic film cooling effectiveness compared to effusion cooling. Yeranee et al. [43] conducted experimental and numerical investigations of a ridge–vortex cooling chamber integrated with a diamond-type TPMS effusion design for turbine blade leading edges. Compared with conventional vortex-film cooling, the proposed configuration achieved up to 21.8 % higher overall cooling effectiveness and improved temperature uniformity without additional pressure loss, demonstrating the strong potential of additively manufactured TPMS-based effusion cooling for advanced turbine applications. In addition, previous studies conducted by the present author evaluated the effects of various TPMS geometrical features on cooling performance, such as unit cell size[44], orientation angle[45], and morphological variations[46]. Investigation of the effect of unit cell size on cooling performance revealed that smaller unit cells lead

to improved performance, even when overall porosity remains constant [44]. This enhancement is primarily attributed to a more uniform distribution of coolant mass flow along the mainstream direction and surface textures that promote the stable formation of a cooling film. The influence of TPMS lattice orientation angle was also examined and showed that the Koch-type TPMS lattice exhibited minimal sensitivity to orientation angle variation while maintaining the highest overall film cooling effectiveness [45]. Further investigation into morphological variations [46] showed that surface patterning induced by geometric modifications can substantially affect cooling behavior. Among the tested configurations, the Koch-type structure again demonstrated superior performance, owing to its ability to sustain an adequate pressure drop and efficient coolant distribution, while also exhibiting relative insensitivity to morphological perturbations.

Despite sustained investigation, the optimization of transpiration cooling employing TPMS structures has yet to be fully achieved, especially concerning flow behavior at the pore scale. Zhou et al [47]. conducted pore-scale simulations and experiments to investigate the influence of pore geometry on TPMS-based transpiration cooling. Their results showed that pore shape significantly affects cooling performance

In a previous study, the effect of unit cell size on transpiration cooling performance was examined using three different unit cell sizes in Diamond-type TPMS structures [44]. The results revealed that larger unit cells led to a deterioration in cooling performance and a more pronounced non-uniformity between the leading and trailing regions. The authors hypothesized that this behavior could be attributed to internal tangential flow effects. This observation is consistent with the findings of Hinse et al [33]., who reported that when a high-speed mainstream flow (33 m/s) passes over a porous medium, the injected coolant tends to be entrained toward the downstream region due to viscous effects. A similar phenomenon may occur in TPMS structures, as their internal channels are fully interconnected. Such internal tangential flow could lead to non-uniform coolant distribution and result in localized hot spots.

However, to the authors' best knowledge, a systematic investigation providing both quantitative and qualitative insights into the effects of internal tangential flow on cooling performance is still lacking, particularly in TPMS structures. As part of a systematic effort to evaluate the influence of internal tangential flow, the present study investigates how this flow phenomenon affects the performance of TPMS-based transpiration cooling. To achieve this, partition walls are introduced within the TPMS structure perpendicular to the mainstream flow direction. The present study experimentally and numerically investigates how the presence of these walls affects the cooling performance of Diamond-type TPMS structures with a large unit cell size (Lc = 3.1 mm).

The results aim to deepen the understanding of the interaction between internal tangential flow and adiabatic film cooling effectiveness in TPMS-based transpiration cooling and to provide design guidance for performance optimization.

2. EXPERIMENT SETUP

2.1 TPMS structure

Triply Periodic Minimal Surface (TPMS) structures exhibit a wide range of geometries, including Diamond, Primitive, Gyroid, Koch, and Neovius types, to name a few [48]. Among these, the Diamond type structure, originally introduced by Schwarz in 1865 [49], is frequently adopted as a representative TPMS owing to its geometric simplicity, high symmetry, and favorable mechanical characteristics. Consequently, it has been extensively studied and widely applied in various engineering fields. The Diamond type TPMS structure is mathematically formulated within the Cartesian coordinate system, as given below.

$$\emptyset(x,y,z) = \sin(X)\sin(Y)\sin(Z) + \sin(X)\cos(Y)\cos(Z) + \cos(X)\sin(Y)\cos(Z) + \cos(X)\cos(Y)\sin(Z) = c \quad (1)$$

The capital letters (X, Y, and Z) denote non-dimensionalized spatial coordinates, derived by scaling the physical coordinates x, y, and z by the unit cell sizes α, β, and γ, respectively:

$$X = \frac{2\pi x}{\alpha}, Y = \frac{2\pi y}{\beta}, and, Z = \frac{2\pi z}{\gamma} \quad (2)$$

Assuming isotropy to leverage the geometric symmetry of the TPMS, this study sets α=β=γ=Lc. The iso-surface, or boundary surface, is defined as the set of points that satisfy the level-set equation for a given constant c. For example, when $c = 0$, Equation (3) yields a unit cell with a porosity of 50%.

$$\emptyset(x,y,z) < c \quad (3)$$

Figure 1 illustrates the geometry of a TPMS unit cell with 50% porosity. The parameter Dp in the figure denotes the pore diameter, defined as the diameter of the largest sphere that can pass through the narrowest channel within the structure [50].

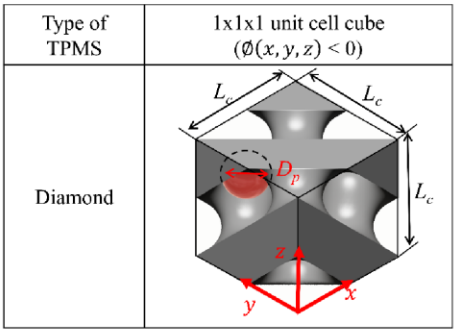

Fig. 1 Unit cell cube of the Diamond type TPMS solid network with 50% porosity.

2.2 Test coupon design

All test coupons based on the Diamond type solid network, with and without partition walls, were fabricated using a stereolithography (SLA) 3D printer with identical unit cell size (L_c = 3.1 mm), actual porosity (ε_a= 36%), pore diameter (D_p=1 mm) and wetted surface area to volume ratio (λ=18.7 cm2/cm3). Consequently, the sole variable in this study is the existence of partition walls. Each configuration was fabricated as a circular test coupon, as shown in Figure 2, with a diamond-type TPMS lattice embedded within the active region. The total active area measured approximately 6.6 cm × 7.0 cm. To minimize the influence of the side wall effect only the central portion of the surface was considered for visualization. The observation area, indicated in blue in Figure 2, was defined as a 2.5 cm × 7.0 cm rectangular region.

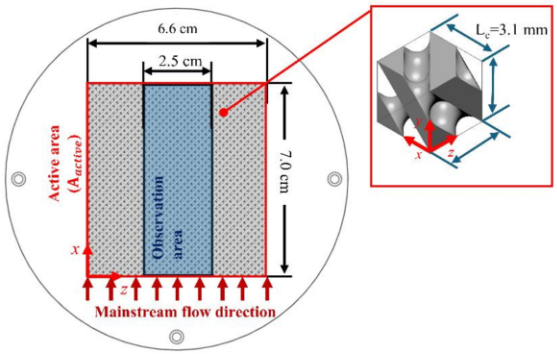

Fig. 2 Schematic of test coupon with an active area featuring TPMS lattice

The partition walls was oriented perpendicular to the mainstream flow to inhibit coolant migration along the flow direction within the porous medium, thereby promoting redirection of the coolant toward the top surface. Two TPMS

test coupons based on the diamond type were designed and fabricated with different configurations: a baseline case without partitions wall, and with partition walls case. The partition wall thickness was set to 0.1 mm, which does not significantly affect the porosity, allowing the average porosity to be considered unchanged across configurations. Figure 3 illustrates the observation area configuration for two different configurations of TPMS structures: (a) without partition walls, (b) with a partition walls. As shown in Figure 3, the inserted partition walls is oriented perpendicular to the mainstream flow direction, thereby inhibiting tangential coolant migration within the TPMS structure. The partition walls are spaced in the streamwise direction at intervals equal to one unit-cell length.

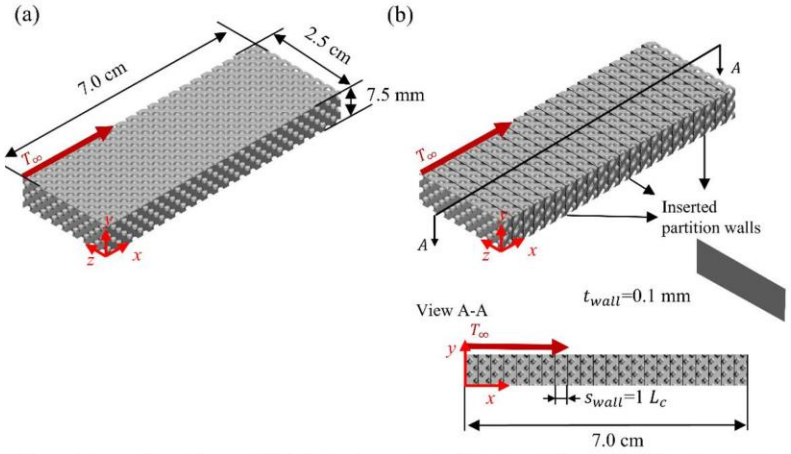

Fig. 3 Geometric configurations of TPMS structures: (a) without partition walls (b) with partition walls inserted perpendicular to the mainstream flow direction, with a pitch equal to one unit cell length.

2.3 Experiment setup

An open-loop, low-speed wind tunnel was employed to evaluate the transpiration cooling performance of TPMS structures. The mainstream flow, supplied by a 30 kW fan, was maintained at 33 m/s, corresponding to a Reynolds number of approximately 256,000, which is representative of conditions in a gas turbine combustor. Additionally, the turbulence intensity within the test section is estimated to be approximately 3%. The coolant proxy was inert nitrogen (N_2), supplied through compressed gas bottles. The coolant flow was regulated by an OMEGA FMA 5400A/5500A series flow controller, capable of adjusting the flow rate between 0 and 200 standard liters per minute (SLPM). The coolant flow was initially directed to a coolant reservoir, where it was conditioned by a honeycomb screen and a perforated plate to promote uniform distribution to the active area of the test coupon. The dashed and dotted lines

inside the reservoir in Figure 4 indicate the locations of the perforated plate and honeycomb, respectively. The reservoir has an internal diameter of 101.6 mm and a height of 44.5 mm.

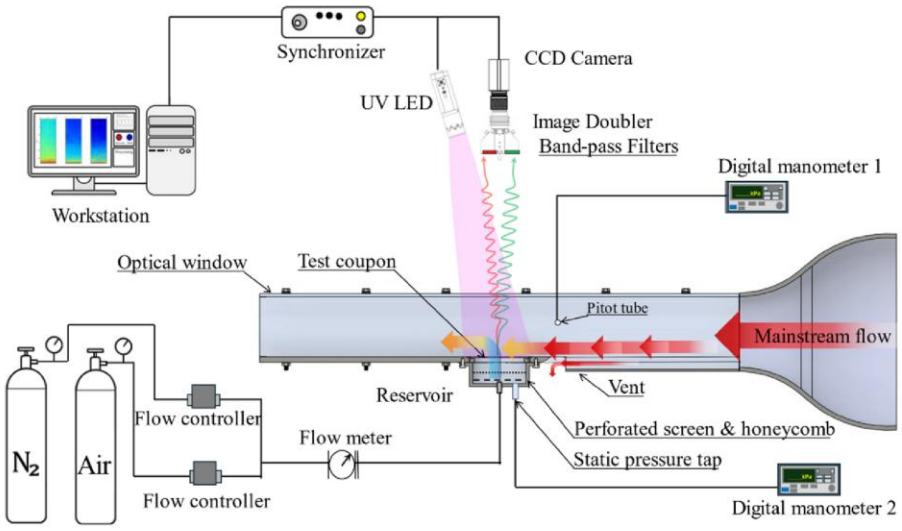

Fig. 4 Schematic of the experimental setup.

In this study, a binary pressure-sensitive paint (PSP) supplied by ISSI was employed to measure adiabatic film cooling effectiveness. The use of PSP for film cooling investigations has been described in detail in our previous works [35,36]. The PSP was applied to the top surface of the test coupon without obstructing the internal channels. The combined thickness of the PSP and base coating was estimated to be less than 20 μm [51]. Consequently, the PSP layer introduces only negligible alterations to the geometry of the TPMS lattices near the top surface of the test coupon.

A key advantage of binary PSP is its ability to enable in-situ, high-resolution measurement of the two-dimensional distribution of film cooling effectiveness while eliminating temperature dependency through the ratio of two signals: one corresponding to oxygen partial pressure and the other serving as a reference. The fluorescence emitted by the oxygen-sensitive molecule near 650 nm and the reference emission near 550 nm can be spectrally separated to avoid overlap. Details of the methodology for film cooling effectiveness measurements using PSP are provided in the next section. An air-cooled UV LED array (ISSI LM2X-DM-400), centered at 400 nm, was used to excite the PSP. The resulting luminescent intensity was recorded using a CCD camera (LaVision Image ProX 2M) equipped with an image

doubler (LaVision) and fitted with bandpass filters for each lens. The filters were centered at 550 nm with a 10 nm full-width at half-maximum (FWHM) and at 650 nm with a 20 nm FWHM.

2.4 Operating Conditions

The operating conditions in this study were selected to reflect coolant usage over an equivalent surface area under representative modern aero-engine environments, corresponding to blowing ratios (BR) of 0.6, 1.0, and 1.4 [8,42]. The blowing ratio is defined as follows:

$$BR = (\rho u)_c/(\rho u)_\infty \tag{4}$$

where ρ and u denote the density and velocity, respectively, and the subscripts c and ∞ refer to the coolant and mainstream flow. The mainstream flow velocity was fixed at 33 m/s, while the coolant velocity was calculated based on the coolant volumetric flow rate ($\dot{Q}_c$), the active surface area (A_{active}) shown in Figure 2, and the surface porosity ($\varepsilon_{surface}$) of the test coupon.

$$u_c = \frac{\dot{Q}_c}{A_{active}\varepsilon_{\text{surface}}} \tag{5}$$

In typical transpiration cooling, the surface porosity is substantially higher than that of effusion cooling systems. Consequently, for an equivalent coolant volumetric flow rate, the coolant velocity is considerably reduced, resulting in a lower blowing ratio compared to effusion cooling. As such, the conventional blowing ratio is not well suited to characterize test conditions in transpiration cooling studies. To overcome this limitation, the present study utilizes the injection ratio (F) as an alternative parameter for describing the cooling condition. The definition of F is provided below.

$$F = \frac{\dot{m}_c}{(\rho u)_\infty A_{active}} \tag{6}$$

where $\dot{m}_c$ is the coolant mass flow rate. In this study, the active area was maintained to match that used in previous transpiration and effusion cooling investigations [8,42]. Injection ratios were selected as $F = 0.68\%$, 1.14%, and 1.60%, corresponding to the coolant mass flow rates used in baseline effusion cooling cases with the same active area at blowing ratios of 0.6, 1.0, and 1.4, respectively.

2.5 Experimental Methodology

In this study, a binary pressure-sensitive paint (PSP) provided by ISSI was employed to measure the adiabatic film cooling effectiveness. The use of PSP for investigating film cooling behavior has been extensively documented in previous studies [52–54]. By invoking the heat and mass transfer analogy, the adiabatic film cooling effectiveness (η_{ad}) was evaluated using the following equation:

$$\eta_{ad} = (T_\infty - T_{ad})/(T_\infty - T_c) \tag{7}$$

$$\eta_{ad} \approx \frac{C_{O2,air} - C_{O2,mix}}{C_{O2,air}} = 1 - \frac{1}{1 + \frac{MM_c}{MM_{air}}\left[\frac{(X_{o_2,air})}{(X_{o_2,mix})} - 1\right]} = 1 - \frac{1}{1 + \frac{MM_c}{MM_{air}}\left[\frac{(P_{o_2})_{air}}{(P_{o_2})_{mix}} - 1\right]} \tag{8}$$

where T_∞, T_{ad}, and T_c are the mainstream, adiabatic wall, and coolant temperatures, respectively. By adopting PSP to measure η_{ad}, Equation (7) can be reformulated in terms of the ratio of oxygen mass concentrations obtained from PSP measurements. Specifically, $C_{O_2,\text{air}}$ and $C_{O_2,\text{mix}}$ represent the oxygen mass concentrations in the mainstream air and the air–nitrogen mixture near the test surface, respectively, while $X_{O_2,\text{air}}$ and $X_{O_2,\text{mix}}$ denote the corresponding mole fractions. MM_{air} and MM_c are the molecular weights of air and coolant, wtith nitrogen used as the coolant proxy in this study. Alternatively, the adiabatic film cooling effectiveness can also be expressed as the ratio of the partial pressure of oxygen in the mainstream air ($P_{O_2,\text{air}}$) to that in the air–nitrogen mixture ($P_{O_2,\text{mix}}$), both of which can be determined using PSP [52].

Measuring adiabatic film cooling effectiveness using the binary PSP requires an accurate in-situ calibration. With careful in-situ calibration, the measurement uncertainty can be derived from Equation 8 through uncertainty propagation analysis [55,56]. For cases where the adiabatic film cooling effectiveness is $\delta\eta_{ad}$=0.8 and $\delta\eta_{ad}$=0.2, the relative measurement uncertainties were estimated to be $\delta\eta_{ad}$=±1.48% and $\delta\eta_{ad}$ =±6.46%, respectively.

Measurement uncertainties of instruments utilized in the experiment are as follows: flow meter (OMEGA FMA5400A/5500A-series); ±1.5% of reading, and pressure transducer (Druck DPI 142); ±0.01% of full scale.

3. EXPERIMENTAL RESULTS AND DISCUSSION

To investigate and confirm the presence of coolant migration along the flow direction within the porous media, the adiabatic film cooling effectiveness (AFE) was measured using pressure-sensitive paint (PSP) for TPMS

configurations with and without partition walls. For both cases, two-dimensional distributions of AFE were measured under three different injection ratio (F) conditions, as shown in Figure 6.

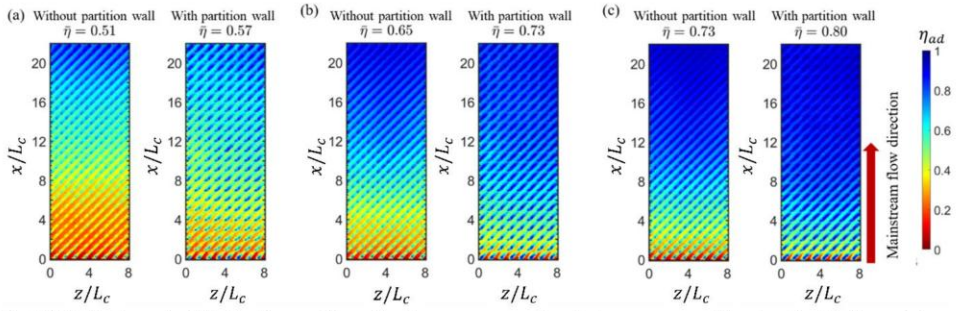

Fig.6 Distribution of adiabatic film cooling effectiveness comparison between cases without and with (S_{wall}=1.0 L_c) a partition wall at varying injection ratios(F): (a) F=0.68%, (b) F=1.14%, and (c) F=1.60%; overall averaged adiabatic film cooling effectiveness is denoted in the title of the sub-panels.

All test coupons maintained a constant actual porosity of 36% and a fixed unit cell size of L_C = 3.1 mm. Therefore, the absence or presence of partition walls was the only variable in this study. The color bar represents the adiabatic film cooling effectiveness (η_{ad}), where red indicates lower effectiveness and blue corresponds to higher effectiveness. The x and y axes in Figure 6 were non-dimensionalized by the unit cell length. The mainstream flow direction is indicated by the red arrow in Figure 6.

From a transpiration cooling perspective, an ideal scenario involves rapid coolant film development near the leading edge, followed by early attainment of a plateau in cooling effectiveness. However, as shown in Figure 6, in the configuration without partition walls, coolant film development is delayed compared to the partitioned configuration, resulting in lower adiabatic film cooling effectiveness, particularly in the upstream region (x/L_c<10). Furthermore, the non-partitioned configuration also exhibits a sudden increase in cooling effectiveness near the trailing edge. This behavior is attributed to internal tangential flow within the porous medium, which transports coolant downstream from the leading edge toward the trailing edge, leading to excessive coolant discharge in the downstream region.

In contrast, the configuration with partition walls exhibits significantly improved adiabatic film cooling effectiveness in the upstream region (x/L_c<10) compared to the case without partition walls. This improvement is attributed to the suppression of tangential coolant migration within the internal channels of the TPMS structure through the implementation of partition walls, thereby promoting coolant discharge toward the surface in the intended injection

direction. The discharged coolant, with tangential migration effectively suppressed, forms a cooling film on the top surface near the leading edge without delay. As a result, a more uniform coolant distribution across the surface is achieved.

A more detailed analysis was conducted through the spanwise-averaged adiabatic film cooling effectiveness as presented in Figure 7. Since the cooling void region on the top surface was predominantly covered by coolant, including it in the averaging process could skew the comparison of adiabatic film cooling performance. Therefore the cooling void region on the top surface was excluded in averaging process to evaluate partition walls effect more precisely. The blue line represents the configuration with partition walls, while the orange line corresponds to the configuration without partition walls. The shaded regions indicate the difference between the two configurations at each streamwise location. For example, the blue-shaded region represents the extent to which the adiabatic film effectiveness in the partitioned configuration exceeds that of the non-partitioned case.

Notably, the blue-shaded region is more pronounced near the leading edge across the all the injection ratio, indicating improved cooling performance with the partitioned configuration in that region. This improvement is attributed to earlier development of the coolant film over the surface through suppression of internal tangential flow, resulting in more uniform adiabatic film cooling effectiveness. However, in the trailing edge region, the adiabatic film effectiveness in the configuration without partition walls increases sharply, forming an orange-shaded region, which is attributed to internal tangential flow within the porous medium. Specifically, coolant is transported downstream within the porous structure due to entrainment by the high-speed mainstream flow (33 m/s), resulting in increased coolant accumulation and discharge near the trailing edge. However, the area of this orange-shaded region decreases as the injection ratio increases. This behavior can be attributed to enhanced coolant film accumulation at higher coolant flow rates. Even without partition walls, the higher coolant flow rate induces a proper pressure-driven discharge toward the surface, thereby reducing the influence of internal tangential coolant migration. As a result, the relative effectiveness gain observed in the non-partitioned case near the trailing edge becomes less pronounced.

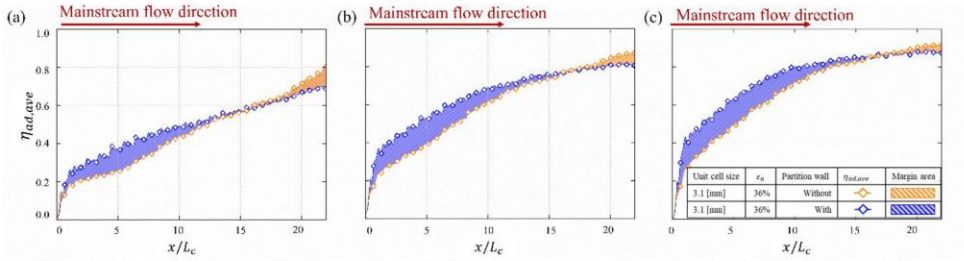

Fig.7 Spanwise averaged adiabatic film cooling effectiveness comparison for without and with partition walls (S_{wall}=1.0 L_c) at varying injection ratios (F): (a) indicate F = 0.68%, (b) indicate F = 1.14%, and (c) indicate F = 1.60%. Shaded regions (Margin area) indicate the local difference between the two cases: blue areas where the partition walls performs better, and orange areas where it performs worse.

Figure 8 quantitatively presents the area-averaged adiabatic film cooling effectiveness ($\bar{\eta}_{ad}$) for configurations with and without partition walls under varying injection ratios. The area-averaged adiabatic film cooling effectiveness is calculated as follows:

$$\bar{\eta}_{ad} = \frac{1}{A_{active}} \int \eta_{ad} \, dA \tag{9}$$

where A_{active} is the active area described in Figure. 2. The effectiveness difference ($\Delta\bar{\eta}_{ad}$) increases with increasing injection ratio. This trend may be attributed to enhanced coolant accumulation and film development near the trailing edge in the partitioned configuration at higher injection ratios, resulting in not only improved effectiveness near the leading edge but also sustained high effectiveness in the trailing edge region.

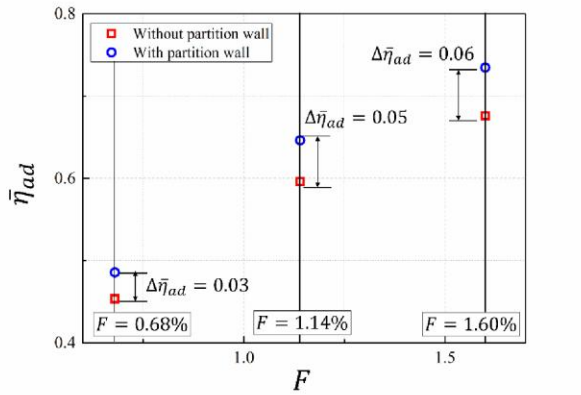

Fig.8 Comparison of area-averaged adiabatic film cooling effectiveness ($\bar{\eta}_{ad}$) for configurations with and without partition walls at different injection ratios.

It is important to note that the characteristic streamwise length of practical combustor liners is significantly greater than that of the observation domain used in this study. Due to the fully interconnected internal channels of TPMS structures, the influence of internal tangential flow is expected to be more pronounced in real engine applications. Consequently, the effectiveness of partition walls is likely to be even more beneficial under real engine conditions.

4. NUMERICAL RESULTS AND DISCUSSION

4.1 Numerical setup

The experimental results discussed in the previous section tend to confirm the existence of internal tangential flow, which significantly affects the transpiration cooling performance of TPMS structures. The introduction of partition walls perpendicular to the mainstream flow direction was found to enhance film cooling effectiveness by suppressing tangential coolant migration within the porous medium. However, PSP measurements are inherently limited to surface-based (2D) evaluations of film cooling effectiveness and do not provide detailed insight into internal coolant transport or film thickness development. To address these limitations, steady-state computational fluid dynamics (CFD) simulations were conducted to gain a deeper understanding of the underlying flow mechanisms. The computational domain consists solely of fluid regions, including the mainstream channel, the TPMS-based porous structure, and the coolant reservoir.

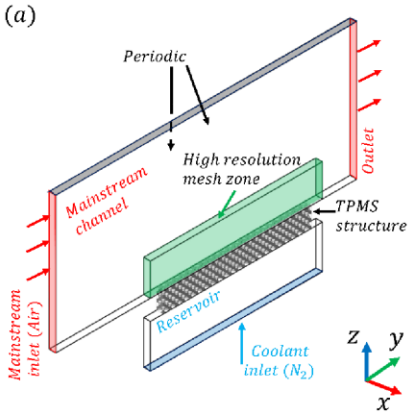

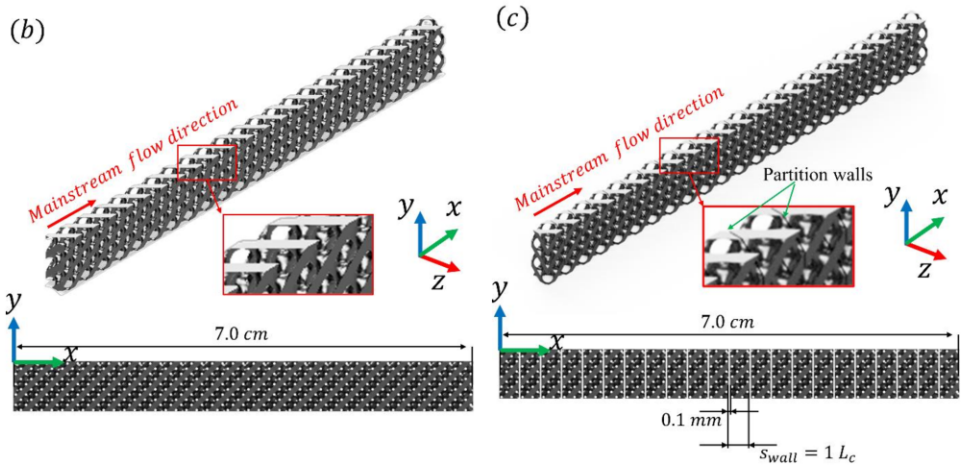

Fig.9 distribution of adiabatic film cooling effectiveness comparison between cases without and with (S_{wall}=1.0 L_c) partition walls at varying injection ratios(F): (a) F=0.68%, (b) F=1.14%, and (c) F=1.60%; overall averaged adiabatic film cooling effectiveness is denoted in the title of the sub-panels.

A constant velocity inlet (u_∞=33 m/s, T_∞=315 K) and a pressure outlet (with a gauge pressure of p=0 Pa) were applied at the inlet and outlet of the channel, respectively, with periodic boundary conditions imposed on the lateral surfaces. A symmetry boundary condition was applied to the top surface of the mainstream channel. Because the experimental test section has a 5 in × 5 in cross-section and is symmetric about the channel mid-plane, only the lower half of the mainstream channel (2.5 in in height) was included in the computational domain. This approach substantially reduces the mesh count and computational cost while maintaining the flow characteristics of the full test section. To replicate the experimental conditions of the PSP-based adiabatic film cooling measurements, only the fluid domains were included in the numerical model. An adiabatic wall boundary condition was imposed on the bottom surface of the mainstream channel to eliminate heat conduction through the wall, while heat transfer within the fluid domain, resulting from thermal mixing between the mainstream and coolant flows, was fully resolved. The bottom boundary of the coolant reservoir was defined as a mass flux inlet supplying pure nitrogen (T_c=300 K), with flow rates corresponding to the experimental injection ratios (F=0.68%, 1.14%, 1.60%). Figures 9 (b) and (c) illustrate the TPMS structures without and with partition walls, respectively. The initial TPMS geometry was generated in MATLAB and exported as an STL (stereolithography) file. As shown in Figure 10, the raw STL geometry (Step 1: STL scripting) contained an excessive number of triangular faces, leading to increased computational cost, high memory demand, and surface irregularities that hindered mesh generation and degraded mesh quality [47]. To address these issues, a

reverse modeling workflow was employed to convert the STL geometry into a high-quality STP (STEP) format. In the cleaning and simplification stage (Step 2), redundant vertices and small-area faces were removed, and the geometry was optimized while preserving essential topological features and boundary edge. Subsequently, in the reverse modeling stage (Step 3), the cleaned STL surface was reconstructed into a NURBS (Non-Uniform Rational B-Splines)-based representation and exported as an STP file. Finally, during the meshing stage (Step 4), the STP geometry was imported, refined, and its internal surfaces were unified into a continuous smooth representation prior to mesh generation for CFD simulations. This workflow significantly improved surface fidelity, reduced mesh generation time, and enabled robust numerical simulations of geometries with complex and small-scale features.

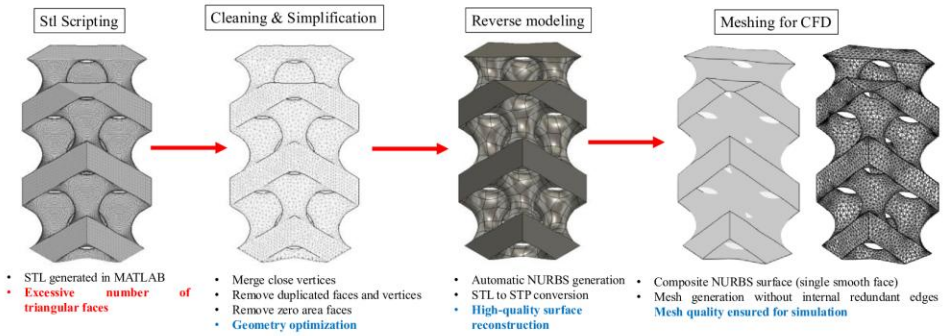

Fig.10 Example Workflow of STL based TPMS geometry conversion to STP for CFD analysis

An unstructured mesh of the computational domain was generated, as shown in Figure 11(a). Sixteen inflation layers were applied at the interface between the mainstream flow and the coolant to accurately resolve near-wall gradients, maintaining y+<1.0. Here, $y^+$is the dimensionless wall distance used to assess the resolution of the near-wall mesh. To evaluate mesh independence, three grid resolutions were tested: Grid 1 (6.2 million cells), Grid 2 (8.0 million cells), and Grid 3 (8.5 million cells). The spanwise-averaged adiabatic film effectiveness was evaluated at an injection ratio of F=0.68%. As shown in Fig. 11 (b), the results for Grid 2 and Grid 3 closely match, with a relative difference of less than 1%, indicating convergence. Therefore, Grid 2 was selected for all subsequent simulations to balance computational cost and accuracy.

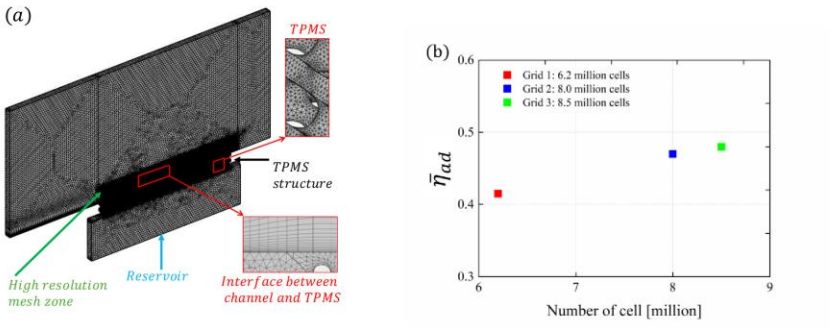

Fig.11 (a) Computational mesh for the Gyroid-type structure, showing boundary-layer refinement near the channel–porous interface and internal surfaces. (b) area-averaged adiabatic film cooling effectiveness for three different grid resolutions at F=0.68% for the configuration with partition walls.

The modeling of turbulent flow constitutes another critical aspect of CFD simulations. Therefore, the validation of Reynolds-Averaged Navier–Stokes (RANS) turbulence models is an essential step and is typically performed through comparison with well-established experimental data. Several turbulence models, including the Standard k-ε, Realizable k-ε, and SST k-ω models, were evaluated for predicting the thermal and flow characteristics of a porous plate subjected to transpiration cooling. As shown in Figure 12, the Realizable k-ε model exhibited the closest agreement with the experimental measurements and most accurately captured the overall trend of the porous plate surface temperature.

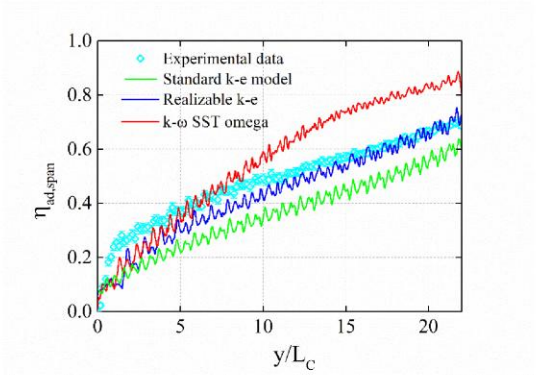

Fig.12 Comparison between CFD and experimental results of spanwise averaged AFE at F=0.68%. Error bars indicate experimental uncertainty.

. The film effectiveness in the leading-edge region is slightly underpredicted. This discrepancy may be attributed to the neglect of surface roughness effects associated with the 3D-printed test coupon, experimental measurement uncertainties, and the inherent limitations of the RANS turbulence model in predicting the complex coolant-mainstream mixing process.

4.2 Numerical setup

In this study, the combination of high-Reynolds-number mainstream flow ($Re_\infty \approx 256{,}000$) and low-Reynolds-number coolant flow within the porous matrix necessitates the selection of an appropriate turbulence model. The coolant Reynolds number within the TPMS structure (Re_{TPMS}) is defined as follows [41]:

$$Re_{TPMS} = \frac{\rho_c u_c d_{h,TPMS}}{\mu_c}, d_{h,TPMS} = \frac{4V}{A_w} \tag{9}$$

where $d_{h,TPMS}$ represents the hydraulic diameter of the TPMS structure, and μ_c is the dynamic viscosity of the coolant. For the Gyroid-type TPMS structure, the coolant Reynolds numbers calculated at the three injection ratios are 78.0 at blowing ratio of *F*=0.68%, 130.1 at *F*=1.14%, and 180.9 at *F*=1.60%. According to the literature, transition from laminar to turbulent flow in porous media typically begins around Re≈300 [57]. Given this range, the SST k-ω turbulence model, which combines the advantages of both the k-ε and k-ω model, was selected [58]. This model accurately resolves both boundary-layer and free-shear flows, making it suitable for analyzing coolant jets interacting with crossflow [59,60]. Numerous studies have also confirmed the efficacy of the SST k- ω model for simulating jets in crossflow scenarios[61,62]. The governing equation was summarized in Table 1.

Table. 1 Governing equations

Governing equation	
The continuity equation	$\nabla \cdot (\rho\vec{u}) = 0$
The momentum equation	$\rho(\vec{u} \cdot \nabla)\vec{u} = -\nabla \mathrm{p}\vec{\mathrm{I}} + \nabla \cdot (\mu + \mu_{\mathrm{T}})(\nabla\vec{\mathrm{u}} + (\nabla\vec{\mathrm{u}})^{\mathrm{T}}) + \vec{F}$
The energy equation	$\rho C_p \vec{u} \cdot \nabla \mathrm{T} + \nabla \cdot (-\mathrm{k}\nabla \mathrm{T}) = \mathrm{Q}$
Turbulent kinetic energy (k) equation	$\rho(\vec{u} \cdot \nabla)\mathrm{k} = \nabla \cdot [(\mu + \mu_T \sigma_{\mathrm{k}})\nabla k] + P - \rho\boldsymbol{\varepsilon}$
Dissipation rate ($\boldsymbol{\varepsilon}$) equation	$\rho(\vec{u} \cdot \nabla)\boldsymbol{\varepsilon} = \nabla \cdot [(\mu + \mu_T \sigma_\omega)\nabla\boldsymbol{\varepsilon}] + \rho C_1 S\boldsymbol{\varepsilon} - \frac{\rho C_2 \boldsymbol{\varepsilon}^2}{\boldsymbol{k} + \sqrt{\boldsymbol{\nu\varepsilon}}}$

These governing equations were numerically solved using COMSOL Multiphysics 6.0 sing a stationary, fully coupled solver. Convergence was achieved when the relative residuals of all dependent variables were reduced below 10^{-5}.

4.3 Numerical results

Figure 13 presents the temperature contours of the mainstream flow channel and the TPMS structure at the lowest injection ratio, for configurations with and without partition walls. To quantify the thermal boundary layer thickness at different streamwise locations, a dimensionless temperature parameter was employed, similar to the recovery factor used in classical boundary layer theory [63]. The dimensionless temperature is defined as

$$\theta(y) = \frac{(T(y) - T_c)}{(T_\infty - T_c)},\ \delta_t{:}\, 0.99\theta(y) \tag{9}$$

Here, θ(y) denotes the dimensionless temperature, and $T(y)$ is the local fluid temperature measured along the wall-normal direction at a given streamwise location. The dimensionless temperature varies from 0 to 1, where $\theta(y) = 0$ corresponds to $T(y) = T_c$(coolant temperature) and $\theta(y) = 1$corresponds to $T(y) = T_\infty$(mainstream temperature). Values between 0 and 1 characterize the temperature transition region within the thermal boundary layer. The thermal boundary layer thickness, δ_t, is defined as the location where $\theta(y) = 0.99$, indicating that 99% of the temperature difference between the coolant and mainstream flow has been recovered. However, the thermal boundary layer thickness alone may not adequately capture variations in coolant-film development, as it primarily represents the outer boundary of the thermal field. Therefore, following Chen et al[64]., an additional coolant-film thickness parameter, δ_{cf}, was introduced and defined at $\theta(y) = 0.75$.

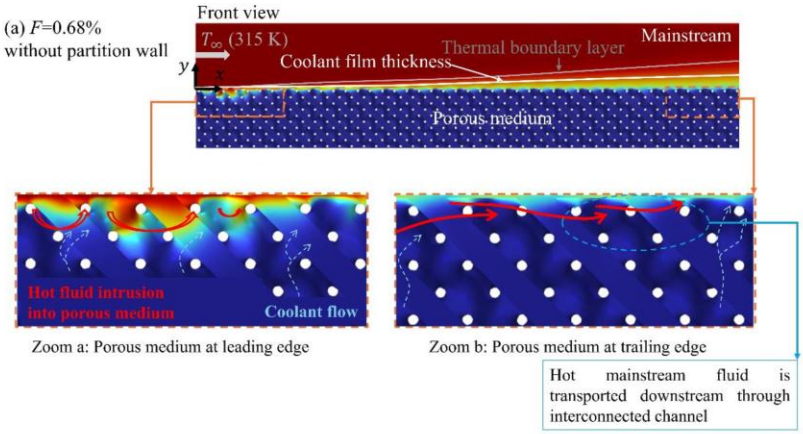

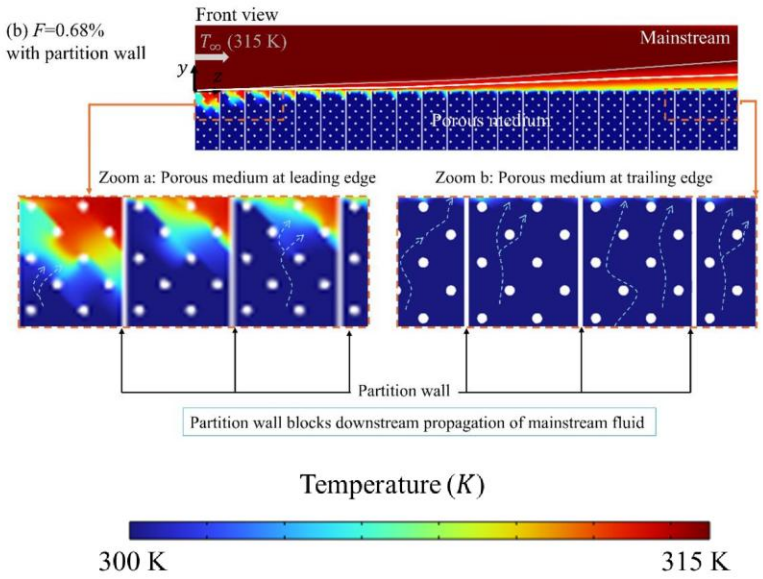

Fig.13 Temperature contours illustrating the effect of partition walls on coolant-film development and hot-fluid penetration within the porous medium at F=0.68%: (a) without a partition walls and (b) with a partition walls.

An interesting observation is that mainstream-flow intrusion into the TPMS structure is observed near the leading edge in both configurations. At the leading edge, the coolant film has not yet fully developed, allowing the hot mainstream fluid to locally penetrate into the open surface grooves of the TPMS structure. In the configuration without partition walls, the penetrated mainstream fluid can propagate downstream through the fully interconnected internal channels of the TPMS structure. As a result, the influence of the hot mainstream fluid extends toward the trailing edge, leading to localized heating within the porous medium. In contrast, the partition walls interrupt the streamwise connectivity of the internal channels and suppress the downstream transport of the penetrated mainstream fluid. Consequently, although mainstream intrusion is still observed near the leading edge, its influence remains confined to that region and does not propagate toward the trailing edge. Once the coolant film becomes fully established downstream, the effect of mainstream intrusion becomes negligible. As coolant continuously exits the TPMS cells and accumulates along the surface, a progressively thicker coolant film develops and shields the wall from the mainstream flow. Consequently, the near-wall momentum of the mainstream is reduced, making further penetration into the TPMS structure increasingly difficult. This effect is further enhanced in the partition-wall configuration, where earlier

establishment of the coolant film provides increased resistance to mainstream intrusion. As a result, the penetration of hot mainstream fluid into the TPMS structure is more effectively suppressed, particularly in the upstream region.

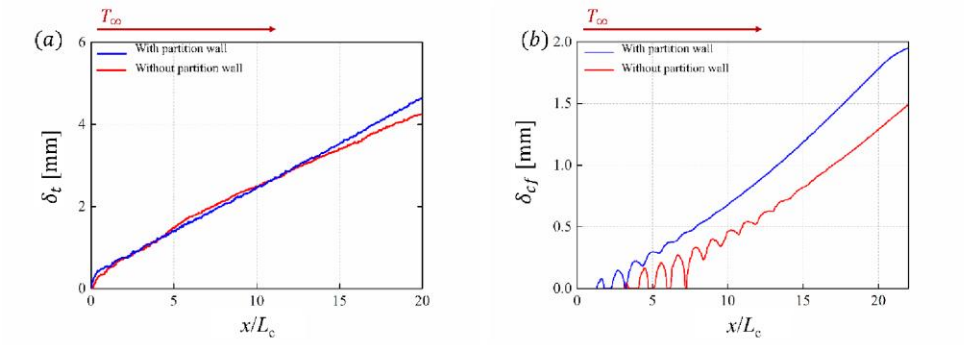

Fig.14 Comparison of the streamwise development of (a) thermal boundary-layer thickness (δ_t) and (b) coolant-film thickness (δ_{cf}) for TPMS structures with and without partition walls at F=0.68%.

Figure 14(a) shows that the partition wall has only a minor influence on the overall development of the thermal boundary layer. In contrast, a substantial increase in coolant-film thickness is observed in Figure 14(b) when partition walls are introduced. These results indicate that the partition wall primarily influences the near-wall coolant layer while having a limited effect on the overall thermal boundary-layer growth. As discussed in Figure 13, the partition wall interrupts the downstream transport of penetrated mainstream fluid through the interconnected channels, thereby suppressing hot-fluid intrusion and promoting the formation and development of the coolant film. Furthermore, Figure 14(b) shows that the coolant-film thickness (δ_{cf}) begins to develop much earlier when partition walls are employed. The first occurrence of δ_{cf} is observed at approximately $x/L_c \approx 1$ for the partition-wall configuration, whereas it does not appear until $x/L_c \approx 2.5$ in the configuration without partition walls. This result indicates that the partition wall facilitates earlier establishment of the coolant film by suppressing hot mainstream intrusion into the interconnected TPMS passages.

5. CONCLUSION

This study systematically investigated the existence of internal tangential flow in TPMS-based transpiration cooling structures and quantified its influence through combined experimental and numerical comparisons of configurations with and without partition walls.

The experimental results demonstrate a consistent trend across all injection-ratio conditions: partition walls improve adiabatic film cooling effectiveness, particularly in the leading-edge region. The results indicate that the high-speed mainstream flow induces internal tangential flow within the TPMS structure, transporting coolant downstream and causing a non-uniform coolant distribution. Consequently, coolant availability near the leading edge is reduced, delaying coolant-film establishment and degrading local cooling performance. By suppressing this internal transport mechanism, partition walls promote earlier coolant-film development and a more uniform coolant distribution, resulting in improved adiabatic film cooling effectiveness.

Numerical simulations provided further insight into the influence of internal tangential flow on transpiration-cooling performance and were consistent with the experimental observations. The results showed that partition walls interrupt the downstream transport of penetrated mainstream fluid through the interconnected TPMS channels, thereby suppressing internal tangential flow. As a result, coolant accumulation in the near-wall region is enhanced, promoting earlier coolant-film establishment and increasing coolant-film thickness. Consequently, a more uniform coolant distribution and improved surface cooling effectiveness are achieved.

A combined analysis of the experimental and numerical results confirms that partition walls promote effective coolant-film formation over the surface by suppressing internal tangential flow within the TPMS structure. Given the fully interconnected nature of TPMS channels, the influence of internal tangential transport is expected to become more pronounced in practical engine applications than in the limited observation domain considered in this study. Consequently, the incorporation of partition walls is anticipated to provide even greater benefits at engine-relevant scales, offering a promising design strategy for enhancing transpiration-cooling performance in advanced thermal management systems.

ACKNOWLEDGEMENTS

The work is supported by the National Research Council of Canada (NRC)'s National Program Office under a Postdoctoral Fellowship Program grant (PDF2024-TM-AF). NRC Aerospace Research Centre's Low-Emission Aviation Program also sponsored the work under project A1-024514.

NOMENCLATURE

A_{active} Active area [mm^2]

A_w	Internal wetted area [mm^2]
CO	Oxygen concentration
c	TPMS level set constant
D_p	Pore diameter [mm]
$d_h, TPMS$	The hydraulic diameter of TPMS [mm]
F	Injection ratio [%]
L_C	Unit cell length [mm]
MM	Molecular weight [$kg/kmol$]
P	Pressure [Pa]
Re	Reynolds number
T	Temperature [K]

GREEKS

α	Unit cell constant for x direction
β	Unit cell constant for y direction
γ	Unit cell constant for z direction
δ_t	Thermal boundary layer thickness
δ_{cf}	Coolant film thickness
ε	Porosity [%]
η	Film cooling effectiveness
θ	Dimensionless temperature
λ	Ratio of wetted surface area to volume [cm^2/cm^3]
$\emptyset$	Level-set equation

SUBSCRIPTS

c	Coolant
∞	Mainstream

ACRONYMS

$TPMS$	Triple Periodic Minimal Surface

PSP	Pressure Sensitive Paint
SLA	Stereolithography
AFE	Adiabatic cooling Film Effectiveness
BR	Blowing Ratio

REFERENCES

[1] Goldstein, R. J., Ibele, W. E., Patankar, S. V., Simon, T. W., Kuehn, T. H., Strykowski, P. J., Tamma, K. K., Heberlein, J. V. R., Davidson, J. H., Bischof, J., Kulacki, F. A., Kortshagen, U., Garrick, S., and Srinivasan, V., "Heat Transfer—A Review of 2003 Literature," International Journal of Heat and Mass Transfer, Vol. 49, Nos. 3–4, 2006, pp. 451–534. https://doi.org/10.1016/J.IJHEATMASSTRANSFER.2005.11.001

[2] Reed, R. C., "The Superalloys: Fundamentals and Applications," Cambridge university press, 2008.

[3] Han, J.-C., Dutta, S., and Ekkad, S., "Gas Turbine Heat Transfer and Cooling Technology," CRC press, 2012.

[4] Khan, M. A., Sundarrajan, S., Natarajan, S., Parameswaran, P., and Mohandas, E., "Oxidation and Hot Corrosion Behavior of Nickel-Based Superalloy for Gas Turbine Applications," Materials and manufacturing processes, Vol. 29, No. 7, 2014, pp. 832–839.

[5] Gupta, S., Chaube, A., and Verma, P., "Review on Heat Transfer Augmentation Techniques: Application in Gas Turbine Blade Internal Cooling," 2012.

[6] Fan, X., Li, L., Zou, J., and Zhou, Y., "Cooling Methods for Gas Turbine Blade Leading Edge: Comparative Study on Impingement Cooling, Vortex Cooling and Double Vortex Cooling," International Communications in Heat and Mass Transfer, Vol. 100, 2019, pp. 133–145. https://doi.org/10.1016/J.ICHEATMASSTRANSFER.2018.12.017

[7] Paitich, L. C., Richer, P., Jodoin, B., Pyo, Y., Yun, S., and Hong, Z., "Directional Effects of Effusion Cooling on the Cooling Film Effectiveness," AIAA Journal, Vol. 60, No. 1, 2022, pp. 423–434. https://doi.org/10.2514/1.J060625

[8] Pyo, Y., Son, J., Richer, P., Jodoin, B., Broumand, M., Yun, S., and Hong, Z., "Isolating Influences of Varying Pitch from the Effects of Non-Zero Compound Angles on Effusion Cooling," The Aeronautical Journal, 2024, pp. 1–21. https://doi.org/10.1017/aer.2024.108

[9] Krewinkel, R., "A Review of Gas Turbine Effusion Cooling Studies," International Journal of Heat and Mass Transfer, Vol. 66, 2013, pp. 706–722. https://doi.org/10.1016/J.IJHEATMASSTRANSFER.2013.07.071

[10] Linn, J., and Kloker, M. J., "Effects of Wall-Temperature Conditions on Effusion Cooling in a Supersonic Boundary Layer," AIAA Journal, Vol. 49, No. 2, 2011, pp. 299–307. https://doi.org/10.2514/1.J050383

[11] Nelson, W.A., Orenstein, R.M., DiMascio, P.S., and Johnson, C.A., "Development of Advanced Thermal Barrier Coatings for Severe Environments," *Proceedings of the ASME 1995 International Gas Turbine and Aeroengine Congress and Exposition*, Vol. 4: Heat Transfer; Electric Power; Industrial and Cogeneration, ASME Paper No. 95-GT-270, Houston, TX, June 5–8, 1995. https://doi.org/10.1115/95-GT-270

[12] Andreini, A., Becchi, R., Facchini, B., Picchi, A., and Peschiulli, A., "The Effect of Effusion Holes Inclination Angle on the Adiabatic Film Cooling Effectiveness in a Three-Sector Gas Turbine Combustor Rig with a Realistic Swirling Flow," International Journal of Thermal Sciences, Vol. 121, 2017, pp. 75–88. https://doi.org/10.1016/j.ijthermalsci.2017.07.003

[13] Schmidt, D. L., Sen, B., and Bogard, D. G., "Film Cooling With Compound Angle Holes: Adiabatic Effectiveness," Journal of Turbomachinery, Vol. 118, No. 4, 1996, pp. 807–813. https://doi.org/10.1115/1.2840938

[14] Andrews, G.E., Alikhanizadeh, M., Tehrani, F.B., Hussain, C.I., and Koshkbar Azari, M.S., "Small Diameter Film Cooling Holes: The Influence of Hole Size and Pitch," *International Journal of Turbo and Jet Engines*, Vol. 5, Nos. 1–4, 1988, pp. 61–72. https://doi.org/10.1515/TJJ.1988.5.1-4.61

[15] Zhou, J., Wang, X., and Li, J., "Influences of Effusion Hole Diameter on Impingement/Effusion Cooling Performance at Turbine Blade Leading Edge," International Journal of Heat and Mass Transfer, Vol. 134, 2019, pp. 1101–1118. https://doi.org/10.1016/J.IJHEATMASSTRANSFER.2019.02.054

[16] Wang, C., Zhang, J., and Zhou, J., "Optimization of a Fan-Shaped Hole to Improve Film Cooling Performance by RBF Neural Network and Genetic Algorithm," Aerospace Science and Technology, Vol. 58, 2016, pp. 18–25. https://doi.org/10.1016/j.ast.2016.08.004

[17] Wang, W., Cui, J., and Qu, S., "Effects of Hole Arrangement and Trenched Hole on Multirow Film Cooling," AIP Advances, Vol. 12, No. 4, 2022. https://doi.org/10.1063/5.0082980

[18] Nathan, M. L., Dyson, T. E., Bogard, D. G., and Bradshaw, S. D., "Adiabatic and Overall Effectiveness for the Showerhead Film Cooling of a Turbine Vane," Journal of Turbomachinery, Vol. 136, No. 3, 2013. https://doi.org/10.1115/1.4024680

[19] Bazdidi-Tehrani, F., and Andrews, G. E., "Full-Coverage Discrete Hole Film Cooling: Investigation of the Effect of Variable Density Ratio," 1994.

[20] Pietrzyk, J. R., Bogard, D. G., and Crawford, M. E., "Effects of Density Ratio on the Hydrodynamics of Film Cooling," Journal of Turbomachinery, Vol. 112, No. 3, 1990, pp. 437–443.

https://doi.org/10.1115/1.2927678

[21] Woo, T. K., Chung, H., Choi, S. M., and Cho, H. H., "Conjugate Heat Transfer on Full-Coverage Film Cooling with Array Jet Impingements with Various Biot Numbers," Experimental Thermal and Fluid Science, Vol. 83, 2017, pp. 1–8. https://doi.org/10.1016/j.expthermflusci.2016.12.008

[22] Cho, H. H., and Rhee, D. H., "Local Heat/Mass Transfer Measurement on the Effusion Plate in Impingement/Effusion Cooling Systems," Journal of Turbomachinery, Vol. 123, No. 3, 2001, pp. 601–608. https://doi.org/10.1115/1.1344904

[23] Horner, M. J., Yoon, C., Furgeson, M., Oliver, T. A., and Bogard, D. G., "Experimental and Computational Investigation of Integrated Internal and Film Cooling Designs Incorporating a Thermal Barrier Coating," Journal of Turbomachinery, Vol. 144, No. 9, 2022. https://doi.org/10.1115/1.4053840

[24] Horner, M. J., Yoon, C., Furgeson, M., Oliver, T. A., and Bogard, D. G., "Experimental and Computational Investigation of Integrated Internal and Film Cooling Designs Incorporating a Thermal Barrier Coating," Journal of Turbomachinery, Vol. 144, No. 9, 2022. https://doi.org/10.1115/1.4053840

[25] Drell, I.L., and Belles, F.E., "Survey of hydrogen combustion properties," NACA Technical Report No. 1383, National Advisory Committee for Aeronautics, 1958

[26] Chiesa, P., Lozza, G., and Mazzocchi, L., "Using Hydrogen as Gas Turbine Fuel," Journal of Engineering for Gas Turbines and Power, Vol. 127, No. 1, 2005, pp. 73–80. https://doi.org/10.1115/1.1787513

[27] Eckert, E. R. G., and Livingood, J. N. B., "Comparison of Effectiveness of Convection-, Transpiration-, and Film-Cooling Methods with Air as Coolant," National advisory committee for aeronautics, 1953.

[28] Weinbaum, S., and Wheeler, H. L., "Heat Transfer in Sweat-Cooled Porous Metals," Journal of Applied Physics, Vol. 20, No. 1, 1949, pp. 113–122. https://doi.org/10.1063/1.1698226

[29] Curry, D., Gomez, A., and Johnston, C., "Radiative, Ablative, and Active Cooling Thermal Protection Studies for the Leading Edge of a Fixed-Straight Wing Space Shuttle," *Proceedings of the 6th Thermophysics Conference*, AIAA Paper 1971-445, Palo Alto, CA, June 23–25, 1971. https://doi.org/10.2514/6.1971-445

[30] Liu, Y. Q., Jiang, P. X., Xiong, Y. Bin, and Wang, Y. P., "Experimental and Numerical Investigation of Transpiration Cooling for Sintered Porous Flat Plates," Vol. 50, 2013, pp. 997–1007. https://doi.org/10.1016/j.applthermaleng.2012.08.028

[31] Nguyentat, T., Hayes, W., Meland, T., Veith, E., and Ellis, D., "Fabrication of a Liquid Rocket Combustion Chamber Liner of Advanced Copper Alloy GRCop-84 via Formed Platelet Liner Technology," 42nd AIAA/ASME/SAE/ASEE Joint Propulsion Conference & Exhibit. https://doi.org/10.2514/6.2006-5192

[32] Ma, J., Luo, X., Li, H., and Liu, Y., "An Experimental Investigation on Transpiration Cooling Based on the Multilaminated Sintered Woven Wire Mesh Structures," Journal of Thermal Science and Engineering Applications, Vol. 8, No. 3, 2016. https://doi.org/10.1115/1.4032921

[33] Hinse, M., Yildiz, K., Richer, P., Jodoin, B., Bourmand, M., Yun, S., and Hong, Z., "Numerical and Experimental Studies of Transpiration Cooling Film Effectiveness over Porous Materials," *Journal of Thermophysics and Heat Transfer*, Vol. 36, No. 4, 2022, pp. 803–817. https://doi.org/10.2514/1.T6510

[34] Huang, Z., Xiong, Y. Bin, Liu, Y. Q., Jiang, P. X., and Zhu, Y. H., "Experimental Investigation of Full-Coverage Effusion Cooling through Perforated Flat Plates," Applied Thermal Engineering, Vol. 76, 2015, pp. 76–85. https://doi.org/10.1016/j.applthermaleng.2014.11.056

[35] Li, X., Liao, Z., Li, H., Jiang, P., and Xu, R., "Phase-Change Transpiration Cooling in Heterogeneous Composite Porous Plates: Heat Transfer Characteristics and Their Prediction," International Journal of Heat and Mass Transfer, Vol. 224, 2024, p. 125290. https://doi.org/10.1016/J.IJHEATMASSTRANSFER.2024.125290

[36] Yeranee, K., and Rao, Y., "A Review of Recent Research on Flow and Heat Transfer Analysis in Additively Manufactured Transpiration Cooling for Gas Turbines," Energies, Vol. 18, No. 13, 2025, p. 3282. https://doi.org/10.3390/en18133282

[37] Mi, Q., Yi, S. H., Gang, D. D., Lu, X. G., and Liu, X. L., "Research Progress of Transpiration Cooling for Aircraft Thermal Protection," Applied Thermal Engineering. Volume 236. https://doi.org/10.1016/j.applthermaleng.2023.121360

[38] Al-Ketan, O., Rowshan, R., and Abu Al-Rub, R. K., "Topology-Mechanical Property Relationship of 3D Printed Strut, Skeletal, and Sheet Based Periodic Metallic Cellular Materials," Additive Manufacturing, Vol. 19, 2018, pp. 167–183. https://doi.org/10.1016/j.addma.2017.12.006

[39] Reynolds, B. W., Fee, C. J., Morison, K. R., and Holland, D. J., "Characterisation of Heat Transfer within 3D Printed TPMS Heat Exchangers," International Journal of Heat and Mass Transfer, Vol. 212, 2023, p. 124264.

https://doi.org/10.1016/J.IJHEATMASSTRANSFER.2023.124264

[40] Li, W., Li, W., and Yu, Z., "Heat Transfer Enhancement of Water-Cooled Triply Periodic Minimal Surface Heat Exchangers," Applied Thermal Engineering, Vol. 217, 2022, p. 119198. https://doi.org/10.1016/J.APPLTHERMALENG.2022.119198

[41] Iyer, J., Moore, T., Nguyen, D., Roy, P., and Stolaroff, J., "Heat Transfer and Pressure Drop Characteristics of Heat Exchangers Based on Triply Periodic Minimal and Periodic Nodal Surfaces," Applied Thermal Engineering, Vol. 209, 2022, p. 118192. https://doi.org/10.1016/J.APPLTHERMALENG.2022.118192

[42] Broumand, M., Son, J., Pyo, Y., Yun, S., and Hong, Z., "TPMS-Based Transpiration Cooling for Film Cooling Enhancement," International Journal of Heat and Mass Transfer, Vol. 231, 2024. https://doi.org/10.1016/j.ijheatmasstransfer.2024.125824

[43] Yeranee, K., Zuo, Q., Rao, Y., and Cheng, Y., "Conjugate Heat Transfer Simulations of Vortex Chamber with Diamond-Type TPMS Effusion for Gas Turbine Blade Leading Edge Cooling," *Proceedings of the Global Power and Propulsion Society Technical Conference (GPPS Shanghai25)*, GPPS-TC-2025-0006, Shanghai, China, Sept. 4–6, 2025.

[44] Son, J., Pyo, Y., Richer, P., Jodoin, B., and Hong, Z., "Impact of Triply Periodic Minimal Surface Structure Unit Cell Size on Transpiration Cooling," Journal of Thermophysics and Heat Transfer, Vol. 0, No. 0, pp. 1–13. https://doi.org/10.2514/1.T7212

[45] Son, J., Broumand, M., Pyo, Y., Richer, P., Jodoin, B., and Hong, Z., "Effects of Lattice Orientation Angle On Tpms-Based Transpiration Cooling," Journal of Engineering for Gas Turbines and Power, 2024, pp. 1–28. https://doi.org/10.1115/1.4067378

[46] Son, J., Richer, P., Jodoin, B., and Hong, Z., "Effect of Morphological Variations in TPMS Lattice Structures on Transpiration Cooling," *Proceedings of the ASME Turbo Expo 2025: Turbomachinery Technical Conference and Exposition*, ASME Paper GT2025-151422, Memphis, TN, June 16–20, 2025. https://doi.org/10.1115/GT2025-151422

[47] Zhou, Z., Lv, Y., He, F., Liu, T., and Wang, J., "Pore-Scale Investigation of Transpiration Cooling Based on Triply Periodic Minimal Surface," International Journal of Thermal Sciences, Vol. 201, 2024. https://doi.org/10.1016/j.ijthermalsci.2024.109019

[48] Al-Ketan, O., and Abu Al-Rub, R. K., "MSLattice: A Free Software for Generating Uniform and Graded Lattices Based on Triply Periodic Minimal Surfaces," Material Design & Processing Communications, Vol. 3, No. 6, 2021, p. e205. https://doi.org/https://doi.org/10.1002/mdp2.205

[49] Schwarz, H. A., "Gesammelte Mathematische Abhandlungen," Springer, Berlin, 1890.

[50] Al-Ketan, O., Ali, M., Khalil, M., Rowshan, R., Khan, K. A., and Abu Al-Rub, R. K., "Forced Convection Computational Fluid Dynamics Analysis of Architected and Three-Dimensional Printable Heat Sinks Based on Triply Periodic Minimal Surfaces," Journal of Thermal Science and Engineering Applications, Vol. 13, No. 2, 2021. https://doi.org/10.1115/1.4047385

[51] Son, J., Pyo, Y., Broumand, M., Hong, Z., Sarafan, S., and Wanjara, P., "Advanced Transpiration Cooling Method Using Additive Manufactured TPMS Structure," *Proceedings of the 62nd Conference of Metallurgists (COM 2023)*, Springer, Cham, 2023. https://doi.org/10.1007/978-3-031-38141-6_59

[52] Han, J. C., and Rallabandi, A. P., "Turbine Blade Film Cooling Using PSP Technique," Frontiers in Heat and Mass Transfer, Vol. 1, No. 1, 2010. https://doi.org/10.5098/hmt.v1.1.3001

[53] Barigozzi, G., Mucignat, C., Abdeh, H., Scandella, D., and Dolci, G., "Assessment of Binary PSP Technique for Film Cooling Effectiveness Measurement on Nozzle Vane Cascade with Cutback Trailing Edge," Experimental Thermal and Fluid Science, Vol. 97, 2018, pp. 431–443. https://doi.org/10.1016/j.expthermflusci.2018.05.015

[54] Liu, T., Sullivan, J. P., Asai, K., Klein, C., and Egami, Y., "Pressure and Temperature Sensitive Paints," Springer, 2005.

[55] Natsui, G., Little, Z., Kapat, J. S., Dees, J. E., and Laskowski, G., "A Detailed Uncertainty Analysis of Adiabatic Film Cooling Effectiveness Measurements Using Pressure-Sensitive Paint," *Journal of Turbomachinery*, Vol. 138, No. 8, 2016. https://doi.org/10.1115/1.4032674

[56] Johnson, B., and Hu, H., "Measurement Uncertainty Analysis in Determining Adiabatic Film Cooling Effectiveness by Using Pressure Sensitive Paint Technique," Journal of Turbomachinery, Vol. 138, No. 12, 2016. https://doi.org/10.1115/1.4033506

[57] Dahmen, W., Gotzen, T., Müller, S., and Rom, M., "Numerical Simulation of Transpiration Cooling through Porous Material," *International Journal for Numerical Methods in Fluids*, Vol. 76, No. 6, 2014, pp. 331–365. https://doi.org/10.1002/fld.3935

[58] Menter, F. R., "Two-Equation Eddy-Viscosity Turbulence Models for Engineering Applications," *AIAA Journal*, Vol. 32, No. 8, 1994, pp. 1598–1605. https://doi.org/10.2514/3.12149

[59] Andrei, L., Andreini, A., Bianchini, C., Caciolli, G., Facchini, B., Mazzei, L., Picchi, A., and Turrini, F., "Effusion Cooling Plates for Combustor Liners: Experimental and Numerical Investigations on the Effect of Density Ratio," Vol. 45, 2014, pp. 1402–1411. https://doi.org/10.1016/j.egypro.2014.01.147

[60] Ledezma, G. A., Lachance, J., Wang, G., Wang, A., and Laskowski, G. M., "Experimental and Numerical Investigation of Effusion Cooling for High Pressure Turbine Components: Part 2—Numerical Results," Vol. 49798, 2016, pp. V05BT17A002.

[61] Menter, F. R., Kuntz, M., and Langtry, R., "Ten Years of Industrial Experience with the SST Turbulence Model," *Turbulence, heat and mass transfer*, Vol. 4, No. 1, 2003, pp. 625–632.

[62] Greiciunas, E., Borman, D., Summers, J., and Smith, S. J., "A Multi-Scale Conjugate Heat Transfer Modelling Approach for Corrugated Heat Exchangers," *International Journal of Heat and Mass Transfer*, Vol. 139, 2019, pp. 928–937. https://doi.org/10.1016/J.IJHEATMASSTRANSFER.2019.05.086

[63] Schlichting, H., and Gersten, K., "Boundary-Layer Theory," springer, 2016.

[64] Chen, X., Krawciw, J., Xia, H., Denman, P. A., Bonham, C., and Carrotte, J. F., "Study of an Effusion-Cooled Plate with High Level of Upstream Fluctuation," *Applied Thermal Engineering*, Vol. 184, 2021. https://doi.org/10.1016/j.applthermaleng.2020.116126

5.6 Porosity Optimization of TPMS Structures for Uniform Coolant Distribution

One of the key challenges in transpiration cooling lies in the optimization of porosity, which plays a crucial role in achieving a uniform coolant mass flow distribution across the surface. As discussed in the previous subsection, locally non-uniform coolant distribution may arise due to internal tangential flow within the porous matrix, directing the coolant preferentially toward the trailing edge. This internal redistribution results in excessive coolant discharge near the trailing edge and insufficient coolant supply in the leading-edge region.

In this context, graded and spatially varying porosity distributions have emerged as promising strategies for improving coolant distribution through local control of permeability. In TPMS structures, porosity can be precisely tailored through their mathematical formulation, typically defined using level-set equations.

Accordingly, the objective of the present study is to enhance the understanding of how spatial porosity distribution influences coolant flow redistribution and to establish design guidelines for performance optimization through the identification of an optimal porosity profile.

In this investigation, three distinct porosity distribution profiles were —steep linear decay (SLD), gradual linear decay (GLD), and exponential decay (ED)— implemented across two TPMS morphologies (Gyroid and Koch). Each graded profiles was systematically compared with a uniform-porosity baseline case. The results demonstrate that functionally graded porosity is a key design strategy for TPMS-based transpiration cooling, as it redistributes coolant toward the leading edge, promotes earlier coolant-film formation, and improves the overall uniformity of cooling performance. Among the configurations investigated, the ED profile provided the most effective and uniform cooling performance, making it the preferred porosity distribution for TPMS-based transpiration cooling. The primary objective of this study is not only to identify the porosity profile that yields the best cooling performance but also to establish practical design guidelines for TPMS combustor liners applicable to real gas turbine engines.

This study was prepared as a research article and is currently under review for publication in *The Aeronautical Journal* (joint journal of the ISABE 2026 Conference, Paper number AeroJ-2026-0292).

ISABE-2026-037

Coolant Redistribution via Functionally Graded Porosity in TPMS Structures for Enhanced Transpiration Cooling

Juchan Son†, Patrick Richer and Bertrand Jodoin
University of Ottawa
Department of Mechanical Engineering
Ottawa
Canada

Sina Kashanj‡, Zekai Hong †
National Research Council Canada
Aerospace Research Centre
Ottawa
Canada

† Affiliated with both University of Ottawa and National Research Council Canada

ABSTRACT

Transpiration cooling based on triply periodic minimal surface (TPMS) structures holds promises as a disruptive cooling technology for next-generation aeroengines. It offers such as high surface area to volume ratio and coolant discharge outlets distributed over the entire surface area, which enable more uniform coolant distribution and thereby improve coolant film formation, as well as deterministic control over pore morphology enabled by their periodicity. However, despite these benefits, TPMS-based transpiration cooling can be further improved by modifications enhancing coolant film distribution. Previous studies have shown that, in transpiration cooling, the coolant can flow within the porous matrix toward the downstream direction before discharging. This internal coolant (tangential) flow leads to skewed coolant distribution between the leading and trailing edges. The present study investigates TPMS lattices with graded porosity along the mainstream flow direction, in which porosity decreases from leading edge to trailing edge. By engineering higher structure permeability in the leading edge, coolant supply in that region is promoted. Three graded porosity profiles were examined and compared with a uniform porosity (UP) baseline: a steep linear decay (SLD), a gradual linear decay (GLD), and an exponential decay (ED). Each graded porosity profile was implemented in two types of TPMS structures, i.e., Koch and Gyroid, to evaluate the effects of porosity grading on internal flow behavior and the resulting adiabatic film cooling effectiveness (AFE). All eight configurations were designed to maintain a constant overall average porosity of 32%. AFE were experimentally determined using binary pressure-sensitive paint (PSP). Results confirm that porosity grading in TPMS lattices can be effective in redistributing coolant to achieve a more effective and uniform cooling film. In particular, higher porosity near the leading edge promotes rapid development of cooling film, mitigating the prominent deficiency associated with transpiration cooling based on uniform lattice structures.

Keywords: Gas turbine; Film Cooling; Transpiration Cooling; TPMS structure; Functional Graded Porosity

NOMENCLATURE

Acronyms

AFE	Adiabatic Film Cooling Effectiveness
AM	Additive Manufacturing
BR	Blowing Ratio
ED	Exponential Decay
GLD	Gradual Linear Decay
SLD	Steep Linear Decay
TPMS	Triple Periodic Minimal Surface
UP	Uniform Porosity

PSP	Pressure Sensitive Paint

Symbols

α	Unit cell constant for x direction
β	Unit cell constant for y direction
γ	Unit cell constant for z direction
ε	Porosity
η_{ad}	Adiabatic film cooling effectiveness
λ	Wetted surface area to volume ratio
ϕ	Level-set equation
ρ	Density
A	1st order coefficient of the polynomial fitting curve
A_{active}	Active area
B	2nd order coefficient of the polynomial fitting curve
C	3rd order coefficient of the polynomial fitting curve
C_{o2}	Oxygen mass concentration
c	Level-set constant
D_p	Pore diameter
F	Injection ratio
L_c	Unit cell size
MM	Molecular Weight
P	pressure
$\dot{Q}_c$	Coolant volumetric flow rate
r	Intensity ratio for binary
T	Temperature
u	Velocity
X_{O2}	Mole fraction

1.0 INTRODUCTION

Over the past several decades, the turbine inlet temperature (TIT) has progressively increased to achieve higher thermal efficiency for gas turbines. Consequently, the turbine inlet temperature in modern gas turbines exceeds the melting point of nickel-based superalloys such as Inconel [1]. Advanced cooling strategies are needed for next-generation gas turbines for hot-gas path components such as combustion liners and turbine blades.

Transpiration cooling has emerged as a particularly promising solution for cooling challenges. In transpiration cooling, coolant is introduced through a porous medium, forming a protective coolant film over metal surfaces that is more effective than those resulted from conventional film cooling techniques (add references here to effusion, etc). Coolant film can thicken the boundary layer and modify the local temperature and velocity gradients near the surface, also known as boundary-layer heat blocking [2]. As a result, heat transfer from the high-temperature mainstream flow to the liner surface is significantly reduced. In addition, the porous medium provides a high wetted surface area relative to its volume, which enhances convective heat transfer between the solid structure and the coolant [3]. The combination of effective film cooling and enhanced internal convection heat transfer makes transpiration cooling a strong candidate for cooling for next-generation gas turbines. Since its initial proposal in the early 1940s [4], the transpiration cooling concept has been explored using various types of porous media, including open-cell foam [5], woven wire mesh [6], and sintered metal [7]. Ma et al. [6] investigated transpiration cooling using sintered woven wire mesh structures with varying porosities (25.6% to 55.1%) and layer configurations, demonstrating that higher average porosity improves cooling effectiveness and reduces pressure drop, while the layer arrangement also significantly affects overall performance. Liu et al. [7] investigated transpiration cooling through sintered porous flat plates fabricated with particle diameters of 40 and 90 μm. Their results show that even minimal coolant injection (a blowing ratio of 0.5%) leads to a substantial reduction in heat transfer from hot gas streams, with cooling effectiveness improving as the injection ratio increases and sintered particle size decreases.

While previous studies have demonstrated the potentials of transpiration cooling, the stochastic nature of pore size distribution in porous media presents significant practical challenges [8]. Porous materials for transpiration cooling are commonly manufactured using powder sintering. However, these fabrication processes inevitably introduce structural imperfections, such as stochastically formed voids and particle agglomeration within the porous matrix. Consequently, the resulting porous medium exhibits not only a non-uniform spatial pore distribution but also a wide range of pore diameters [9], which may lead to the formation of local hot spots. Li et al. [10] investigated phase-change transpiration cooling in heterogeneous ceramic matrix composites,

emphasizing the critical influence of pore structure on cooling performance. Specifically, variations in pore size and permeability resulted in non-uniform coolant distribution, which led to the formation of local hot spots and a reduction in overall cooling effectiveness. König et al. [11] conducted experimental and numerical investigations on transpiration cooling using carbon/carbon (C/C) ceramic matrix composites, with particular emphasis on the effects of nonuniform coolant outflow caused by the porous structure. Their study demonstrated that the inherent heterogeneity in pore arrangement, originating from the composite manufacturing process, led to uneven mass injection, which subsequently affected both the formation and the uniformity of the cooling film. Therefore, overcoming these limitations and achieving reliable implementation of transpiration cooling necessitate the development of precisely controlled, deterministic porous media.

The emergence of additive manufacturing (AM) techniques has enabled the fabrication of porous lattice structures with precisely controlled deterministic geometries [12]. Among the various candidates, triply periodic minimal surface (TPMS) lattices have attracted increasing interest due to their unique geometric characteristics, including continuously interconnected channels, smooth curvature, and a high surface-area-to-volume ratio, making them highly suitable for a wide range of engineering applications [13]. These properties make TPMS structures attractive not only for the design of high-efficiency heat exchangers but also as deterministic porous media for next-generation transpiration cooling systems [14–16].

Despite their high cooling effectiveness, conventional stochastic porous materials have shown limited applicability in practical turbine components because of their inherently low mechanical strength and structural instability caused by random pore distributions[17,18]. In contrast, TPMS structures offer superior mechanical integrity owing to their continuous, smooth, and triply periodic surface geometry, which eliminates structural discontinuities and promotes efficient load transfer throughout the interconnected network. Recent studies have demonstrated that TPMS-based lattice structures exhibit superior mechanical performance compared to conventional stochastic porous architectures at equivalent relative densities. Araya et al[19]. reported that Gyroid lattices fabricated using laser powder bed fusion achieved higher yield strength than stochastic Voronoi structures. This improvement was attributed to the continuous and smoothly curved geometry of TPMS structures, which promotes more uniform stress distribution and minimizes stress concentrations, thereby enhancing structural integrity and mechanical durability.

Preliminary investigations have demonstrated that TPMS-based transpiration cooling can achieve significantly improved adiabatic film cooling effectiveness comparing to conventional effusion cooling. Broumand et al. [20] examined 3D-printed TPMS lattice structures with varying porosities for transpiration cooling applications. Their results demonstrated a substantial improvement in cooling performance compared to conventional effusion cooling configurations, with film cooling effectiveness increasing by up to fivefold. Further investigation [21] demonstrated that small unit cell sizes enhance AFE when the porosity is kept constant. In a subsequent investigation, the impact of lattice orientation relative to the mainstream flow was studied using three different types of TPMS geometries [22]. It was found that increasing the top-surface tortuosity and aligning the void pattern with the mainstream flow direction enhances adiabatic film cooling effectiveness.

Despite these recent advances, TPMS-based transpiration cooling can be further optimized, as has been repeated found in past studies, uniform lattice structures actually produce non-uniform film cooling effectiveness as cooling films build gradually. In addition, an uneven distribution of coolant mass flow was found when uniform porous media are used for transpiration cooling [23]. Hinse et al. [24] investigated transpiration cooling using metal foam porous media and found that viscous entrainment from the mainstream flow induces tangential coolant motion within the porous matrix. This internal tangential flow results in non-uniform coolant discharge and leads to an uneven adiabatic film cooling effectiveness.

A similar phenomenon can be expected for the TPMS-based transpiration cooling systems to what was found in general porous media, as illustrated in Fig. 1. As previously discussed, the mainstream flow on the lattice surface can induce internal tangential flow within the porous media due to viscosity. This induced internal tangential flow causes an uneven distribution of coolant along the mainstream direction, which leads to excessive coolant release near the trailing edge and inadequate supply near the leading edge. As a result, this non-uniform discharge may compromise cooling performance in the leading-edge region, where effective thermal protection is most critical.

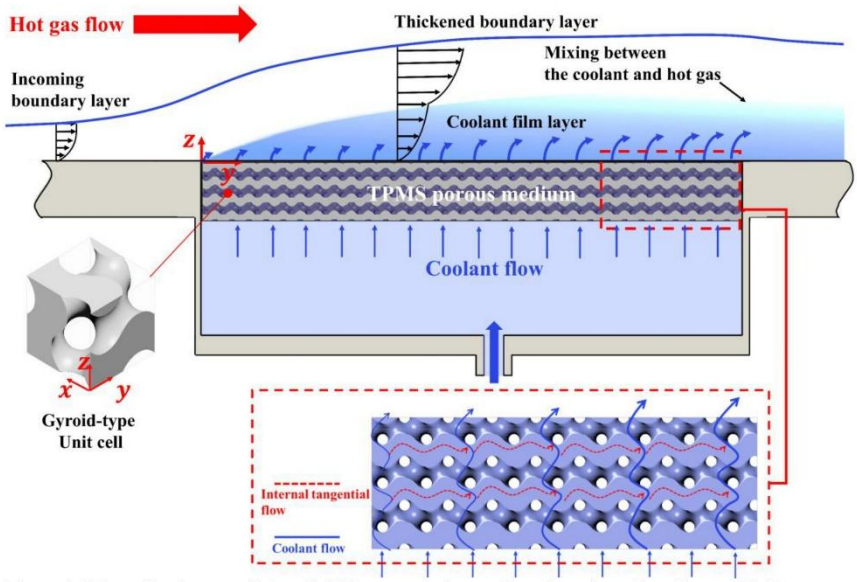

Figure 1 Schematic of near-wall flow field for transpiration cooling, featuring a Gyroid type TPMS structure. In the zoomed-in view, the coolant gas is visualized in blue and the internal tangential coolant flow within the porous medium is indicated by red arrows.

Dong et al.[25] conducted a numerical investigation demonstrating that varying local porosity can reduce the maximum temperature on the hot side by approximately 40%. To the best of our knowledge, many existing studies remain limited to numerical investigations due to significant constraints in conventional manufacturing technologies. Advances in additive manufacturing have made it possible to fabricate complex geometries [26]. TPMS structures are inherently natural to precision control over porosity distribution due to mathematical definitions. Cheng et al. [27] were the first to conduct experimental and numerical transpiration cooling investigations of a nose cone using functionally graded TPMS-based porous plates fabricated via AM (additive manufacturing). Their results show that graded porosity significantly enhanced temperature uniformity, with improvements of up to 66% compared to uniform designs. However, existing research has primarily focused on linear porosity gradients. No prior studies have systematically investigated the influence of different porosity profiles on transpiration cooling performance.

The present study investigates the effects of functionally graded porosity on transpiration cooling performance using TPMS-based structures. Two TPMS types, namely the Gyroid and Koch type, are considered. For each TPMS type, four distinct porosity profiles are examined: uniform porosity (UP), steep linear decay (SLD), gradual linear decay (GLD), and exponential decay (ED). All eight test coupons were designed to maintain a constant overall porosity while using identical unit cell sizes in order to isolate the effect of porosity grading. As a result, the porosity profile along the mainstream flow direction was the only independent variable in this study. This study aims to provide insights into how different functional porosity gradients influence coolant distribution and overall cooling effectiveness.

2.0 EXPERIMENTAL APPROACH

2.1 TPMS structure

In this study, two types of TPMS structures, namely Gyroid and Koch type, are selected to investigate the influence of porosity grading on the performance of transpiration cooling. TPMS structures are defined by level-set equations. The porosity of TPMS structures can be controlled by their level-set ($\emptyset$) equations by varying the constant c. The level-set equation for Gyroid and Koch type are as follows:

$$\emptyset_{Gyroid}(x,y,z) = \sin(X)\sin(Y) + \sin(Y)\cos(Z) + \sin(Z)\cos(X) = c \quad (1)$$

$$\emptyset_{Koch}(x,y,z) = cos(2X)\,sin(Y)\,cos(Z) + cos(2Y)\,sin(Z)\,cos(X) + cos(2Z)\,sin(X)\,cos(Y) = c \quad (2)$$

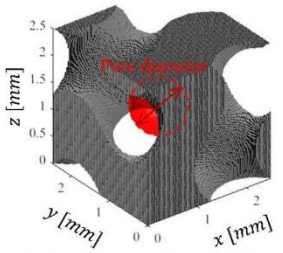

Figure 2 Unit cell cube of a Gyroid type TPMS structure with 50% porosity

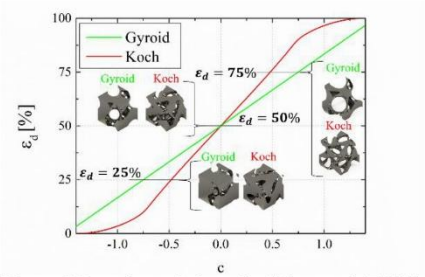

Figure 3 Porosity variation of solid-network TPMS lattices as a function of level-set constant c.

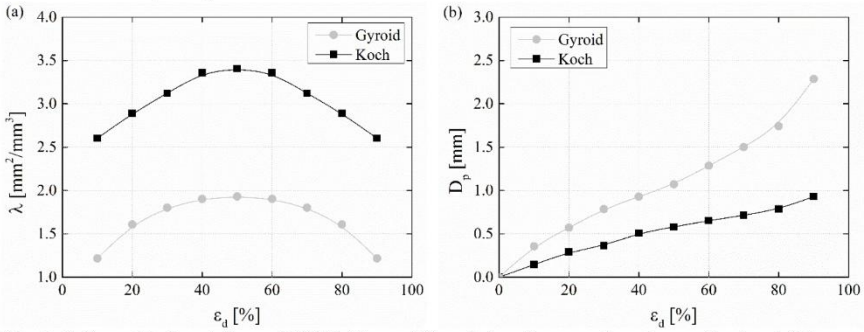

Figure 4 Geometrical variations of TPMS Ttypes. (a) wetted surface area to volume ratio λ and (b) pore diameter D_p as functions of porosity ε_d.

where $X=2\pi x/\alpha$, $Y=2\pi y/\beta$, and $Z=2\pi z/\gamma$, and α, β, and γ are the unit cell size in x, y, and z directions. In this study, the unit cell was set to be isotropic ($\alpha=\beta=\gamma=L_c$=2.5 mm). The iso-surface, or boundary surface, is defined where the level-set equation equals the constant c. This surface divides the volume into two distinct regions: solid and void. For instance, when c=0, the two sub-domains have equal volume, resulting in a porosity of 50%. In this study, the solid network is defined as follows:

$$\emptyset(x,y,z) < c \tag{3}$$

Fig. 2 illustrates a Gyroid type unit cell solid network. The parameter D_p denotes the pore diameter of the structure, defined as the diameter of the largest inscribed sphere that can pass through the narrowest constriction within the porous channel [28]. Fig. 3 shows the relationship between the threshold value c and the resulting porosity ε_d: the porosity can be precisely controlled by adjusting the value of c. Both the pore diameter (D_p) of the TPMS unit cell and the wetted surface-area-to-volume ratio (λ) vary as functions of the prescribed porosity, as shown in Fig. 4.

2.2 Printability test and actual porosity

All eight test coupons used in this study were designed and fabricated to implement local porosity gradients using a stereolithography (SLA) 3D printer. A commercial SLA printer (Form 3, Formlabs) was used, which operates with a 405 nm UV laser and achieves a resolution of 25 μm in all directions. A high-temperature resin, capable of withstanding a heat deflection temperature of 238 °C at 0.45 MPa, was selected for printing. However, it is important to note that discrepancies between the designed geometry and the final 3D-printed part are a well-known issue in additive manufacturing processes[29]. This discrepancy is primarily induced by unintended over-solidification, namely excessive material deposition resulting from surplus laser energy input, which partially fills the designed void regions and thereby reduces the actual porosity of the final product. Such deviations are frequently observed in TPMS structures fabricated via AM, where the measured porosity is often lower than the intended design value[13]. To account for these effects and ensure consistent actual porosity across test samples, this study examines the discrepancy between the designed porosity and the resulting manufactured (actual) porosity. The actual porosity (ε_a) was estimated based on the measured mass of the printed samples, as detailed below.

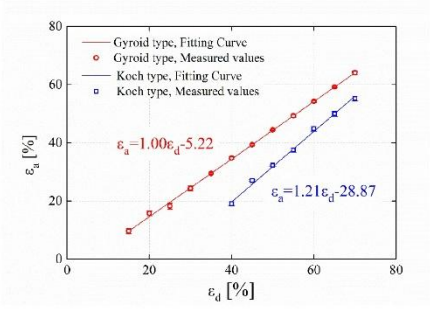

Figure 5 Actual porosity as a function of design porosity.

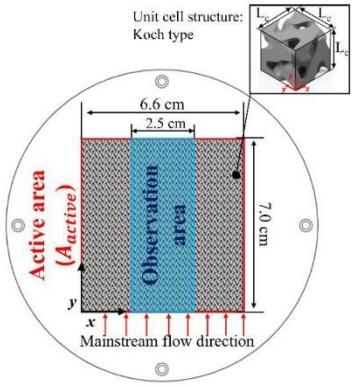

Figure 6 Schematic of the circular test coupon, with the observation area assigned at the center.

$$\varepsilon_a = (1 - \frac{M_a}{M_s}) \times 100 \quad (4)$$

Here, M_s refers to the mass of a fully solid specimen with the same outer dimensions as the target TPMS lattice structure while M_a denotes the mass of the fabricated TPMS lattice. The procedure for estimating actual porosity is described in detail in the authors' previous study [30]. Fig. 5 illustrates the actual porosity values as a function of the designed porosity.

As shown in Fig. 5, the printability limit of design porosity for the Gyroid type TPMS was found to be 15%, which results in an actual porosity of 9.8%. Below this threshold, local pore clogging was observed, indicating a manufacturing limit. In contrast, the Koch type structure exhibited a tighter printability limit at 40% of design porosity, resulting in an actual porosity of 19.5%, which suggests that it is more prone to clogging than the Gyroid type. This difference in printability is attributed to the smaller pore size of the Koch structure under equivalent porosity conditions, as illustrated in Fig. 4. Notably, the printability limits for both TPMS types correspond to a similar pore diameter of approximately D_p=0.5 mm.

2.3 Test coupon design and test rig

The geometry of the test coupon is shown in Fig. 6. The circular test coupon has a diameter of 123.8 mm and a thickness of 7.6 mm. The active area for studying transpiration cooling is in the center of the circular coupon and isa 6.6 cm by 7.0 cm rectangle. However, to minimize the influence of inactive regions near the edges of the test coupon, only the central portion of the active area, highlighted in blue in Fig. 6, was used for measuring adiabatic film cooling effectiveness. All two-dimensional distributions of adiabatic film cooling effectiveness reported later in this paper correspond to this observation area.

Four different porosity distribution profiles along the mainstream flow direction are considered: uniform porosity (UP), steep linear decay (SLD), gradual linear decay (GLD), and exponential decay (ED). Each porosity profile was achieved by varying the level-set constant c as a function of position along the flow direction. The resulting local porosity values for all eight test coupons are presented in Fig. 7. The UP profile of the Koch and Gyroid types have a uniform actual porosity of approximately 32%. In the SLD profile, the trailing-edge porosity was set to the printable threshold identified in the printability tests (Fig. 5). The leading-edge porosity was then defined using a linear function, ensuring that the average porosity matched that of the UP profile. As a result, the SLD profile exhibits a linear porosity gradient, decreasing from 54% to 9.8% for the Gyroid structure and from 46% to 19.2% for the Koch structure. In the GLD profile, the porosity distribution was also designed to decrease linearly along the mainstream direction, but with a more gradual slope than that of the SLD profile. As shown in Fig. 7, the leading-edge porosity in the GLD profile was selected to fall approximately midway between the UP and SLD profile, providing a more gradual porosity gradient. This design facilitates the investigation of intermediate porosity behavior while maintaining a comparable overall average porosity. For the Gyroid type, the actual porosity decreases from 44% at the leading edge to 20% at the trailing edge. Similarly, in the Koch structure, the actual porosity decreases from 38% to 27% across the same span. Lastly, the ED profile initiates with a high leading-edge porosity, equivalent to that of the SLD profile. However, in contrast to the linear reduction observed in SLD, the ED profile exhibits a more rapid decline in porosity along the mainstream direction, governed by an exponential decay function. Despite this steep initial gradient, the overall average porosity remains comparable to that of the other profiles, as illustrated in Fig. 7.

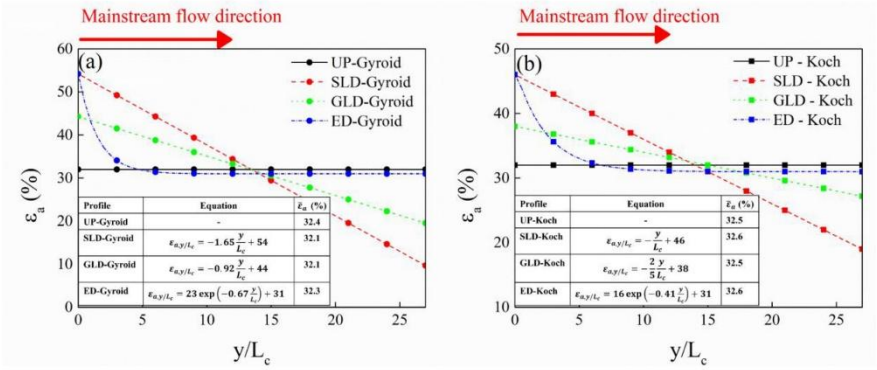

Figure 7 Actual porosity variation along the mainstream flow direction for different profiles (a) Gyroid (b) Koch type

A concise overview of the experimental setup is schematically illustrated in Fig. 8, while a detailed description of the experimental facility can be found in previous studies [31,32]. The blower, driven by a 30 kW AC motor, generates an airflow that moves at 33 m/s in the test section, representative of typical flow conditions in gas turbine combustors. This velocity was measured using a Pitot tube positioned at the center of the test section cross-section near the leading edge of the test coupon. The test section features a square cross-section of 127 mm × 127 mm. The Reynolds number of the mainstream flow was estimated to be approximately 256,000, with a free-stream turbulence intensity of around 3%. In this study, inert nitrogen (N_2) was used as a coolant proxy, supplied from a compressed gas cylinder. The coolant flow rate was regulated using a mass flow controller (Omega FMA 5400A/5500A series).

2.4 PSP methodology

A binary pressure sensitive paint (PSP) from ISSI was used to evaluate adiabatic film cooling effectiveness. The use of PSP has been discussed in details in previous works [31,33] . The paint was applied to the test coupon top surface using an airbrush without clogging the coolant passages. The total thickness of the applied PSP and basecoat layers was estimated to be less than 20 µm [34]. A UV LED array (ISSI LM2X-DM-400), air-cooled and centered at 400 nm, was used to excite the PSP. The resulting luminescent emission was captured using a CCD camera (LaVision Image ProX 2M) equipped with a LaVision image doubler. Bandpass filters were installed on each lens of the image doubler, one centered at 550 nm with a full width at half maximum (FWHM) of 10 nm, and the other centered at 650 nm with an FWHM of 20 nm.

The adiabatic film cooling effectiveness (AFE), η_{ad}, is defined as below:

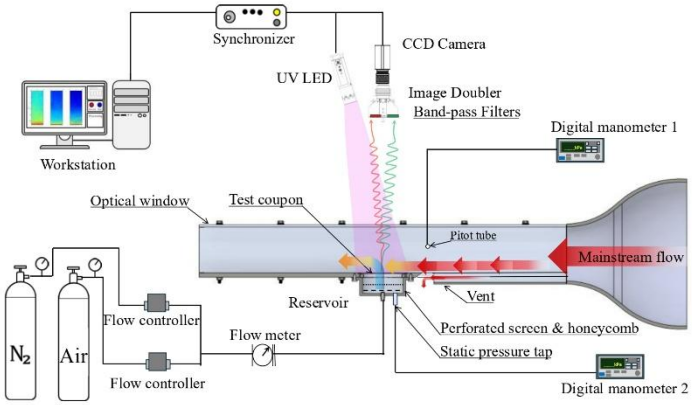

Figure 8 Schematic of the test rig.

$$\eta_{ad} = (T_\infty - T_{ad})/(T_\infty - T_c) \tag{5}$$

Here, T denotes temperature, and the subscripts ∞, ad, and c refer to the mainstream flow, the adiabatic wall, and the coolant, respectively. Under the assumption of a turbulent flow with a Lewis number close to unity, the heat and mass transfer analogy can be invoked, allowing the temperature-based expression in Eq. (5) to be reformulated in terms of species mass concentration.

$$\eta_{ad} \approx \frac{T_m - T_{ad}}{T_m - T_c} \approx \frac{C_{O2,\infty} - C_{O2,ad}}{C_{O2,\infty} - C_{O2,c}} = 1 - \frac{C_{O2,ad}}{C_{O2,\infty}} \tag{6}$$

Here, C_{O2} denotes the oxygen mass fraction. When nitrogen is used as the coolant, $C_{O2,c}$ in Eq. (6) becomes zero, allowing the final expression to be simplified accordingly. Eq. (6) can be expressed in terms of the ratio of oxygen partial pressures, as obtained through the PSP measurement technique.

$$\eta_{ad} = 1 - \frac{C_{O2,ad}}{C_{O2,\infty}} = 1 - \frac{1}{1 + \frac{MM_c}{MM_\infty}\left[\frac{\left(X_{o_2,\infty}\right)}{\left(X_{o_2,ad}\right)} - 1\right]} = 1 - \frac{1}{1 + \frac{MM_c}{MM_\infty}\left[\frac{p}{p_{ref}} - 1\right]} \tag{7}$$

Here, $X_{o_2,\infty}$ and $X_{o_2,ad}$ represent the corresponding mole fractions in the mainstream air and in the air–nitrogen mixture near the test surface, respectively. $MM_\infty$and MM_c refer to the molecular weights of air and the coolant, respectively; in this study, nitrogen was used as the coolant proxy. The luminescent intensity of the binary PSP shows an approximate second-order polynomial relationship with the oxygen partial pressure, as expressed below:

$$\frac{p}{p_{ref}} = A + B\left(\frac{r_{ref}}{r}\right) + C\left(\frac{r_{ref}}{r}\right)^2 \tag{8}$$

where

$$\frac{r_{ref}}{r} = \frac{\left(\frac{I_{ref} - I_{dark}}{I - I_{dark}}\right)_{PT}}{\left(\frac{I_{ref} - I_{dark}}{I - I_{dark}}\right)_{T}} \tag{9}$$

Here, r_{ref}/r denotes the normalized ratio of fluorescence intensities, with both values corrected by subtracting the dark signal to eliminate background signal. The coefficients A, B, and $C$are temperature-independent polynomial constants, and Irepresents the measured luminescent intensity. Further details on the PSP calibration procedure and the associated measurement uncertainty are provided in the authors' previous studies [20,31].

2.5 Test conditions

The blowing ratio (BR) is the primary experimental parameter for evaluating effusion cooling performance and is defined as follows:

$$BR = (\rho u)_c/(\rho u)_m \tag{10}$$

where ρ and u represent density and velocity, respectively. The mainstream flow velocity was maintained at 33 m/s, while the coolant velocity was calculated based on the volumetric flow rate $\dot{Q}_c$, the active area A_{active}(as shown in Fig. 6), and the surface porosity $\varepsilon_{\text{surface}}$of the test coupon.

$$u_c = \frac{\dot{Q}_c}{A_{active}\varepsilon_{\text{surface}}} \tag{11}$$

Compared to effusion cooling, transpiration cooling typically features a significantly higher surface porosity, which leads to a much lower blowing ratio (BR) under the same coolant flow rate per unit area. As a result, the conventional BR is not well-suited for describing test conditions in transpiration cooling studies. To address this limitation, an alternative parameter known as the injection ratio (F) is introduced to more appropriately characterize transpiration cooling. It is defined as follows:

$$F = \frac{\dot{m}_c}{(\rho u)_m A_{active}} \tag{12}$$

Here, $\dot{m}_c$ represents the coolant mass flow rate. In this study, the active area was consistent with that used in previous studies on transpiration and effusion cooling [20,31]. The injection ratio F was set to 0.68%, 1.14%, and 1.60%, corresponding to the coolant flow rates used in effusion cooling cases with the same A_{active}at blowing ratios (BR) of 0.6, 1.0, and 1.4, respectively.

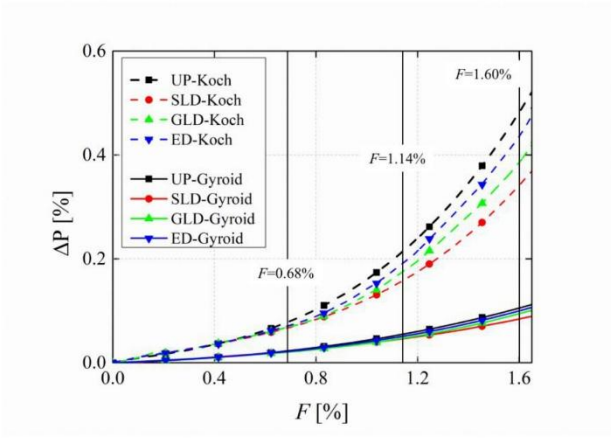

Figure 9 Percentage pressure drop across test coupons

The percentage pressure drops (ΔP) across the test coupon was evaluated based on the ratio of the measured static pressure difference to the upstream static pressure. The upstream and downstream static pressures were obtained from the static port of a pitot tube located in the test section, and a static pressure tap on the bottom wall of the coolant reservoir, respectively. The locations of the pitot tube and pressure tap are illustrated in Fig. 8. The percentage pressure drop is defined as follows:

$$\Delta P = \frac{P_{reservoir} - P_{mainstream}}{P_{mainstream}} * 100 \tag{13}$$

Fig. 9 presents the percentage pressure drops as a function of the injection ratio F for all eight test coupons. As shown in Fig. 9, the Koch-type structures exhibit higher pressure drops comparing to the Gyroid-type. This behavior can be attributed to the smaller pore diameters and higher wetted surface area-to-volume ratios of the Koch structures, as illustrated in Fig. 4, even when the overall average actual porosity is maintained at a similar level. A similar trend was observed for both the Gyroid and Koch types: among all profiles, the SLD profile consistently showed the lowest pressure drop. This is attributed to the relationship between pressure loss and porosity in TPMS structures. Zhuang et al. [35] reported that the permeability of porous media increases exponentially with porosity. Additionally, pore diameter, which significantly affects flow resistance, increases more rapidly at higher porosity levels, as shown in Fig. 4. As a result, even with the same overall average porosity, the SLD profile, which maintains higher porosity region near the leading edge, yields the lowest pressure drop among the tested cases.

3.0 RESULTS AND DISCUSSION

3.1 2D distribution of AFE

Fig. 10 presents two-dimensional distributions of adiabatic film cooling effectiveness (η_{ad}) for the Gyroid type structure across four distinct porosity profiles at three injection ratios. Both the streamwise (y) and spanwise (x) coordinates are non-dimensionalized by the TPMS unit cell size (L_c = 2.5 mm). The color scale reflects the magnitude of η_{ad}, with red indicating lower cooling effectiveness and blue representing higher effectiveness. The direction of the mainstream flow is indicated by red arrows.

As depicted in Fig. 10, the adiabatic film cooling effectiveness increases consistently with the injection ratio, showing a monotonic rise from F = 0.68% to F = 1.60% across all profiles. This behavior contrasts with conventional effusion cooling, where increasing coolant injection beyond a blowing ratio of 0.6 often leads to diminished film effectiveness due to jet lift-off and subsequent coolant entrainment into the mainstream flow [36]. In this study, the observed trend in which higher coolant injection leads to improved cooling performance is more

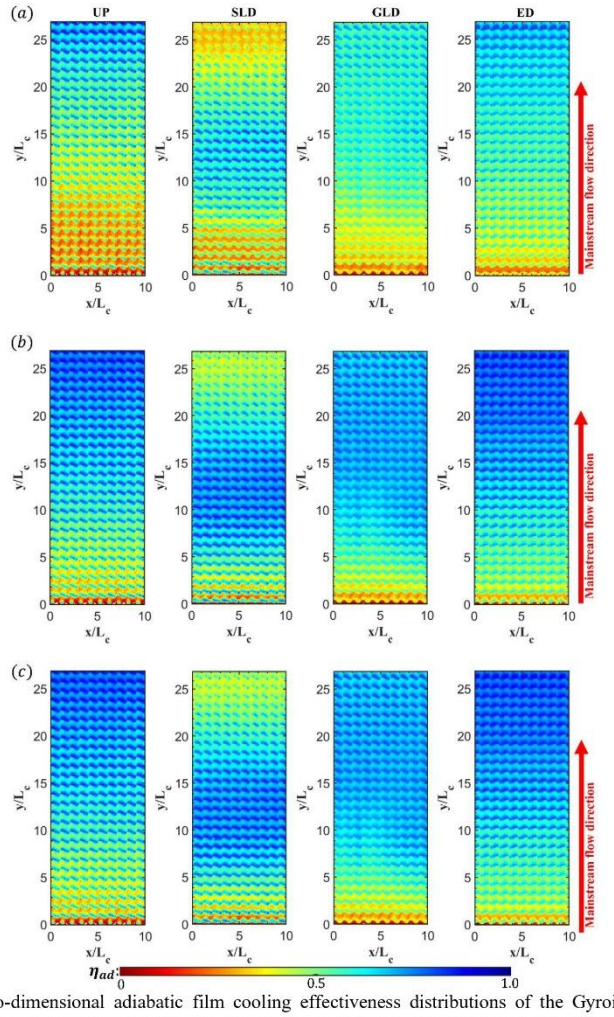

Figure 10 Two-dimensional adiabatic film cooling effectiveness distributions of the Gyroid type TPMS structures. Measurements were made for all four porosity profiles at three injection ratios: (a) F = 0.68%, (b) F = 1.14%, and (c) F = 1.60%.

consistent with practical engine operation. Under high-power settings, engines typically demand greater cooling, which coincides with increased coolant availability due to higher pressure drops across the combustor liners.

In the UP profile, a gradual development of the cooling film is observed along the mainstream flow direction. This behavior is attributed to the accumulation of coolant, which progressively thickens the film and enhances thermal protection downstream. In contrast, the SLD profile demonstrates a more pronounced growth in adiabatic film cooling effectiveness near the leading edge, extending to the midpoint of the observation area. This enhancement is attributed to the intentionally higher porosity in the upstream region, which facilitates greater coolant discharge early in the flow path. However, a noticeable decline in cooling performance is observed downstream, likely due to insufficient coolant availability near the trailing edge. The steep porosity gradient, from 54% to 10%, in the SLD profile results in a disproportionate injection of coolant toward the leading edge, leaving the downstream region inadequately protected and ultimately leading to a non-uniform and suboptimal cooling. More importantly, the GLD profile sustains a relatively uniform cooling performance throughout the observation

area, avoiding the pronounced decline seen downstream in the SLD case. These results indicate that a gradual reduction in porosity along the mainstream flow direction not only enhances cooling near the leading edge but also improves the overall uniformity of film cooling effectiveness. Finally, the ED profile was found to yield the best adiabatic film cooling effectiveness among the four porosity profiles studied, showing a modest improvement over the GLD case which in turn is already a significant enhancement comparing to the baseline UP profile. While the leading-edge porosity of the ED profile is comparable to that of the SLD case to facilitate a quick build-up of cooling film, porosity decreases much more rapidly in the ED profile to conserve coolant consumption once the cooling film is rapidly established. In addition, the porosity in the ED profile stay relatively uniform following the initial rapid drop, as indicated in Fig. 7, leading to a more uniform and sustained cooling film after the leading-edge cooling film build-up.

Fig. 11 presents comparisons of the adiabatic film cooling effectiveness of the Koch-type TPMS for all four porosity profiles as well. Overall, the Koch structure exhibits higher film cooling effectiveness than the Gyroid

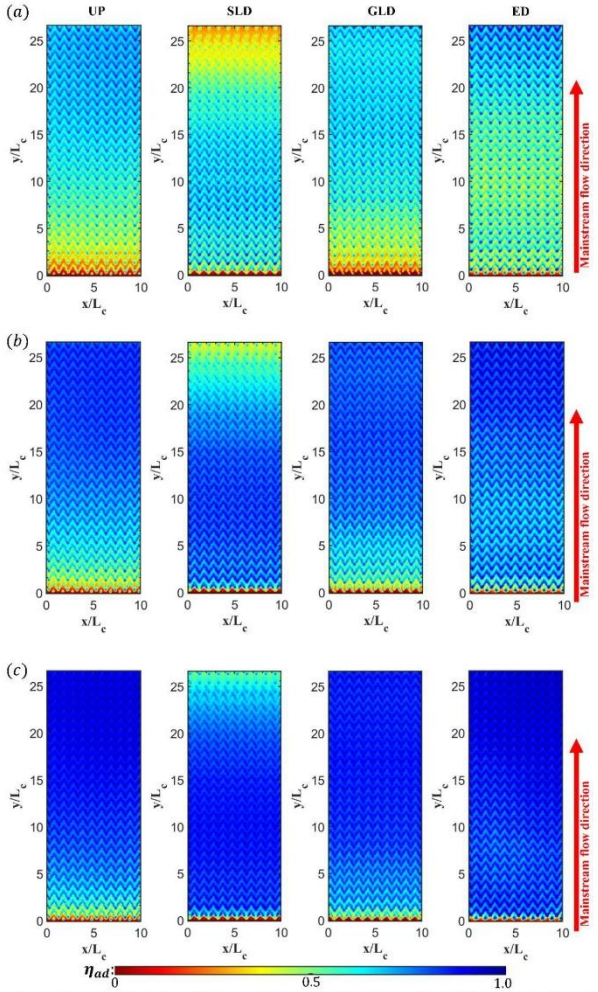

Figure 11 Two-dimensional adiabatic film cooling effectiveness distributions of the Koch-type TPMS structures. Measurements were made for all four porosity profiles at three injection ratios: (a) F = 0.68%, (b) F = 1.14%, and (c) F = 1.60%.

type under identical injection ratio conditions. This enhancement can be attributed to the relatively high pressure drop associated with the Koch-type TPMS, which makes it less susceptible to undesirable internal tangential flow. The Gyroid type exhibits both a larger pore diameter and a lower wetted surface area to volume ratio compared to the Koch type, which are two key parameters influencing pressure drop characteristics in TPMS structures. As a result, the Gyroid type 's lower flow resistance makes it more susceptible to the viscous effects of the mainstream flow, allowing internal tangential flow to develop more readily. This leads to excessive coolant discharge near the trailing edge and an insufficient supply near the leading edge, which limits the accumulation of coolant film and ultimately results in reduced adiabatic film effectiveness. In contrast, the Koch structure maintains a higher pressure drop, which helps to suppress internal tangential flow disturbances and supports a more uniform and efficient distribution of coolant.

Moreover, similar trends in porosity profiles of Koch-type TPMS structures were observed to those of the Gyroid type. Transitioning from the UP to the SLD profile resulted in enhanced cooling effectiveness near the leading edge; however, the excessive coolant consumption in the upstream region led to a deterioration of cooling performance downstream. In contrast, the GLD and ED profiles promoted more efficient coolant utilization, achieving both higher overall cooling effectiveness and improved uniformity of the cooling film. A more detailed analysis of the influence of porosity profiles on the spatial distribution of film cooling effectiveness is presented in the following section.

3.2 Spanwise averaged adiabatic film cooling effectiveness

Figs. 12 and 13 present the spanwise-averaged adiabatic film cooling effectiveness for both Gyroid and Koch types of TPMS structures. The averages were calculated excluding the surface void regions, as these areas are assumed to be fully submerged in coolant and do not accurately represent external coolant film development behavior.

As shown in Figs. 12 and 13, the development of the adiabatic film cooling effectiveness from the leading edge was gradual for the UP profile for both Gyroid and Koch types of TPMS. Therefore, the adiabatic cooling film effectiveness near the leading edge is relatively low comparing to the other profiles. This behavior, as previously discussed, is attributed to the gradual building-up of the cooling film. The undesirable internal tangential flow, which transports coolant downstream and leads to an imbalance in coolant discharge, further slows the development of initial cooling film. In contrast, the SLD profile provides very high adiabatic cooling film effectiveness in the leading-edge region; however, its performance declines sharply beyond the midpoint of the test coupon. This effect becomes even more pronounced at lower injection ratios.

On the other hand, the GLD profile, with its more gradual porosity gradient, effectively mitigates the shortcomings of both the UP and SLD profiles. It enhances the cooling effectiveness near the leading edge more efficiently than the UP case, while avoiding the rapid deterioration of film effectiveness in the downstream region observed in the SLD profile. Finally, the ED profile demonstrated the highest uniformity in film cooling effectiveness for both the Koch and Gyroid types.

The corresponding area-averaged adiabatic film cooling effectiveness and the standard deviation (STD) of the film cooling effectiveness for each case are summarized in Table 1. As shown in Table 1, for the Gyroid type the two preferred porosity profiles, GLD and ED, consistently exhibit improvements in area-averaged adiabatic film cooling effectiveness comparing to the baseline UP profile. In addition, the two preferred functionally graded porosity profiles also show consistently lower standard deviations comparing to the UP profile, indicating enhanced uniformity in adiabatic film cooling effectiveness. A similar trend was observed for the Koch type.

It should also be highlighted that although the GLD and ED profiles yield similarly optimal adiabatic cooling films, as indicated by high mean values and low standard deviations, the measurement area of this study is limited and can be shorter than the full length of an engine combustor. In practice, the ED profile should be the preferred option, because usually the transpiration cooling is expected to cover a longer section of surface area in the flow direction. The ED profile quickly reaches a stable porosity level after the initial rapid drop in porosity, making the profile ideal for almost all practical engine geometries. In contrast, if a GLD profile is adopted for a longer surface, the cooling film protection is expected to be inadequate in the downstream areas. Therefore, among all three graded porosity profiles, the ED porosity profile is expected to work with well with engine geometries of various lengths and provides effective and uniform cooling films.

To illustrated the benefits of ED profile, the proposed graded porosity profile of this study, over the baseline uniform profile (UP), a moving average was applied to the spanwise-averaged film cooling effectiveness profiles of the UP and ED profiles, as shown in Figs. 12 and 13. The moving average was calculated over a smoothing interval corresponding to one unit cell size to smooth local fluctuations and facilitate a clearer comparison, as presented in Figs. 14 and 15.

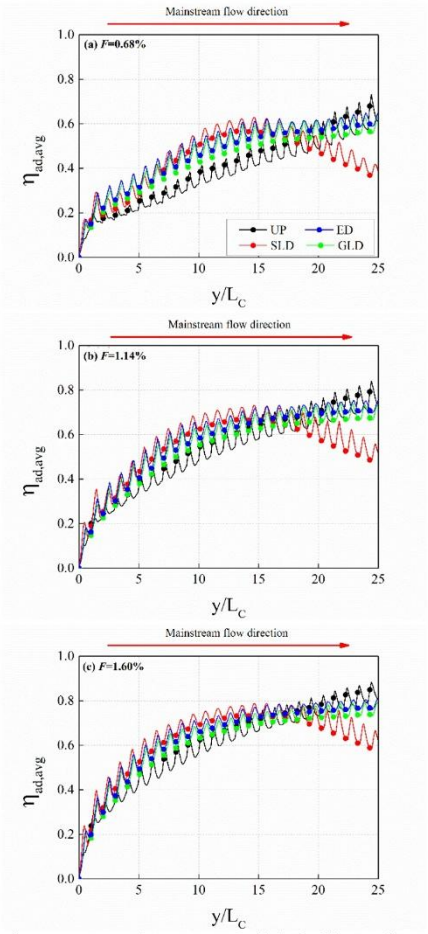

Figure 12 Spanwise-averaged adiabatic film cooling effectiveness for the Gyroid type structure across all porosity profiles.

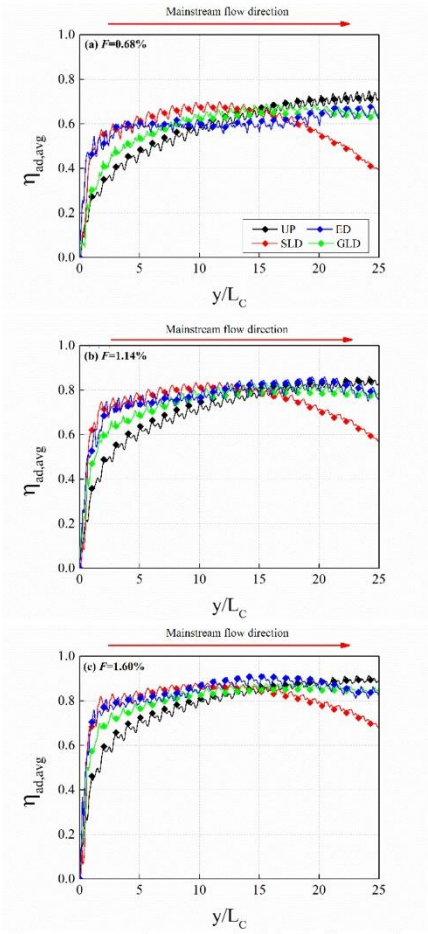

Figure 13 Spanwise-averaged adiabatic film cooling effectiveness for the Koch type structure across all porosity profiles.

Table 1 Area-averaged adiabatic film cooling effectiveness and standard deviation (STD) of adiabatic film cooling effectiveness for each porosity profile and TPMS type.

Porosity Profile	UP		SLD		GLD		ED	
Gyroid type								
	$\bar{\eta}_{ad}$	STD	$\bar{\eta}_{ad}$	STD	$\bar{\eta}_{ad}$	STD	$\bar{\eta}_{ad}$	STD
F=0.68%	0.41	0.17	0.44	0.14	0.47	0.13	0.49	0.14
F=1.14%	0.55	0.17	0.56	0.15	0.57	0.15	0.59	0.16
F=1.60%	0.62	0.17	0.62	0.15	0.63	0.15	0.65	0.15
Koch type								
F=0.68%	0.58	0.15	0.57	0.15	0.59	0.14	0.60	0.14
F=1.14%	0.71	0.15	0.71	0.16	0.74	0.14	0.76	0.13
F=1.60%	0.78	0.14	0.78	0.15	0.80	0.13	0.82	0.12

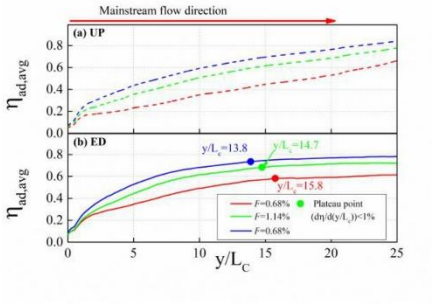

Figure 14 Comparison of moving-averaged, spanwise-averaged adiabatic film cooling effectiveness for the (a) UP and (b) ED profiles of the Gyroid type TPMS structure. The moving average was applied using a window length equivalent to one unit cell to smooth local fluctuations.

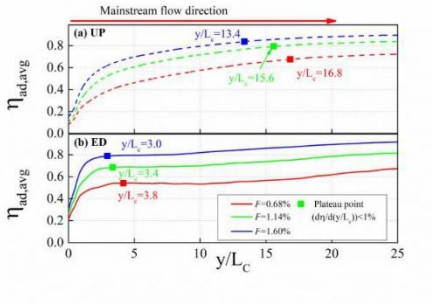

Figure 15 Comparison of moving-averaged, spanwise-averaged adiabatic film cooling effectiveness for the (a) UP and (b) ED profiles of the Koch type TPMS structure. The moving average was applied using a window length equivalent to one unit cell to smooth local fluctuations.

The plateau points shown in Figs. 14 and 15 were identified based on the locations where the local slope of the curve decreased to below 1% $\left(\frac{d\eta}{d(y/L_C)} < 1\%\right)$. In the case of the Gyroid structure in Fig. 14, the UP profile exhibits a gradual increase in film cooling effectiveness along the entire streamwise direction within the observation area, with no clear plateau points observed at all injection ratios. In contrast, for the ED profile, the high porosity near the leading edge facilitates rapid development and accumulation of the coolant film, resulting in the appearance of plateau points in the middle region of the test coupon. In the case of the Koch-type structure shown in Fig. 15, the UP profile exhibits plateau points located in the middle region of the test coupon, confirming that Koch type is the preferred TPMS type for transpiration cooling, as reported in a previous study [33]. In comparison, for the ED profile, the plateau points appear much earlier, specifically near the leading edge, indicating rapid development of the cooling film. This result suggests that the exponentially graded porosity in the ED profile provides more efficient distribution of coolant. As a result, it enables rapid establishment of cooling film and promotes uniform cooling effectiveness across the entire surface.

4.0 CONCLUSION

This study investigated the effects of functionally graded porosity profiles on transpiration cooling performance using two types of triply periodic minimal surface (TPMS) types: Gyroid and Koch. The implementation of graded porosity in TPMS structures has a pronounced effect in enhancing cooling performance, particularly in the leading-edge region. To improve the uniformity of film cooling, this study explores three functionally graded porosity profiles: steep linear decay (SLD), gradual linear decay (GLD), and exponential decay (ED), and compares them with a uniform porosity (UP) baseline, while maintaining a comparable overall average porosity.

The results demonstrated that the porosity gradient has a significant impact on both the spatial distribution and uniformity of adiabatic film cooling effectiveness. While the UP baseline exhibits gradual film development along the mainstream direction, it suffers from low cooling effectiveness near the leading edge. In contrast, the SLD profile achieves high effectiveness early on but shows quick deterioration downstream, particularly under low injection ratio conditions, due to insufficient coolant supply downstream.

The GLD and ED profiles effectively mitigated these drawbacks. The GLD profile provides balanced performance by enhancing the leading-edge cooling while preserving downstream effectiveness. The ED profile, with its steep porosity decay, yielded the most uniform cooling performance across the observation region for both TPMS types. The two preferred graded porosity profiles, GLD and ED, significantly improve the spatial uniformity of the cooling film. The analysis of plateau point locations reveals that both the GLD and ED profiles enable earlier formation and stabilization of the coolant film compared to the UP baseline. This trend was consistently observed in both Gyroid and Koch types lattices, indicating that properly designed porosity grading profiles lead to more uniform and effective transpiration cooling films.

It should also be noted that although the GLD and ED profiles exhibit comparable cooling uniformity within the observation area of the present study, the dimension of the observation area in the main flow direction is shorter than those of practical combustor liners. In real engine applications, where transpiration cooling must extend over longer surfaces, the ED profile is expected to be advantageous. Its rapid stabilization following the initial porosity decay enables sustained and uniform cooling performance over extended streamwise distances.

This study demonstrates that functionally graded TPMS structures are effective in enhancing transpiration cooling performance. By optimizing the porosity distribution, film uniformity can be improved through more efficient coolant utilization, resulting in more effective cooling film over a large area. These findings offer practical design guidance for the development of combustion liners featuring TPMS lattices for next-generation aero-engines.

ACKNOWLEDGMENTS

The work is supported by the National Research Council of Canada's National Program Office's Ideation Fund - the Round 6 Small Teams Initiative and New Beginnings Initiative (Project INBR6-001187). NRC Aerospace Research Centre's Low-Emission Aviation Program also sponsored the work under project A1-024515.

REFERENCES

[1] M.A. Khan, S. Sundarrajan, S. Natarajan, P. Parameswaran, E. Mohandas, Oxidation and hot corrosion behavior of nickel-based superalloy for gas turbine applications, Materials and Manufacturing Processes 29, pp. 832–839, 2014.

[2] Q. Mi, S.H. Yi, D.D. Gang, X.G. Lu, X.L. Liu, Research progress of transpiration cooling for aircraft thermal protection, Appl Therm Eng, vol 236, 2024. https://doi.org/10.1016/j.applthermaleng.2023.121360.

[3] D. Curry, A. Gomez, C. Johnston, Radiative, ablative, and active cooling thermal protection studies for the leading edge of a fixed-straight wing space shuttle, in: *AIAA 6th Thermophysics Conference*, American Institute of Aeronautics and Astronautics (AIAA), Paper No. 71-445, 1971.

[4] S. Weinbaum and H. L. Wheeler, Jr., Heat Transfer in Sweat-Cooled Porous Metals, J Appl Phys, vol. 20, no. 1, pp. 113–122, 1949. https://doi.org/10.1063/1.1698226[5] B. Krittacom, P. Amatachaya, R. Sangchot, Energy balance in Al-Co open-celled foam of transpiration cooling, in: Applied Mechanics and Materials, Trans Tech Publications Ltd, 2014: pp. 41–45. https://doi.org/10.4028/www.scientific.net/AMM.575.41.

[6] J. Ma, X. Luo, H. Li, Y. Liu, An experimental investigation on transpiration cooling based on the multilaminated sintered woven wire mesh structures, J Therm Sci Eng Appl, vol 8, 2016. https://doi.org/10.1115/1.4032921.

[7] Y.Q. Liu, P.X. Jiang, Y. Bin Xiong, Y.P. Wang, Experimental and numerical investigation of transpiration cooling for sintered porous flat plates, in: Appl Therm Eng, pp. 997–1007, 2013. https://doi.org/10.1016/j.applthermaleng.2012.08.028.

[8] K. Yeranee, Y. Rao, A review of recent research on flow and heat transfer analysis in additively manufactured transpiration cooling for gas turbines, Energies, vol. 18, no. 13, 2025. https://doi.org/10.3390/en18133282

[9] H. Xu, R. Su, Y. He, X. Zhang, C. Hu, D. Tang, Research progress on the failure modes and failure mechanisms of the transpiration cooling structure, International Communications in Heat and Mass Transfer, vol 167, pp. 109399, 2025. https://doi.org/10.1016/J.ICHEATMASSTRANSFER.2025.109399.

[10] X. Li, Z. Liao, H. Li, P. Jiang, R. Xu, Phase-change transpiration cooling in heterogeneous composite porous plates: Heat transfer characteristics and their prediction, Int J Heat Mass Transf, vol 224, pp. 125290, 2024. https://doi.org/10.1016/J.IJHEATMASSTRANSFER.2024.125290.

[11] V. König, M. Rom, S. Müller, M. Selzer, S. Schweikert, J. Von Wolfersdorf, Numerical and Experimental Investigation of Transpiration Cooling with Carbon/Carbon Characteristic Outflow Distributions, J Thermophys Heat Trans, vol 33, pp. 449–461. 2019. https://doi.org/10.2514/1.T5457.

[12] Z. Min, G. Huang, S.N. Parbat, L. Yang, M.K. Chyu, Experimental investigation on additively manufactured transpiration and film cooling structures, J Turbomach, vol 141, 2019. https://doi.org/10.1115/1.4042009.

[13] O. Al-Ketan, R. Rowshan, R.K. Abu Al-Rub, Topology-mechanical property relationship of 3D printed strut, skeletal, and sheet based periodic metallic cellular materials, Addit Manuf, vol 19, pp. 167–183, 2018. https://doi.org/10.1016/j.addma.2017.12.006.

[14] B.W. Reynolds, C.J. Fee, K.R. Morison, D.J. Holland, Characterisation of Heat Transfer within 3D Printed TPMS Heat Exchangers, Int J Heat Mass Transf, vol 212, pp. 124264, 2023. https://doi.org/10.1016/J.IJHEATMASSTRANSFER.2023.124264.

[15] W. Li, W. Li, Z. Yu, Heat transfer enhancement of water-cooled triply periodic minimal surface heat exchangers, Appl Therm Eng, vol 217, pp. 119198, 2022. https://doi.org/10.1016/J.APPLTHERMALENG.2022.119198.

[16] J. Son, Y. Pyo, M. Broumand, Z. Hong, S. Sarafan, P. Wanjara, Advanced transpiration cooling method using additively manufactured TPMS structure, in: Conference of Metallurgists, Springer Nature Switzerland, Cham, pp. 449–451, 2023.

[17] H. Sun, H. Ma, L. Yan, H. Fu, Y. Luan, P. Zunino, Numerical simulations on the performance of transpiration cooling implemented with perforated flat plates, Appl. Therm. Eng, vol 238, pp. 12194, 2024. https://doi.org/10.1016/j.applthermaleng.2023.121943.

[18] K. Yeranee, Y. Rao, A Review of Recent Research on Flow and Heat Transfer Analysis in Additively Manufactured Transpiration Cooling for Gas Turbines, Energies (Basel), vol 18, pp. 3282, 2025. https://doi.org/10.3390/en18133282.

[19] M. Araya, M. Jaskari, T. Rautio, T. Guillén and A. Järvenpää, Assessing the compressive and tensile properties of TPMS-Gyroid and stochastic Ti64 lattice structures: A study on laser powder bed fusion manufacturing for biomedical implants, J Sci Adv Mater Devices, vol. 9, no. 1, 2024, p. 100663. https://doi.org/10.1016/j.jsamd.2023.100663

[20] M. Broumand, J. Son, Y. Pyo, S. Yun, Z. Hong, TPMS-based transpiration cooling for film cooling enhancement, Int J Heat Mass Transf, vol 231, pp. 125824, 2024. https://doi.org/10.1016/j.ijheatmasstransfer.2024.125824.

[21] J. Son, Y. Pyo, P. Richer, B. Jodoin, Z. Hong, Impact of TPMS structure unit cell size on transpiration cooling, in: *AIAA SciTech 2025 Forum*, American Institute of Aeronautics and Astronautics (AIAA), Paper 0329, 2025.

[22] J. Son, M. Broumand, Y. Pyo, P. Richer, B. Jodoin, Z. Hong, Effects of Lattice Orientation Angle On Tpms-Based Transpiration Cooling, J Eng Gas Turbine Power, pp. 1–28, 2024. https://doi.org/10.1115/1.4067378.

[23] Y. Yang, J. Mao, P. Chen, H. Zhang, H. Tang, Numerical investigation on transpiration cooling performance with different porosities and mainstream pressure gradients, International Journal of Thermal Sciences, vol 184, pp. 107991, 2023. https://doi.org/10.1016/J.IJTHERMALSCI.2022.107991.

[24] M. Hinse, P. Richer, B. Jodoin, K. Yildiz, S. Yun, Z. Hong, Numerical and experimental studies of transpiration cooling film effectiveness over porous materials, in: AIAA Propulsion and Energy 2020 Forum, American Institute of Aeronautics and Astronautics Inc, AIAA, 2020: pp. 1–20, 2020. https://doi.org/10.2514/6.2020-3947.

[25] W. Dong, J. Wang, S. Chen, B. Ai, X. Luo, Modelling and investigation on heat transfer deterioration during transpiration cooling with liquid coolant phase-change, Appl Therm Eng, vol 128, pp. 381–392, 2018. https://doi.org/10.1016/J.APPLTHERMALENG.2017.08.155.

[26] Y. Liu, T. Liu, R. Ding, F. He, J. Wang, Experimental and numerical investigation of transpiration cooling with gradient porosity layout for the thermal protection of nose cone, Aerosp Sci Technol, vol 149, pp. 109140, 2024. https://doi.org/10.1016/J.AST.2024.109140.

[27] Z. Cheng, R. Xu, P. Jiang, Transpiration cooling with phase change by functionally graded porous media, Int J Heat Mass Transf, vol 205, 2023. https://doi.org/10.1016/j.ijheatmasstransfer.2023.123862.

[28] O. Al-Ketan, M. Ali, M. Khalil, R. Rowshan, K.A. Khan, R.K. Abu Al-Rub, Forced Convection Computational Fluid Dynamics Analysis of Architected and Three-Dimensional Printable Heat Sinks Based on Triply Periodic Minimal Surfaces, J Therm Sci Eng Appl, vol 13, 2021. https://doi.org/10.1115/1.4047385.

[29] Y. Lu, Z. Cui, L. Cheng, J. Li, Z. Yang, H. Zhu, C. Wu, Quantifying the discrepancies in the geometric and mechanical properties of the theoretically designed and additively manufactured scaffolds, J Mech Behav Biomed Mater, vol 112, 2020. https://doi.org/10.1016/j.jmbbm.2020.104080.

[30] J. Son, Y. Pyo, P. Richer, B. Jodoin, Z. Hong, Impact of Triply Periodic Minimal Surface Structure Unit Cell Size on Transpiration Cooling, J Thermophys Heat Trans, pp. 1–13. https://doi.org/10.2514/1.T7212.

[31] Y. Pyo, J. Son, P. Richer, B. Jodoin, M. Broumand, S. Yun, Z. Hong, Isolating influences of varying pitch from the effects of non-zero compound angles on effusion cooling, The Aeronautical Journal, pp. 1–21, 2024. https://doi.org/10.1017/aer.2024.108.

[32] Z. Lei, A. Mahallati, M. Cunningham, P. Germain, Influence of inlet swirl on the aerodynamics of a model turbofan lobed mixer, in: *ASME International Mechanical Engineering Congress and Exposition*, vol. 44441, pp. 807–819, 2010.

[33] J. Son, P. Richer, B. Jodoin, Z. Hong, Effect of morphological variations in TPMS lattice structures on transpiration cooling, in: ASME Turbo Expo, American Society of Mechanical Engineers, vol. 88827, Paper V006T13A003, 2025.

[34] K.-J. Moon, H. Mori, M. Furukawa, Simultaneous measurement method of pressure and temperature using dual-layer PSP/TSP with lifetime-based method, Meas Sci Technol, vol 29, pp. 125301, 2018. https://doi.org/10.1088/1361-6501/aae408.

[35] Z. ya Zhang, H. Zhang, J. Zhang, S. kun Qin, M. de Duan, Study on flow field characteristics of TPMS porous materials, Journal of the Brazilian Society of Mechanical Sciences and Engineering, vol 45, 2023. https://doi.org/10.1007/s40430-023-04113-0.

[36] L.C. Paitich, P. Richer, B. Jodoin, Y. Pyo, S. Yun, Z. Hong, Directional Effects of Effusion Cooling on the Cooling Film Effectiveness, AIAA Journal, vol 60, pp. 423–434, 2022. https://doi.org/10.2514/1.J060625.

5.7 Comparison of Cooling Mechanisms Between Effusion and TPMS-Based Transpiration Cooling

The cooling performance of transpiration cooling is governed by two complementary mechanisms: external film cooling and conjugate heat transfer (CHT). Previous studies on TPMS-based transpiration cooling have primarily employed pressure-sensitive paint (PSP) to evaluate adiabatic film effectiveness (AFE), demonstrating the superior coolant-film formation achieved by TPMS structures. However, because AFE represents only the footprint of the coolant film under adiabatic conditions, it excludes the contribution of conjugate heat transfer (CHT), including internal convection and solid conduction. Consequently, the respective contributions of film cooling and conjugate heat transfer to the overall cooling performance remain unclear. Accordingly, the objective of the present study is to elucidate the cooling mechanisms governing effusion and TPMS-based transpiration cooling and to establish design guidelines through a quantitative comparison of the contributions of film cooling and conjugate heat transfer.

In this investigation, three cooling configurations—a baseline effusion cooling configuration, a 45° compound-angle effusion cooling configuration, and a Koch-type TPMS-based transpiration cooling configuration—were experimentally evaluated. Adiabatic film effectiveness (AFE) and overall film effectiveness (OFE) were measured using pressure-sensitive paint (PSP) and temperature-sensitive paint (TSP), respectively, enabling the respective contributions of film cooling and conjugate heat transfer to be quantified.

The results demonstrate that the 45° compound-angle configuration improves cooling performance primarily through enhanced film cooling, whereas TPMS-based transpiration cooling fundamentally changes the dominant cooling mechanism from conjugate heat transfer to coolant-film protection. The interconnected porous network promotes uniform coolant discharge, continuous coolant-film formation, and enhanced internal heat transfer, resulting in the highest and most uniform cooling performance among the configurations investigated. These findings establish that TPMS architectures should be designed to maximize uniform coolant-film formation while maintaining effective internal heat transfer, making TPMS-based transpiration cooling the preferred cooling strategy for next-generation gas turbine combustor liners.

This study is written as a research article and published as a peer-reviewed journal paper, *International Journal of Heat and Mass Transfer*.

International Journal of Heat and Mass Transfer 274 (2027) 129836

Contents lists available at ScienceDirect

International Journal of Heat and Mass Transfer

journal homepage: www.elsevier.com/locate/ijhmt

A comparative study of cooling mechanisms in effusion and TPMS-based transpiration cooling

Juchan Son [a,b], Patrick Richer [a], Bertrand Jodoin [a], Sina Kashanj [b], Mohsen Broumand [b], Zekai Hong [a,b,*]

[a] Department of Mechanical Engineering, University of Ottawa, 161 Louis-Pasteur Private, Ottawa, Ontario K1N 6N5, Canada
[b] Aerospace Research Center, National Research Council of Canada, 1200 Montreal Road, Ottawa, Ontario K1A 0R6, Canada

ARTICLE INFO

Keywords:
Gas turbine
Film cooling
Heat transfer
TPMS
Transpiration cooling

ABSTRACT

Additively manufactured transpiration cooling based on triply periodic minimal surface (TPMS) lattices has emerged as a promising thermal management strategy for next-generation gas turbines. However, the relative contributions of external film cooling and conjugate heat transfer (CHT), comprising internal convection and solid conduction, remain unclear. This study experimentally quantifies these contributions by independently measuring adiabatic film effectiveness (AFE) and overall film effectiveness (OFE) using pressure-sensitive paint (PSP) and temperature-sensitive paint (TSP), respectively. Three configurations were investigated: baseline effusion cooling with zero compound angle, effusion cooling with a 45° compound angle, and Koch-type TPMS-based transpiration cooling. The 45° compound-angle configuration enhanced both AFE and OFE relative to the baseline by improving lateral coolant spreading and suppressing jet lift-off, with the improvement primarily attributed to enhanced film cooling. TPMS-based transpiration cooling achieved substantially higher AFE and OFE over the investigated injection ratios through more effective coolant-film formation and enhanced internal heat transfer. CHT remained the primary contributor to the overall cooling performance of both effusion configurations, whereas film cooling became dominant for the TPMS configuration. The temperature-based comparison of AFE and OFE suggests a greater relative role of external film cooling in the investigated Koch-type TPMS configuration than in the effusion configurations under the tested conditions.

1. Introduction

Gas turbines are extensively employed in aircraft propulsion and power generation owing to their high power density and thermal efficiency. Increasingly stringent environmental regulations and the growing demand for higher engine efficiency have driven a continuous increase in turbine inlet temperature (TIT), which now exceeds the temperature capability of conventional nickel-based superalloys [1,2]. Consequently, hot-section components, such as combustor liners and turbine blades, are subjected to severe thermal loads that can accelerate material degradation and reduce service life [3]. To ensure reliable operation under these extreme conditions, advanced cooling technologies have become indispensable for maintaining component durability while enabling further improvements in engine efficiency.

Gas turbine cooling technologies can be broadly classified into internal and external cooling methods. As illustrated in Fig. 1, thermal management strategies have evolved, driven by the increasing demand for higher cooling performance under progressively higher turbine inlet temperatures. The earliest and simplest approach is convection cooling, in which a portion of the compressor discharge air flows through internal passages to remove heat from the liner by forced convection [3–5]. Although this technique effectively reduces the metal temperature, its cooling capability becomes insufficient under the severe thermal loads encountered in modern gas turbines. To improve internal heat transfer, impingement cooling was subsequently developed, in which arrays of impinging jets generate high local heat transfer coefficients on the inner surface of the liner [6,7]. Nevertheless, both convection and impingement cooling are limited by the direct exposure of the external surface to the hot mainstream gases [8]. To provide direct thermal protection, film cooling has become the predominant external cooling technology for gas turbine hot-section components [9]. Among various film cooling techniques, effusion cooling is regarded as one of the most

https://doi.org/10.1016/j.ijheatmasstransfer.2026.129836
Received 27 July 2026; Received in revised form 10 October 2026; Accepted 1 November 2026
Available online 11 November 2026
0017-9310/Crown Copyright © 2026 Published by Elsevier Ltd. This is an open access article under the CC BY-NC-ND license (http://creativecommons.org/licenses/by-nc-nd/4.0/).

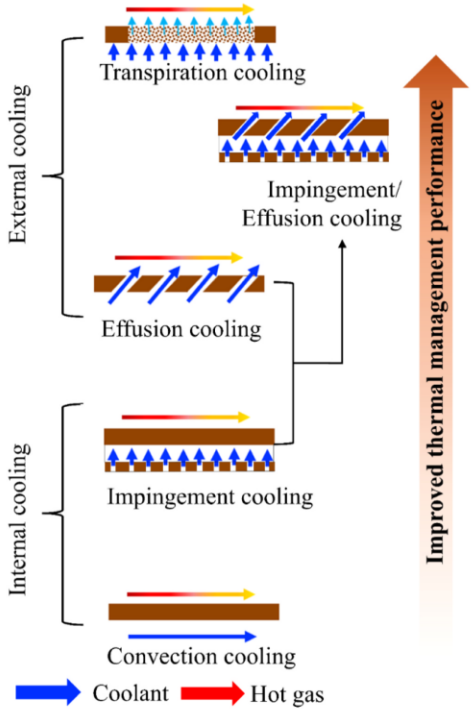

Fig. 1. Schematic illustration of the evolution of gas turbine cooling technologies.

advanced configurations. In this approach, coolant is discharged through an array of discrete inclined holes to form a protective coolant film over the external surface, thereby reducing the heat transfer from the mainstream gas [10]. Further enhancement has been achieved through double-wall cooling, in which internal impingement cooling is combined with external effusion cooling to simultaneously increase internal heat transfer and improve coolant film coverage [11]. Despite these developments, these cooling strategies require a considerable amount of high-pressure compressor discharge air, which penalizes the overall engine efficiency.

Consequently, transpiration cooling has emerged as one of the most promising cooling technologies for next-generation gas turbines. Originally proposed in the 1940s [12], transpiration cooling supplies coolant through an interconnected porous structure, providing simultaneous internal convective cooling and nearly continuous external film protection [13,14]. Compared with discrete-hole effusion cooling, the distributed porous architecture promotes uniform coolant discharge, suppresses jet lift-off, enhances coolant coverage, and improves thermal protection over the entire cooled surface [13]. Conventional transpiration cooling structures have been fabricated using porous media such as sintered powder [15], woven mesh wires [16], melt casting [17], perforated plates [18], and composite porous materials [19]. The distributed coolant injection through the porous structure produces a nearly continuous coolant film over the surface while simultaneously enhancing internal convective heat transfer, thereby providing superior thermal protection against the hot mainstream gases. Despite these advantages, the application of conventional transpiration cooling in gas turbine engines has remained limited because of challenges with mechanical strength, limited geometric flexibility, and manufacturing challenges associated with traditional stochastic porous materials [20].

Recent advances in additive manufacturing (AM) have created new opportunities for fabricating deterministic porous structures with precisely controlled geometries. Among various deterministic porous architectures, triply periodic minimal surface (TPMS) structures have emerged as promising candidates for transpiration cooling because of their superior mechanical performance relative to conventional stochastic porous media, highly interconnected pore network, and compatibility with additive manufacturing (AM). Araya et al. [21] demonstrated that gyroid lattices fabricated by laser powder bed fusion exhibited higher yield strength than stochastic Voronoi structures. This improvement was attributed to the continuous and smoothly curved TPMS topology, which promotes a more uniform stress distribution while reducing stress concentrations. Furthermore, the interconnected pore network enables more uniform coolant transport and distribution throughout the porous structure [22]. These characteristics make TPMS architectures particularly well suited for transpiration cooling applications, where efficient coolant transport, superior structural integrity, and a high specific surface area are essential. The large surface area-to-volume ratio promotes enhanced convective heat transfer between the coolant and the solid matrix, thereby improving the overall cooling performance [23,24].

Recent investigations have demonstrated that TPMS-based transpiration cooling significantly outperforms conventional effusion cooling in terms of adiabatic film effectiveness (AFE). An earlier study from this group [25] showed that additively manufactured TPMS lattices with different porosities improved film cooling effectiveness by up to a factor of five compared with conventional effusion cooling, highlighting the advantages of distributed coolant injection. Subsequently, we reported that reducing the TPMS unit cell size while maintaining a constant porosity further enhanced AFE through more uniform coolant distribution over the cooled surface [26]. Further optimization of TPMS topology and lattice orientation revealed that increasing the top-surface tortuosity and aligning the pore network with the mainstream flow direction promoted improved coolant coverage, leading to higher adiabatic film effectiveness [27].

More recently, research has shifted toward optimizing the thermal performance of TPMS-based transpiration cooling through geometric tailoring and topology optimization. The authors' previous study [28] demonstrated that functionally graded porosity distributions in Gyroid and Koch TPMS structures promoted earlier coolant film establishment, resulting in improved spatial uniformity of adiabatic film effectiveness and more efficient coolant utilization. At the pore scale, Zhou et al. [29] showed that the geometry of the pore diameter, which is defined as the smallest flow passage within the TPMS structure, plays a critical role in determining coolant flow resistance and cooling effectiveness. Brimacombe et al. [30] experimentally investigated Gyroid TPMS structures with porosities ranging from 0.3 to 0.5 and reported that the cooling effectiveness was primarily governed by the coolant injection ratio. In addition, Yeranee et al. [31] applied density-based topology optimization to printable diamond TPMS lattices for gas turbine trailing-edge cooling and achieved heat transfer enhancements of up to 150% compared with conventional pin-fin designs. More recently, He et al. [32] proposed a hybrid TPMS-based transpiration–film cooling configuration incorporating a porous TPMS layer beneath the film cooling surface, demonstrating enhanced cooling performance through the combined effects of improved internal convection and more uniform coolant film formation.

Despite the promising results reported in recent studies, the respective contributions of external film cooling and internal heat transfer to the overall cooling performance of TPMS-based transpiration cooling remain unclear. To the best of the authors' knowledge, this distinction has not yet been quantitatively investigated. Comparing AFE and OFE provides a temperature-based assessment of this relationship. Fig. 2

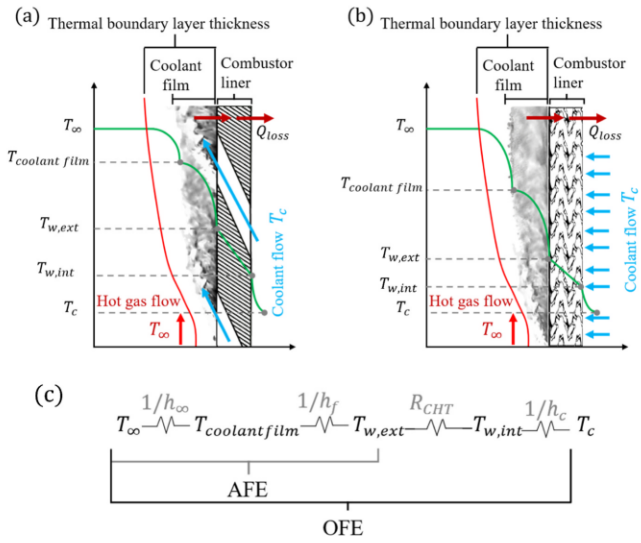

Fig. 2. Schematic of temperature profiles normal to the surface for (a) conventional effusion cooling and (b) TPMS-based transpiration cooling. (c) conceptual thermal resistance network illustrates the relationship between adiabatic film cooling effectiveness (AFE) and overall film cooling effectiveness (OFE).

schematically illustrates the distinct temperature profiles normal to the surface for effusion cooling (Fig. 2a) and TPMS-based transpiration cooling (Fig. 2b).

AFE represents the effectiveness of the coolant film alone by assuming an adiabatic wall, thereby eliminating the influence of solid heat conduction and convective heat transfer due to internal channels, henceforth referred to as conjugate heat transfer (CHT). Consequently, AFE primarily characterizes the coolant film's ability to thermally shield the surfaces. In contrast, OFE incorporates the combined effects of external film cooling and CHT thereby representing the overall thermal protection provided by the cooling system. For transpiration cooling, the distributed coolant injection promotes earlier film establishment, broader surface coverage, and a thicker coolant layer. Furthermore, the interconnected porous architecture provides a significantly larger coolant–solid interfacial area, thereby reducing the resistance associated with conjugate heat transfer (R_{CHT}) and enhancing internal heat transfer within the cooling structure.

To assess the cooling mechanisms of both effusion and TPMS-based transpiration cooling, a comparative experimental study was performed using three cooling configurations: (i) a baseline effusion cooling configuration with a zero compound angle, (ii) effusion cooling with a 45° compound angle, and (iii) transpiration cooling based on a Koch-type TPMS lattice. AFE was measured using pressure-sensitive paint (PSP) to characterize the equivalent adiabatic film protection, while OFE was evaluated using temperature-sensitive paint (TSP) to characterize the actual wall-temperature response involving film cooling and conjugate heat transfer. The present study extends the authors' previous investigations of TPMS geometric effects on AFE by jointly comparing AFE and OFE to provide a temperature-based assessment of the relative roles of external film cooling and CHT. The comparisons of AFE and OFE provide insight into the relationship between coolant film formation and overall effectiveness under the investigated conditions.

2. EXPERIMENT SETUP

2.1. Effusion cooling test coupons

Two effusion cooling configurations were investigated in this study: a baseline configuration with a zero compound angle and an improved design featuring a 45-degree compound angle. The two parameters defining the orientation of a single effusion cooling hole are illustrated in Fig. 3, i.e., the inclination angle (α) and the compound angle (β). The inclination angle (α) is defined as the angle between the cooling hole axis and the target surface in the streamwise plane (A–A view).

A shallow inclination angle promotes coolant attachment to the wall by reducing jet lift-off, thereby improving downstream film coverage [33]. The compound angle (β) is defined as the angle between the projection of the hole axis onto the surface and the mainstream flow direction (top view). Introducing a compound angle enhances lateral coolant spreading and improves the uniformity of the coolant film over the protected surface [34,35].

The two different effusion test coupons investigated in this study are shown in Fig. 4. Both coupons were fabricated using Inconel 718. The

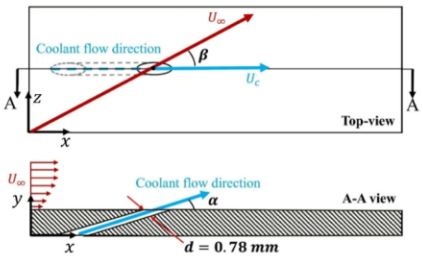

Fig. 3. Diagram of a single effusion cooling hole.

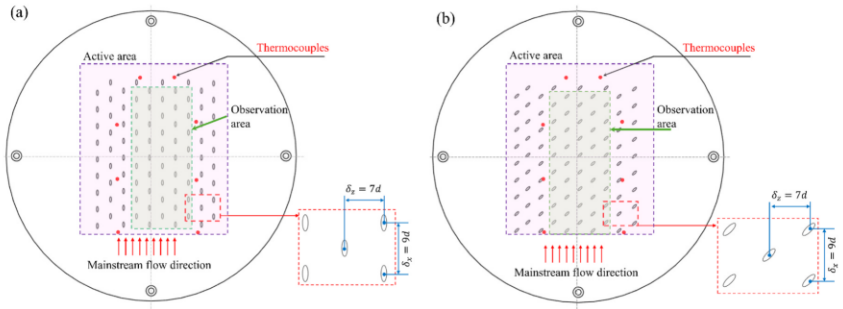

Fig. 4. Schematic of the effusion cooling test coupons: (a) baseline configuration without a compound angle (β = 0°) and (b) compound-angle configuration (β = 45°).

outer diameter of the circular coupons is 123.8 mm and the thickness is 1.6 mm. The effusion holes were manufactured using electrical discharge machining (EDM) with a hole diameter of 0.78 mm and an inclination angle (α) of 20°. The diameters of all effusion cooling holes were measured using Grade Z pin gauges with a maximum tolerance of ±0.0025 mm. The average hole diameter of the two test coupons was measured to be 0.77 ± 0.01mm. As shown in Fig. 4, both PSP and TSP were applied to the red-shaded region of each test coupon. Data analysis was restricted to the central observation area (green-shaded region) to minimize side wall effects. The thermocouple locations used for TSP calibration are indicated by the red dots.

The first effusion cooling configuration, referred to as the baseline configuration, consists of straight holes with a zero compound angle arranged in a staggered pattern. As shown in Fig. 4(a), the spanwise and streamwise pitches are maintained at 7d and 9d.

The second effusion cooling coupon is identical to the baseline case with the exception that a 45° compound angle was introduced, as illustrated in Fig. 4(b). Previous experimental work by Pyo et al. [10] demonstrated that the compound angle governs the trade-off between streamwise coolant penetration and lateral coolant spreading. Larger compound angles increase lateral coverage but shorten the downstream protection because of enhanced mixing with the mainstream, whereas smaller compound angles improve streamwise penetration at the expense of spanwise coverage. Based on these observations, a compound angle of 45° was selected as a compromise to achieve balanced coolant coverage in both the streamwise and spanwise directions.

2.2. TPMS structure and transpiration cooling test coupon

Based on the authors' previous investigations [36], the Koch-type triply periodic minimal surface (TPMS) was selected for the present study because of its superior transpiration cooling performance. Compared with other TPMS topologies, such as the Gyroid and Diamond structures, the Koch structure possesses a highly tortuous surface morphology and a large wetted surface area, which promote uniform coolant distribution and enhance internal heat transfer. These characteristics make it a promising candidate for transpiration cooling applications. TPMS geometries are mathematically described using level-set equations, in which the porosity is controlled by varying the level-set constant, c. The level-set equation for the Koch TPMS is given by

$$\varnothing_{Koch}(x,y,z) = \cos(2X)\sin(Y)\cos(Z) + \cos(2Y)\sin(Z)\cos(X) + \cos(2Z)\sin(X)\cos(Y) = c \quad (1)$$

where X = 2πx/α, Y= 2πy/β, and Z = 2πz/γ, and α, β, and γ are the unit cell size in x, y, and z directions, respectively. The level-set equation defines an iso-surface that partitions the unit cell into solid and void domains. The TPMS solid structure is generated by assigning one side of the iso-surface as the solid phase and the other as the pore space according to

$$\varnothing(x,y,z) < c \quad (2)$$

When $c = 0$, the solid and void domains occupy equal volumes, corresponding to a porosity of 50%. Fig. 5 illustrates the Koch TPMS unit cell and the definition of the pore diameter, D_p, which is defined as the diameter of the largest inscribed sphere that can pass through the narrowest constriction of the interconnected pore network [37].

The intricate three-dimensional connected pore network of TPMS structures cannot be manufactured using conventional subtractive fabrication methods and is therefore enabled by additive manufacturing (AM). In the present study, all TPMS test coupons were fabricated from Inconel 718 using an EOS M290 laser powder bed fusion (LPBF) system. Discrepancies between the designed and fabricated geometries are inevitable and have been widely reported in the additive manufacturing literature [38]. These dimensional deviations become increasingly significant as the characteristic feature size approaches the manufacturing limits. In particular, the actual pore size is often reduced because of melt pool enlargement, partially melted powder particles adhering to the surface, and the finite resolution of the LPBF process, resulting in lower porosity than the designed value [22,39].

Fig. 6(a) compares the intended top-surface boundary defined by the CAD model (magenta dashed line) with the fabricated TPMS structure observed using a KEYENCE VHX-2000 digital 3D microscope. The printed structure exhibits a noticeable reduction in the void opening compared with the designed geometry, indicating dimensional

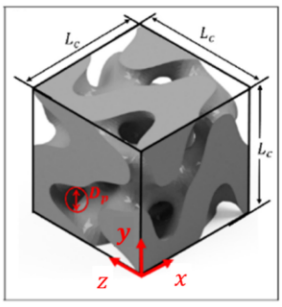

Fig. 5. Unit cell cube of the Koch type TPMS solid network with 50% porosity.

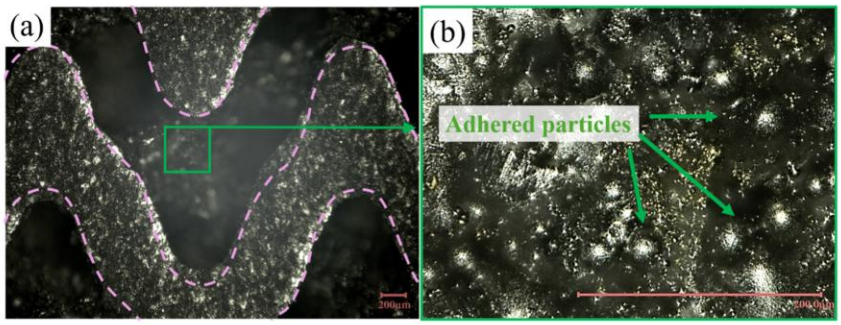

Fig. 6. Microscopic images of the additively manufactured Koch-type TPMS test coupon fabricated from Inconel 718 using laser powder bed fusion (LPBF): (a) comparison of the designed and fabricated top-surface geometry with the dashed curves indicating the designed surface texture; (b) magnified view of the internal channel showing partially fused powder particles.

deviations introduced during the LPBF process. These deviations become increasingly pronounced as the characteristic pore size approaches the manufacturing resolution limit, posing a significant challenge to the fabrication of fine TPMS architectures. The magnified image in Fig. 6(b) reveals that partially fused powder particles adhering to the channel surfaces, together with melt pool expansion during the LPBF process, reduce the effective pore opening relative to the designed geometry. Consequently, the fabricated TPMS structure exhibits lower porosity and permeability than the nominal design. These manufacturing-induced geometric deviations should therefore be considered when interpreting the experimental cooling performance of the TPMS-based transpiration cooling configuration.

To account for manufacturing-induced geometric deviations, the actual porosity of the fabricated TPMS structures was determined using a mass-based method. While the nominal porosity is directly prescribed by the TPMS level-set equation, the actual porosity was calculated from the measured mass of the fabricated lattice according to

$$\varepsilon_a = \left(1 - \frac{M_a}{M_s}\right) \times 100 \tag{3}$$

where M_a is the actual mass of the fabricated TPMS lattice and M_s is the mass of a fully dense (solid) reference specimen with identical external dimensions. The mass measurements were performed using a precision electronic balance (Scientech SA-80) with a resolution of 0.1 mg. Fig. 7 compares the nominal and measured porosities of the additively manufactured Koch-type TPMS structures for three unit-cell sizes. For all unit-cell sizes, the measured porosity is consistently lower than the nominal value because of LPBF-induced geometric deviations. The excellent linear correlations ($R^2 = 0.999$) provide empirical calibration relationships for predicting the achievable porosity and compensating for manufacturing-induced deviations during TPMS design.

In the present study, a unit-cell size of $L_c = 2.5$mm with a nominal porosity of 50%, corresponding to an actual porosity of approximately 40%, was selected because it provided the best compromise between printability and preservation of the intended TPMS topology. The corresponding pore diameter (D_p) and internal wetted area-to-volume ratio (λ) are 0.44 mm and 2.14 mm^2/mm^3, respectively, with the latter being defined as the internal wetted area divided by the unit-cell volume. Fig. 8 illustrates the TPMS-based transpiration cooling test coupon employed in the present study.

The geometric parameters of the three cooling configurations investigated in the present study are summarized in Table 1.

2.3. Experimental setup

The experimental facility has been detailed in the authors' previous studies [10,40]; therefore, only a brief overview is presented here. A schematic of the experimental facility is shown in Fig. 9.

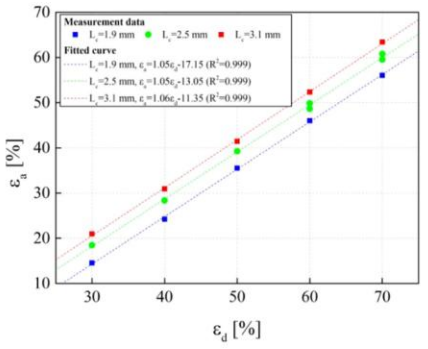

Fig. 7. Relationship between the nominal (ε_d) and measured (ε_a) porosities of LPBF-fabricated Koch-type TPMS structures for different unit-cell sizes.

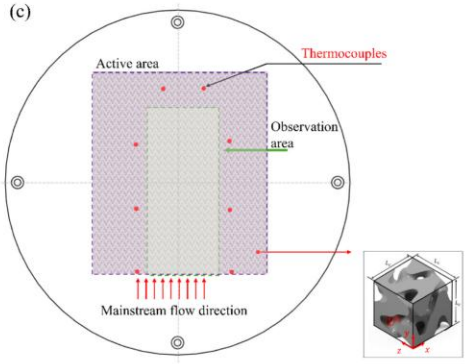

Fig. 8. Schematic of the TPMS-based transpiration cooling test coupon.

Table 1
Geometrical parameters of the effusion cooling and TPMS-based transpiration cooling configurations investigated in the present study.

Effusion cooling					
Type	α	β	δ_x	δ_z	d [mm]
Base line effusion		0 °			
Compound angle	20 °	45 °	9d	7d	0.78
Transpiration cooling					
Type	L_v [mm]	ϵ_d [%]	ϵ_n [%]	D_p [mm]	λ [mm^2/mm^3]
Koch	2.5	50%	40%	0.44	2.14

The mainstream airflow was supplied by a centrifugal blower driven by a 30 kW AC motor, providing a uniform approach flow through a square test section with a cross-sectional area of 127 mm × 127 mm. The mainstream velocity was maintained at 33 m/s, corresponding to a Reynolds number of approximately 2.56×10^5. The velocity was measured using a Pitot tube positioned upstream of the test coupon, while the mainstream temperature (T_∞) was monitored using a K-type thermocouple installed adjacent to the Pitot tube. Throughout the experiments, the mainstream temperature was maintained at approximately 292 K by a centralized air-conditioning system, and the free-stream turbulence intensity was approximately 3%. Nitrogen (N_2) was employed as the coolant proxy. The coolant flow rate was regulated using an Omega FMA5400A/5500 A mass flow controller with a measurement range of 0–200 SLPM before the coolant entered the coolant reservoir through a flexible heating hose (Thermolab 702S). Inside the reservoir, a perforated plate and a honeycomb flow straightener were installed to ensure a spatially uniform coolant distribution beneath the test coupon. To minimize heat loss from the coolant supply system, the reservoir was fabricated using stereolithography (SLA) with a high-temperature photopolymer resin (Formlabs) because of its low thermal conductivity. In addition, the outer surface of the reservoir was wrapped with vinyl foam insulation to further reduce heat losses, thereby maintaining a nearly uniform coolant temperature.

The coolant temperature (T_c) was monitored using two K-type thermocouples installed beneath the test coupon inside the coolant plenum. The temperature difference between the center and the side wall was consistently below 0.5 °C, confirming a nearly uniform coolant temperature distribution. The coolant was heated to 313 K using an electrical heating hose controlled by a variable transformer. Temperature acquisition and system control were performed using a National Instruments data acquisition system with LabVIEW software. AFE and OFE were measured using PSP and TSP, respectively. The detailed principles of both techniques have been described in the authors' previous studies [41]; a brief overview is provided in the following paragraph.

The binary PSP (ISSI, Innovative Scientific Solutions Incorporated) responds to local oxygen partial pressure through oxygen quenching, from which the adiabatic film effectiveness (AFE) is evaluated. As illustrated in Fig. 10(a), the binary PSP consists of an oxygen-sensitive luminophore and an oxygen-insensitive reference luminophore embedded in an oxygen-permeable polymer binder. The ratio of their emission intensities compensates for temperature variations and non-uniform illumination. The paint was excited using a 400 nm ultraviolet LED array (ISSI LM2X DM400), and the luminescent emissions were simultaneously recorded using a CCD camera (LaVision ImagePro X2M) equipped with an image doubler and band-pass filters centered at 650 nm (20 nm FWHM) and 550 nm (10 nm FWHM).

As illustrated in Fig. 10(b), the UniCoat TSP (ISSI) determines the surface temperature through thermal quenching. Unlike PSP, its oxygen-impermeable polymer binder eliminates oxygen quenching, making the luminescent intensity solely temperature dependent. The paint was excited using a 455 nm royal-blue LED array (Thorlabs M455L4), and the emitted fluorescence was recorded through a band-pass filter centered at 630 nm (60 nm FWHM). The resulting surface temperature distribution was used to determine the OFE.

2.4. PSP and TSP methodology

The adiabatic film effectiveness (η_{ad}) is defined as

$$\eta_{ad} = \frac{T_{aw} - T_\infty}{T_c - T_\infty} \tag{4}$$

where T_∞, T_{aw}, and T_c denote the mainstream, adiabatic wall, and coolant temperatures, respectively. For turbulent flows with a turbulent Lewis number close to unity ($Le_t \approx 1$), the heat–mass transfer analogy is

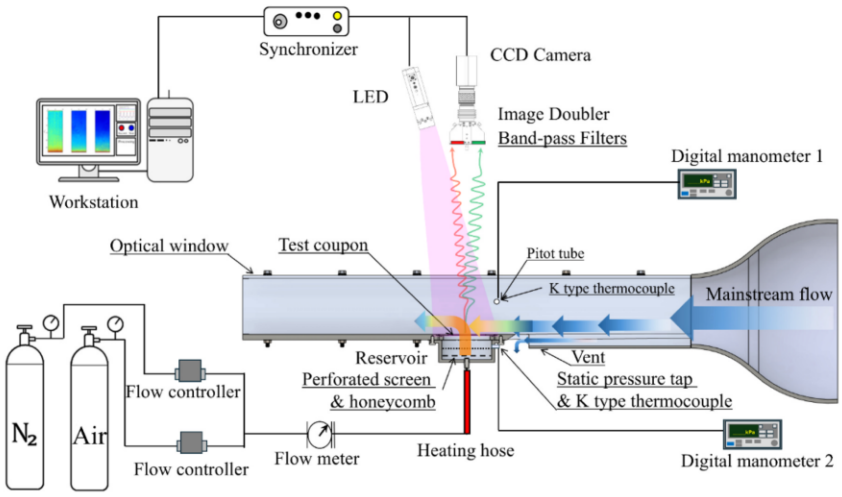

Fig. 9. Schematic of the experimental setup.

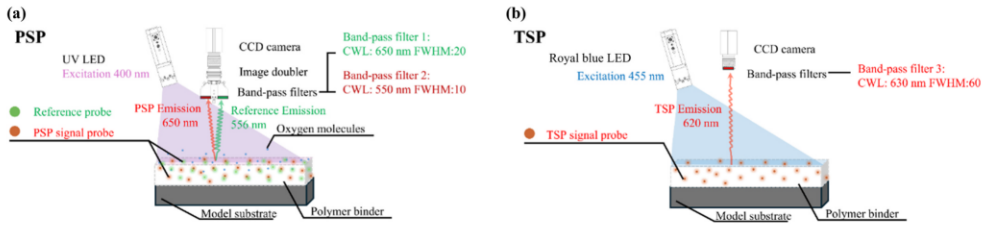

Fig. 10. Schematic illustrations of the measurement principles of (a) binary PSP and (b) TSP.

applicable [42,43], allowing the temperature-based definition to be reformulated in terms of oxygen concentration as

$$\eta_{ad} = \frac{T_{aw} - T_\infty}{T_c - T_\infty} \approx \frac{C_{aw} - C_\infty}{C_c - C_\infty} = \frac{C_{O2,fg} - C_{O2,\infty}}{C_{O2,c} - C_{O2,\infty}} = 1 - \frac{C_{O2,fg}}{C_{O2,\infty}} \tag{5}$$

where $C_{O_2,\infty}$ and $C_{O_2,fg}$ are the oxygen concentrations in the mainstream air and the coolant–mainstream mixture adjacent to the test surface, respectively. Since nitrogen was employed as the coolant, the oxygen concentration in the coolant is zero, resulting in the simplified expression. The PSP intensity ratio was converted to adiabatic film effectiveness using the Stern–Volmer calibration [44].

$$\eta_{ad} \approx 1 - \frac{C_{O2,fg}}{C_{O2,\infty}} = 1 - \frac{1}{1 + \frac{MM_{fg}}{MM_\infty}\left[\left(\frac{X_{O_2,\infty}}{X_{O_2,fg}}\right) - 1\right]} = 1 - \frac{1}{1 + \frac{MM_{fg}}{MM_\infty}\left[\frac{p}{p_{ref}} - 1\right]} \tag{6}$$

where X_{O_2} denotes the oxygen mole fraction and MM represents the molecular weight of the corresponding gas mixture. The oxygen partial pressure was determined from the binary PSP intensity ratio

$$\frac{p}{p_{ref}} = A + B\left(\frac{r_{ref}}{r}\right) + C\left(\frac{r_{ref}}{r}\right)^2, \quad where \ \frac{r_{ref}}{r} = \frac{\left(\frac{I_{ref} - I_{dark}}{I - I_{dark}}\right)_{PT}}{\left(\frac{I_{ref} - I_{dark}}{I - I_{dark}}\right)_{T}} \tag{7}$$

Here, r and r_{ref} denote the normalized intensity ratios of the oxygen-sensitive and temperature-reference luminophores, respectively. Since both probes exhibit temperature sensitivity while only the signal probe is sensitive to oxygen partial pressure, the ratio r_{ref}/r provides temperature compensation, thereby eliminate the influence of temperature on the pressure measurement. Here, I is the measured luminescent intensity, I_{ref} is the reference intensity acquired under no-flow conditions, and I_{dark} is the background intensity recorded with the excitation source switched off. The coefficients A, B, and C are temperature-independent polynomial calibration coefficients.

A detailed uncertainty analysis is reported in Ref. [36], where the uncertainty of the measured adiabatic film effectiveness was estimated to be ±1.3% at $\eta_{ad} = 0.8$ and ±5.5% at $\eta_{ad} = 0.2$.

In the present study, the OFE was determined using temperature-sensitive paint (TSP). To perform TSP measurements, the coolant was heated to approximately 313 K, while the mainstream flow remained at ambient temperature at approximately 293 K. The resulting temperature difference produced a non-uniform surface temperature field governed by the combined effects of coolant film formation, wall conduction, and internal convective heat transfer. The overall film effectiveness (ϕ) is defined as

$$\phi = \frac{T_w - T_\infty}{T_c - T_\infty} \tag{8}$$

where T_w, T_∞, and T_c denote the wall, mainstream, and coolant temperatures, respectively.

The TSP coating was applied directly to the test surface, and the normalized luminescent intensity was calibrated against known surface temperatures. Accordingly, the normalized intensity can be expressed as a function of the surface temperature as

$$f(T) = \frac{I - I_{dark}}{I_{ref} - I_{dark}} \tag{9}$$

where I_{ref} and I denote the reference and measured luminescent intensities, corresponding to the known reference temperature and the unknown surface temperature, respectively. The TSP was calibrated by establishing the relationship between the normalized luminescent intensity and the surface temperature under controlled heating conditions. A polyimide flexible heater installed beneath the test coupon was used to vary the surface temperature through a variable transformer. The surface temperature was determined from the average of eight K-type thermocouples distributed around the observation area. The resulting calibration data were accurately represented by a first-order polynomial:

$$\frac{I - I_{dark}}{I_{ref} - I_{dark}} = DT + E \tag{10}$$

where D and E are calibration coefficients, and T is the local surface temperature.

The uncertainty analysis for the TSP paint measurements yielded representative relative uncertainties of ±0.5% and ±5.6% at overall film cooling effectiveness values of $\phi = 0.75$ and $\phi = 0.10$, respectively.

2.5. Testing conditions

The operating conditions were selected to facilitate a direct comparison between the TPMS-based transpiration cooling and corresponding effusion cooling scenarios. For the effusion cooling cases, the blowing ratio (BR), a widely used non-dimensional parameter in effusion cooling studies, was varied between 0.6 and 1.4, corresponding to typical gas turbine operating conditions. The blowing ratio is defined as

$$BR = \frac{\rho_c u_c}{\rho_m u_m} \tag{11}$$

where ρ and u denote the density and velocity of the coolant (c) and mainstream (m), respectively. The coolant exit velocity was calculated from

$$u_c = \frac{\dot{Q}_c}{A_{active} * \varepsilon_{surface}} \tag{12}$$

where $\dot{Q}_c$ is the coolant volumetric flow rate, A_{active} is the total surface area including voids, and $\varepsilon_{surface}$ is the surface porosity.

Transpiration cooling features a surface with almost evenly distributed voids with a surface porosity typically one to two orders of magnitude higher than that of conventional effusion cooling. Consequently, the blowing ratio is not an appropriate basis for comparison,

and the injection ratio (F) is instead adopted:

$$F = \frac{\rho_c u_c}{\rho_m u_m}\frac{A_{Cool}}{A_{active}} = BR * \varepsilon_{surface} = \frac{\dot{m}_c}{\rho_m u_m A_{active}} \quad (13)$$

where $\dot{m}_c$ is the coolant mass flow rate. To ensure a fair comparison, both effusion and TPMS-based transpiration cooling configurations were tested at coolant flow rates equivalent to baseline effusion cooling blowing ratios of 0.6, 1.0, and 1.4, corresponding to injection ratios of $F = 0.68$%, 1.14%, and 1.60%, respectively. The active cooling area and mainstream velocity were maintained identical to those in the previous comparative study [10]. The operating conditions and blowing ratios for each test coupon are summarized in Table 2 to facilitate comparison.

In addition to the operating condition, the pressure drop across the cooling structure is an important hydraulic parameter because it represents the coolant pumping requirement. The percentage pressure drop (ΔP) is defined as

$$\Delta P = \frac{P_{reservoir} - P_{testsection}}{P_{reservoir}} * 100 \quad (14)$$

where $P_{reservoir}$ is the static pressure measured in the coolant reservoir beneath the test coupon after the flow straighteners, and $P_{testsection}$ is the mainstream static pressure measured at the leading edge of the test section. The locations where each pressure was measured in the experimental setup are indicated in Fig. 9. The measured pressure drops are summarized in Fig. 11. As expected, the pressure drop increases with increasing coolant flow rate for both cooling configurations. However, the TPMS-based transpiration cooling exhibits a substantially lower pressure drop than the effusion cooling over the entire operating range. This behavior is primarily attributed to the significantly higher surface porosity of the TPMS structure (approximately 40% actual porosity) compared with the effusion cooling configuration (approximately 1%), which provides a much lower hydraulic flow resistance through the cooling structure at any given flow rate. It is worth noting that such a low pressure drop is not representative of practical transpiration-cooling systems. Nevertheless, the present TPMS test coupon represents a first attempt to fabricate a TPMS-based transpiration-cooling structure using metal additive manufacturing. Although its relatively high porosity led to a lower pressure drop than desired, this configuration serves as a practical baseline for the experimental assessment of cooling performance. Our past investigations [25,26] have clearly indicated that the pressure drop across TPMS-based transpiration cooling coupon can be engineered to better match the levels of effusion cooling by adjusting a combination of parameters, including TPMS type, porosity, and unit cell size. In addition, additional engineering designs, such as perforated plates can be used in conjunction with the TPMS-based transpiration cooling coupons to exactly match the pressure drops of conventional effusion cooling designs.

The Reynolds numbers for the effusion cooling (Re_{eff}) and TPMS-based transpiration cooling (Re_{TPMS}) were evaluated as [45]

$$Re_{eff} = (\rho_c u_c d)/\mu_c \quad (15\text{-}1)$$

$$Re_{TPMS} = (\rho_c u_c d_h)/\mu_c \quad (15\text{-}2)$$

Table 2
Operating conditions and corresponding blowing and injection ratios for the effusion and TPMS-based transpiration cooling configurations.

Main flow velocity [m/s]	33		
Effusion cooling			
Blowing ratio	0.6	1.0	1.4
Injection ratio	0.68%	1.14%	1.60%
Transpiration cooling			
Blowing ratio	0.017	0.029	0.041
Injection ratio	0.68%	1.14%	1.60%

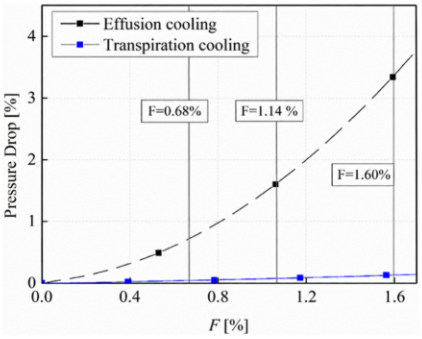

Fig. 11. Comparison of the percentage pressure drop across the effusion cooling and TPMS-based transpiration cooling test coupons as a function of the injection ratio (F).

where ρ_c, u_c, and μ_c denote the coolant density, characteristic coolant velocity, and coolant dynamic viscosity, respectively, and d is the effusion-hole diameter. For the TPMS-based transpiration cooling configuration, the characteristic length was taken as the hydraulic diameter, d_h, defined as $d_h = 4\,V/A_w$, where V and A_w are the volume of the lattice structure and wetted surface area of the TPMS lattice, respectively.

The Re_{eff} were 1067, 1778, and 2490 for F = 0.68%, 1.14%, and 1.60%, respectively. The corresponding Re_{TPMS} values were 75, 126, and 176, respectively. Previous studies have shown that transition to turbulence in TPMS lattices occurs at a critical Reynolds number of approximately $Re_{TPMS} \approx 300$ [46]. Since all Re_{TPMS} values in the present study are well below this threshold, the flow within the TPMS lattice is expected to remain laminar.

TPMS structures exhibit a periodic tortuous geometry that may influence both film cooling performance and internal heat transfer. A nondimensional parameter, surface tortuosity (τ), was defined to characterize the waviness of a surface void within a TPMS unit cell [47]. The surface tortuosity can be calculated using the following expression:

$$\tau = l/L_c \quad (16)$$

where l represents the arc length of a surface void of a single unit cell. The authors' previous study [27] showed that the Koch-type TPMS structure exhibits greater surface tortuosity and a larger internal wetted area than the Diamond and Gyroid structures. Greater surface tortuosity suppresses mainstream channeling along the recessed surface passages and facilitates coolant transport toward the top surface, thereby promoting coolant-film formation. In addition to these effects on external film formation, the large internal wetted area and geometric curvature of the interconnected passages may contribute to enhanced internal convection and conjugate heat transfer.

To further consider these internal heat transfer effects, the flow characteristics within the TPMS passages must also be examined beyond a representative Reynolds number. Even within a single unit cell, the flow velocity varies spatially, and its distribution is influenced by the local cross-sectional area of the pore throats and the channel geometry. Local acceleration and deceleration, curvature-induced changes in flow direction, and secondary flows can therefore influence fluid mixing within the TPMS cells. The present study focused on evaluating adiabatic film cooling effectiveness through surface mass-transfer measurements and overall film cooling effectiveness through surface temperature measurements. Although the pore-scale internal velocity field and local heat transfer characteristics were not directly investigated, relevant numerical studies provide further insight into the

influence of TPMS geometry on internal convection.

In particular, Wang et al. [48] numerically compared the internal flow and heat transfer characteristics of Koch, I-WP, Primitive, and Neovius structures. Under the investigated conditions, the maximum velocity in the Primitive structure was approximately 2.5 times the minimum velocity, whereas the Koch structure exhibited smaller velocity variations and a relatively uniform velocity distribution. The tortuous passages of the Koch structure were also reported to induce continuous changes in flow direction and stronger flow disturbances, thereby enhancing fluid mixing and convective heat transfer. These findings provide additional support for the potential of the Koch geometry to enhance internal heat transfer. Taken together, its favorable film cooling performance reported in previous studies, greater surface tortuosity, larger internal wetted area, and potential for enhanced internal convection motivated the selection of the Koch-type TPMS structure for comparison with effusion cooling in the present study.

3. Results and discussions

3.1. 2D distribution of AFE and OFE

Fig. 12 presents the two-dimensional distributions of adiabatic film

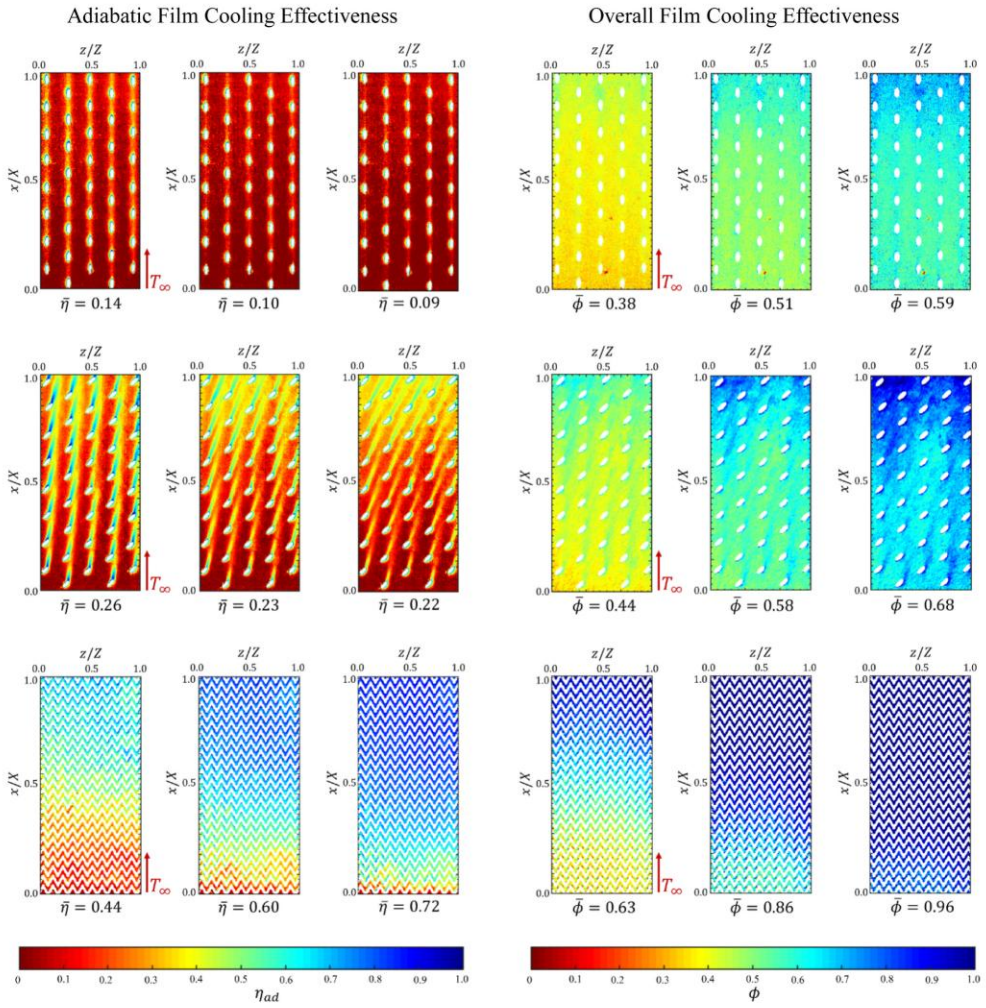

Fig. 12. Two-dimensional distributions of adiabatic film effectiveness (AFE, left) and overall film effectiveness (OFE, right) for the three cooling configurations at injection ratios of F = 0.68%, 1.14%, and 1.60%. The rows correspond to (top) baseline effusion cooling, (middle) 45° compound-angle effusion cooling, and (bottom) TPMS-based transpiration cooling.

effectiveness (AFE) and the corresponding overall film effectiveness (OFE) for all three cooling configurations investigated.

In all color maps, blue represents high cooling effectiveness. The streamwise (x/X) and spanwise (z/Z) coordinates are normalized by the dimensions of the observation area. The left and right columns show the AFE and OFE distributions, respectively. The first, second, and third rows correspond to baseline effusion cooling with a zero compound angle, effusion cooling with a 45° compound-angle, and TPMS-based transpiration cooling. The white regions represent surface voids, i.e., the effusion cooling holes and surface grooves of TPMS lattices, which were excluded from the analysis during post-processing. The area-averaged cooling effectiveness is reported under each 2D color map.

Compared with the baseline effusion cooling case, the introduction of a 45° compound angle substantially enhances the AFE at all three injection ratios, as shown in Fig. 12. In the baseline configuration, the coolant jets remain primarily aligned with the mainstream direction, limiting their ability to penetrate the inter-column gaps between adjacent hole rows. Consequently, these regions are cooled mainly through turbulent mixing between the coolant and the mainstream, causing rapid coolant dilution and deterioration of the cooling film.

By contrast, the 45° compound angle redirects part of the coolant momentum toward the spanwise direction, enabling deeper penetration into the inter-column gaps and improving lateral film coverage [35]. The interpretations of lateral coolant spreading is inferred from the measured effectiveness distributions and previous literature [35].

A distinct feature of the OFE distributions in Fig. 12 is the substantially smaller spatial temperature gradient than that observed in the corresponding AFE distributions. In particular, the inter-column regions that exhibit relatively low AFE are largely thermally compensated in the OFE contours. This behavior is consistent with the coupled effects of solid conduction and internal convection within CHT. Heat conduction within the metallic test coupon can redistribute heat between the regions beneath the coolant jets and the adjacent inter-column regions, moderating spatial variations associated with non-uniform film coverage. In addition, internal convection within the cooling holes exchanges heat between the solid and the coolant. Together, these processes may help explain the smoother OFE distributions, although their individual contributions are not independently quantified. Consequently, the OFE distributions become considerably more uniform than the corresponding AFE distributions for both effusion cooling configurations.

Although the compound-angle configuration produces a pronounced enhancement in AFE, the corresponding improvement in OFE is comparatively modest. Relative to the baseline configuration, the area-averaged AFE increases from 0.14 to 0.26, from 0.10 to 0.23, and from 0.09 to 0.22 at injection ratios of 0.68%, 1.14%, and 1.60%, respectively, whereas the corresponding OFE increases from 0.38 to 0.44, from 0.51 to 0.58, and from 0.59 to 0.68, respectively. The smaller improvement in OFE compared with AFE arises because areas inadequately protected by cooling film coverage are still cooled by heat conduction within the metal liner, which is reflected in the OFE measurements. Furthermore, introducing a compound angle preserves the number of cooling holes and the internal wetted area. At equal coolant flow rate, internal convective heat transfer is therefore expected to remain identical, which may help explain why the improvement in OFE is less pronounced than that in AFE. These results indicate that the principal benefit of the compound angle lies in enhancing coolant film formation and lateral coverage, while it does not alter the underlying CHT (conjugate heat transfer).

Comparing with both effusion cooling configurations, TPMS-based transpiration cooling exhibits substantially higher AFE over the entire observation area, as shown in Fig. 12. Even with the introduction of a 45° compound angle, effusion cooling provides effective protection only in the vicinity of the cooling holes because the coolant is discharged through a limited number of discrete holes. In contrast, the coolant discharges are more distributed over the surface in the case of TPMS-based transpiration cooling, establishing a more continuous and spatially uniform coolant film. This distributed coolant injection significantly improves cooling film coverage, thereby reducing the formation of localized gaps in cooling film coverage that are commonly observed in effusion cooling.

Another notable feature is the opposite trend of AFE to increasing injection ratio. For both effusion cooling configurations, the area-averaged AFE decreases as the injection ratio increases because the higher coolant momentum promotes jet lift-off, reducing coolant attachment to the wall [49]. In contrast, the AFE of the TPMS-based transpiration cooling continuously increases with increasing injection ratio. This behavior is attributed to the significantly lower coolant discharge velocity through the porous surface, which may suppress lift-off. For example, at $F = 0.68\%$, the mean coolant exit velocity from the TPMS surface is approximately 0.47 m/s, whereas the corresponding effusion jet velocity is approximately 21 m/s. Consequently, the coolant remains attached to the wall even at the highest injection ratio investigated, resulting in progressively improved film coverage with increasing coolant flow rate.

The superiority of TPMS-based transpiration cooling is also evident in the OFE distributions shown in Fig. 12. In addition to forming a more uniform coolant film, the highly interconnected porous network provides a substantially larger wetted surface area than conventional effusion cooling, thereby enhancing CHT, which involves both internal convective heat transfer within the TPMS lattice and solid heat conduction through the wall. As a result, TPMS-based transpiration cooling achieves considerably higher OFE than both effusion cooling configurations, despite all test coupons being fabricated from the same material. It is noteworthy that, at the lowest injection ratio ($F = 0.68\%$), the leading-edge region exhibits relatively low OFE despite the large internal heat transfer area of the TPMS structure. This behavior is attributed to insufficient coolant supply during the initial stage of coolant injection and may also be associated with local hot-gas ingestion into the highly porous structure under low injection ratio conditions [17,29].

Hinse et al. [17] investigated transpiration cooling using porous metal foams and reported that viscous effects of the mainstream induced tangential coolant motion within the porous matrix, resulting in nonuniform coolant discharge and a nonuniform distribution of adiabatic film cooling effectiveness. Furthermore, pore-scale simulations of TPMS-based transpiration cooling by Zhou et al. [29] showed local mainstream penetration into the porous matrix. The authors' previous comparison of three TPMS topologies [36] also showed that the Gyroid configuration, which had a lower pressure drop than the Koch configuration, exhibited lower adiabatic film cooling effectiveness and delayed coolant-film formation. These differences in film cooling performance were particularly pronounced at low coolant consumption. In that study, adverse mainstream–coolant interactions were proposed as a possible explanation for this behavior, rather than directly demonstrated. This effect becomes less pronounced with increasing injection ratio, and an area-averaged OFE of 0.96 is achieved at the highest operating condition.

3.2. Spanwise-averaged AFE and OFE

Fig. 13 compares the spanwise-averaged AFE and OFE for all three cooling configurations at injection ratios of $F = 0.68\%$, 1.14%, and 1.60%. The black and gray curves denote the spanwise-averaged AFE and OFE, respectively, while the shaded region between them represents the additional thermal protection provided by CHT, or the difference between OFE and AFE. Unlike AFE, which reflects only the effectiveness of the coolant film alone, OFE corresponds to both film cooling and CHT within the test coupons. Consequently, OFE exceeds AFE over the entire streamwise extent for all cases. It is also evident that the difference between OFE and AFE is greatest near the leading edge and gradually decreases downstream. Near the leading edge, the coolant film has not yet been established, resulting in zero AFE and a greater contribution of

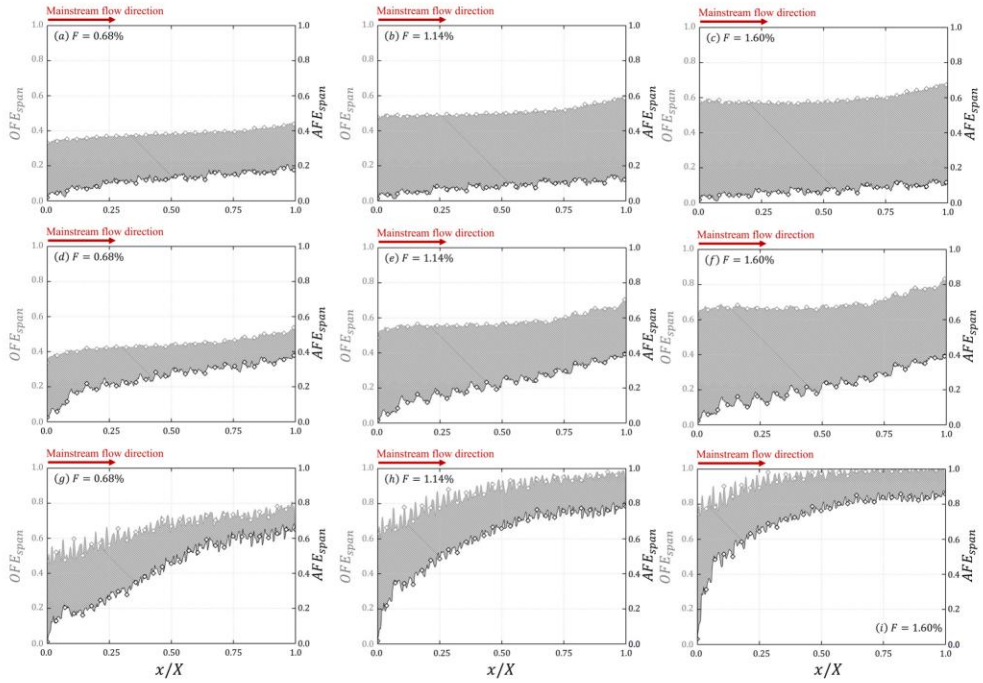

Fig. 13. Spanwise-averaged distributions of adiabatic film effectiveness (AFE) and overall film effectiveness (OFE) for all three cooling configurations at injection ratios of F= 0.68%, 1.14%, and 1.60%. (a)–(c): baseline effusion cooling of zero compound angle, (d)–(f):effusion cooling with 45° compound-angle, and (g)–(i): TPMS-based transpiration cooling. The black curves represent the spanwise-averaged AFE (right axis), whereas the gray curves represent the spanwise-averaged OFE (left axis).

CHT to the overall cooling performance. As the coolant film develops downstream, the external heat load is increasingly reduced by film cooling, thereby diminishing the relative contribution of CHT.

The spanwise-averaged distributions for the baseline effusion cooling configuration (zero compound angle), shown in Fig. 13(a–c), exhibit the largest differences between OFE and AFE among the three cooling configurations. As discussed in the previous section, the coolant jets remain aligned with the mainstream flow and provide limited lateral spreading, leaving the inter-column regions insufficiently protected. Consequently, in the inter-column regions, where an adequate coolant film is absent, the AFE remains close to zero, while CHT provides a substantial contribution to the overall thermal protection. Furthermore, increasing the injection ratio progressively reduces AFE because the higher jet momentum promotes jet lift-off and weakens coolant attachment to the wall. In contrast, CHT becomes more effective as the coolant flow rate increases, resulting in a progressively larger difference between OFE and AFE, with the maximum difference observed at F = 1.60%. These results highlight the role of CHT in the overall cooling performance of the baseline effusion cooling configuration.

The spanwise-averaged distributions of both AFE and OFE for the 45° compound-angle effusion cooling configuration are presented in Fig. 13 (d–f). Compared with the baseline configuration, the 45-degree compound angle substantially enhances AFE at all injection ratios owing to improved lateral film coverage and reduced jet lift-off, as discussed in the previous section. Consequently, the shaded area between OFE and AFE, representing the contribution of CHT, is noticeably smaller than that of the baseline configuration, particularly at the lowest injection ratio (F=0.68%). This behavior indicates that the improved coolant film greatly reduces heat flux that reaches the metal liner, thereby increasing the relative contribution of film cooling to the overall thermal protection. As a result, OFE is consistently higher than that of the baseline configuration despite both test coupons having identical materials and hole spacing. At the trailing edge ($x/X = 1$), the discrepancy between OFE and AFE decreases from approximately 0.22 for the baseline configuration to 0.17 for the 45-degree compound-angle case at F= 0.68%, further demonstrating the greater contribution of film cooling. However, as the injection ratio increases, AFE gradually decreases because of the onset of jet lift-off, whereas the contribution of CHT increases with coolant flow rate leading to enhanced internal convection. Consequently, the discrepancy between OFE and AFE becomes progressively larger at higher injection ratios, indicating that CHT again becomes increasingly important to the overall cooling performance.

The TPMS-based transpiration cooling configuration, shown in Fig. 13(g–i), exhibits substantially higher spanwise-averaged AFE and OFE than both effusion cooling configurations at all injection ratios. Unlike effusion cooling, AFE increases continuously with increasing injection ratio. This behavior is consistent with the low coolant discharge velocity limiting jet lift-off and allowing the coolant film to develop progressively over the porous surface. At the leading edge (x/X = 0), the TPMS configuration also exhibits considerably higher OFE (approximately 0.52) than both effusion cooling configurations (approximately 0.35) at an injection ratio of 0.68%. This observation is

consistent with a wall-temperature response involving internal convection and solid conduction before a fully developed coolant film is established. As the coolant film develops downstream, AFE increases and approaches OFE.

3.3. Temperature-based assessment of film cooling and conjugate heat transfer

The area-averaged AFE and OFE were compared to provide a temperature-based assessment of external film protection and the overall thermal response under conjugate heat transfer conditions. AFE characterizes the equivalent adiabatic-wall reference associated with the external coolant film, whereas OFE characterizes the normalized wall-temperature response resulting from the coupled effects of external film cooling, solid conduction, and internal convection.

Using the definitions of AFE and OFE given in Section 2.4 (Eqs. (4) and (8)), their difference can be expressed as

$$\phi - \eta_{ad} = \frac{T_w - T_{aw}}{T_c - T_\infty} \tag{17}$$

For common reference temperatures T_c and T_∞, Eq. (17) follows directly from the effectiveness definitions and represents the normalized wall-temperature departure from an adiabatic-wall reference.

For baseline effusion cooling with a zero-compound angle, the area-averaged difference between AFE and OFE increases from 0.24 to 0.41 and 0.50 at $F = 0.68\%$, 1.14%, and 1.60% (or corresponding BR = 0.6, 1.0 and 1.4), respectively. This increasing separation results from decreasing AFE and increasing OFE, showing that weaker adiabatic film protection does not necessarily imply lower overall effectiveness.

With a 45° compound angle, the corresponding differences are 0.18, 0.35, and 0.46. Compared with the baseline configuration, the smaller differences accompany improved AFE and OFE, consistent with the improved lateral film coverage discussed previously.

For TPMS-based transpiration cooling, the differences in AFE and OFE are 0.19, 0.26, and 0.24 at F = 0.68%, 1.14%, and 1.60%, respectively. The difference initially increases and then decreases slightly at the highest injection ratio, despite the continued increase in coolant flow rate. This behavior may be explained by very effective film protection at F = 1.60%, bringing the equivalent adiabatic-wall temperature closer to the coolant reference temperature. The resulting reduction in the temperature difference driving solid–coolant heat exchange may limit the additional wall-temperature change associated with CHT.

To compare the effectiveness differences relative to the corresponding OFE, the normalized effectiveness difference is defined as follows:

$$R_\Delta = \frac{\bar{\phi} - \bar{\eta}_{ad}}{\bar{\phi}} = 1 - \frac{\bar{\eta}_{ad}}{\bar{\phi}} \tag{18}$$

This ratio expresses the difference as a fraction of the measured OFE. Fig. 14 presents the area-averaged AFE and OFE−AFE difference, whose sum equals the area-averaged OFE. The error bars indicate the propagated uncertainties. Percentages express these quantities as fractions of the area-averaged OFE, corresponding to R_Δ for the dark-colored regions and $1 - R_\Delta$ for the light-colored regions.

For baseline effusion cooling (Fig. 14(a)), R_Δ increases from 63% to 80% and 85% as F increases from 0.68% to 1.14% and 1.60%, respectively. Thus, the increasing effectiveness difference discussed above also becomes larger relative to OFE, consistent with the deterioration in adiabatic film protection at higher injection ratios.

For the 45° compound-angle configuration (Fig. 14(b)), the corresponding ratios are 40%, 60%, and 67%. These lower ratios indicate that

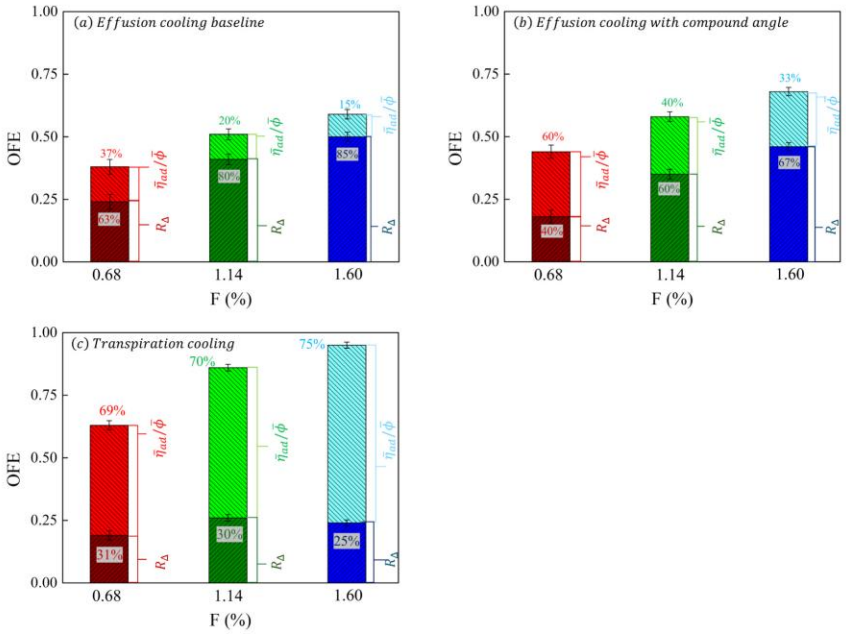

Fig. 14. Percentages in the dark- and light-colored regions indicate R_Δ and $1 - R_\Delta$, respectively, for (a) baseline effusion cooling, (b) 45° compound-angle effusion cooling, and (c) TPMS-based transpiration cooling at $F = 0.68\%$, 1.14%, and 1.60%. The total bar height represents the area-averaged OFE.

AFE remains closer to OFE on a normalized basis, consistent with the improved lateral film coverage discussed previously.

A markedly different trend is observed for TPMS-based transpiration cooling (Fig. 14(c)). Compared with the discrete jets of effusion cooling, coolant discharge through the spatially distributed pores promotes more extensive film coverage. Consistent with this behavior, the TPMS configuration achieves the highest AFE and OFE, while the normalized effectiveness difference, R_Δ, decreases from 31% to 30% and 25% at F = 0.68%, 1.14%, and 1.60%, respectively. From F = 0.68–1.14%, the absolute effectiveness difference, OFE−AFE, increases. However, AFE increases proportionally more than the absolute effectiveness difference, resulting in a slight decrease in R_Δ. At F = 1.60%, the area-averaged AFE reaches approximately 0.72, with local values exceeding 0.85 over the downstream region, indicating that the equivalent adiabatic-wall temperature approaches the coolant reference temperature. The high OFE likewise indicates that the actual wall temperature approaches this reference. Under these conditions, the wall–coolant temperature difference may become smaller, limiting the additional wall-temperature change associated with CHT.

These findings indicate that the investigated TPMS configuration combines effective external film protection with high overall effectiveness. Its distributed coolant discharge improves film coverage compared with the effusion configurations, while its extensive internal wetted area may facilitate solid–coolant heat exchange. These characteristics suggest potential for reducing wall temperatures and thermal loading in gas turbine hot-section components, with possible benefits for component durability and maintenance intervals. However, such benefits require further validation under engine-relevant operating conditions.

3.4. Implications of Biot Number on Cooling Performance

In addition to matching the coolant flow conditions, matching the Biot number to realistic engine conditions is also important to ensure representative conjugate heat transfer. The Biot number (Bi) is defined as

$$Bi = \frac{ht}{k} \tag{19}$$

where h is the external convective heat transfer coefficient, $t$is the wall thickness, and $k$is the thermal conductivity of the test coupon material.

The present experiments were conducted using Inconel 718 test coupons under atmospheric conditions. The average external heat transfer coefficient was estimated using the empirical correlation reported in Ref. [50], resulting in a Biot number of approximately 0.04. However, this correlation was developed for effusion cooling, and the estimated external heat transfer coefficient has not been independently validated for TPMS-based transpiration cooling. In practical gas turbine combustors, however, the operating pressure is substantially higher, exceeding 40 bar in modern high-pressure-ratio engines [51]. The resulting increase in the external convective heat transfer coefficient leads to considerably larger Biot numbers than those achieved in the present experiments. Albert et al. [52] emphasized that preserving the appropriate dimensionless parameters is essential for obtaining experimentally relevant heat transfer characteristics. Representative engine-scale studies have reported Biot numbers of approximately 0.36 [53] and 1.0–2.1 under realistic combustor operating conditions [54]. A comparison between the present and engine-representative Biot numbers is summarized in Table 3.

The cooling effectiveness obtained from the present study should therefore be interpreted as two limiting cases. The AFE represents the upper limit corresponding to an adiabatic wall (Bi → ∞), where heat conduction through the wall is neglected and only the external coolant film contributes to thermal protection. In contrast, the measured OFE corresponds to a low-Biot-number condition in which CHT provides a relatively large contribution to the overall cooling performance. Since practical gas turbine engines operate at intermediate Biot numbers, the actual overall film effectiveness is expected to lie between these two limiting cases.

Table 3
Comparison of Biot numbers for the present experiments and representative gas turbine engine conditions.

	AFE	OFE	Actual engine
$k\left[\frac{W}{mK}\right]$	Not applicable	11.3	~ 13 [54]
Bi	∞ (adiabatic)	0.04	0.36 [53]; 1.0–2.1 [54]

The influence of CHT on the overall thermal response in effusion cooling depends on the Biot number. In particular, CHT appears to have a substantial influence on effusion cooling under the engine-relevant Biot-number conditions. However, the relative importance of film cooling and CHT may change considerably with the Biot number. The present study establishes limiting cases for practical gas turbine operation. Similarly, for TPMS-based transpiration cooling, the relative importance of film cooling and CHT to the overall cooling performance varies with substantially different Biot numbers, from very-low-Biot-number limit (Bi → 0) considered in this study to an adiabatic-wall condition. The present study compares the AFE and OFE of TPMS-based transpiration cooling with those of conventional effusion cooling at extreme Biot numbers and evaluates the corresponding temperature-based ratios. Further validation is required at Biot numbers that are relevant for specific engine conditions.

To more closely reproduce engine-representative Biot numbers under atmospheric conditions, the coupon thermal conductivity would need to be reduced. This will be the focus of future work to further assess the cooling performance under engine-relevant Biot number conditions.

4. Conclusions

An experimental investigation was conducted to evaluate the cooling performance of TPMS-based transpiration cooling in comparison with effusion cooling configurations, including a baseline configuration and a 45° compound-angle configuration. Pressure-sensitive paint (PSP) and temperature-sensitive paint (TSP) were employed to separately measure the adiabatic film effectiveness (AFE) and overall film effectiveness (OFE), enabling the respective contributions of external film cooling and conjugate heat transfer (CHT) to be quantified. By jointly comparing AFE and OFE across these configurations, the present study extends the authors' previous investigations that evaluated geometric effects solely in terms of adiabatic film effectiveness and provides a temperature-based assessment of the relative roles of external film cooling and conjugate heat transfer (CHT). The major findings are summarized as follows.

1. The 45° compound-angle significantly improves the effusion cooling performance. The compound angle enhanced lateral coolant spreading by directing the coolant into the inter-column regions while simultaneously suppressing jet lift-off, resulting in improved film coverage and higher AFE and OFE. Nevertheless, at moderate and high injection ratios, the temperature-based assessment suggested a greater relative role of CHT than external film cooling.
2. The TPMS-based transpiration cooling configuration consistently outperformed both effusion cooling configurations in terms of both AFE and OFE over the entire range of injection ratios investigated. Unlike conventional effusion cooling, the TPMS lattice produced a uniformly distributed coolant film that became increasingly effective with increasing injection ratio because of the low coolant discharge velocity and the absence of jet lift-off.
3. Area-averaged AFE and OFE provided a temperature-based assessment of the relative roles of external film cooling and CHT. The fraction (OFE − AFE)/OFE, used as an indicator of the temperature

response associated with CHT, ranged from 63% to 85% for the baseline effusion configuration and 40–67% for the 45° compound-angle configuration; however, CHT still contributed 60–67% of the overall cooling performance except at the lowest injection ratio. For the TPMS-based transpiration cooling configuration, AFE/OFE ranged from 69% to 75%, suggesting a greater relative role of external film cooling under the tested conditions.

4. The Biot number in the present study is relatively low compared with those under engine-relavent conditions. Changes in Biot number may alter the relative roles of film cooling and CHT. Future work will assess coolant distribution and cooling effectiveness under matched pressure-loss conditions representative of gas turbine operation and under more representative Biot numbers and thermal conditions.

Overall, under the investigated conditions, TPMS-based transpiration cooling achieved higher AFE and OFE than both effusion configurations, with the temperature-based assessment suggesting a greater relative role of external film cooling. This combination yields substantially improved thermal protection and offers significant potential for reducing wall thermal stress and extending the service life of gas turbine combustor liners.

Nomenclature

A_{active}	Active area [mm^2]
A_w	Internal wetted area [mm^2]
A	Constant term of the polynomial fitting curve for PSP
B	1st order coefficient of the polynomial fitting curve for PSP
C	2nd order coefficient of the polynomial fitting curve for PSP
C_{O2}	Oxygen concentration
c	TPMS level set constant
D	1st order coefficient of the linear fitting curve for TSP
D_p	Pore diameter [mm]
d	Hole diameter [mm]
d_h	The hydraulic diameter of TPMS [mm]
E	Constant term of the linear fitting curve for TSP
F	Injection ratio [%]
I	Intensity of PSP
L_C	Unit cell length [mm]
MM	Molecular weight
P	Pressure [Pa]
R_Δ	Normalized effectiveness difference
r	Intensity ratio for binary PSP
T	Temperature [K]
GREEKS	
α	Unit cell constant for x direction
β	Unit cell constant for y direction
γ	Unit cell constant for z direction
ε	Porosity [%]
η_{ad}	Film cooling effectiveness
δ_x	Streamwise pitch
δ_z	Spanwise pitch
τ	Tortuosity
$\varnothing$	Level-set equation
ϕ	Overall cooling effectiveness
$\bar{\phi}$	Area averaged Overall cooling effectiveness
SUBSCRIPTS	
ad	Adiabatic
c	Coolant
$dark$	Dark condition
m	Mainstream
ref	Reference
ACRONYMS	
$TPMS$	Triple Periodic Minimal Surface
PSP	Pressure Sensitive Paint
SLA	Stereolithography
$SLPM$	Standard Liter Per Minute
AFE	Adiabatic Film Effectiveness
BR	Blowing Ratio
TSP	Temperature Sensitive Paint
OFE	Overall film cooling effectiveness
CHT	Conjugate Heat Transfer

CRediT authorship contribution statement

Juchan Son: Writing – review & editing, Writing – original draft, Visualization, Methodology, Investigation, Data curation, Conceptualization. **Patrick Richer:** Writing – review & editing, Visualization, Methodology, Data curation, Conceptualization. **Bertrand Jodoin:** Writing – review & editing, Visualization, Supervision, Methodology, Investigation, Data curation, Conceptualization. **Sina Kashanj:** Writing – review & editing, Visualization, Methodology, Data curation, Conceptualization. **Mohsen Broumand:** Writing – review & editing, Visualization, Methodology, Data curation, Conceptualization. **Zekai Hong:** Writing – review & editing, Visualization, Supervision, Resources, Methodology, Data curation, Conceptualization.

Declaration of Competing Interest

The authors declare that they have no known competing financial interests or personal relationships that could have appeared to influence the work reported in this paper.

Acknowledgements

The work is supported by the National Research Council of Canada (NRC)'s National Program Office under a Small Teams Initiative (Round 6) and Postdoctoral Fellowship Program grant (PDF2024-TM-AF). NRC Aerospace Research Centre's Low-Emission Aviation Program also sponsored the work under project A1–024514.

References

[1] O.O. Badran, Gas-turbine performance improvements, Appl. Energy 64 (1999) 263–273, https://doi.org/10.1016/S0306-2619(99)00088-4.
[2] P. Caron, T. Khan, Evolution of Ni-based superalloys for single-crystal gas turbine blade applications, Aerosp. Sci. Technol. 3 (1999) 513–523, https://doi.org/10.1016/S1270-9638(99)00108-X.
[3] P. Ligrani, Heat transfer augmentation technologies for internal cooling of turbine components of gas turbine engines, 1-32, Int. J. Rotat. Mach. 2013 (2013) 275653, https://doi.org/10.1155/2013/275653.
[4] J.-C. Han, Recent studies in turbine blade cooling, Int. J. Rotat. Mach. 10 (2004) 443–457, https://doi.org/10.1155/S1023621X04000442.
[5] S. Gupta, A. Chaube, P. Verma, Review on heat transfer augmentation techniques: application in gas turbine blade internal cooling, J. Eng. Sci. Technol. Rev. 5 (2012) 57–62, https://doi.org/10.25103/jestr.051.11.
[6] N. Zuckerman, N. Lior, Jet impingement heat transfer: physics, correlations, and numerical modeling, Adv. Heat. Transf. 39 (2006) 565–631, https://doi.org/10.1016/S0065-2717(06)39006-5.
[7] X. Fan, L. Li, J. Zou, Y. Zhou, Cooling methods for gas turbine blade leading edge: comparative study on impingement cooling, vortex cooling and double vortex cooling, Int. Commun. Heat. Mass. Transf. 100 (2019) 133–145, https://doi.org/10.1016/j.icheatmasstransfer.2018.12.017.
[8] W. Wang, Y. Yan, Y. Zhou, J. Cui, Review of advanced effusive cooling for gas turbine blades, Energies 15 (2022) 8568, https://doi.org/10.3390/en15228568.
[9] R. Krewinkel, A review of gas turbine effusion cooling studies, Int. J. Heat. Mass. Transf. 66 (2013) 706–722, https://doi.org/10.1016/j.ijheatmasstransfer.2013.07.071.
[10] Y. Pyo, J. Son, P. Richer, B. Jodoin, M. Broumand, S. Yun, Z. Hong, Isolating Influences of Varying Pitch from the Effects of Non-Zero Compound Angles on Effusion Cooling, Aeronaut. J. 129 (2025) 1–21, https://doi.org/10.1017/aer.2024.108.
[11] H.H. Cho, D.H. Rhee, Local Heat/Mass Transfer Measurement on the Effusion Plate in Impingement/Effusion Cooling Systems, J. Turbomach. 123 (2001) 601–608, https://doi.org/10.1115/1.1344904.
[12] S. Weinbaum, H.L. Wheeler, Heat Transfer in Sweat-Cooled Porous Metals, J. Appl. Phys. 20 (1949) 113–122, https://doi.org/10.1063/1.1698226.
[13] E.R.G. Eckert, J.N.B. Livingood, Comparison of Effectiveness of Convection-, Transpiration-, and Film-Cooling Methods with Air as Coolant, NACA Technical Note 3010, National Advisory Committee for Aeronautics, Washington, DC, 1953.
[14] D. Curry, A. Gomez, C. Johnston, Radiative, Ablative, and Active Cooling Thermal Protection Studies for the Leading Edge of a Fixed-Straight Wing Space Shuttle. Proceedings of the 6th AIAA Thermophysics Conference, AIAA Paper 71-445, 1971, https://doi.org/10.2514/6.1971-445.
[15] Y.Q. Liu, P.X. Jiang, Y.B. Xiong, Y.P. Wang, Experimental and Numerical Investigation of Transpiration Cooling for Sintered Porous Flat Plates, Appl. Therm. Eng. 50 (2013) 997–1007, https://doi.org/10.1016/j.applthermaleng.2012.08.028.

[16] J. Ma, X. Luo, H. Li, Y. Liu, An Experimental Investigation on Transpiration Cooling Based on the Multilaminated Sintered Woven Wire Mesh Structures, J. Therm. Sci. Eng. Appl. 8 (2016) 041004, https://doi.org/10.1115/1.4032921.
[17] M. Hinse, K. Yildiz, P. Richer, B. Jodoin, M. Broumand, S. Yun, Z. Hong, Numerical and Experimental Studies of Transpiration Cooling Film Effectiveness over Porous Materials, J. Thermophys. Heat. Transf. 36 (2022) 803–817, https://doi.org/10.2514/1.T6533.
[18] Z. Huang, Y.B. Xiong, Y.Q. Liu, P.X. Jiang, Y.H. Zhu, Experimental Investigation of Full-Coverage Effusion Cooling through Perforated Flat Plates, Appl. Therm. Eng. 76 (2015) 76–85, https://doi.org/10.1016/j.applthermaleng.2014.11.056.
[19] X. Li, Z. Liao, H. Li, P. Jiang, R. Xu, Phase-Change Transpiration Cooling in Heterogeneous Composite Porous Plates: Heat Transfer Characteristics and Their Prediction, 125290, Int. J. Heat. Mass. Transf. 224 (2024) 125290, https://doi.org/10.1016/j.ijheatmasstransfer.2024.125290.
[20] S. Zhang, X. Li, J. Zuo, J. Qin, K. Cheng, Y. Feng, W. Bao, Research Progress on Active Thermal Protection for Hypersonic Vehicles, 100646, Prog. Aerosp. Sci. 119 (2020) 100646, https://doi.org/10.1016/j.paerosci.2020.100646.
[21] M. Araya, M. Jaskari, T. Rautio, T. Guillén, A. Järvenpää, Assessing the compressive and tensile properties of TPMS-gyroid and stochastic Ti64 lattice structures: a study on laser powder bed fusion manufacturing for biomedical implants, J. Sci. Adv. Mater. Devices 9 (2024) 100663, https://doi.org/10.1016/j.jsamd.2023.100663.
[22] O. Al-Ketan, R. Rowshan, R.K. Abu Al-Rub, Topology–mechanical property relationship of 3d-printed strut-, skeletal-, and sheet-based periodic metallic cellular materials, Addit. Manuf. 19 (2018) 167–183, https://doi.org/10.1016/j.addma.2017.12.006.
[23] T. Femmer, A.J.C. Kuehne, M. Wessling, Estimation of the structure-dependent performance of 3-D rapid-prototyped membranes, Chem. Eng. J. 273 (2015) 438–445, https://doi.org/10.1016/j.cej.2015.03.029.
[24] W. Li, W. Li, Z. Yu, Heat transfer enhancement of water-cooled triply periodic minimal surface heat exchangers, Appl. Therm. Eng. 217 (2022) 119198, https://doi.org/10.1016/j.applthermaleng.2022.119198.
[25] M. Broumand, J. Son, Y. Pyo, S. Yun, Z. Hong, TPMS-Based Transpiration Cooling for Film Cooling Enhancement, 125824, Int. J. Heat. Mass. Transf. 231 (2024) 125824, https://doi.org/10.1016/j.ijheatmasstransfer.2024.125824.
[26] J. Son, Y. Pyo, P. Richer, B. Jodoin, Z. Hong, Impact of Triply Periodic Minimal Surface Structure Unit Cell Size on Transpiration Cooling, J. Thermophys. Heat. Transf. 40 (2026) 253–265, https://doi.org/10.2514/1.T7212.
[27] J. Son, M. Broumand, Y. Pyo, P. Richer, B. Jodoin, Z. Hong, Effects of Lattice Orientation Angle on TPMS-Based Transpiration Cooling, J. Eng. Gas. Turbines Power 147 (2025) 061010, https://doi.org/10.1115/1.4067378.
[28] J. Son, P. Richer, B. Jodoin, S. Kashanj, Z. Hong, Coolant Redistribution via Functionally Graded Porosity in TPMS Structures for Enhanced Transpiration Cooling, Unpublished results (manuscript under review at The Aeronautical Journal).
[29] Z. Zhou, Y. Lv, F. He, T. Liu, J. Wang, Pore-Scale Investigation of Transpiration Cooling Based on Triply Periodic Minimal Surface, 109019, Int. J. Therm. Sci. 201 (2024) 109019, https://doi.org/10.1016/j.ijthermalsci.2024.109019.
[30] B.J. Brimacombe, J.A. Scobie, J.M. Flynn, C.M. Sangan, O.J. Pountney, Effect of Porosity and Injection Ratio on the Performance of Transpiration Cooling through Gyroids, Int. J. Turbomach. Propuls. Power 8 (2023) 50, https://doi.org/10.3390/ijtpp8040050.
[31] K. Yeranee, Y. Rao, Q. Zuo, J. Xie, Thermal Performance Enhancement for Gas Turbine Blade Trailing Edge Cooling with Topology-Optimized Printable Diamond TPMS Lattice, 109649, Int. J. Heat. Fluid. Flow. 110 (2024) 109649, https://doi.org/10.1016/j.ijheatfluidflow.2024.109649.
[32] F. He, C. He, S. Xie, Z. Zhou, J. Xu, M. Li, Synergistic Thermal Protection Performance of TPMS Transpiration–Film Cooling Coupled with Silica Aerogel Thermal Barrier Coating, 130612, Appl. Therm. Eng. 294 (2026) 130612, https://doi.org/10.1016/j.applthermaleng.2026.130612.
[33] D.G. Bogard, K.A. Thole, Gas Turbine Film Cooling, J. Propuls. Power 22 (2006) 249–270, https://doi.org/10.2514/1.18034.
[34] S. Haydt, S. Lynch, Cooling Effectiveness for a Shaped Film Cooling Hole at a Range of Compound Angles, J. Turbomach. 141 (2019) 041005, https://doi.org/10.1115/1.4041603.
[35] D.L. Schmidt, B. Sen, D.G. Bogard, Film Cooling with Compound-Angle Holes: Adiabatic Effectiveness, J. Turbomach. 118 (1996) 807–813, https://doi.org/10.1115/1.2840938.
[36] J. Son, P. Richer, B. Jodoin, Z. Hong, Effect of Morphological Variations in TPMS Lattice Structures on Transpiration Cooling. Proceedings of the ASME Turbo Expo 2025: Turbomachinery Technical Conference and Exposition, ASME Paper GT2025-151422, V006T13A003, Memphis, TN, USA, 2025, https://doi.org/10.1115/GT2025-151422.
[37] O. Al-Ketan, M. Ali, M. Khalil, R. Rowshan, K.A. Khan, R.K. Abu Al-Rub, Forced Convection Computational Fluid Dynamics Analysis of Architected Three-Dimensional Printable Heat Sinks Based on Triply Periodic Minimal Surfaces, J. Therm. Sci. Eng. Appl. 13 (2021) 011020, https://doi.org/10.1115/1.4047385.
[38] Y. Lu, Z. Cui, L. Cheng, J. Li, Z. Yang, H. Zhu, C. Wu, Quantifying the Discrepancies in the Geometric and Mechanical Properties of Theoretically Designed and Additively Manufactured Scaffolds, 104080, J. Mech. Behav. Biomed. Mater. 112 (2020) 104080, https://doi.org/10.1016/j.jmbbm.2020.104080.
[39] C. Yan, L. Hao, A. Hussein, D. Raymont, Evaluations of Cellular Lattice Structures Manufactured Using Selective Laser Melting, Int. J. Mach. Tools Manuf. 62 (2012) 32–38, https://doi.org/10.1016/j.ijmachtools.2012.06.002.
[40] Z. Lei, A. Mahallati, M. Cunningham, P. Germain, Influence of Inlet Swirl on the Aerodynamics of a Model Turbofan Lobed Mixer. Proceedings of the ASME 2010 International Mechanical Engineering Congress and Exposition, ASME Paper IMECE2010-39116, 2010, pp. 807–819, https://doi.org/10.1115/IMECE2010-39116.
[41] J. Son, P. Richer, B. Jodoin, S. Kashanj, M. Broumand, Z. Hong, Comparison of Adiabatic and Overall Film Cooling Effectiveness for Effusion Cooling Using Pressure- and Temperature-Sensitive Paint, June 15–19. Proceedings of the ASME Turbo Expo 2026: Turbomachinery Technical Conference and Exposition, ASME Paper GT2026-176858, Milan, Italy, 2026, https://doi.org/10.1115/GT2026-176858.
[42] J.-C. Han, A.P. Rallabandi, Turbine Blade Film Cooling Using PSP Technique, Front. Heat. Mass. Transf. 1 (2010) 013001, https://doi.org/10.5098/hmt.v1.1.3001.
[43] M.J. Rigby, A.B. Johnson, M.L.G. Oldfield, Gas Turbine Rotor Blade Film Cooling with and without Simulated NGV Shock Waves and Wakes. Proceedings of the ASME 1990 International Gas Turbine and Aeroengine Congress and Exposition, ASME Paper 90-GT-078, Brussels, Belgium, 1990, https://doi.org/10.1115/90-GT-078.
[44] G. Barigozzi, C. Mucignat, H. Abdeh, D. Scandella, G. Dolci, Assessment of binary PSP technique for film cooling effectiveness measurement on nozzle vane cascade with cutback trailing edge, Exp. Therm. Fluid. Sci. 97 (2018) 431–443, https://doi.org/10.1016/j.expthermflusci.2018.05.015.
[45] B.W. Reynolds, C.J. Fee, K.R. Morison, D.J. Holland, Characterisation of heat transfer within 3D printed TPMS heat exchangers, 124264, Int. J. Heat. Mass. Transf. 212 (2023) 124264, https://doi.org/10.1016/J.IJHEATMASSTRANSFER.2023.124264.
[46] W. Dahmen, T. Gotzen, S. Müller, M. Rom, Numerical Simulation of Transpiration Cooling through Porous Material, Int. J. Numer. Methods Fluids 76 (2014) 331–365, https://doi.org/10.1002/fld.3935.
[47] J. Fu, H.R. Thomas, C. Li, Tortuosity of Porous Media: Image Analysis and Physical Simulation, 103439, Earth-Sci. Rev. 212 (2021) 103439, https://doi.org/10.1016/j.earscirev.2020.103439.
[48] J. Wang, K. Chen, M. Zeng, T. Ma, Q. Wang, Z. Cheng, Investigation on Flow and Heat Transfer in Various Channels Based on Triply Periodic Minimal Surfaces (TPMS), 116955, Energy Convers. Manag. 283 (2023) 116955, https://doi.org/10.1016/j.enconman.2023.116955.
[49] J.J. Scrittore, K.A. Thole, S.W. Burd, Investigation of Velocity Profiles for Effusion Cooling of a Combustor Liner, J. Turbomach. 129 (2007) 518–526, https://doi.org/10.1115/1.2720492.
[50] H.D. Ammari, N. Hay, D. Lampard, The Effect of Density Ratio on the Heat Transfer Coefficient from a Film-Cooled Flat Plate, J. Turbomach. 112 (1990) 444–450, https://doi.org/10.1115/1.2927679.
[51] A.H. Lefebvre, D.R. Ballal, Boca Raton, FL. Gas Turbine Combustion: Alternative Fuels and Emissions, 3rd ed, CRC Press, 2010.
[52] J.E. Albert, D.G. Bogard, F. Cunha, Adiabatic and Overall Effectiveness for a Film-Cooled Blade, June 14–17. Proceedings of the ASME Turbo Expo 2004: Power for Land, Sea, and Air, ASME Paper GT2004-53998, Vienna, Austria, 2004, pp. 251–259, https://doi.org/10.1115/GT2004-53998. June 14–17.
[53] K.L. Harrison, D.G. Bogard, Use of the Adiabatic Wall Temperature in Film Cooling to Predict Wall Heat Flux and Temperature, June 9–13. Proceedings of the ASME Turbo Expo 2008: Power for Land, Sea, and Air, ASME Paper GT2008-51424, Berlin, Germany, 2008, pp. 1197–1207, https://doi.org/10.1115/GT2008-51424. June 9–13.
[54] J. Maikell, D.G. Bogard, J. Piggush, A. Kohli, Experimental simulation of a film-cooled turbine blade leading edge including thermal barrier coating effects, J. Turbomach. 133 (2011) 011007, https://doi.org/10.1115/1.4000537.

Chapter 6

Conclusions

The studies presented in this thesis establish design guidelines for TPMS-based transpiration cooling of gas turbine combustor liners through systematic investigations of lattice geometry, coolant distribution, and cooling mechanisms. The findings provide practical recommendations for designing next-generation combustor liners capable of achieving higher cooling effectiveness, improved coolant utilization, and enhanced durability while supporting the continued increase in turbine inlet temperature. The main conclusions are summarized as follows:

1) The Influence of TPMS Unit Cell Size on Transpiration Cooling Performance: Reducing unit cell size significantly enhances transpiration cooling performance by promoting earlier and more uniform film formation. Smaller unit cells facilitate more effective coolant transport to the surface due to their shallower surface void depth, enabling earlier film formation, resulting in higher film cooling effectiveness. Smaller unit cells are less susceptible to internal tangential flow than larger ones. In larger unit cells, stronger internal tangential flow transports coolant downstream, delaying film development, particularly at low injection ratios. However, excessively small unit cells may introduce manufacturability constraints and increase the risk of clogging, indicating the need for an optimal unit cell size.
2) The Influence of TPMS Porosity on Transpiration Cooling Performance: Increasing porosity enhances transpiration cooling performance by improving coolant distribution and promoting more uniform surface coverage. Higher porosity levels result in greater film cooling effectiveness, particularly at elevated coolant flow rates. Compared to conventional effusion cooling, TPMS-based transpiration cooling achieves significantly higher effectiveness—up to several times greater—due to its continuous and evenly distributed coolant supply, while avoiding film lift-off effects. However, the performance advantage diminishes at lower porosity and flow conditions, indicating a coupled dependence on both parameters.
3) The Influence of TPMS Orientation Angle on Transpiration Cooling Performance: The orientation of TPMS surface features relative to the mainstream flow significantly affects cooling performance. Configurations with surface void perpendicular to the mainstream promote more effective coolant discharge and earlier film formation, resulting in higher

film cooling effectiveness compared to parallel orientations, where coolant is more readily channeled downstream. The sensitivity to orientation varies with TPMS geometry. Increased surface tortuosity reduces orientation sensitivity by promoting more uniform coolant distribution. Among the investigated structures, the Koch-type TPMS exhibited the lowest sensitivity to orientation while maintaining high overall cooling effectiveness, indicating superior robustness under varying flow directions.

4) The Influence of TPMS Morphology on Transpiration Cooling Performance: TPMS morphology significantly influences transpiration cooling performance and its sensitivity to geometric variations. The Diamond-type structure exhibits higher cooling effectiveness than the Gyroid-type but also shows strong sensitivity to morphological changes, making it less suitable for applications involving complex or curved surfaces. In contrast, the Koch-type demonstrates minimal sensitivity to morphological variations due to its complex and distributed surface features, while maintaining high overall cooling effectiveness. Importantly, low sensitivity to morphological variation does not necessarily guarantee superior cooling performance, as effectiveness is also governed by factors such as pressure drop and flow distribution. Among the geometries considered, the Koch-type exhibits both high cooling performance and minimal sensitivity to morphological variations, making it a strong candidate for applications involving complex geometries.
5) The Influence of Internal Tangential Flow on Transpiration Cooling: Internal tangential flow within TPMS structures leads to non-uniform coolant distribution by transporting coolant downstream, resulting in insufficient cooling near the leading edge and localized accumulation near the trailing edge. This behavior hinders the formation of a stable and uniform cooling film. The introduction of partition walls effectively suppresses internal tangential flow, promoting coolant discharge in the intended direction. As a result, cooling effectiveness near the leading edge is significantly improved, and a more uniform and stable cooling film is established across the surface. These findings confirm that controlling internal flow pathways is critical for achieving uniform coolant distribution and enhanced transpiration cooling performance.
6) Functionally graded porosity significantly improves transpiration cooling performance by enhancing coolant distribution and film uniformity. Compared to uniform porosity, graded profiles promote earlier film formation and better utilization of coolant, particularly near the leading edge. Among the profiles investigated, the GLD (gradual linear decay) and ED (exponential decay) configurations provide the most balanced and effective performance. GLD improves leading-edge cooling while maintaining downstream effectiveness,

whereas ED achieves the highest overall uniformity and rapid stabilization of the cooling film. These results demonstrate that appropriate porosity grading enables more uniform and efficient cooling over extended surfaces, with the ED profile being particularly advantageous for practical applications requiring sustained cooling performance over long streamwise distances.

7) Simultaneous measurements of adiabatic film cooling effectiveness (AFE) and overall film cooling effectiveness (OFE) revealed the relative contributions of coolant-film protection and conjugate heat transfer (CHT) to the overall cooling performance. While conventional effusion cooling relies primarily on conjugate heat transfer to reduce wall temperature, TPMS-based transpiration cooling fundamentally shifts the dominant cooling mechanism toward coolant-film protection by generating a continuous and uniformly distributed coolant film that shields the wall from the hot mainstream before it reaches the surface. As a result, the heat load imposed on the wall is substantially reduced, thereby decreasing the reliance on conjugate heat transfer. The interconnected porous network also enhances internal convective heat transfer, providing an additional contribution to cooling performance. As a result, TPMS-based transpiration cooling achieves higher overall cooling effectiveness and superior spatial uniformity than conventional effusion cooling. These findings demonstrate that future TPMS combustor liners should be designed to maximize uniform coolant discharge and continuous coolant-film formation while maintaining sufficient internal heat transfer, thereby optimizing both film cooling and conjugate heat transfer.

Chapter 7

Future Work

7.1 Potential Challenges for Engine Applications and Future Work

1) Density-Ratio Effect: The experiments in this study were conducted at a coolant-to-mainstream density ratio close to unity, whereas engine-relevant density ratios are typically approximately two [109,110] . This difference may lead to an overestimation of the relative advantage of transpiration cooling over effusion cooling. Previous effusion-cooling studies reported AFE differences of less than 20% between density ratios of approximately 2 and 1.2 near the injection region, with the differences becoming negligible farther downstream [109–111]. However, the influence of density ratio on the cooling effectiveness of the present TPMS structures has not yet been established. At a fixed injection ratio and for a given geometry, a 2.35-fold increase in density ratio reduces the coolant discharge velocity by the same factor. Accordingly, the discharge velocity at F = 1.60% and DR = 2.35 corresponds approximately to that measured at F = 0.68% and near-unity density ratio. For a conservative sensitivity assessment, the associated reduction in TPMS AFE is assumed to follow the reduction observed between these two injection ratios. Even under this assumption, the resulting TPMS AFE remains higher than the highest effusion-cooling AFE measured in this study. However, this velocity-based comparison does not account for other density-ratio effects, and its applicability requires further experimental validation.
2) Pressure-Drop: Pressure drops of approximately 1% have been reported in gas turbine combustor liner cooling studies [112]. In the present study, the pressure drop across the TPMS coupon was approximately 0.45% for the most favorable configuration examined. Nevertheless, the relationship between pressure drop and coolant injection ratio can vary substantially with TPMS unit cell size, porosity, and type of TPMS architecture, potentially affecting coolant delivery and cooling performance. Further experimental investigations are therefore needed to establish quantitative relationships between lattice geometry and pressure drop, enabling flow resistance optimization and reliable integration of TPMS structures into combustor liner designs.
3) Biot-Number Effects: The OFE experiments in this study were conducted using Inconel 718 coupons at ambient temperature and atmospheric pressure, yielding a Biot number of approximately 0.03, below the representative engine range of 0.36–2.1 [113]. At this low

Biot number, the conductive thermal resistance within the wall is small relative to the external convective thermal resistance. Consequently, the influence of wall conduction on overall cooling performance may differ from that under engine conditions. Although the observations concerning coolant distribution and external film formation provide a basis for engine applications, both the absolute overall cooling effectiveness and the relative performance of different geometries require further validation at engine-relevant Biot numbers.

4) Effect of Turbulence Intensity: In practical gas turbine operation, turbulence intensity can reach up to 35% at the combustor exit [114] and typically ranges from 10% to 20% near combustor walls [115,116]. While the influence of turbulence intensity on effusion cooling has been extensively studied [106], its impact on transpiration cooling—particularly for deterministic TPMS-based porous structures—remains unclear.
5) Mechanical Strength Assessment: Ensuring sufficient mechanical strength is critical for transpiration-cooled liners. Conventional stochastic porous media, despite their cooling effectiveness, often suffer from low mechanical strength due to stress concentration in irregular ligament structures. In contrast, TPMS structures, with their uniform and deterministic geometry, are expected to offer improved mechanical performance. Experimental investigations using representative materials, such as nickel-based superalloys, are necessary to evaluate their structural integrity.
6) Material Innovation: In addition to aerodynamic optimization, material advancements—particularly in thermal barrier coatings—should be pursued to further enhance cooling performance and durability. The integration of advanced materials can complement TPMS-based cooling strategies in high-temperature environments.
7) Structural Optimization and Hybrid Configuration: One of the key advantages of additive manufacturing lies in its ability to realize complex geometries with high design flexibility and minimal constraints on material selection. From this perspective, further enhancement of transpiration cooling performance can be achieved through structural optimization. For instance, high thermal conductivity materials, such as copper ($k \approx 400$ W/m·K), may be incorporated into regions not directly exposed to the hot gas flow to enhance heat dissipation through the lattice. In contrast, regions directly exposed to high-temperature gases can be fabricated using nickel-based superalloys with superior thermal resistance and oxidation stability. Furthermore, hybrid cooling concepts that combine transpiration cooling with effusion cooling may also be considered. Such approaches can leverage the

advantages of both techniques, including enhanced heat transfer performance, improved mechanical robustness, and controlled pressure drop.

Bibliography

[1] F. Nasiri, F. Bayat, S. Mobayen, S.H. Hosseinnia, Gas Turbines Power Regulation Subject to Actuator Constraints, Disturbances and Measurement Noises, **IEEE Access** 9 (2021) 40155–40164. https://doi.org/10.1109/ACCESS.2021.3064893.

[2] C. Borgnakke, **Fundamentals of Thermodynamics**, John Wiley & Sons, Hoboken, NJ, 2025.

[3] T.K. Ibrahim, M.M. Rahman, Study on Effective Parameter of the Triple-Pressure Reheat Combined Cycle Performance, **Therm. Sci.** 17 (2013) 497–508. https://doi.org/10.2298/TSCI111016143I.

[4] M.A. Khan, S. Sundarrajan, S. Natarajan, P. Parameswaran, E. Mohandas, Oxidation and Hot Corrosion Behavior of Nickel-Based Superalloy for Gas Turbine Applications, **Mater. Manuf. Process.** 29 (2014) 832–839. https://doi.org/10.1080/10426914.2014.901530.

[5] J.-C. Han, Recent Studies in Turbine Blade Cooling, **Int. J. Rotat. Mach.** 10 (2004) 443–457. https://doi.org/10.1155/S1023621X04000442.

[6] S. Gupta, A. Chaube, P. Verma, Review on Heat Transfer Augmentation Techniques: Application in Gas Turbine Blade Internal Cooling, **J. Eng. Sci. Technol. Rev.** 5 (2012) 57–62. https://doi.org/10.25103/jestr.051.11.

[7] P. Ligrani, Heat Transfer Augmentation Technologies for Internal Cooling of Turbine Components of Gas Turbine Engines, **Int. J. Rotat. Mach.** 2013 (2013) 275653. https://doi.org/10.1155/2013/275653.

[8] N. Zuckerman, N. Lior, Jet Impingement Heat Transfer: Physics, Correlations, and Numerical Modeling, **Adv. Heat Transf.** 39 (2006) 565–631. https://doi.org/10.1016/S0065-2717(06)39006-5.

[9] X. Fan, L. Li, J. Zou, Y. Zhou, Cooling Methods for Gas Turbine Blade Leading Edge: Comparative Study on Impingement Cooling, Vortex Cooling and Double Vortex Cooling, **Int. Commun. Heat Mass Transf.** 100 (2019) 133–145. https://doi.org/10.1016/j.icheatmasstransfer.2018.12.017.

[10] W. Wang, Y. Yan, Y. Zhou, J. Cui, Review of Advanced Effusive Cooling for Gas Turbine Blades, **Energies** 15 (2022) 8568. https://doi.org/10.3390/en15228568.

[11] R. Krewinkel, A Review of Gas Turbine Effusion Cooling Studies, **Int. J. Heat Mass Transf.** 66 (2013) 706–722. https://doi.org/10.1016/j.ijheatmasstransfer.2013.07.071.

[12] Y. Pyo, J. Son, P. Richer, B. Jodoin, M. Broumand, S. Yun, Z. Hong, Isolating Influences of Varying Pitch from the Effects of Non-Zero Compound Angles on Effusion Cooling, **Aeronaut. J.** 129 (2025) 1–21. https://doi.org/10.1017/aer.2024.108.

[13] H.H. Cho, D.H. Rhee, Local Heat/Mass Transfer Measurement on the Effusion Plate in Impingement/Effusion Cooling Systems, **J. Turbomach.** 123 (2001) 601–608. https://doi.org/10.1115/1.1344904.

[14] J.-C. Han, S. Dutta, S.V. Ekkad, **Gas Turbine Heat Transfer and Cooling Technology**, 2nd ed., CRC Press, Boca Raton, FL, 2012.

[15] E.R.G. Eckert, J.N.B. Livingood, Comparison of Effectiveness of Convection-, Transpiration-, and Film-Cooling Methods with Air as Coolant, **NACA Technical Note 3010**, National Advisory Committee for Aeronautics, Washington, DC, 1953.

[16] D. Curry, A. Gomez, C. Johnston, Radiative, Ablative, and Active Cooling Thermal Protection Studies for the Leading Edge of a Fixed-Straight Wing Space Shuttle, in: **Proceedings of the 6th AIAA Thermophysics Conference**, AIAA Paper 71-445, 1971.

[17] S. Weinbaum, H.L. Wheeler, Heat Transfer in Sweat-Cooled Porous Metals, **J. Appl. Phys.** 20 (1949) 113–122. https://doi.org/10.1063/1.1698226.

[18] Y.Q. Liu, P.X. Jiang, Y.B. Xiong, Y.P. Wang, Experimental and Numerical Investigation of Transpiration Cooling for Sintered Porous Flat Plates, **Appl. Therm. Eng.** 50 (2013) 997–1007. https://doi.org/10.1016/j.applthermaleng.2012.08.028.

[19] J. Ma, X. Luo, H. Li, Y. Liu, An Experimental Investigation on Transpiration Cooling Based on the Multilaminated Sintered Woven Wire Mesh Structures, **J. Therm. Sci. Eng. Appl.** 8 (2016) 041004. https://doi.org/10.1115/1.4032921.

[20] M. Hinse, P. Richer, B. Jodoin, K. Yildiz, S. Yun, Z. Hong, Numerical and Experimental Studies of Transpiration Cooling Film Effectiveness over Porous Materials, in: **AIAA Propulsion and Energy 2020 Forum**, AIAA Paper 2020-3947, American Institute of Aeronautics and Astronautics, 2020. https://doi.org/10.2514/6.2020-3947.

[21] Z. Huang, Y.B. Xiong, Y.Q. Liu, P.X. Jiang, Y.H. Zhu, Experimental Investigation of Full-Coverage Effusion Cooling through Perforated Flat Plates, **Appl. Therm. Eng.** 76 (2015) 76–85. https://doi.org/10.1016/j.applthermaleng.2014.11.056.

[22] X. Li, Z. Liao, H. Li, P. Jiang, R. Xu, Phase-Change Transpiration Cooling in Heterogeneous Composite Porous Plates: Heat Transfer Characteristics and Their Prediction, **Int. J. Heat Mass Transf.** 224 (2024) 125290. https://doi.org/10.1016/j.ijheatmasstransfer.2024.125290.

[23] Q. Mi, S.H. Yi, D.D. Gang, X.G. Lu, X.L. Liu, Research Progress of Transpiration Cooling for Aircraft Thermal Protection, **Appl. Therm. Eng.** 236 (2024) 121360. https://doi.org/10.1016/j.applthermaleng.2023.121360.

[24] S. Zhang, X. Li, J. Zuo, J. Qin, K. Cheng, Y. Feng, W. Bao, Research Progress on Active Thermal Protection for Hypersonic Vehicles, **Prog. Aerosp. Sci.** 119 (2020) 100646. https://doi.org/10.1016/j.paerosci.2020.100646.

[25] O. Al-Ketan, R. Rowshan, R.K. Abu Al-Rub, Topology–Mechanical Property Relationship of 3D Printed Strut, Skeletal, and Sheet-Based Periodic Metallic Cellular Materials, **Addit. Manuf.** 19 (2018) 167–183. https://doi.org/10.1016/j.addma.2017.12.006.

[26] B.W. Reynolds, C.J. Fee, K.R. Morison, D.J. Holland, Characterisation of Heat Transfer within 3D Printed TPMS Heat Exchangers, **Int. J. Heat Mass Transf.** 212 (2023) 124264. https://doi.org/10.1016/j.ijheatmasstransfer.2023.124264.

[27] W. Li, W. Li, Z. Yu, Heat Transfer Enhancement of Water-Cooled Triply Periodic Minimal Surface Heat Exchangers, **Appl. Therm. Eng.** 217 (2022) 119198. https://doi.org/10.1016/j.applthermaleng.2022.119198.

[28] J. Iyer, T. Moore, D. Nguyen, P. Roy, J. Stolaroff, Heat Transfer and Pressure Drop Characteristics of Heat Exchangers Based on Triply Periodic Minimal and Periodic Nodal Surfaces, **Appl. Therm. Eng.** 209 (2022) 118192. https://doi.org/10.1016/j.applthermaleng.2022.118192.

[29] S. Biswas, S. Ramachandra, P. Hans, S.P. Suresh Kumar, Materials for Gas Turbine Engines: Present Status, Future Trends and Indigenous Efforts, **Trans. Indian Natl. Acad. Eng.** 7 (2022) 1035–1053. https://doi.org/10.1007/s41745-022-00295-z.

[30] T.M. Pollock, S. Tin, Nickel-Based Superalloys for Advanced Turbine Engines: Chemistry, Microstructure and Properties, **J. Propuls. Power** 22 (2006) 361–374. https://doi.org/10.2514/1.18239.

[31] D. Furrer, H.-J. Fecht, Ni-Based Superalloys for Turbine Discs, **JOM** 51 (1999) 14–17. https://doi.org/10.1007/s11837-999-0005-y.

[32] S. Wu, Y. Zhao, W. Li, W. Liu, Y. Wu, F. Liu, Research Progresses on Ceramic Materials of Thermal Barrier Coatings on Gas Turbine, **Coatings** 11 (2021) 79. https://doi.org/10.3390/coatings11010079.

[33] M.S. Sahith, G. Giridhara, R.S. Kumar, Development and Analysis of Thermal Barrier Coatings on Gas Turbine Blades—A Review, **Mater. Today Proc.** 5 (2018) 2746–2751. https://doi.org/10.1016/j.matpr.2018.01.060.

[34] Rolls-Royce plc, **The Jet Engine**, John Wiley & Sons, Chichester, UK, 2015.

[35] R.S. Bunker, Evolution of Turbine Cooling, in: **Proceedings of the ASME Turbo Expo 2017: Turbomachinery Technical Conference and Exposition**, ASME Paper GT2017-63205, Charlotte, NC, USA, 2017. https://doi.org/10.1115/GT2017-63205

[36] W.A. Nelson, R.M. Orenstein, P.S. DiMascio, C.A. Johnson, Development of Advanced Thermal Barrier Coatings for Severe Environments, in: **Proceedings of the ASME 1995 International Gas Turbine and Aeroengine Congress and Exposition**, Vol. 4: Heat Transfer; Electric Power; Industrial and Cogeneration, ASME Paper 95-GT-270, Houston, TX, USA, 1995. https://doi.org/10.1115/95-GT-270.

[37] J.B. Anderson, E.J. Boyd, D.G. Bogard, Experimental Investigation of Coolant-to-Mainstream Scaling Parameters with Cylindrical and Shaped Film Cooling Holes, in: **Proceedings of the ASME Turbo Expo 2015: Turbine Technical Conference and Exposition**, Vol. 5B: Heat Transfer, ASME Paper GT2015-43072, Montreal, QC, Canada, 2015. https://doi.org/10.1115/GT2015-43072.

[38] S. Park, E.Y. Jung, S.H. Kim, H.S. Sohn, H.H. Cho, Enhancement of Film Cooling Effectiveness Using Backward Injection Holes, **Int. J. Therm. Sci.** 110 (2016) 314–324. https://doi.org/10.1016/j.ijthermalsci.2016.08.001.

[39] G.E. Andrews, M. Alikhanizadeh, F.B. Tehrani, C.I. Hussain, M.S.K. Azari, Small Diameter Film Cooling Holes: The Influence of Hole Size and Pitch, **Int. J. Turbo Jet Engines** 5 (1988) 61–72. https://doi.org/10.1515/TJJ.1988.5.1-4.61.

[40] C. Wang, J. Zhang, J. Zhou, Optimization of a Fan-Shaped Hole to Improve Film Cooling Performance by RBF Neural Network and Genetic Algorithm, **Aerosp. Sci. Technol.** 58 (2016) 18–25. https://doi.org/10.1016/j.ast.2016.08.004.

[41] W. Wang, J. Cui, S. Qu, Effects of Hole Arrangement and Trenched Hole on Multirow Film Cooling, **AIP Adv.** 12 (2022) 045224. https://doi.org/10.1063/5.0082980.

[42] B. Facchini, L. Tarchi, L. Toni, A. Ceccherini, Adiabatic and Overall Effectiveness Measurements of an Effusion Cooling Array for Turbine Endwall Application, **J. Turbomach.** 132 (2010) 011006. https://doi.org/10.1115/1.3213555.

[43] G. Wang, G. Ledezma, J. Delancey, A. Wang, Experimental Study of Effusion Cooling with Pressure-Sensitive Paint, **J. Eng. Gas Turbines Power** 139 (2017) 021901. https://doi.org/10.1115/1.4034943.

[44] F. Bazdidi-Tehrani, G.E. Andrews, Full-Coverage Discrete Hole Film Cooling: Investigation of the Effect of Variable Density Ratio, **J. Eng. Gas Turbines Power** 116 (1994) 587–596. https://doi.org/10.1115/1.2906860.

[45] A. Andreini, R. Becchi, B. Facchini, A. Picchi, A. Peschiulli, The Effect of Effusion Holes Inclination Angle on the Adiabatic Film Cooling Effectiveness in a Three-Sector Gas Turbine Combustor Rig with a Realistic Swirling Flow, **Int. J. Therm. Sci.** 121 (2017) 75–88. https://doi.org/10.1016/j.ijthermalsci.2017.07.003.

[46] D.L. Schmidt, B. Sen, D.G. Bogard, Film Cooling with Compound Angle Holes: Adiabatic Effectiveness, **J. Turbomach.** 118 (1996) 807–813. https://doi.org/10.1115/1.2840938.

[47] L. Yang, W. Dai, Y. Rao, M.K. Chyu, A Machine Learning Approach to Quantify the Film Cooling Superposition Effect for Effusion Cooling Structures, **Int. J. Therm. Sci.** 162 (2021) 106774. https://doi.org/10.1016/j.ijthermalsci.2020.106774.

[48] S. Acharya, Y. Kanani, Advances in Film Cooling Heat Transfer, in: E.M. Sparrow, J.P. Abraham, J.M. Gorman (Eds.), **Advances in Heat Transfer**, Vol. 49, Academic Press, 2017, pp. 91–156. https://doi.org/10.1016/bs.aiht.2017.10.001.

[49] R.J. Goldstein, E.R.G. Eckert, F. Burggraf, Effects of Hole Geometry and Density on Three-Dimensional Film Cooling, **Int. J. Heat Mass Transf.** 17 (1974) 595–607. https://doi.org/10.1016/0017-9310(74)90007-6.

[50] A.K. Sinha, D.G. Bogard, M.E. Crawford, Film-Cooling Effectiveness Downstream of a Single Row of Holes with Variable Density Ratio, **J. Turbomach.** 113 (1991) 442–449. https://doi.org/10.1115/1.2927894.

[51] S. Bernsdorf, M.G. Rose, R.S. Abhari, Modeling of Film Cooling—Part I: Experimental Study of Flow Structure, **J. Turbomach.** 128 (2006) 141–149. https://doi.org/10.1115/1.2098768.

[52] T. Nguyentat, W. Hayes, T. Meland, E. Veith, D. Ellis, Fabrication of a Liquid Rocket Combustion Chamber Liner of Advanced Copper Alloy GRCop-84 via Formed Platelet Liner Technology, in: **Proceedings of the 42nd AIAA/ASME/SAE/ASEE Joint Propulsion Conference & Exhibit**, AIAA Paper 2006-5192, Sacramento, CA, USA, 2006. https://doi.org/10.2514/6.2006-5192.

[53] M. Hinse, K. Yildiz, P. Richer, B. Jodoin, M. Broumand, S. Yun, Z. Hong, Numerical and Experimental Studies of Transpiration Cooling Film Effectiveness over Porous Materials, **J. Thermophys. Heat Transf.** 36 (2022) 803–817. https://doi.org/10.2514/1.T6533.

[54] G. Huang, Z. Liao, R. Xu, Y. Zhu, P.X. Jiang, Self-Pumping Transpiration Cooling with a Protective Porous Armor, **Appl. Therm. Eng.** 164 (2020) 114485. https://doi.org/10.1016/j.applthermaleng.2019.114485.

[55] A.V. Murray, P.T. Ireland, T.H. Wong, S.W. Tang, A.J. Rawlinson, High Resolution Experimental and Computational Methods for Modelling Multiple Row Effusion Cooling Performance, **Int. J. Turbomach. Propuls. Power** 3 (2018) 4. https://doi.org/10.3390/ijtpp3010004.

[56] A. Wambersie, H. Wong, P. Ireland, I. Mayo, Experiments of Transpiration Cooling Inspired Panel Cooling on a Turbine Blade Yielding Film Effectiveness Levels over 95%, in: **Proceedings of the 14th European Conference on Turbomachinery Fluid Dynamics and Thermodynamics (ETC 2021)**, Gdańsk, Poland, 2021. https://doi.org/10.57060/ETC2021-560.

[57] G. Huang, Y. Zhu, Z.-Y. Liao, Z. Huang, P.-X. Jiang, Transpiration Cooling with Bio-Inspired Structured Surfaces, **Bioinspir. Biomim.** 15 (2020) 036016. https://doi.org/10.1088/1748-3190/ab6bdf.

[58] G. Huang, Z. Min, L. Yang, P.-X. Jiang, M.K. Chyu, Transpiration Cooling for Additively Manufactured Porous Plates with Partition Walls, **Int. J. Heat Mass Transf.** 124 (2018) 1076–1087. https://doi.org/10.1016/j.ijheatmasstransfer.2018.03.110.

[59] Y. Yang, J. Mao, P. Chen, H. Zhang, H. Tang, Numerical Investigation on Transpiration Cooling Performance with Different Porosities and Mainstream Pressure Gradients, **Int. J. Therm. Sci.** 184 (2023) 107991. https://doi.org/10.1016/j.ijthermalsci.2022.107991.

[60] W. Dong, J. Wang, S. Chen, B. Ai, X. Luo, Modelling and Investigation on Heat Transfer Deterioration During Transpiration Cooling with Liquid Coolant Phase-Change, **Appl. Therm. Eng.** 128 (2018) 381–392. https://doi.org/10.1016/j.applthermaleng.2017.08.155.

[61] Y. Liu, T. Liu, R. Ding, F. He, J. Wang, Experimental and Numerical Investigation of Transpiration Cooling with Gradient Porosity Layout for the Thermal Protection of Nose Cone, **Aerosp. Sci. Technol.** 149 (2024) 109140. https://doi.org/10.1016/j.ast.2024.109140.

[62] L. Han, Y. Zhang, Z. Zhang, W. Zhang, S. Liu, W. Li, Numerical Investigation of Flow Distribution and Transpiration Cooling Performance in Heterogeneous Porous Media with Reacting Coolant, **Appl. Therm. Eng.** 249 (2024) 123468. https://doi.org/10.1016/j.applthermaleng.2024.123468.

[63] F. Ackowiak, B. Ciupek, Ł. Brodzik, K. Yeranee, Y. Rao, A Review of Recent Research on Flow and Heat Transfer Analysis in Additively Manufactured Transpiration Cooling for Gas Turbines, **Energies** 18 (2025) 3282. https://doi.org/10.3390/en18133282.

[64] H. Xu, R. Su, Y. He, X. Zhang, C. Hu, D. Tang, Research Progress on the Failure Modes and Failure Mechanisms of the Transpiration Cooling Structure, **Int. Commun. Heat Mass Transf.** 167 (2025) 109399. https://doi.org/10.1016/j.icheatmasstransfer.2025.109399.

[65] V. König, M. Rom, S. Müller, M. Selzer, S. Schweikert, J. von Wolfersdorf, Numerical and Experimental Investigation of Transpiration Cooling with Carbon/Carbon Characteristic Outflow Distributions, **J. Thermophys. Heat Transf.** 33 (2019) 449–461. https://doi.org/10.2514/1.T5457.

[66] H. Sun, H. Ma, L. Yan, H. Fu, Y. Luan, P. Zunino, Numerical Simulations on the Performance of Transpiration Cooling Implemented with Perforated Flat Plates, **Appl. Therm. Eng.** 238 (2024) 121943. https://doi.org/10.1016/j.applthermaleng.2023.121943.

[67] K. Yeranee, Y. Rao, A Review of Recent Research on Flow and Heat Transfer Analysis in Additively Manufactured Transpiration Cooling for Gas Turbines, **Energies** 18 (2025) 3282. https://doi.org/10.3390/en18133282.

[68] E. Ryshkewitch, Compression Strength of Porous Sintered Alumina and Zirconia: Ninth Communication to Ceramography, **J. Am. Ceram. Soc.** 36 (1953) 65–68.

[69] N. Miyazaki, T. Hoshide, Influence of Porosity and Pore Distributions on Strength Properties of Porous Alumina, **J. Mater. Eng. Perform.** 27 (2018) 4345–4354. https://doi.org/10.1007/s11665-018-3500-x.

[70] A.B. Wassell, J.K. Bhangu, The Development and Application of Improved Combustor Wall Cooling Techniques, in: **Proceedings of the ASME 1980 International Gas Turbine Conference and Products Show**, Vol. 1A: General, ASME Paper 80-GT-66, New Orleans, LA, USA, 1980. https://doi.org/10.1115/80-GT-66.

[71] L. Yang, W. Chen, M.K. Chyu, A Convolution Modeling Method for Pore Plugging Impact on Transpiration Cooling Configurations Perforated by Straight Holes, **Int. J. Heat Mass Transf.** 126 (2018) 1057–1066. https://doi.org/10.1016/j.ijheatmasstransfer.2018.06.068.

[72] A.E. Jakus, N.R. Geisendorfer, P.L. Lewis, R.N. Shah, 3D-Printing Porosity: A New Approach to Creating Elevated Porosity Materials and Structures, **Acta Biomater.** 72 (2018) 94–109. https://doi.org/10.1016/j.actbio.2018.03.039.

[73] M. Kim, D.H. Shin, J.S. Kim, B.J. Lee, J. Lee, Experimental Investigation of Effusion and Transpiration Air Cooling for Single Turbine Blade, **Appl. Therm. Eng.** 182 (2021) 116156. https://doi.org/10.1016/j.applthermaleng.2020.116156.

[74] Z. Min, G. Huang, S.N. Parbat, L. Yang, M.K. Chyu, Experimental Investigation on Additively Manufactured Transpiration and Film Cooling Structures, **J. Turbomach.** 141 (2019) 051009. https://doi.org/10.1115/1.4042009.

[75] H.A. Schwarz, **Gesammelte Mathematische Abhandlungen**, Springer, Berlin, 1890.

[76] O. Al-Ketan, R.K. Abu Al-Rub, Multifunctional Mechanical Metamaterials Based on Triply Periodic Minimal Surface Lattices, **Adv. Eng. Mater.** 21 (2019) 1900524. https://doi.org/10.1002/adem.201900524.

[77] Z.A. Qureshi, E. Elnajjar, O. Al-Ketan, R.A. Al-Rub, S.B. Al-Omari, Heat Transfer Performance of a Finned Metal Foam–Phase Change Material System Incorporating Triply Periodic Minimal Surfaces, **Int. J. Heat Mass Transf.** 170 (2021) 121001. https://doi.org/10.1016/j.ijheatmasstransfer.2021.121001.

[78] I. Hussain, O. Al-Ketan, F. Renda, M. Malvezzi, D. Prattichizzo, L. Seneviratne, R.K. Abu Al-Rub, D. Gan, Design and Prototyping of Soft–Rigid Tendon-Driven Modular Grippers Using Interpenetrating Phase Composite Materials, **Int. J. Rob. Res.** 39 (2020) 1635–1646. https://doi.org/10.1177/0278364920907697.

[79] I. Maskery, L. Sturm, A.O. Aremu, A. Panesar, C.B. Williams, C.J. Tuck, R.D. Wildman, I.A. Ashcroft, R.J.M. Hague, Insights into the Mechanical Properties of Several Triply Periodic Minimal Surface Lattice Structures Made by Polymer Additive Manufacturing, **Polymer** 152 (2018) 62–71. https://doi.org/10.1016/j.polymer.2017.11.049.

[80] C. Han, Y. Li, Q. Wang, S. Wen, Q. Wei, C. Yan, L. Hao, J. Liu, Y. Shi, Continuous Functionally Graded Porous Titanium Scaffolds Manufactured by Selective Laser Melting for Bone Implants, **J. Mech. Behav. Biomed. Mater.** 80 (2018) 119–127. https://doi.org/10.1016/j.jmbbm.2018.01.013.

[81] T. Femmer, A.J.C. Kuehne, M. Wessling, Estimation of the Structure-Dependent Performance of 3-D Rapid Prototyped Membranes, **Chem. Eng. J.** 273 (2015) 438–445. https://doi.org/10.1016/j.cej.2015.03.029.

[82] N. Song, W. Pu, L. Qiao, B. Wu, R. Liu, F. Luo, Numerical Simulation Study on the Heat Transfer and Flow Characteristics of Fuel/Lubricating Oil Heat Exchanger

Based on Triply Periodic Minimal Surface, **Appl. Therm. Eng.** 257 (2024) 124437. https://doi.org/10.1016/j.applthermaleng.2024.124437.

[83] J. Son, Y. Pyo, M. Broumand, Z. Hong, S. Sarafan, P. Wanjara, Advanced Transpiration Cooling Method Using Additive Manufactured TPMS Structure, in: **Proceedings of the 62nd Conference of Metallurgists (COM 2023)**, Springer, Cham, 2023. https://doi.org/10.1007/978-3-031-38141-6_59.

[84] Z. Zhou, Y. Lv, F. He, T. Liu, J. Wang, Pore-Scale Investigation of Transpiration Cooling Based on Triply Periodic Minimal Surface, **Int. J. Therm. Sci.** 201 (2024) 109019. https://doi.org/10.1016/j.ijthermalsci.2024.109019.

[85] B.J. Brimacombe, J.A. Scobie, J.M. Flynn, C.M. Sangan, O.J. Pountney, Effect of Porosity and Injection Ratio on the Performance of Transpiration Cooling through Gyroids, **Int. J. Turbomach. Propuls. Power** 8 (2023) 50. https://doi.org/10.3390/ijtpp8040050.

[86] K. Yeranee, Y. Rao, Q. Zuo, J. Xie, Thermal Performance Enhancement for Gas Turbine Blade Trailing Edge Cooling with Topology-Optimized Printable Diamond TPMS Lattice, **Int. J. Heat Fluid Flow** 110 (2024) 109649. https://doi.org/10.1016/j.ijheatfluidflow.2024.109649.

[87] F. He, C. He, S. Xie, Z. Zhou, J. Xu, M. Li, Synergistic Thermal Protection Performance of TPMS Transpiration–Film Cooling Coupled with Silica Aerogel Thermal Barrier Coating, **Appl. Therm. Eng.** 294 (2026) 130612. https://doi.org/10.1016/j.applthermaleng.2026.130612.

[88] A. Zamiri, J.T. Chung, Large Eddy Simulation of Compound Angle Effects on Cooling Effectiveness and Flow Structure of Fan-Shaped Holes, **Int. J. Heat Mass Transf.** 178 (2021) 121599. https://doi.org/10.1016/j.ijheatmasstransfer.2021.121599.

[89] S.V. Ekkad, D. Zapata, J.-C. Han, Film Effectiveness over a Flat Surface with Air and CO_2 Injection Through Compound Angle Holes Using a Transient Liquid Crystal Image Method, **J. Turbomach.** 119 (1997) 587–593. https://doi.org/10.1115/1.2841162.

[90] G. Huang, L. He, Influence of Inhomogeneous Porosity on Effusion Cooling, **Int. J. Heat Mass Transf.** 144 (2019) 118675. https://doi.org/10.1016/j.ijheatmasstransfer.2019.118675.

[91] W. Chen, K. Wang, Y. Wang, S. Tu, Z. Liu, H. Su, Numerical Investigation and Optimal Design of Transpiration Cooling Plate Structure for Gradient Porosity, **Int. J. Therm. Sci.** 197 (2024) 108755. https://doi.org/10.1016/j.ijthermalsci.2023.108755.

[92] M. Afshar, A.P. Anaraki, H. Montazerian, J. Kadkhodapour, Additive Manufacturing and Mechanical Characterization of Graded Porosity Scaffolds Designed Based on Triply Periodic Minimal Surface Architectures, **J. Mech. Behav. Biomed. Mater.** 62 (2016) 481–494. https://doi.org/10.1016/j.jmbbm.2016.05.027.

[93] N. Roudbarian, E. Jebellat, S. Famouri, M. Baniasadi, R. Hedayati, M. Baghani, Shape-Memory Polymer Metamaterials Based on Triply Periodic Minimal Surfaces, **Eur. J. Mech. A Solids** 96 (2022) 104676. https://doi.org/10.1016/j.euromechsol.2022.104676.

[94] C. Bhat, Y.S. Romario, L. Beránek, P. Saxena, R. Ghosh, W. Macek, M. Ramezani, C.P. Jiang, Fabrication Investigation and Properties Evaluation of Advanced Metal-Ceramic Lattice Composites Engineered by Ceramic Additive Manufacturing and

Infiltration Casting Process, **Int. J. Adv. Manuf. Technol.** 145 (2026) 3537–3558. https://doi.org/10.1007/s00170-026-18488-6.

[95] J. Yang, V. Moosabeiki, L. Bai, M. Cruz Saldívar, M.A. Leeflang, X. Chen, A.A. Zadpoor, M.J. Mirzaali, Strategy for Hybrid Connection of Porous Strut and Triply Periodic Minimal Surface Lattice Structures, **Nat. Commun.** 17 (2026) 9699. https://doi.org/10.1038/s41467-026-77560-7.

[96] O. Al-Ketan, M. Ali, M. Khalil, R. Rowshan, K.A. Khan, R.K. Abu Al-Rub, Forced Convection Computational Fluid Dynamics Analysis of Architected Three-Dimensional Printable Heat Sinks Based on Triply Periodic Minimal Surfaces, **J. Therm. Sci. Eng. Appl.** 13 (2021) 011020. https://doi.org/10.1115/1.4047385.

[97] Y. Lu, Z. Cui, L. Cheng, J. Li, Z. Yang, H. Zhu, C. Wu, Quantifying the Discrepancies in the Geometric and Mechanical Properties of Theoretically Designed and Additively Manufactured Scaffolds, **J. Mech. Behav. Biomed. Mater.** 112 (2020) 104080. https://doi.org/10.1016/j.jmbbm.2020.104080.

[98] C. Yan, L. Hao, A. Hussein, D. Raymont, Evaluations of Cellular Lattice Structures Manufactured Using Selective Laser Melting, **Int. J. Mach. Tools Manuf.** 62 (2012) 32–38. https://doi.org/10.1016/j.ijmachtools.2012.06.002.

[99] T. Liu, J.P. Sullivan, K. Asai, C. Klein, Y. Egami, **Pressure and Temperature Sensitive Paints**, Springer, Berlin, Heidelberg, 2005.

[100] J.-C. Han, A.P. Rallabandi, Turbine Blade Film Cooling Using PSP Technique, **Front. Heat Mass Transf.** 1 (2010) 013001. https://doi.org/10.5098/hmt.v1.1.3001.

[101] H. Abdeh, M. Miranda, S. Rouina, G. Barigozzi, Development of PSP Technique for Vane Film Cooling Investigations, in: **Energy Procedia** 126 (2017) 802–809. https://doi.org/10.1016/j.egypro.2017.08.285.

[102] K.-J. Moon, H. Mori, M. Furukawa, Simultaneous Measurement Method of Pressure and Temperature Using Dual-Layer PSP/TSP with Lifetime-Based Method, **Meas. Sci. Technol.** 29 (2018) 125301. https://doi.org/10.1088/1361-6501/aae408.

[103] G. Barigozzi, C. Mucignat, H. Abdeh, D. Scandella, G. Dolci, Assessment of Binary PSP Technique for Film Cooling Effectiveness Measurement on Nozzle Vane Cascade with Cutback Trailing Edge, **Exp. Therm. Fluid Sci.** 97 (2018) 431–443. https://doi.org/10.1016/j.expthermflusci.2018.05.015.

[104] M.J. Rigby, A.B. Johnson, M.L.G. Oldfield, Gas Turbine Rotor Blade Film Cooling with and without Simulated NGV Shock Waves and Wakes, in: **Proceedings of the ASME 1990 International Gas Turbine and Aeroengine Congress and Exposition**, Vol. 4: Heat Transfer; Electric Power; Industrial and Cogeneration, ASME Paper 90-GT-078, Brussels, Belgium, 1990. https://doi.org/10.1115/90-GT-078.

[105] H. Schlichting, K. Gersten, **Boundary-Layer Theory**, 9th ed., Springer, Berlin, Heidelberg, 2016.

[106] X. Chen, J. Krawciw, H. Xia, P.A. Denman, C. Bonham, J.F. Carrotte, Study of an Effusion-Cooled Plate with High Level of Upstream Fluctuation, **Appl. Therm. Eng.** 184 (2021) 116126. https://doi.org/10.1016/j.applthermaleng.2020.116126.

[107] H. Otsu, K. Fujita, T. Ito, Application of the Transpiration Cooling Method for Reentry Vehicles, in: **Proceedings of the 45th AIAA Aerospace Sciences Meeting and Exhibit**, AIAA Paper 2007-1209, Reno, NV, USA, 2007. https://doi.org/10.2514/6.2007-1209.

[108] M. Hinse, **Investigation of Transpiration Cooling Film Protection for Gas Turbine Engine Combustion Liner Application**, M.A.Sc. Thesis, University of Ottawa, Ottawa, ON, Canada, 2021.

[109] S. Baldauf, M. Scheurlen, A. Schulz, S. Wittig, Correlation of Film-Cooling Effectiveness from Thermographic Measurements at Enginelike Conditions, **J. Turbomach.** 124 (2002) 686–698. https://doi.org/10.1115/1.1504443.

[110] A.K. Sinha, D.G. Bogard, M.E. Crawford, Film-Cooling Effectiveness Downstream of a Single Row of Holes with Variable Density Ratio, **J. Turbomach.** 113 (1991) 442–449. https://doi.org/10.1115/1.2927894.

[111] D.R. Pedersen, E.R.G. Eckert, R.J. Goldstein, Film Cooling with Large Density Differences Between the Mainstream and the Secondary Fluid Measured by the Heat-Mass Transfer Analogy, **J. Heat Transfer** 99 (1977) 620–627. https://doi.org/10.1115/1.3450752.

[112] H. Ozogul, I.E. Tin, Overall Cooling Effectiveness of Effusion Cooled and Thermal Barrier Coated Swirl Stabilized Liquid Fueled Combustor Liner in Reacting Flow Conditions, **Proc. ASME Turbo Expo** 7A (2023) V07AT11A005. https://doi.org/10.1115/GT2023-103503.

[113] K.L. Harrison, D.G. Bogard, Use of the Adiabatic Wall Temperature in Film Cooling to Predict Wall Heat Flux and Temperature, in: **Proceedings of the ASME Turbo Expo 2008: Power for Land, Sea, and Air**, Berlin, Germany, 2008, pp. 1197–1207. https://doi.org/10.1115/GT2008-51424.

[114] D.R. Ballal, A.H. Lefebvre, Flame Quenching in Turbulent Flowing Gaseous Mixtures, **Symp. (Int.) Combust.** 16 (1977) 1689–1698. https://doi.org/10.1016/S0082-0784(77)80447-5.

[115] T. Bacci, A. Picchi, T. Lenzi, B. Facchini, Turbulence Intensity Measurements Across a NGV Cooled Cascade with Representative Lean Burn Combustor Outflow, in: **Proceedings of the 13th European Conference on Turbomachinery Fluid Dynamics and Thermodynamics (ETC 2019)**, Lausanne, Switzerland, 2019. https://doi.org/10.29008/ETC2019-100.

[116] M. Folk, R.J. Miller, J.D. Coull, The Impact of Combustor Turbulence on Turbine Loss Mechanisms, **J. Turbomach.** 142 (2020) 091009. https://doi.org/10.1115/1.4047615.